Waste to Fuel:
Designing a cobalt based catalyst and process for once-through Fischer-Tropsch synthesis operated at high conversion

THESIS

presented for the degree of

DOCTOR OF PHILOSOPHY

by

Chelsea Lyn Tucker

BSc. Eng. (Hons) Chemical Engineering, UCT, South Africa

Supervisor: Eric van Steen

Catalysis Institute

Department of Chemical Engineering

University of Cape Town

2020

Dedicated to my parents

Thank you for teaching me to be great, but only ever wanting me to be happy.

Acknowledgements

To my phenomenal supervisor Eric van Steen, thank you for teaching me everything I know. Thank you for investing so much time into me and this project and for all the endless hours discussing catalytic phenomenon and reactor configurations. You are the most brilliant supervisor a PhD student could ever ask for. You once said that research is like a good bottle of wine; you need to age ideas until they are mature enough to be shared. Thank you for being the winemaker of my research!

I am deeply grateful to my collaborator's Ankur Bordoloi and Arno de Klerk, both of whom hosted me at the Indian Institute of Petroleum in Dehradun, India and the University of Alberta, Canada respectively. Thank you for providing a new perspective on catalysis and Fischer-Tropsch refining, and for growing my curiosity for this exciting field.

I am incredibly grateful to Braam van Dyk for being the most insightful mentor and guiding me through this fascinating world of catalysis and opening my eyes to a world of opportunities.

The scientific support provided to this project is gratefully acknowledged. Thank you to Michael Claeys for invaluable discussions on in-situ magnetometer results and to Patricia Kooyman for your amazing TEM work. Thanks to the Catalysis Institute technical team - Portia Johnston, Waldo Koorts, Rachel Cupido and Chantal Le Roux - for creating the most incredible environment for scientific discovery. Thanks to the UCT Analytical Laboratory (Sandeeran Govender) for support on catalyst characterisation and to Miranda Waldron, Nasseela Hytoolakhan Lal Mahomed and Naomi Harrisankar for assisting with the characterisation of the zinc aluminate samples.

I am very grateful to SASOL Group Technology, University of Cape Town Postgraduate Funding Office, Catalysis Society of South Africa (CATSA), the Queen Elizabeth Diamond Jubilee Scholarship and the Loreal-UNESCO Women in Science Fellowship for the financial support and the opportunity to travel to numerous local and international conferences throughout my MSc and PhD.

Thank you to my high school science teachers - Carla Esterhuizen, Angela Yatt, Sue Marsden and Emma Harridge - for cultivating my curiosity for the world's scientific mysteries. Teachers mould us into the adults we become; brilliant teachers mould us into the people we hope to be. You are all, truly, brilliant.

To my family - Barbara, Arther and Ashley Tucker - thank you for being there for me throughout this entire process. Your encouragement and advice have been invaluable to this project, and your never-ending love and support have meant everything to me. To my friends Pierre Cilliers, Kevin Wu, Nicholas Cherry and Jessica Kohler thanks for keeping me sane and for the multiple wonderful nights of wine and amazing chats. Thank you, Maximilian Hahn, for being the most incredible partner, friend and personal chef. Thanks for cheering me up after reactor breakages and writer's block, and for listening to me for hours on end. I love you and I could not have done this without you.

Declaration

I, Chelsea Lyn Tucker, hereby declare that the work on which this thesis is based is my original work (except where acknowledgements indicate otherwise) and that neither the whole work nor any part of it has been, is being, or is to be submitted for another degree in this or any other university. I authorise the University to reproduce for the purpose of research either the whole or any portion of the contents in any manner whatsoever.

Signature: Signed by candidate Date: 14/10/2020

Declaration on inclusion of publications in a PhD thesis

"I confirm that I have been granted permission by the University of Cape Town's Doctoral Degrees Board to include the following publication(s) in my PhD thesis, and where co-authorships are involved, my co-authors have agreed that I may include the publication(s)"

- C.L. Tucker, E. van Steen, M. Claeys, Decoupling the deactivation mechanism of Pt-Co/Al_2O_3 at high conversion for once-through biomass-to-liquid operation, *Cat. Sci. Tech.* Advance article (2020)

- C.L. Tucker, E. van Steen, Activity and selectivity of a cobalt-based Fischer-Tropsch catalyst operating at high conversion for once-through biomass-to-liquid operation, *Catal. Today.* **342** (2020) 115–123.

- C.L. Tucker, E. van Steen, Effect of crystallite size distribution on the oxidation and re-reduction of cobalt in the Fischer-Tropsch synthesis – a thermodynamic analysis, *Catal. Lett.* (under review)

Signature Removed

Signature: Date: 14/10/2020

Student name: Chelsea Lyn Tucker Student number: TCKCHE002

Synopsis

The production of fuels from waste on a small-scale decentralized level may enhance the liquid fuel security of Sub-Saharan Africa. The Fischer-Tropsch process can be used to convert waste into drop-in fuels. However, operating at small scale in remote locations requires a plant design with lower capital requirements, a greater level of simplicity and utility self-sufficiency. A plant design using an air-fed biogas reformer (without an air separation unit) and a single pass Fischer-Tropsch configuration is proposed. A fundamental requirement of this particular design is that it needs to operate at a higher Fischer-Tropsch conversion than typically seen in industry (55 – 65%).

High conversion conditions result in a high partial pressure of H_2O and low partial pressures of CO and H_2 within the Fischer-Tropsch reactor. These conditions have been reported to negatively affect the activity, selectivity and stability of cobalt-based catalysts. To date, no study has investigated the cause of this phenomenon, nor has a catalyst been developed specifically to operate under high conversion conditions.

The objective of this study is to investigate the mechanisms behind these phenomena and provide catalyst design improvements that facilitate operation at high conversion conditions. Furthermore, a detailed design of the proposed once-through Fischer-Tropsch biogas-to-fuel plant will be evaluated using data from the catalytic experiments.

An investigation into the effect of high conversion on the activity and selectivity of 0.05Pt-22Co/Al_2O_3 was conducted in a slurry bed reactor at T = 220°C, P = 20 bar, with a feed simulating synthesis gas generated from air-blown reforming (H_2:CO:N_2= 4:2:6). Space velocity was decreased to increase conversion to between X_{CO} = 40% and X_{CO} = 97%. The rate of CO consumption decreased with increasing conversion. Increasing the CO conversion was found to have negligible effect on CO_2 selectivity (an unwanted by-product) up to a CO conversion of 75%, after which a strong increase was observed. This was attributed to the enhanced of water-gas shift activity of Co^0 under hydrothermal conditions. The production of CO_2 raised the H_2/CO ratio within the reactor resulting in a large increase in the CH_4 selectivity (an unwanted by-product), a decrease in the chain growth probability and thus a decrease in the C_{5+} selectivity (fuel product).

In order to improve unfavourable selectivity obtained at high conversion in the Fischer-Tropsch synthesis, the effect of adding manganese (Mn) to 0.05Pt-22Co/Al_2O_3 was explored. The catalyst (0.05Pt-22Co/Al_2O_3) was impregnated with increasing amounts of manganese, resulting in six Mn-Pt-Co/Al_2O_3 catalysts with Mn:Co mass ratios of 0, 0.04, 0.09, 0.14, 0.23 and 0.47:1. The optimal level of manganese promotion was found at a Mn:Co mass ratio of 0.14:1. At this level of manganese promotion, CO_2 and CH_4

selectivity was decreased by up to 6 C-% and 12 C-% (X_{CO} = 90%) respectively whilst turn-over frequency was improved by 100%. The maximum in the C_{5+} yield as a function of CO-conversion was shifted from X_{CO} = 78% to X_{CO} = 91%, thus making operation at high conversion feasible from an activity and selectivity perspective.

Operating Pt-Co/Al_2O_3 at conversion levels higher than X_{CO} = 70% was shown to lead to rapid irreversible deactivation, with a total activity loss of 50% between X_{CO} = 70% and 97%. Using a combination of spent catalyst characterisation via transmission electron microscopy, temperature programmed reduction/hydrogenation as well as an in-situ magnetometer, this irreversible deactivation was attributed to both sintering and cobalt aluminate formation. At very high conversion (X_{CO} > 97%) enhanced reversible deactivation was exhibited due to the oxidation and re-reduction Co^0 to Co(II)O. This oxidation/reduction cycle is the result of a thermodynamic conversion limit: at a mean Co^0 crystallite size of 6 nm (as obtained with Pt-Co/Al_2O_3), the maximum achievable conversion (assuming a lognormal distribution of crystallites, $\sigma = 0.5$) is X_{CO} = 88%. A log-normal distribution of cobalt crystallites with an average size of 8 nm (and the same variance) is required to obtain a maximum conversion of up to X_{CO} = 98%.

In order to limit deactivation due to cobalt aluminate formation at conversions higher than X_{CO} = 70%, zinc aluminate was investigated as a novel support material for a platinum promoted cobalt catalyst. Zinc aluminate thermodynamically limits the formation of cobalt aluminate and facilitates the formation of larger sized cobalt crystallites. The catalyst, 0.04Pt-23Co/$ZnAl_2O_4$ exhibited minimal signs of irreversible deactivation at high conversion with a total rate loss of 0.08 mmol /min/g (0.62 to 0.54 mmol /min/g), whilst the rate loss over 0.05Pt-22Co/Al_2O_3 amounted to 0.47 mmol /min/g (from 0.74 to 0.27 mmol /min/g). The zinc aluminate supported catalyst exhibited equal selectivity towards CO_2, CH_4 and C_{5+} as Pt-Co/Al_2O_3 and an improved turnover frequency, thus making it a viable replacement support for cobalt under high conversion conditions.

A once-through waste-to-fuel process (using biogas from the anaerobic digestion of waste as a raw material) was designed using the experimentally determined selectivity and activity data from the Fischer-Tropsch synthesis. The syngas generation step of this design incorporates a tri-reformer and water-gas shift reactor. Syngas is then fed into the Fischer-Tropsch reactor, which produces largely waxy products at lower conversions (X_{CO} = 60%) and largely naphtha/distillate products at higher conversions (X_{CO} > 80%). The Fischer-Tropsch products were partially refined to distillate (low density diesel) by means of flash tanks and an atmospheric distillation column. At lower conversion levels, a hydrocracker must be used to improve distillate yields. All light hydrocarbons and syngas are fed to a combined cycle power plant, which produced electricity for the plant, thus satisfying the plant's utility self-sufficiency objective.

The plant design was evaluated to find an optimal conversion at which to operate, and to gauge the effectiveness of the catalyst design improvements. An optimal conversion of X_{CO} = 80% was found for Mn-Co/Al_2O_3 (Mn:Co = 0.14) at a production level of 329 bbl/day distillate from a feed of 16 tonnes of municipal solid waste per hour. This represents a 12% increase in production of distillate when compared to Pt-Co/Al_2O_3 at the same conversion. A shift from an alumina support to a zinc aluminate support will be necessary as the optimal conversion for this process lies above the X_{CO} = 70% deactivation threshold.

Contents

List of figures

Figure 4-4: H_2 (■), CO_2 (▲)and CO (●) exit volumetric flow rate as a function of temperature for Pt-Co/Al_2O_3 reduced at 350°C for 0 h (▲,■,●), 2 h (△, □ , ○) and 12 h (▲,■,●) in a water-gas shift fixed bed reactor with feed CO:H_2O = 1:1, volumetric flow rate = 300 ml/min, cat weight = 0.5 g.

Figure 4-5: Selectivity towards methane (CO_2 free basis) (b) for Pt-Co/Al_2O_3 at 20 bar, 220°C, H_2: CO: N_2=4:2:6 (*Run 1*). Closed symbols (●) changing volumetric flow rate. Open symbols (○) standard volumetric flow rate 1000ml_n/min).

Figure 4-6: Methane selectivity on a CO_2-free basis as a function of CO-conversion over Pt-Co/Al_2O_3 at 20 bar, 220°C (*Run 1*: feed ratio H_2: CO: N_2: CO_2= 4:2:6:0: ☐; *Run 2*: feed ratio H_2: CO: N_2: CO_2= 4:2:6:0: ○; feed ratio H_2: CO: N_2: CO_2= 4:2:3:3 ●).

Figure 4-7: H_2/CO-ratio within the reactor as a function of CO-conversion over Pt-Co/Al_2O_3 at 20 bar, 220°C, H_2: CO: N_2 = 4:2:6 (*Run 1*).

Figure 4-8: Methane selectivity as a function of (a) CO-conversion and (b) H_2/CO-ratio within the reactor over Pt-Co/Al_2O_3 at 220°C and 20 bar (inlet partial pressure of N_2: 10 bar; filled symbol $(H_2/CO)_{inlet}$=2: *Run 1* ■ and *Run 2* ●; *Run 3* $(H_2/CO)_{inlet}$=2.5: ☐, $(H_2/CO)_{inlet}$=3: ◊, $(H_2/CO)_{inlet}$=3.5: ✳, $(H_2/CO)_{inlet}$=4: Δ and $(H_2/CO)_{inlet}$=5: ✕).

Figure 4-9: Methane selectivity as a function of the partial pressure of water in the feed keeping the partial pressure of synthesis gas in the feed constant (T=220°C, p=20 bar; feed N_2:H_2:CO:H_2O = 6-x:4:2:x (x=0-3)). Closed symbols: with externally added water; Open symbols: water removed.

Figure 4-10: Chain growth probability (C_3-C_8) as a function of CO-conversion.

Figure 4-11: Olefin content as a function of CO-conversion (C_2: ▲; C_4: ■; C_6: ♦).

Figure 4-12: Selectivity (a) and yield (b) towards liquid hydrocarbons (C_{5+}) as a function of the conversion of CO over Pt-Co/Al_2O_3 at 220°C and 20 bar (feed: H_2: CO: N_2 = 4:2:6).

Figure 5-1: Rate of reaction as a function of time on stream during the initial 100 h period for Mn-Pt-Co/Al_2O_3 with Mn:Co = 0 - 0.47.

Figure 5-2: Percentage rate loss over the first 100 h period (○) and Co_3O_4 crystallite size (●) as (a) a function of Mn:Co ratio from 0 – 0.47 and (b) a function of Co_3O_4 crystallite size.

Figure 5-3: Turnover frequency for each catalyst as a function of Mn:Co ratio at ca. X_{CO} = 40% at 100 hours on stream.

Figure 5-4: The selectivity of CO_2 (a), CH_4 (b) and C_{5+} (c), C_4 olefins content (d) and chain growth probability alpha value (e) as a function of CO conversion for Mn-Pt-Co/Al_2O_3 with Mn:Co = 0 – 0.47.

Figure 5-5: The yield of C_{5+} as a function of CO conversion for Mn-Pt-Co/Al_2O_3 with Mn:Co = 0 and 0.14.

Figure 6-1: CO conversion as a function of time on stream with Pt-Co/Al_2O_3 in a slurry reactor at 220°C and 20 bar with a feed N_2:H_2:CO = 3:2:1. Space velocity of CO: ● 1.73 mmol CO/min/g, ◊ 1.03 mmol CO/min/g, + 0.94-0.83 mmol CO/min/g, Δ 0.62-0.42 mmol CO/min/g × 0.21 mmol CO/min/g.

Figure 6-2: CO conversion, X_{CO}, and water partial pressure in the feed (bar) as a function of time on stream for a slurry bed run with constant partial pressure of synthesis gas in the feed (T = 220°C, p = 20 bar; feed N_2:H_2:CO:H_2O = 6-x:4:2:x (x = 0-3)).

Figure 6-3: Rate of change of activity with time as a function of reactor partial pressure of water and conversion (for high conversion run only) for Pt-Co/Al_2O_3 in a slurry reactor (N_2:H_2:CO = 3:2:1, 220°C, 20 bar). Key: ● high conversion run, ■ 'simulated' high conversion run.

Figure 10-10: Sensitivity analysis of the hydrocracker showing the Fischer-Tropsch product distribution (-) and the feed to the atmospheric distillation column after hydrocracking (---) for X_{CO} = ● 60%, ● 70%, ● 80%, ● 90% .

Figure 10-11: Atmospheric distillation column showing the number of stages as well as the feed stage and the side stream product stage based on the sensitivity analysis in Appendix J.

Figure 10-12: Sensitivity analysis of the atmospheric distillation column showing the change in the side stream distillate hydrocarbon distribution as a function of (a) side stream flow rate, (b) inlet temperature, (c) reboiler duty and (d) reflux ratio.

Figure 10-13: Effect of the oxygen:feed ratio to the combustion unit on the electricity produced by the steam turbine.

Figure 10-14: Effect of pump exit pressure on the electricity produced by the steam turbine (left axis) and electricity required for the pump (right axis).

Figure 10-15: Carbon flow diagram of the Fischer-Tropsch plant operating at X_{CO} = 60% showing the distribution of carbon throughout the plant, including the distribution of carbon in (C-%) of different species in each section.

Figure 10-16: Hydrocarbon distribution C_2 to C_{40} for ─ Fischer-Tropsch products and ─ side stream distillate (distillate product) for X_{CO} = (a) 60%, (b) 70%, (c) 80% and (d) 90% for Pt-Co/Al_2O_3 for the case with a hydrocracker.

Figure 10-17: Distillate production as a function of conversion for Pt-Co/Al_2O_3 and Mn-Pt-Co/Al_2O_3 with and without hydrocracking.

Figure 10-18: Electricity production as a function of conversion for Pt-Co/Al_2O_3 and Mn-Pt-Co/Al_2O_3 with and without hydrocracking.

Figure 10-19: Energy balance for base case design X_{CO} = 60% for Pt-Co/Al_2O_3 showing the lower heating values of reactants and products as well as the power generated from the plant.

List of tables

Nomenclature

Abbreviations

AAS: Atomic Absorption Spectroscopy

ASF: Anderson-Schulz-Flory

ASU: Air separation unit

BTL: Biomass-to-liquid

CTL: Coal-to-liquid

DOR: Degree of reduction

FT: Fischer-Tropsch

GC: Gas chromatography

HTFT: High temperature Fischer-Tropsch

ICP: Inductively coupled plasma

LTFT: Low temperature Fischer-Tropsch

ml_n: Millilitre normal

MSW: Municipal solid waste

OTP: Olefin to paraffin ratio

PSA: Pressure swing adsorption

SMDS: Shell Middle Distillate Synthesis

TCD: Thermal conductivity detector

TCI: Total cost indicator

TOF: Turn over frequency

TPR: Temperature programmed reduction

TPH: Temperature programmed hydrogenation

WGS: Water-gas shift

WTL: Waste-to-liquid

X_{CO}: Conversion of CO in Fischer-Tropsch synthesis

XRD: X-ray diffraction

Glossary

Anaerobic digestion: The decomposition of organic waste aided by microorganisms in the absence of oxygen to produce biogas.

Biogas: A mixture of methane and carbon dioxide produced from the anaerobic digestion of a carbonaceous substance.

Diesel: A mixture of hydrocarbons predominantly containing C_{10}-C_{22} that meets the specifications dictated by the location where it is sold.

Distillate: A mixture of hydrocarbons predominantly containing C_{10}-C_{22}.

Drop-in fuels: A fuel that is completely interchangeable for gasoline, diesel or jet fuel. i.e. requiring no changes to the engine, fuel system or fuel distribution network.

Fischer-Trospch synthesis: Catalytic reaction that converts syngas into a mixture of long chain hydrocarbons.

Gasification: Process that converts solid carbon material (organic or fossil fuel) into syngas under oxygen scarce environment.

Organic waste: Waste material consisting of biodegradable matter that can be broken down into carbon dioxide, methane or simple organic molecules.

Reforming: Process that converts methane or methane-containing gas into syngas.

Slurry bed reactor: Mixed reactor in which gas is passed through a liquid medium that contains suspended solid catalyst particles thereby creating turbulence.

Soxhlet: Laboratory apparatus used to extract a compound with limited solubility in a solvent from one with no solubility. In this case used to extract wax from catalyst using xylene.

Syngas: Mixture of hydrogen and carbon monoxide.

Turn over frequency: A measure of the performance of a catalyst defined by the number of mols of reactant consumed divided by the mols of Co^0 as measured via hydrogen chemisorption.

Chapter 1

Fischer Tropsch waste-to-fuels for Sub-Saharan Africa

1.1. Liquid fuel crisis in Africa

The World Bank estimates that Sub-Saharan Africa is the most oil-dependent region in the world [1,2]. Despite holding 10% of the world's oil reserves [3], the African continent possesses only 2.4 % of the its refining capacity [4]. Low levels of liquid fuel production result in a disproportionate amount of countries in the region that are net-importers of fuel and thus vulnerable to oil-price shocks and regional fuel shortages [5]. Yet, the region remains heavily reliant on liquid fuels for primary energy consumption. Of particular importance is diesel which accounts for the majority of transportation fuel consumption [5,6] as well as both baseload and backup electricity generation. In countries such as Senegal (West Africa), up to 90% of electricity is generated via diesel and heavy fuel oil [7].

Improving local liquid fuel production is particularly challenging in the region due to under-developed infrastructure and unreliable transportation networks. In terms of the latter, there are only two countries that currently have pipelines to transport liquid fuels - Kenya and South Africa [1,5]. This means that petroleum products are predominantly transported via trucks. This is both an economic hindrance on local petroleum production as well as a significant safety risk. Nigeria and Kenya hold the 3rd and 4th spot globally for the largest number of deaths due to oil tanker explosions [8], just behind Pakistan and North Korea.

Low-carbon liquid fuel security in Sub-Saharan Africa may be improved substantially by small-scale decentralized production of fuels. This would negate the issue of inadequate infrastructure and transportation. Frameworks like this have worked well in Brazil with ethanol-based biofuels, however typical biofuels from food-crops require both land and water, thus reducing food production [9], which may enhance food shortages in an already crop-vulnerable region. An ideal solution, in theory, would be the creation of fuels from municipal solid waste (MSW) – an ever-increasing resource in developing nations [10].

1.2. Waste as a raw material

It has been estimated that approximately 1.3 billion tonnes of municipal solid waste (MSW) is produced globally every year [10]. Waste generation and composition vary significantly based on the region with developed nations in North America and Europe producing just under half the global total [10]. Due to

rapid urbanisation however, Africa is likely to see an increase in projected urban waste of up to 200% in the next decade, of which over 50% is organic waste [10] (see Figure 1-1).

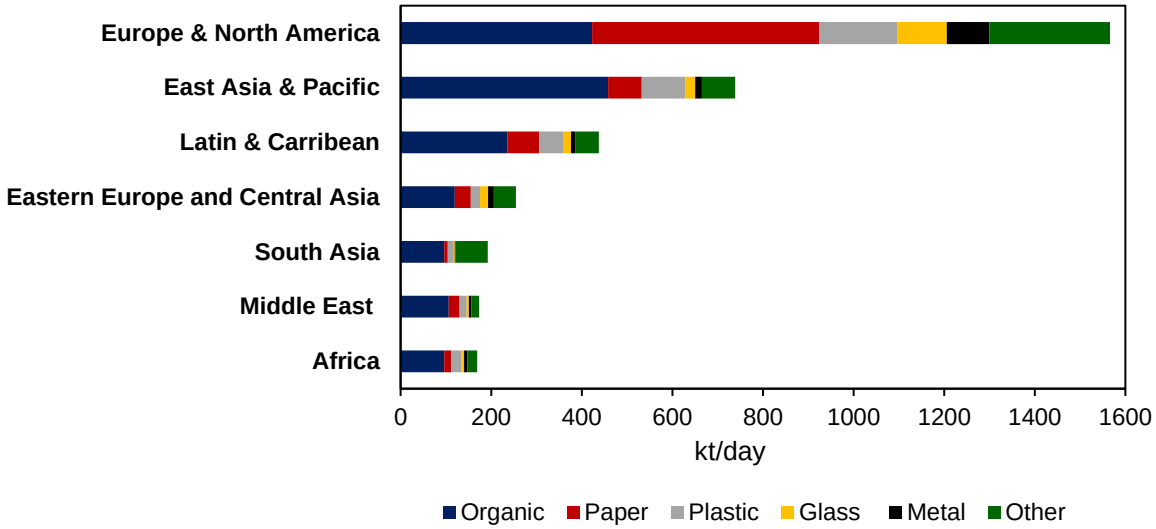

Figure 1-1: Worldwide waste composition breakdown. Data taken from [10].

Many types of MSW such as glass, metal and paper can be reused and recycled. Organic waste (i.e. made up of food waste or biomass), on the other hand, provides a unique challenge as it is not only non-recyclable but also produces CH_4, a strong greenhouse gas, on decomposition.

Traditional waste management systems for organic matter consist of dumping, landfills and incineration. These methods lead to increased land scarcity [11] and significant greenhouse gas emissions [12]. It has been reported [12,13] that up to 1 ton (equivalent) of CO_2 can be saved per ton of waste combusted rather than sent to landfill due to the potency of CH_4 as a greenhouse gas.

1.3. Waste-to-fuel technology

Thus, an enticing option, especially for developing regions in Sub-Saharan Africa, is to divert organic municipal solid waste from landfills and to convert it into fuels. Many thermochemical and biochemical techniques exist for this process (see Fig. 1-2).

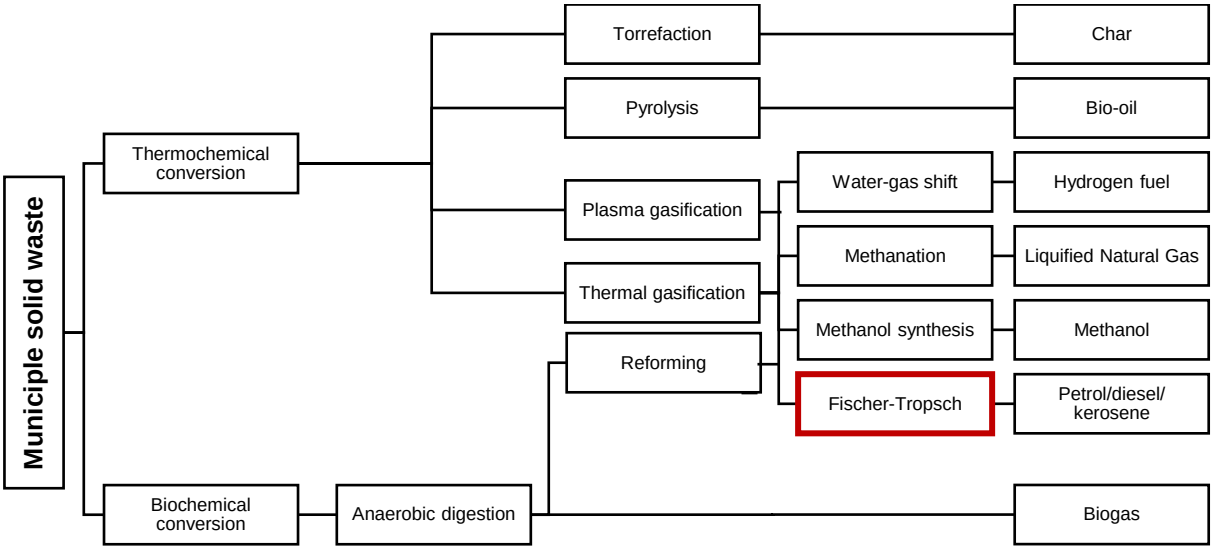

Figure 1-2: Conversion routes for waste or biomass to fuel.

1.3.1. Thermochemical conversion

Thermochemical conversion consists of processes that use heat and/or catalysts to produce fuel from waste [14]. These processes produce a wide variety of fuel types (char, H_2, bio-oil etc.) and are capable of both small-scale and large-scale operation.

Torrefaction and pyrolysis (see Fig. 1-2) involve the temperature-induced conversion of waste or biomass under oxygen-free conditions to produce char (a solid, partially carbonized fuel with a relatively low moisture content) and/or bio-oil (complex mixture of oxygenated organic compounds) [14,15].

Thermal gasification involves the conversion of a carbonaceous species (organic waste in this case) under low-oxygen conditions at temperatures as high as 1200°C. This results in the formation of a mixture of syngas (CO and H_2) as well as CH_4, CO_2, N_2 and small quantities of hydrocarbons [16]. Plasma gasification, which involves the same chemistry as thermal gasification, uses a plasma arc (6000 – 10 000 °C) as a heat source.

Syngas produced from gasification can further be converted via the water-gas shift reaction, methanation, methanol synthesis or Fischer-Tropsch synthesis reaction to hydrogen, synthetic natural gas, methanol or syncrude (refined to diesel, petrol or jet fuel) respectively (see Fig 1-2).

1.3.2. Biochemical conversion

Whilst many commercialized biochemical technologies exist to convert biomass or oils to fuel [17], anaerobic digestion is the only biochemical technique that can use organic municipal solid waste as a

feedstock. Anaerobic digestion refers to the low temperature decomposition of organic waste by microorganisms in an oxygen-scarce environment. The product of this process is biogas – a mixture of CH_4 and CO_2 with a composition of between 55% - 75% and 30% - 45% respectively [18]. Biogas can be reformed to syngas which can be used to generate fuels in a similar manner to syngas produced from gasification [19].

1.3.3. Fischer-Trospch synthesis

Of all the technological routes used to convert syngas to fuels, the Fischer-Tropsch synthesis (see Fig 1-2) may be the most important for the African context due to the production of drop-in fuels that require no alterations to current generators, vehicle engines or fuel distribution networks (as would not be the case for methanol, hydrogen, LNG or bio-oil).

The Fischer-Tropsch synthesis converts syngas into a mixture of water and long-chained hydrocarbons which can be refined to diesel, petrol and kerosene. The classification of Fischer-Tropsch plants are based on the feedstock for syngas generation: coal-to-liquid (CTL), gas-to-liquid (GTL), biomass-to-liquid (BTL) or waste-to-liquid (WTL). In the past, CTL and GTL formed the bulk of Fischer-Tropsch plants due to the high production cost of BTL or WTL [20]. However, due to increasing environmental regulations in the past 20 years, widespread development of BTL and WTL plants has been seen worldwide [21].

1.4. Commercial Fischer-Tropsch BTL and WTL

Whilst research into Fischer-Tropsch waste and biomass-based fuels developed rapidly in the 21st century, the progress for commercialization has, unfortunately, been slower than anticipated and involved a number of false starts [17,22]. Table 1-1 illustrates the Fischer-Tropsch BTL and WTL plants that have either been planned, commissioned, operational or in some cases mothballed between 2008 and 2020.

In 2008, CHOREN set up the first commercial biomass-to-liquid (BTL) plant with a capacity of 5000 bbl/day in Freiberg, Germany [23]. The plant used a three-stage gasification process as well as the Fischer-Tropsch based proprietary Shell Middle Distillate Synthesis (SMDS). Despite initial success, the company filed for insolvency in July 2011 [24] and operations at the plant were ceased by early 2012.

NSE Biofuels, a joint venture between Neste Oil and Stora Enso set up a demonstration BTL facility in Finland in 2010 with a 14 bbl/day capacity with plans to upscale to a ca. 2000 bbl/day facility [24]. The upscaled project, however, did not gain enough traction, or funding, to become a reality [24] and the demonstration plant eventually stopped operation [17]. Further plans to build BTL plants, such as Ajos BTL – with a capacity of ca. 2500 bbl/day - and Solena Fuels GreenSky project - with a capacity for bio

jet and biodiesel of ca. 1157 bbl/day, were frozen due in part to lack of governmental and legislative support [24].

Despite the initial lack of success of these plants, a new generation of demonstration and commercial syngas waste-to-fuel and biomass-to-fuel plants have been commissioned or planned between 2015 and 2020. Total's BioTFuel project, based on standard O_2 blown thermal gasification, plans to start the demonstration of their new biomass-to-fuel plant in 2020. The plant, which will be the largest of its kind in operation, will convert a mixture of straw, forest waste, energy crops and coal into diesel and jet fuel.

Velocys, a US-based company and a subsidiary of Oxford Catalysts Group, has been actively involved in developing a new highly active catalyst as well as microchannel reactor [25]. Red Rock Biofuels, a BTL plant designed with Velocys technology to supply Southwest Airlines and FedEx Express, will reportedly be ready for operation in late 2020 [26]. This plant uses externally heated gasification technology. Velocys has also recently collaborated with Shell to develop a WTL plant in the UK that will produce jet-fuel for British Airways [27,28]. In December 2018, the company began work on the pre-FEED (Front End Engineering and Design) for this project.

Fulcrum Bioenergy is also active in the waste-to-liquid market having signed a licencing deal with BP and Johnson Matthey in September 2018 to commission a ca. 2100 bbl/day WTL plant. Construction on the plant is expected to begin in 2020 [29].

Table 1-1: Planned, operational and mothballed Fischer-Tropsch WTL and BTL plants

Companies involved	*Project Name*	*Location*	*Feedstock*	*Target Product*	*Syngas generation*	*ASU*	*Conversion Technology*	*Approx. capacity[1] (bbl/day)*	*Status*	*Ref.*
CHOREN	Sigma Plant	Freiberg, Germany	Dry biomass	Diesel	Carbo-V gasification	Yes	Fischer-Tropsch	5000	Operation ceased in 2012	[23,30,31]
Neste Oil and Stora Enso	NSE Biofuels	Varkaus, Finland	Forestry residue	Biocrude for renewable diesel	Circulating fluidized bed gasification	Yes	Fischer-Tropsch	14	Demonstration, upscale plans ceased in 2010	[32]
CEA / Air Liquide	SYNDIÈSE-BtS	Bure-Saudron, France	Forest and agricultural waste	Naphtha, kerosene diesel	Thermal O_2 blown, high pressure gasifier	Yes	Fischer-Tropsch	530	Operational 2014	[24]
Solena Fuels	GreenSky	Thurrock, Essex, UK	MSW	Jet Fuel	Plasma gasification	No	Fischer-Tropsch	1157	Mothballed in 2016	[21,33]
Vapo Oy	Ajos BTL	Kemi, Finland	Logging waste	Biodiesel	Carbo-V gasification	Yes	Fischer-Tropsch	2500	Project frozen in 2014	[24]
Red Rock Biofuels, Velocys	Red Rock Biofuels	Oregon, USA	Woody Biomass	Jet Fuel	TCG gasifier - externally heated, air blown	No	Fischer-Tropsch	1100	Operation expected 2020	[17,27]
Fulcrum Bioenergy, BP, Johnson Matthey	Sierra Biofuels	Nevada, USA	MSW	Jet fuel	TRI externally heated gasifier/steam reformer	No	Fischer-Tropsch	684	Construction expected to begin in 2020	[21,29]
Total	BioTFuel Project	Dunkirk, France	Biomass + Coal	Diesel, Jet fuel	Thermal gasifier	Yes	Fischer-Tropsch	5000	Demonstration expected 2020	[17,34]
Fulcrum BioEnergy	CenterPoint BioFuels Plant	Gary, Indiana, USA	MSW	Jet fuel	TRI externally heated gasifier/steam reformer	No	Fischer-Tropsch	2152	Construction expected to begin in 2022.	[29]
Velocys, Shell, British Airways	UK Waste-to-Jet	North East Lincolnshire, UK	MSW	Jet fuel	Unknown	N/A	Fischer-Tropsch	Unknown	Construction expected to begin 2021.	[28]

[1] Converted from t/year, gal/year, m^3/year where appropriate

1.5. Tackling small-scale waste-to-liquid for Sub-Saharan Africa

The growth of Fischer-Tropsch BTL and WTL over the past 10 years should not be understated. However, whilst the technology is undoubtably mature, and the fuel quality is high, the capital costs involved for BTL and WTL Fischer-Tropsch projects remains a challenge [26].

One of the primary factors that influences the success of WTL is scale. Unlike coal which is mined centrally (close to the Fischer-Tropsch plant) and natural gas which can be transported via pipelines, waste is generated in a delocalized manner throughout a region making working at large scale impractical. However, designing a small-scale Fischer-Tropsch plant results in a significant loss of economies of scale [35,36]. This is shown in Figure 1-3 which indicates a high specific total cost indicator (TCI) for smaller-scale BTL plants between 50 and 20 000 bbl/day [37].

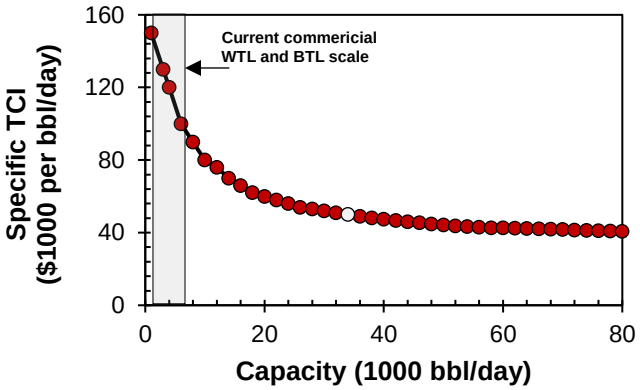

Figure 1-3: Scale dependency for BTL based on scaled-down a CTL plants using gasification technology based on calculations by Boerrigter [37] using an industrial 34 000 bbl/day GTL plant as a reference (indicated as open circle), and scaling up for the additional cost of biomass gasification. Constant scaling factor of 0.7 applied throughout and TCI of BTL assumed to be 60% higher than similar GTL [37].

The scale of all commercial BTL and WTL plants mentioned in Table 1-1 lie within the highlighted region to the left of Figure 1-3, with high specific total cost indicator per bbl/day. To reduce the loss of economy of scale, small-scale decentralized WTL plants require an innovative design that prioritizes simplicity and capital cost efficiency.

Furthermore, Fischer-Tropsch plants in remote areas (as would likely be true for decentralized small-scale plants in Sub-Saharan Africa) may have very little access to infrastructure, utilities and technical services, unlike current implementation of BTL and WTL (Table 1-1). Fischer-Tropsch plants in areas with limited infrastructure are likely to have higher capital costs per barrel due to the complexity of

building-up the surrounding area to satisfy the requirements of the plant. For instance, the Escravos project in Nigeria reportedly cost 8 times the capital cost of Oryx in Qatar, despite the same capacity of 34 000 bbl/day [38,39]. Due to remote locational issues, it would be highly beneficial for a decentralized WTL plant to be self-sustaining in terms of utilities and electricity (off-grid) as to not rely on the local infrastructure or energy generation capacity [36].

1.6. Design philosophy for decentralized Fischer-Tropsch waste-to-liquid

There is thus a need for a design of a small-scale decentralized waste-to-liquid plant for a remote Sub-Saharan African context that prioritizes low capital costs, simplicity and electrical self-sufficiency. These major requirements differ from typical commercialized WTL/BTL processes (Table 1-1) that are often designed in a similar manner to large scale CTL plants and have access to adequate infrastructure and technical services. This section will explore the design philosophy to help meet these requirements. Further exploration and evaluation of a more detailed design will be conducted in chapters 9 and 10.

1.6.1. Typical design and cost breakdown

Whilst there is no 'standard' design when it comes to the development of WTL and BTL plants, most designs consist of syngas generation, Fischer-Tropsch synthesis and separation/upgrade to final fuel products. The choice of technology used in each section is dependent on context, location, feedstock and scale (Table 1-1).

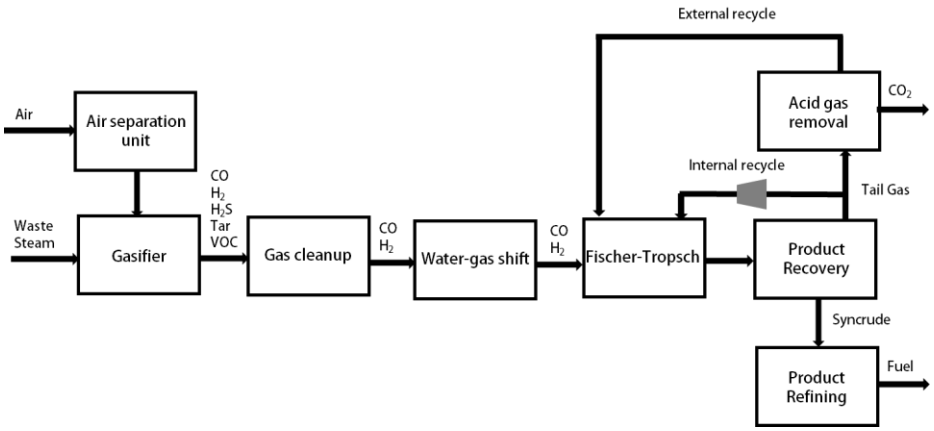

Figure 1-4: Typical configuration for a Fischer-Tropsch BTL/WTL plant.

A typical design (similar to the Total's BioTFuel project, Table 1-1) of a Fischer-Tropsch based BTL plant is shown in Figure 1-4. This plant design includes an air separation unit to provide pure oxygen to the syngas generation plant, an O_2 blown gasifier [37] to produce syngas, a water-gas shift reactor which provides the correct H_2/CO ratio for the Fischer-Tropsch process, a Fischer-Tropsch reactor, product recovery as well as a refining section. The typical conversion for a Fischer-Tropsch reactor is

ca. 55 – 65% [40], meaning that to ensure high yields, a recycle is needed. To avoid a build-up of CO_2 in the recycle, acid gas removal is employed.

Boerrigter [37] investigated the capital cost breakdown for equipment of a BTL plant, with a similar configuration to that seen in Figure 1-4, with the exception that acid gas removal was done during the gas clean-up stage. The estimated cost breakdown is shown in Table 1-2.

Table 1-2: Estimated breakdown of main equipment costs for biomass to liquid plant [37].

Cost items	*Percentage of cost*
Air separation unit	28
Gasifier	19
H_2 manufacturing + water gas shift	6
Acid gas removal	22
Fischer-Tropsch synthesis	16
Product upgrading	9

Of the total equipment costs, syngas manufacture is estimated to be is responsible for the largest proportion of up to 47% (see Table 1-2) with air separation and gasification contributing 28% and 19% respectively. It is noted by Boerrigter [37] that the cost of both units could be halved if methane gas was used as a feedstock (as for gas-to-liquid). Acid gas removal via a Rectisol unit is estimated to cost up to 22% of the total equipment cost whilst the Fischer-Tropsch unit itself accounts for only 16%. Equipment required for product upgrading, H_2 manufacturing and a water-gas shift unit contribute a total of 15%.

1.6.2. Air separation unit removal

In order to decrease the high capital cost [35] associated with Fischer-Tropsch plants, it has been suggested that the most expensive unit, the air separation unit (ASU), be removed for small-scale waste-to-liquid operation [41]. Without the air separation unit, however, syngas generation must occur using air rather than pure oxygen. The use of air is only possible using a once-through (single pass) synthesis scheme (see Fig. 1-5), without internal and external recycle streams (Fig. 1-4). This is done to avoid a build-up of nitrogen as the syngas stream would now contain approximately 40 vol. % N_2 [42].

It must be noted that the cost benefits of the removal of the air separation unit have been the subject of debate for many years [41,43–45]. It has been argued, that benefits of once-through operation are negated due to the low thermal efficiency of air, potentially larger compression volumes and the Fischer-Tropsch diluent factor. In contrast, Jess et al. [46] reported that utilising syngas produced via partial oxidation with air revealed direct cost benefits. A once-through Fischer-Tropsch reactor system removes the requirement for an expensive recycle compressor and excess nitrogen may plays an

important role in heat removal from the exothermic Fischer-Tropsch reaction [46]. Furthermore, the removal of the air-separation unit and recycle enables the possible removal of the Rectisol unit (required to remove CO_2 which acts as an inert in the process, and will build up in a recycle loop), which is shown to be a huge cost contributor (see Table 1-2).

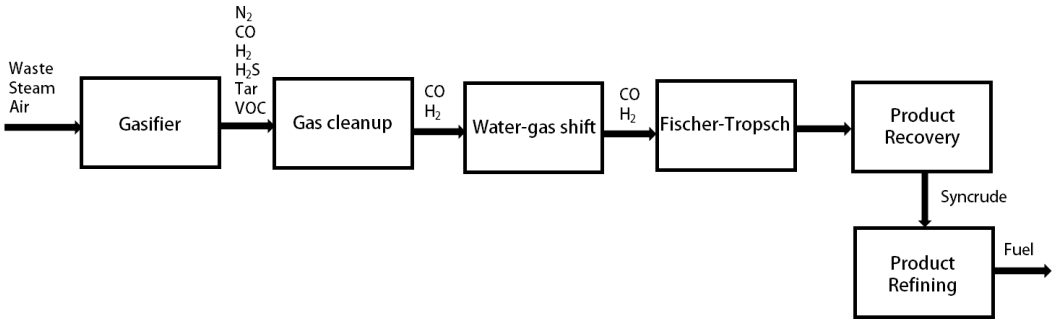

Figure 1-5: Schematic of the small-scale WTL plant with neither an ASU nor internal/external recycles.

Most critical to a once-through design, however, is the choice of conversion associated with the Fischer-Tropsch reactor. Whilst a recycle system maintains overall conversions of carbon monoxide of above 90%, a typical per pass conversion is only ca. 55-65% [40]. Thus, for this system to be economically viable, the Fischer-Tropsch synthesis would also have to be operated at a higher conversion than typically seen in industry. Operating at high conversion will result in a high partial pressure of water (water being a significant product of the Fischer-Tropsch reaction) and low partial pressure of reactants, CO and H_2. These conditions have been reported to adversely affect Fischer-Tropsch catalysts. This will be discussed in further detail in Section 1.6.5 and Chapter 2.

1.6.3. Reforming over gasification

Gasification is typically regarded as the gold standard for the conversion of coal, biomass, waste and other solid carbonaceous species to syngas. This technology is well developed and commercially established, making it an attractive option for engineers and investors alike. To date, all industrial implementations of waste and biomass to liquid have used gasification as their syngas generation technique (see Table 1-1), and most authors who propose new designs use the same strategy [47–51].

However, there are significant challenges when it comes to gasification, the simplest of which is the cost. Boerrigter [37] estimates that gasification costs up to 19% of equipment costs for BTL (Table 1-2) whilst the US Department of Energy estimates this can cost up to 70% [52]. The amount of heat required for gasification can also be enormous – easily a few hundred-thousand MW depending on the scale. In addition to this, gasification also requires a feedstock that is dry. This means a reduction to

~10-15% moisture [49] from 30 – 60 wt.% [53] leading to a decrease in pre-processing costs and energy requirements.

Furthermore, for the purpose of converting municipal solid waste, gasifiers may not be ideal as they are not flexible when it comes to the type of feedstock. Changes to ash content, ash fusion temperature, feed reactivity, agglomeration and particle size in the feed may require an entirely different gasifier design, rather than simply process variable changes [54]. In remote locations, this may be problematic as organic municipal solid waste material is particularly variable in type. In cases where there is no access to laboratory services to confirm feed specifications, gasifiers may operate non-ideally or require constant maintenance and adjustment.

Gasification also generates syngas with major impurities. Depending on the type of biomass or waste used, and the type of gasifier employed, syngas can contain particulates, sulphur compounds such as hydrogen sulphide, carbonyl sulphide and organic sulphur, nitrogen compounds such as ammonia and HCN (especially for air-blown gasification), volatile metals, halogens, tars, hydrocarbons and aromatics [55]. This increases the complexity of syngas cleaning required.

For both these reasons it has been suggested that, specifically for remote small-scale waste applications, biogas reforming [56–59] (biochemical conversion, Section 1.3.2) be used as a syngas generation technique rather than waste gasification. Biogas is generated via anaerobic digestion of municipal-solid waste, wet biomass, sludge, human and farm waste (see Figure 1-2). The resulting gas is a mixture of primarily CH_4 and CO_2 with small contaminants such as ammonia and hydrogen sulphide. Table 1-3 gives the typical concentrations of each of the components of biogas [60].

Table 1-3: Concentration of components of biogas in vol. % [60]

Component	*Typical Composition (vol. %)*
Methane (CH_4)	55 – 70
Carbon Dioxide (CO_2)	30 – 45
Hydrogen Sulphide (H_2S)	0 – 0.5
Ammonia (NH_3)	0 – 0.05
Water Vapour (H_2O)	1 – 5
N2	0 – 5

Figure 1-6 illustrates a schematic of the once-through WTL plant if biogas reforming were used. A notable change to the block flow is the location of the gas clean up section. Due to the relatively high concentration of H_2S in biogas, and the fact that H_2S a known poison of standard reforming catalysts [61], the gas clean up step needs to occur before the reformer.

The concept of using biogas as a feed for the Fischer-Tropsch is relatively novel [58,62], even though the implications for remote fuel production from waste are significant. Firstly, anaerobic digestion is a well-established technology that is both inexpensive and scalable. There are currently anaerobic digestion units in 22 Sub-Saharan African countries [63], with 9 countries having sizable digestors (> 100 m^3) that may be used as a basis for this design.

In addition, gas reforming typically costs up to 60% less than gasification [37] and unlike gasification, biogas generation allows for feed flexibility. The concentration of the various components of biogas do change with different feedstocks. However the CH_4:CO_2 ratio rarely drops below 1, irrespective of the type of raw material used [57]. Whilst this means that the feed rate of steam and/or air may need to be adjusted, this change can be made online without alterations to the reformer itself. Furthermore, whilst biogas reforming requires a sizable amount of heat, the fact that waste does not have to be dried (wet material is digested) decreases energy requirements significantly.

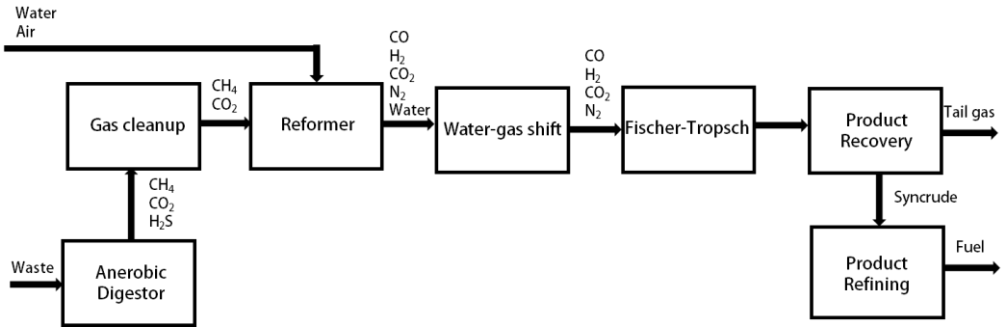

Figure 1-6: Schematic of the small-scale WTL plant using anaerobic digestion and a biogas reformer as the syngas generation technique.

Whilst economic analyses of biogas reforming in the context of fuel production are scarce - an investigation into the techno-economic comparability between gasification and biogas reforming for hydrogen production, conducted by Yao et al. [64], showed that the capital cost the entire process (incl. cleaning, anaerobic digestion) for a duel fluidized gasifier system was 22% more than for biogas steam reforming for the same output.

1.6.4. Electricity and fuel

A consequence of the single pass design is the inevitable surplus of tail-gas containing CO, H_2, methane and light hydrocarbons, even at relatively high single pass conversions. In order to utilize this tail-gas, a gas-fired power generation unit may be employed (see Figure 1-7). Power generation could also have an added benefit of driving compressors, thus satisfying the off-grid design requirement, which is particularly favourable for remote locations.

In addition, co-producing electricity may decrease production costs. A study by Liu et al. [20] used a detailed process simulation, life cycle analysis and a cost analysis to study 16 designs for biomass-to-liquid. This study showed that the liquid fuel production costs for once-through coal-to-liquid, coal-and-biomass-to-liquid hybrid and biomass-to-liquid systems could be reduced by as much 47%, 37% and 10% respectively by introducing electricity as a co-product and providing decarbonized electricity to the grid as an independent power producer [20].

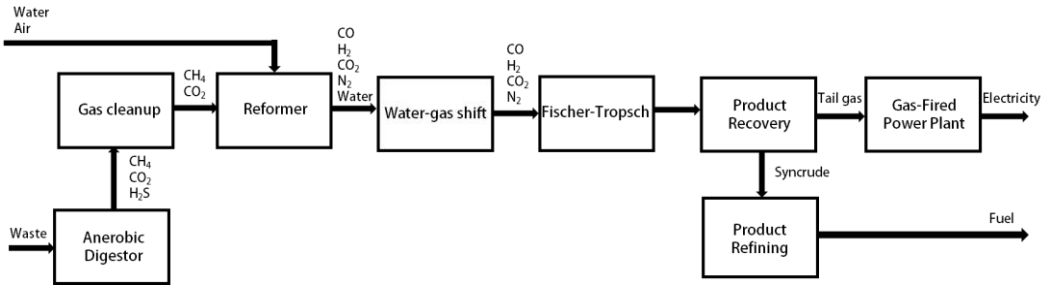

Figure 1-7: Schematic of the small scale WTL plant with co-production of electricity.

1.6.5. High conversion condition

One of the key features of this design philosophy is the removal of the expensive air separation unit and the Fischer-Tropsch recycle streams. This necessitates that the Fischer-Tropsch reactor operate at a higher conversion than typically seen in industry (55 - 65%). This means that the reactor will need to operate under a high partial pressure of product water, and a low partial pressure of reactants, carbon monoxide and hydrogen.

With regards to operation at high conversion, the design of a Fischer-Tropsch catalyst is fundamentally important. Industrial catalysts are not designed to withstand the extreme partial pressures at high conversion and are reported to operate unfavourably under these conditions (discussed in detail in Chapter 2). No previous investigation has attempted to understand the mechanisms causing this unfavourable behaviour, nor has any study attempted to design a catalyst for such conditions.

Chapter 2

Fischer-Tropsch cobalt catalysts at high conversion

To decrease the cost of the Fischer-Tropsch process and increase the viability of small-scale remote WTL, a once-through reactor configuration without air separation unit has been suggested (Section 1.6). This necessitates the removal of both internal and external recycle streams [65]. Thus, the Fischer-Tropsch synthesis is required to operate at a higher conversion than is typically seen in industry.

Fischer-Tropsch systems that are operated at high conversion have high partial pressures of water [66] and low partial pressures of carbon monoxide and hydrogen. The effect of this hydrothermal environment on cobalt catalysts is not entirely understood [67], however, it has been reported that both of these conditions seen at high conversion can alter the activity, selectivity and stability of Fischer-Tropsch catalysts [65,67–70].

2.1. Fischer-Tropsch chemistry

The Fischer-Tropsch (FT) process is a surface polymerization reaction that converts syngas into a wide range of products including diesel, petrol, kerosene, wax and olefins [71]. A major by-product of the process is water. The Fischer-Tropsch reaction to paraffins and olefins can formally be represented by equations 2-1 and 2-2 respectively [72]:

$$n\,CO + (2n+1)H_2 \rightarrow C_nH_{2n+2} + nH_2O \qquad \textbf{2-1}$$

$$n\,CO + 2nH_2 \rightarrow C_nH_{2n} + nH_2O \qquad \textbf{2-2}$$

In addition to the formation of hydrocarbons, various side reactions are possible, which produce undesirable side products such as carbon dioxide and carbon. These can be stoichiometrically be represented as:

$$CO + H_2O \rightarrow CO_2 + H_2 \qquad \text{(Water-gas shift reaction)} \qquad \textbf{2-3}$$

$$2CO \rightarrow CO_2 + C \qquad \text{(Boudouard reaction)} \qquad \textbf{2-4}$$

2.2. Catalyst system

The only metals that have the required CO hydrogenation activity necessary for the Fischer-Tropsch process are ruthenium, nickel, cobalt and iron [73] . The relative costs of these materials have been reported numerous times between 2001 and 2015, as shown in Table 2-1 [71,74–76]. Ruthenium has limited commercial availability and is costly [71]. Nickel, although far cheaper, has a high selectivity towards methane and has been reported to produce volatile carbonyls under moderate CO partial pressures [71]. Iron and cobalt are therefore considered to be the only practical catalysts available for the Fischer-Tropsch synthesis.

Table 2-1: Relative cost of metals that display CO hydrogenation activity.

Metal	*Relative Price*			
	2001	2004	2007	2015 [1]
Fe [2]	1	1	1	1
Co	1000	1000	250	220
Ni	250	250	140	95
Ru	50000	48000	76000	32500
Source	[71]	[74]	[75]	[76]

[1] Priced as bulk metals;
[2] Based on cost of scrap iron

Table 2-2: Comparison of cobalt and iron as Fischer-Tropsch synthesis catalysts adapted from [77].

Parameter	*Cobalt*	*Iron*
Relative Cost (2016)	220	1
Deactivation	Resistant to deactivation	Less resistant to deactivation
Activity at low conversion	Comparable	
Temperature of FTS	Only LTFT	HTFT and LTFT
Extent of WGS reaction	Insignificant except at very high conversions	Significant throughout conversion range
H_2/CO Ratio	~ 2	0.5-2.5

Khodakov et al. [77] compared iron- and cobalt-based Fischer-Tropsch catalysts in terms of their advantages and disadvantages as well as suitability to different Fischer-Tropsch conditions (see Table 2-2). Cobalt-based catalysts are more expensive than iron (see Table 2-1) but have been reported to be more resistant to deactivation, thus limiting the amount of downtime required for catalyst replacement. In addition, at high conversions, cobalt is less affected by the increase in the water partial pressure in the system as the active cobalt phase has a lesser catalytic effect on the water-gas shift (WGS) reaction than iron at Fischer-Tropsch conditions [78]. This also means that cobalt can achieve a greater selectivity to fuels at high conversion.

2.2.1. Cobalt active phase

There is consensus amongst the scientific community that metallic cobalt is the catalytically active phase in cobalt-based Fischer-Tropsch synthesis [79]. Cobalt carbides and oxidized cobalt species, such as Co_3O_4 and Co(II)O, are much less active or not active at all in the Fischer-Tropsch synthesis. Their

formation is often associated with catalyst deactivation and reduced rates [80]. It has been reported [79,81,82] that the Fischer-Tropsch reaction is not structure-sensitive for cobalt crystallites larger than 6-8 nm. This means that for larger crystallite sizes, the rate of reaction is proportional to the amount of cobalt surface sites [77,79,82]. However for smaller crystallite sizes, the turnover frequency has been reported to decrease with decreasing crystallite size [82], attributed to a combination of nonclassical structure sensitivity and CO-induced surface restructuring [83].

2.2.2. Support material

The purpose of using a support material for cobalt catalysts is to disperse cobalt and produce stable metallic cobalt crystallites after reduction. Typical supports used for cobalt catalysts are Al_2O_3, SiO_2 and TiO_2 with typical loadings of 10-30 g of cobalt to 100 g of support [73]. Carbon [82,84,85] has also been investigated as a potential support material. Table 2-3 illustrates a comparison between these supports.

The effect of supports on the activity, selectivity and stability of the Fischer-Tropsch reaction are still not fully understood [86]. Different support materials have different electronic properties, porosities, surface areas and mechanical strengths [68,77,87]. It widely believed that these properties affect particle size, catalyst activity, reducibility, stability and selectivity despite large crystallite sizes having reported structural independence [77,79,86].

The effect of support materials on the activity of cobalt catalysts is a greatly disputed subject. A study by Reuel and Bartholomew [88] reported that for cobalt loadings of 3 wt. % the catalytic activity decreased as a function of support material as follows: $Co/TiO_2 > Co/Al_2O_3 > Co/SiO_2 > Co/C$. This claim was refuted by Oukaci et al. [89] who believed that having higher loadings of cobalt would affect the conclusions drawn in the study.

Alumina (Al_2O_3) is the most commonly used support material for cobalt catalysts [77]. Alumina-supported catalysts are reported to have a higher activity despite lower surface area, a better resistance to breakage within a slurry bed reactor and a greater level of dispersion [68,77]. However, alumina has been reported to strongly interact with cobalt which leads to the formation of small crystallites and results in the catalyst being very hard to reduce without the addition of a reduction promoter [77,87]. Nobel metal reduction promoters such as Pt, Ru and Re are, therefore, generally added to Al_2O_3-supported cobalt catalysts.

Table 2-3: Comparison between alumina, silica, titania and carbon as support material for cobalt-based Fischer-Tropsch systems. Characterization results based on unpromoted catalysts.

Parameter	*Al_2O_3*	*SiO_2*	*TiO_2*	*Carbon*
Industrial use	Sasol, Chevron, Statoil	Shell	Exxon	Not in use commercially
Activity of catalyst [1,2]	Based at low loading[1]: $Co/TiO_2 > Co/SiO_2 > Co/Al_2O_3 > Co/C$ Based on number of surface sites[2,8]: $Co/Al_2O_3 > Co/TiO_2 > Co/SiO_2$			
Interactions with cobalt[4]	Strong	Moderate	Strong	Weak
Reduction temperature (RT) [2,3]	350°C	350°C	300°C	350°C
Degree of reduction [2,3]	30%	64%	52%	Unknown[9]
Ease of reduction [2,3,10]	$SiO_2 > TiO_2 >$ Carbon$> Al_2O_3$			
Cobalt dispersion[2,3,6]	~10 %	< 5 %	2-10%	5-10%
Strength[4]	Robust	Moderately robust	Weak	Weak
Pore radius[2,5,4]	~ 5 nm	~10 nm	~15 nm	~6 nm
Pore volume[2,5]	~ 0.5cm^2/g	1-2cm^2/g	~ 0.4cm^2/g	~0.6cm^2/g
Surface area support[3,5,7]	~ 150m^2 /g	100-650m^2 /g	~ 50m^2 /g	150-200m^2/g
Reactivity with cobalt[4]	May form $CoAl_2O_4$.	May form Co_2SiO_4	May form Co_2TiO_4	None
Effect of high conversion[6]	Rapid deactivation	Rapid deactivation	Rapid deactivation	Unreported

[1] [88] [2] [87] [3] [90] [4] [77] [5] [85] [6] [68] [7] [89]
[8] No carbon support was tested in this study [87].
[9] Back titration methods interfered with oxidation of carbon nanofiber support [90]
[10] Based on TPR profiles given in [87,90]

Silica (SiO_2) has a high surface area and is a weakly interacting support. Weak interactions with cobalt are favourable and result in a greater ease of reduction [77,91]. However, cobalt supported on SiO_2 has been reported to have a lower dispersion and is less robust when compared to Al_2O_3.

Cobalt supported on titania (TiO_2) has a relatively good dispersion and is comparatively easy to reduce. The major problem with TiO_2 is its lack of robustness and susceptibility to breakage in slurry bed reactors. To make the support more robust, a high temperature process is required by which to convert TiO_2 from its anatase phase to its rutile form. The resulting TiO_2 is reported to have a far lower surface area than its counterparts, Al_2O_3 and SiO_2 [89]. TiO_2 has also been reported to have low attrition resistance, difficulty achieving uniform dispersion [89] and a high methanation turnover rate [79,89].

In order to evaluate the effects of homogenous high conversion partial pressures, a slurry bed reactor (CSTR with wax medium) will be used. This requires a very robust catalyst to prevent mechanical breakage. Thus, for the purposes of this investigation, Co/Al_2O_3 will be used as a base catalyst for testing at high conversion. Due to the low level of reducibility (strong cobalt-support interactions), a reduction promoter may be necessary.

2.2.3. Nobel metal promoters

Various promoters can be added to cobalt catalyst systems to enhance their reducibility, activity, selectivity and in some cases deter deactivation [77,87,92]. The addition of noble metals (Ru, Rh, Pt and Pd) has been shown to have a significant effect on the reducibility of cobalt in these catalysts. Noble metals reduce at lower temperatures than cobalt oxides and catalyse the reduction process [87]. Pt and Ru in particular are often utilized as reduction promoters for cobalt catalysts supported on Al_2O_3 due to the strong metal-support interactions of the system which results in a difficulties when reducing Co_3O_4 to its metallic state [93].

According to Nabaho et al. [93], the production and availability of platinum is 10 times greater than other noble metals used for reduction promotion. Platinum reportedly has remarkable effect on the reducibility of cobalt oxide particles on the surface of oxidic supports [87,93–96], especially when strong metal-support interactions are present [94,95]. In one report, addition of 0.5 wt.% Pt to 15 wt.% Co-Al_2O_3 was found to shift the first peak on a TPR spectrum ($Co_3O_4 \rightarrow CoO$) by as much as 150-200°C [95]. Slightly different results were reported for 0.5 wt.% Pt - 20 wt.% Co on Al_2O_3 where the first peak in the TPR spectrum ($Co_3O_4 \rightarrow Co(II)O$) was only shifted by 64°C, whilst the second peak ($Co(II)O \rightarrow Co^0$) exhibited a shift of 105°C from 520°C to 415°C [94]

Thus, in order to enhance the reducibility of a cobalt on alumina system, platinum will be co-impregnated onto the catalyst resulting in a base catalyst of Pt-Co/Al_2O_3 being used for the high conversion study.

2.3. Activity at high conversion

The kinetics of the Fischer-Tropsch reaction are widely studied, and various kinetic expressions for a cobalt catalyst have been proposed [70,79,105,106,97–104]. Table 2-4 summarizes the kinetic expressions proposed during the past 65 years, as well as the catalyst, reactor and conditions used for these studies. This is by no means a comprehensive list; however, it does illustrate the evolution of proposed Fischer-Tropsch reaction kinetics over the last half century.

Table 2-4: Summery of kinetic studies and proposed kinetic expressions between 1949 and 2014. Adapted from Yates and Satterfield [99].

Study	*Catalyst*	*Reactor*	*T (ºC)*	*P (bar)*	*H_2/CO*		*Ref*
Brötz (1949)	$Co/MgO/ThO_2$/kieselguhr	FBR	185-200	1	2	$-R_{H_2+CO} = \left(\frac{k_1 P H_2^2}{P_{CO}}\right)$	[98]
Anderson (1956)	Co/ ThO_2/kieselguhr	FBR	186-207	1	0.9-3.5	$-R_{H_2+CO} = \left(\frac{a P_{H_2} P_{CO}}{1 + b P_{H_2}^2 P_{CO}}\right)$	[99]
Yang et al. (1979)	$Co/CuO/Al_2O_3$	FBR	235-270	1.7-5.5	1-3	$-R_{H_2+CO} = \left(\frac{a P_{H_2}}{P_{CO}^{0.5}}\right)$	[105]
Outi et al. (1981)	Co/Al_2O_3	FBR	250	1	0.2-4	$-R_{CO} = \left(\frac{a P_{H_2} P_{CO}^{0.5}}{(1 + b P_{CO}^{0.5})^3}\right)$	[97]
Wang (1987)	$Co/B/Al_2O_3$	FBR	181	1-2	0.25-4.0	$-R_{CO} = \left(\frac{a P_{H_2}^{0.68}}{P_{CO}^{0.5}}\right)$	[109]
Sarup & Wojciechowski (1989)	Co/kieselguhr	Berty	190	1-2	0.5-8.3	$-R_{CO} = \left(\frac{a P_{CO}^{0.5} P_{H_2}^{0.5}}{\left(1 + b P_{CO}^{0.5} + c P_{H_2}^{0.5} + d P_{CO}\right)^2}\right)$	[100]
Withers et al. (1990)	Co/Zr/SiO2	Slurry	220-280	20	0.5-2	$-R_{CO} = \left(\frac{k C_{H_2}}{1 + \frac{K C_{H_2O}}{C_{CO} C_{H_2}}}\right)$	[104]
Yates & Satterfield (1991)	$Co/MgO/SiO_2$	Slurry	220-240	7.9	240	$-R_{CO} = \left(\frac{a P_{CO} P_{H_2}}{(1 + b P_{CO})^2}\right)$	[101]
Van Steen & Schulz (1999)	$Co/MgO/ThO_2/SiO_2$	CSTR	190-210	2.7-6.1	Various	$-R_{CO} = \left(\frac{\frac{a P_{CO}}{P_{H_2O}} P_{H_2}^{1.5}}{\left(1 + b P_{H_2} (P_{CO}/P_{H_2O})\right)^2}\right)$	[102]
Li et al. (2002)	$Pt\text{-}Co/Al_2O_3$	CSTR	210	29.3	2	$-R_{CO} = \left(\frac{k P_{CO}^a P_{H_2}^b}{1 + m\left(\frac{P_{H_2O}}{P_{H_2}}\right)}\right)$	[67]
Botes et al. (2009)	$Co/Pt/Al_2O_3$	Slurry	230	5-40	1.6-3.2	$-R_{CO} = \left(\frac{a \cdot p_{H_2}^{0.75} \cdot p_{CO}^{0.5}}{\left(1 + b \cdot p_{CO}^{0.5}\right)^2}\right)$	[103]
Ma et al. (2014)	Co/Al_2O_3	CSTR	205-230	14-25	1-2.5	$-R_{CO} = \left(\frac{a \cdot p_{H_2}^{0.88} \cdot p_{CO}^{-0.31}}{(1 + \frac{b P_{H_2O}}{P_{H_2}})}\right)$	[78]

At high conversion, three major factors affect the activity of the Fischer-Tropsch reaction - the low partial pressures of CO and H_2 and a high partial pressure of H_2O. In all kinetic expressions shown in Table 2-4, the intrinsic rate of reaction is strongly dependent on CO and H_2. A decrease in the partial pressure of either of these reactants would decrease the intrinsic rate of reaction, to a varying degree.

Figure 2-1 illustrates the effect of high conversion on the partial pressure of reactants and products within the Fischer-Tropsch reactor held at 20 bar for a feed containing $N_2/H_2/CO$ (3/2/1) to mimic a system with no air-separation unit. At high conversions, the partial pressure of CO and H_2 drops to very low levels.

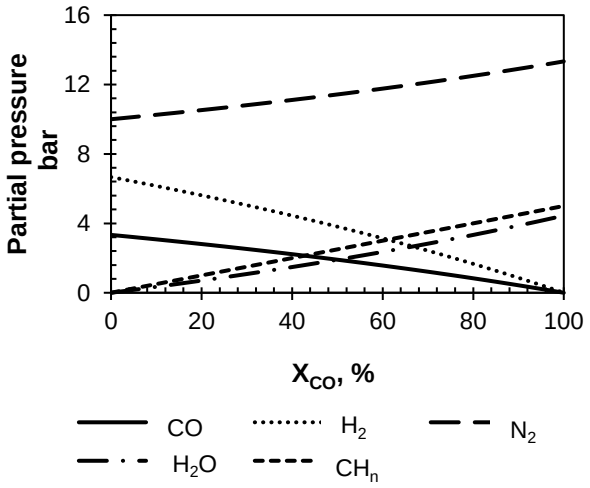

Figure 2-1: Effect of increasing conversion on the partial pressure of various components in the FT synthesis for a reactor at 20 bar and $N_2/H_2/CO$=3/2/1.

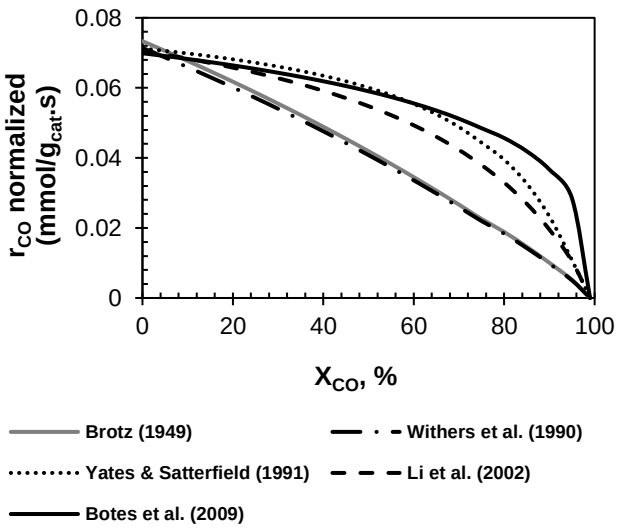

Figure 2-2: Effect of increasing conversion on the rate as predicted for various rate expressions as presented in Table 3-4 for a feed of $N_2/H_2/CO$=3/2/1 at 20 bar.

Thus, it is theoretically expected that at high conversion a decrease in the rate is due purely to low partial pressures of CO and H_2. Figure 2-2 shows the change in rate of CO with conversion as modelled by various rate expressions [67,101,102,106,110] shown in Table 2-4. The rate expressions are normalized with respect to the constants given in Botes [103]. The rate of CO is seen to decrease, albeit at differing rates, with an increase in conversion. For more recently developed rate expressions [67,101,110] the decline in activity becomes stronger at $X_{CO} > 80\%$.

The effect of elevated water partial pressure on the rate is slightly more complicated. Researchers' understanding of the influence of water on Fischer-Tropsch kinetics has changed over the years. Water

was excluded entirely from kinetic expressions until 1990 (see Table 2-4), after which time it started to be proposed as a rate-influencing product [70,100,102]. Whilst some authors suggest water has a positive effect on the rate during water co-feeding experiments [111,112] others have shown negative [67] or no effect [101].

Thus, the effect of elevated water partial pressure of on the activity of cobalt catalysts is often reported to be not fully understood and dependent on the type of support used [65]. This statement is supported by Li et al. [67] who reviewed studies by Schulz et al. [111] and Kim et al. [113] both of whom reported increases in activity with water addition for Co^o catalysts supported on silica and titania respectively. Storsæter et al. [68], too, reported that for $ReCo/Al_2O_3$ and Co/Al_2O_3 catalysts, a slight increase in the rate of hydrocarbon formation was found for an increase in local water partial pressure. Yet Li et al. [67] reported a distinct decrease in activity of a cobalt catalyst supported on alumina upon the addition of water. It was postulated that the addition of water decreases competitive adsorption and, therefore, the concentration of CO and/or H_2 on the surface. This led to the formation of a kinetic expression (Row 10, Table 2-4) where a variable *m* was added, describing the water effect.

2.4. Selectivity at high conversion

The selectivity of the Fischer-Tropsch reaction is quite complex due to the reaction producing a large range of hydrocarbons (both olefin and paraffin) rather than one or two discreet products. In addition, the formation of unfavourable side products such as methane (CH_4) and carbon dioxide (CO_2) decrease selectivity towards the desired fuel range products (C_{5+}).

2.4.1. Anderson-Schulz-Flory (ASF) model

The distribution of products is often described via the Anderson-Schulz-Flory (ASF) model. In this model, the distribution of a component type (i) with a chain length (m) can be described as a function of the chain growth probability (α) [108]

$$\sum_n^i m_n^i = (1-\alpha)\alpha^{n-1} \qquad \textbf{2-5}$$

with the chain growth probability defined according to the rate of chain propagation (k_p) and the rate of chain termination (k_t) as seen in Equation 2-6 [114].

$$\alpha = \frac{k_p}{k_p + k_t} \qquad \textbf{2-6}$$

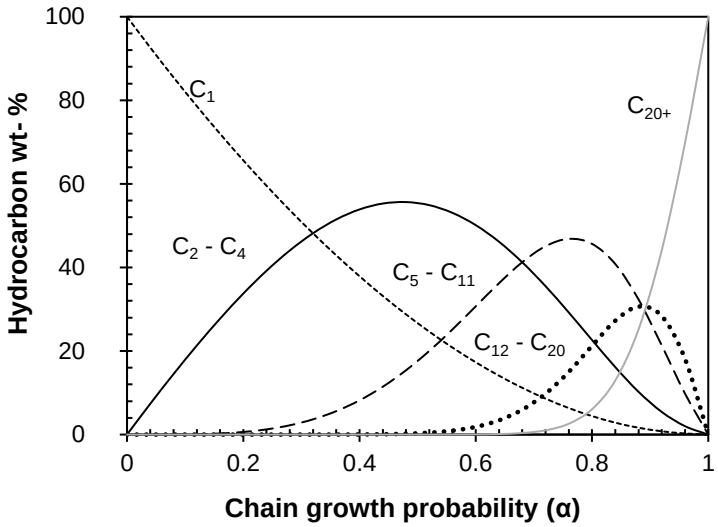

Figure 2-3: Theoretical selectivity according to the ASF model adapted from [115].

Using these equations, a theoretical product selectivity can be plotted as a function of chain growth probability as shown in Figure 2-3. According to this model, methane selectivity decreases with an increase in chain growth probability whilst C_2-C_4, C_5-C_{11} and C_{12}-C_{20} all follow parabolic-like trends, reaching maxima at increasing chain growth probability for increasing chain lengths. In order to attain chain lengths of C_{20+}, a high chain growth probability is required.

Certain process variables (temperature, pressure, H_2/CO ratio, conversion and space velocity) can affect various aspects of the product distribution as illustrated in Table 2-5. An increase in temperature is reported to hinder chain growth, produce more methane and increase carbon deposition [115]. Pressure may have the opposite effect, increasing chain growth probability and decreasing methane selectivity. An increase in the H_2/CO ratio is thought to decrease the chain growth probability and to increase methane selectivity. Due to high H_2 surface coverages at these conditions, the possibility for carbon deposition also decreases. Increasing the space velocity (and thus decreasing residence time and conversion) is reported to cause an increase in the olefin:paraffin ratio and a decrease in methane selectivity.

Table 2-5: Factors affecting the product selectivity. ↑ Increase; ↓ Decrease; * Complex relation or no change. Adapted from de Deugd et al. [72] and van der Laan and Beenackers [115].

	Chain growth probability	Olefin/paraffin ratio	Methane selectivity	Carbon deposition
Temperature ↑	↓	*	↑	↑
Pressure ↑	↑	*	↓	*
H_2:CO ratio ↑	↓	↓	↑	↓
Space velocity ↑	*	↑	↓	*

2.4.2. Effect of conversion

The selectivity of CO_2 , CH_4, C_{5+} and olefins and within the Fischer-Tropsch synthesis have all been reported to be dependent on CO conversion [65,67,68,78]. The relationship between conversion and selectivity has been difficult to establish in the past due to the complexity and interlinkages between conversion, space velocity and water partial pressure. In addition, only low to moderate conversion ranges (between 10% and 50%) were studied previously [67,68]. Only two studies [65,78] have addressed these effects at conversion levels up to 94 %.

2.4.2.1. Carbon dioxide selectivity

Carbon dioxide selectivity has been reported to increase slightly with conversions up to ca. 75%, after which it rises rapidly [65,78]. These trends are illustrated in Figure 2-4. The increase in carbon dioxide selectivity at high conversion has been previously attributed to the conversion of metallic cobalt to oxidised species such as Co(II)O and $CoAl_2O_4$ [65,78]. It is suggested in these studies that one or more of these oxidised species may be active in the water-gas shift reaction [65,78]. This may be possible as cobalt has been used for several water-gas shift catalysts in the past (see Appendix A for list of cobalt water-gas shift catalysts). However, there is little to no literature confirming the water-gas shift activity over bulk cobalt oxide or cobalt aluminate.

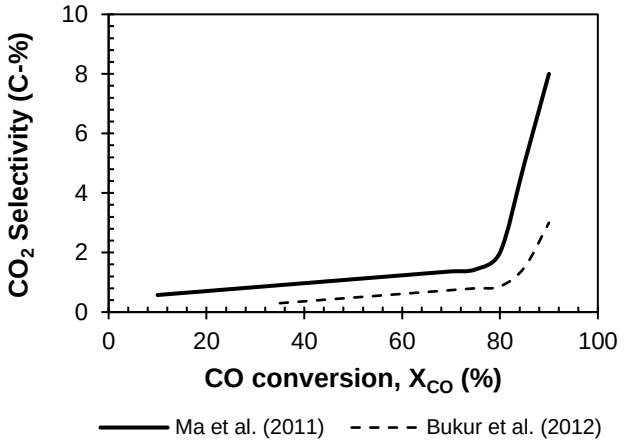

Figure 2-4: Effect of CO conversion on CO_2 selectivity. Trends approximated from [65,78].

2.4.2.2. Methane selectivity

For cobalt supported on Al_2O_3 (see Figure 2-5), a decrease in methane selectivity with increase in CO conversion was reported by Ma et al. [78], Bukur et al. [65] and Storsæter et al. [68]. Li et al. [67] reported no change in methane selectivity with conversion.

Interestingly, in the case of Ma et al. [78], after a CO conversion of 80% is reached, the methane selectivity rapidly increased. Ma et al. [78] ascribed this to an increase in the rate of the methanation due to the formation of Co(II)O and $CoAl_2O_4$ at high conversions. The absence of increase in methane selectivity reported by Bukur et al. [65] was attributed to the reactor type used (PBR rather than slurry). It was hypothesized that the high partial pressure of water is limited to the bottom portion catalyst bed in a PBR, thereby decreasing the impact of oxidation [65].

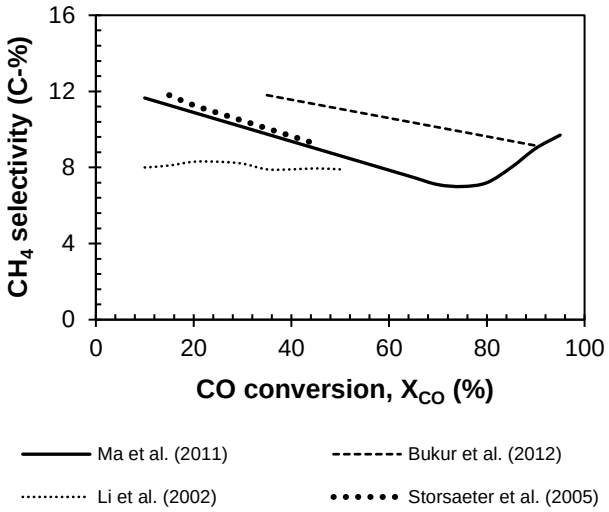

Figure 2-5: Effect of CO conversion on CH_4 selectivity. Trends approximated from [65,67,68,70].

2.4.2.3. C_{5+} selectivity

With a few exceptions, the effect of conversion on the full range of hydrocarbon selectivity (C_{5+}, C_2-C_4, olefin content and chain growth probability) is not widely explored in literature. C_{5+} selectivity is by far the most frequently reported and has been shown to increase upon increasing conversion (see Fig. 2-6) [65,68,78].

Various explanations for this increase exist, albeit none have been experimentally proven. Firstly, it has been attributed to an increase in secondary reactions of primary olefins with increased residence times in the catalyst pores [68]. Secondly, it has been explained by the inhibition of secondary hydrogenation of 1-olefins and chain termination by water, thereby increasing the chain growth probability [65]. Additional explanations, such as water's ability to lower the CO dissociation barrier by CO interaction or the rate of transport of CO and H_2, have also been suggested [116]. Interestingly, above X_{CO} = 80%, Ma et al. [78] reported that the C_{5+} began to level off. This may be expected due to the CO_2 and CH_4 selectivities rising rapidly at this point.

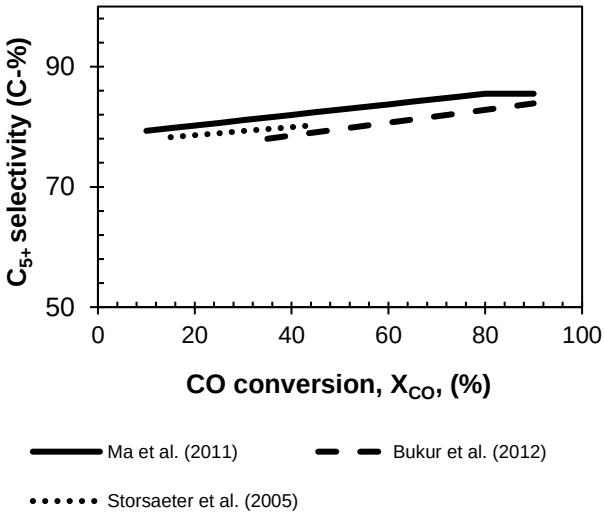

Figure 2-6: Effect of conversion on C_{5+} selectivity. Trends approximated from [65,68,78].

2.4.2.4. Olefin/paraffin ratio

Ma et al. [78] reported that increasing the CO conversion decreased the C_4 olefin-to-paraffin ratio (OTP). This can be explained by the phenomena of competitive adsorption between CO and the alkenes. Bukur et al. [65] reported similar findings in that the 1-olefin content for all C_2-C_5 hydrocarbons decreased with increasing CO conversion. This observation was explained [65] by an increase in secondary reactions to 1-olefins such as hydrogenation, isomerization, reabsorption or inclusion in growing chains due to an increase in conversion.

Storsæter et al. [68] indicated a similar trend for both Co/Al_2O_3 and $ReCo/Al_2O_3$ with a drop in OTP ratio of 0.8 and 0.5 for conversion increases of 11.5 - 44.8 % and 21.3 - 47.6 % respectively. However, the explanation for this phenomenon differs slightly, namely, that water inhibits secondary hydrogenation reactions of olefins, which would increase the OTP ratio.

2.5. Deactivation at high conversion

Catalyst deactivation is an unfortunate but unavoidable challenge for catalysis engineers and scientists. Various mechanisms for deactivation exist. However, the predominant mechanism in a system is specific to the type of catalyst, support, promoters and process conditions (pressure, temperature, and conversion).

The highly hydrothermal conditions of high conversion are expected to negatively affect the stability of cobalt-based catalysts [67,69], albeit few studies exist to confirm this. In one study, Kiss et al. [69] exposed a silica-supported cobalt catalyst to a low space velocity to simulate 90% conversion for a total

of 2 weeks. The catalyst demonstrated a 50% loss in activity over the time-period. Possible causes for the reduced catalyst stability under hydrothermal conditions include cobalt oxidation [69,80,117–119], formation of cobalt-support compounds [119–123], sintering of cobalt nanoparticles [69,80,124,125] and carbon deposition.

2.5.1. Cobalt oxidation

Cobalt oxidation is widely reported as a major cause of deactivation in cobalt catalysts in hydrothermal environments [65,66,78,79,81,117,126,127]. Even though, from a purely thermodynamic point of view, the oxidation of bulk cobalt to Co(II)O or Co_3O_4 with water should not be feasible under Fischer-Tropsch conditions [66,67,79,117,118], it is still widely reported in experimental studies [66,78,118] involving nano-sized crystallites. Such crystallites may oxidize under these conditions due to surface energy contributions [117].

Figure 2-7 shows the cobalt crystallite size dependent phase diagram for the oxidation of metallic cobalt with water yielding iso Co(II)O and hydrogen as described by van Steen et al. [117]. The lines in both graphs indicate the thermodynamic transition point at which Co^0 will convert to Co(II)O for various sized crystallites.

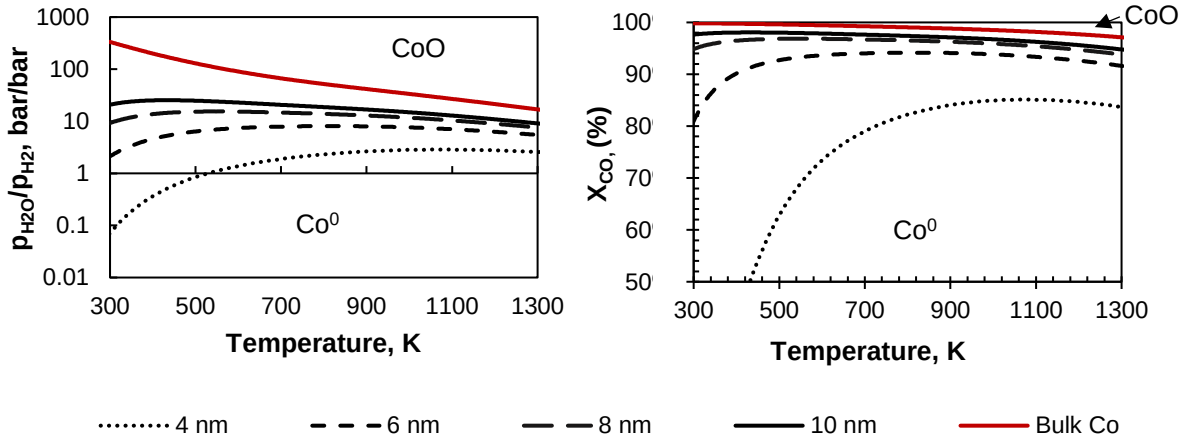

Figure 2-7: Cobalt stability diagram showing the thermodynamic transition point from Co^0 to Co(II)O for various cobalt crystallite sizes as a function of temperature, p_{H2O}/p_{H2} ratio (left) and CO conversion (right). Calculated at $H_2/CO = 2$. Calculated according to [117] using data from [128].

At low temperature Fischer-Tropsch conditions (493K) the formation of cobalt oxide from bulk metallic cobalt requires a partial pressure of water to hydrogen (p_{H2O}/p_{H2}) of above 133 (Figure 2-7). The formation of cobalt oxide from smaller metallic cobalt crystallites is much more facile and may occur if $p_{H2O}/p_{H2} > 1.2$ for cobalt particles of a size of 4 nm. This corresponds to a CO conversion of 62% with

a typical feed for the Fischer-Tropsch synthesis (i.e. with $H_2/CO=2$). Under hydrothermal Fischer-Tropsch conditions, oxidation may become possible for larger nanoparticle sizes. The formation of Co(II)O at high conversion conditions is therefore hypothesized to be likely.

Hydrothermal conditions have been shown experimentally to cause cobalt oxidation [66,78,119,129]. Saib et al. [91] performed X-ray adsorption near edge structure spectroscopy (XANES) measurements at standard Fischer-Tropsch conditions for 100 days, showing that whilst standard conditions (low conversion) are highly reducing environments, oxidation may occur in very water-rich and hydrogen-poor environments. Similarly, Ma et al. [78] used XANES to show that there was more Co(II)O present at higher CO conversions of 90% and 72% than at standard CO conversions of 43%.

2.5.2. Formation of mixed metal oxides

The formation of Co(II)O is a reversible form of deactivation as Co(II)O can reduce at Fischer-Tropsch conditions and thus, once the partial pressure of water or conversion is decreased, the cobalt species may return to its metallic form. Catalyst deactivation from the formation of mixed metal-oxides on the other hand is an irreversible form of deactivation. In the case of Co/Al_2O_3, cobalt aluminate ($CoAl_2O_4$) may be formed through a reaction of Co^0 or Co(II)O with the alumina support in the presence of water in the Fischer-Tropsch synthesis [66,126]. $CoAl_2O_4$ is generally termed non-reducible as it can only be reduced at high temperatures (>900 ˚C) due to its high thermal stability [130]. The three reactions relevant to the formation of $CoAl_2O_4$ are illustrated in equations 2-8 to 2-10

$$Co+H_2O \leftrightarrow CoO+H_2 \quad \textbf{(Cobalt oxidation)} \quad \textbf{2-8}$$

$$CoO+Al_2O_3 \leftrightarrow CoAl_2O_4 \quad \textbf{(Indirect metal-oxide formation)} \quad \textbf{2-9}$$

$$Co+H_2O+Al_2O_3 \leftrightarrow CoAl_2O_4+H_2 \quad \textbf{(Direct metal-oxide formation)} \quad \textbf{2-10}$$

The change in Gibbs free energy of a reaction ($\Delta G°_{rxn}$) can be used to determine the thermodynamic feasibility of a reaction. Figure 2-8 illustrates the $\Delta G°_{rxn}$ of bulk Co^0 oxidation as well direct (Co^0 to $CoAl_2O_4$) and indirect (Co(II)O to $CoAl_2O_4$) metal-oxide formation.

The oxidation of bulk Co^0 has a positive $\Delta G°_{rxn}$ from 300 K until > 1100 K, implying the oxidation of bulk cobalt is not feasible at standard conditions, as discussed with respect to Figure 2-7. The direct and indirect formation of $CoAl_2O_4$, however, have a negative $\Delta G°_{rxn}$ and are thermodynamically feasible throughout the entire temperature range (300 K – 1200 K).

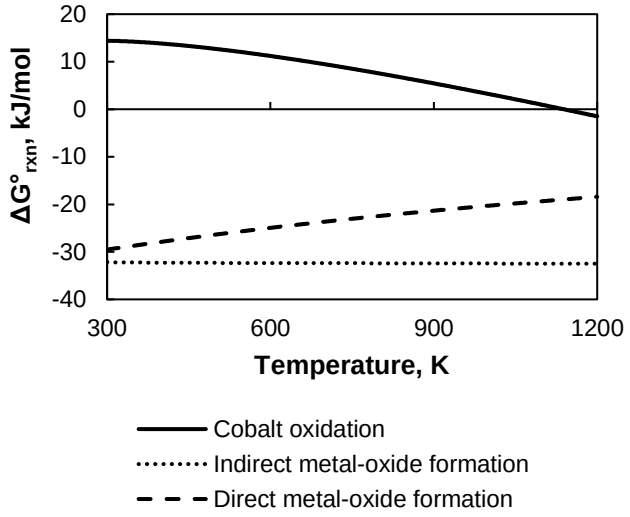

Figure 2-8: Gibbs free energy of reaction for reactions to cobalt oxide and cobalt aluminate across a temperature range. Data taken from [128].

The amount of $CoAl_2O_4$ formed is hypothesized to increase at high conversion conditions as the formation of these structures is kinetically enhanced by increasing partial pressures of water [91]. Hydrothermal Fischer-Tropsch environments have been linked to $CoAl_2O_4$ formation in the past. For instance, Jacobs et al. [131] reported sudden irreversible catalyst deactivation for 0.5Pt-15Co/Al_2O_3 for a feed containing 6 bar water (exit $P_{H_2O}/P_{H_2} = 1.7$) attributed to the formation of a cobalt aluminate-like species as identified using X-ray absorption near edge spectroscopy (XANES) and extended X-ray fine structure (EXAFS). Moodley et al. [123] showed using XANES that cobalt aluminate formation under standard Fischer-Tropsch conversions (exit $P_{H_2O}/P_{H_2} = 1 – 1.5$) is minimal, but rapid formation of cobalt aluminate was observed under more extreme conditions (exit $P_{H_2O}/P_{H_2} = 2.2$). Li et al. [67] also attributed the strong catalyst deactivation and concomitant increase in CO_2-formation upon increasing the water added to the feed (exit $P_{H_2O}/P_{H_2} = 0.59$) to cobalt aluminate formation. Kiss et al. [69] reported a needle-like phase forming after exposing Co/SiO_2 to $X_{CO} > 90\%$ for two weeks. This was attributed to the formation of cobalt silicates

2.5.3. Sintering at high conversion

Sintering is thermodynamically-driven crystallite growth, that results in a loss of active surface area and thus activity [80,132,133]. According to Goodman et al. [134], the mechanism for sintering can be broadly classified as either particle migration and coalescence or atomic ripening. The former involves the movement of nanoparticles, whilst the latter involves the movement of atomic or molecular moieties containing a single or a few metal atoms. In both cases the thermodynamic driving force is the

minimization of surface energy by an increase in crystallite size. Hydrothermal environments (high temperatures and high partial pressures of water) accelerate both mechanisms [94,135,136].

Several studies propose sintering as the primary form of deactivation under high water partial pressures. Bertole et al. [116] investigated the effect of water on a rhenium-promoted unsupported cobalt catalyst under 4 bar and 8 bar water, showing that only 80% of activity lost under water-rich conditions could be regained using hydrogen treatment. Sintering was suggested as the mechanism due to the irreversibility of the deactivation. Kiss et al. [69] reported for Co-Re/SiO_2 that an increase in X_{CO} from 55% to between 80% and > 90% induced a crystallite size growth from an average of 5 nm to between 8 nm and 11 nm based on TEM analysis. It was later proposed by the authors that sintering is a by-product of oxidation, through the "wetting" of the support by cobalt oxide islands [137].

Recently, Claeys et al. [124] provided evidence for the dependence of sintering behaviour on both H_2O and CO partial pressure. Using an in-situ magnetometer it was shown that very little sintering is exhibited in H_2O/H_2 environments even at very high H_2O partial pressures. A surface sub-carbonyl type mechanism over the water-modified alumina support was proposed.

2.5.4. Carbon deposition

The Fischer-Tropsch synthesis proceeds via chain growth on the surface. Thus, there are large amounts of carbon containing molecules on the surface of the catalyst, which may act as precursors for the formation of inactive carbon [80] (amorphous, graphitic, polymeric, refractory etc.) that can block active sites. The Boudouard reaction (equation 2-4) is also a likely cause of inactive carbon [138]. Carbon deposition has, in the past, been linked to an increase in conversion or a decrease in space velocity [115].

Inactive carbon can have several effects on cobalt catalysts. Firstly, the formation of carbon on the surface of cobalt crystallites, or the exposure of cobalt to pure CO can lead to the cobalt carbide formation, which is inactive for the Fischer-Tropsch synthesis [80]. Carbon can also geometrically block cobalt which can retard the diffusion rate of species on the surface and therefore slow the rate of reaction.

Carbon deposition is generally understood to be a long-term deactivation mechanism as convincingly shown by Moodley et al. [139]. In this study, spent Pt-Co/Al_2O_3 was removed periodically from a slurry bed reactor over a 6-month period. The samples were subsequently wax-treated and characterized via

temperature programmed hydrogenation. The study concluded that time-on-stream is likely the controlling factor for carbon formation on both the support and cobalt.

2.6. Potential solutions to high conversion effects

Sections 2.4 and 2.5 discussed the negative effects that operating at high conversions may have on the activity, selectivity and stability of cobalt catalysts. The following two sections will discuss potential solutions to these issues.

2.6.1. Manganese promotion for improved activity and selectivity

The addition of small amounts of manganese (Mn) reportedly improves dispersion, increases the rate of CO consumption and C_{5+} selectivity and decreases the selectivity towards methane [129,140,141]. Thus, the addition of manganese to Pt-Co/Al_2O_3 may improve both activity and selectivity at high conversion.

2.6.1.1. Activity promotion

Activity promotion by Mn is widely reported in experimental studies [141–144]. This phenomenon is thought to be dependent on the concentration of Mn as well as the method used to deposit Mn on the surface.

Dinse et al. [141] and Johnson et al. [142] reported that small concentrations of Mn (Mn:Co ratio < 0.125) improved the rate whilst Mn/Co ratios above 0.125 caused a decrease in rate. Thiessen et al. [144] also reported an increase in rate with Mn promotion for Co/CNT at 1 bar, with a rate maxima at Mn:Co = 0.075. Morales et al. [143] suggests that whilst Mn promotion improves the rate of Co catalysts, it is dependent on the preparation method. In a study which loaded increasing amounts of Mn onto Co/TiO_2 prepared via incipient wetness impregnation and homogenous deposition precipitation, it was found that only the latter had an increased performance at 1 bar.

The reason for the increase in activity with Mn promotion is still a highly debated topic in literature [90,140–142,144]. Zhang et al. [140] suggests that Mn improved the dispersion of Co^0 [77]. However, an increase in dispersion with increasing Mn content is not always reported [90,142]. For instance, Bezemer et al. [90] reports a decrease in dispersion of 1.3% (from 7.8%) with increases in Mn:Co between 0 and 0.1. In other cases, dispersion is reported to increase until a maximum at a specific Mn:Co ratio after which it is reported to decrease. This maximum has been reported to be between a Mn:Co ratio of 0.1 and 0.3 [142,145,146]. Another explanation suggests that MnO increases activity

of adjacent Co-sites through promotion of CO dissociation via Lewis acid-base interaction with Mn^{2+} [141,142].

2.6.1.2. Selectivity promotion

Mn promotion is also reported to improve selectivity – especially at low pressures and low conversions [129,140,141,144]. Dinse et al. [141] reported that promotion of Co/SiO_2 with Mn in a 0.125 Mn/Co ratio led to a decrease (ca. 10 C-%) in CH_4 selectivity, increase (ca.15 C-%) in C_{5+} selectivity and an increase in the olefin/paraffin ratio when operating at 1 bar. These findings are supported by in numerous sources [77,90,129,140,143]. At the same pressure, Thiessen et al. [144] and Bezemer [90] reported a significant decreases in CH_4 selectivity of ca. 35 C-% and 13 C-% when increasing the Mn:Co ratio from 0 to 0.3 and 0.1 respectively. At these conditions, the effect of Mn promotion on selectivity was also reported to be more significant than the effect of increasing conversion between 0 and 25% [141].

The change in selectivity has been linked to the effect of Mn on the linear-to-bridge CO adsorption. Morales et al. [147] used DRIFTS (diffuse reflectance infrared spectroscopy) and found a less intense bridge CO adsorption band for a Mn-promoted catalyst. Bridge-adsorbed CO molecules are expected to have weaker C-O bonds, and thus may be easier to hydrogenate. It may thus be inferred that Mn addition promotes strong C-O bonds may limit rapid hydrogenation to CH_4 [145]. This is, however, a relatively controversial theory as both Zhang et al. [140] and Johnson et al. [142] reported increased peak areas for bridging CO using FTIR. Johnson et al. [142], suggests that the results from Morales et al. [147] may be explained by cobalt size effects, as enhanced C-O bonding directly contradicts with activity improvement which is attributed to enhanced C-O dissociation. Another explanation for the enhanced selectivity [142] is improved CO adsorption as identified using CO-TPD and analysing the CO desorption temperatures which increased with increasing Mn content.

2.6.2. Zinc aluminate support for improved stability

In order to improve the stability of cobalt under the hydrothermal conditions of high conversion, it has been suggested that an alternative support be used. The problem with using typical oxidic support material is that at high conversion, and thus high partial pressures of water, these supports may form irreducible compounds such as cobalt aluminate cobalt silicate and cobalt titanite (see Section 2.5.2). Carbon has recently been suggested as a good substitution for support due to its inability to form such metal-support oxides. However, carbon is very weak and less chemically stable than oxidic supports [77,83–85].

A potentially better option to decrease the formation of cobalt-support compounds would be to support cobalt on a mixed-metal oxide as they do not form irreducible compounds with cobalt, effectively eliminating the possibility of irreversible deactivation due to cobalt aluminate formation [77].

Zinc aluminate in particular has been identified as a possible suitable support for cobalt catalysts in the Fischer-Tropsch process due to its hydrothermal stability, its relatively inexpensive nature and the fact that it does not reduce at Fischer-Tropsch conditions [148,149]. The amount of research available on the effect of using zinc aluminate rather than alumina as a support for a cobalt-based Fischer-Tropsch process is scarce [149].

One of the earliest articles regarding zinc modified alumina as a support investigated the effect of different modifications (Zn, Mg, Ni, Re) to alumina-supported cobalt catalysts [73]. In this investigation, Zn-γ-Al_2O_3 with 10 wt. % Zn was prepared, however the extent of transformation to zinc aluminate was not analysed. The study concluded that modifying alumina with zinc had a strong negative effect on the activity of the catalyst, no noticeable effect on the C_{5+} yield and increased the selectivity of CO_2. These negative results were attributed to the chemical/site effects rather than dispersion [150].

However, recent studies contradicted the earlier claims that the addition of zinc to alumina had a negative influence on the catalyst [148,149,151].

Du et al. [151] modified alumina supports with zinc yielding predominately a $ZnAl_2O_4$ phase. The $Co/ZnAl_2O_4$ catalysts were found to exhibit improved sintering-resistance, weakened cobalt-support interactions and improved reduction from Co(II)O to Co^0. The cobalt catalyst modified by zinc was furthermore found to exhibit the highest Fischer-Tropsch synthesis activity and hydrothermal stability.

Liu et al. [148] synthesized $Co/ZnAl_2O_4$ and Co/Al_2O_3 and compared these in terms of activity and selectivity. During catalyst reactor testing, the co-precipitated $Co/ZnAl_2O_4$ sample exhibited lower methane selectivity, higher C_2-C_4 selectivity and higher olefin/paraffin ratio than the Co/Al_2O_3 at similar conversions.

Chapter 3

Scope and Novelty of Work

3.1. Objectives

The overall objective of this study is to investigate the mechanisms behind the negative selectivity, activity and stability of a typical industrial catalyst – Pt-Co/Al_2O_3 – at high conversion and to investigate the effectiveness of catalyst design improvements that facilitate operation at these conditions. Thereafter, a detailed design of the once-through Fischer-Tropsch biogas-to-fuel plant (biogas from the anaerobic digestion of organic waste) will be proposed using data from the catalytic experiments. Thereafter, the design will be evaluated to determine an optimal conversion and maximum fuel production.

3.2. Conceptual framework

This thesis is broken down into two primary sections – catalyst development (or improvement for high conversion conditions) and process development. Figure 3-1 illustrates how Chapters 4 through 10 fit together conceptually.

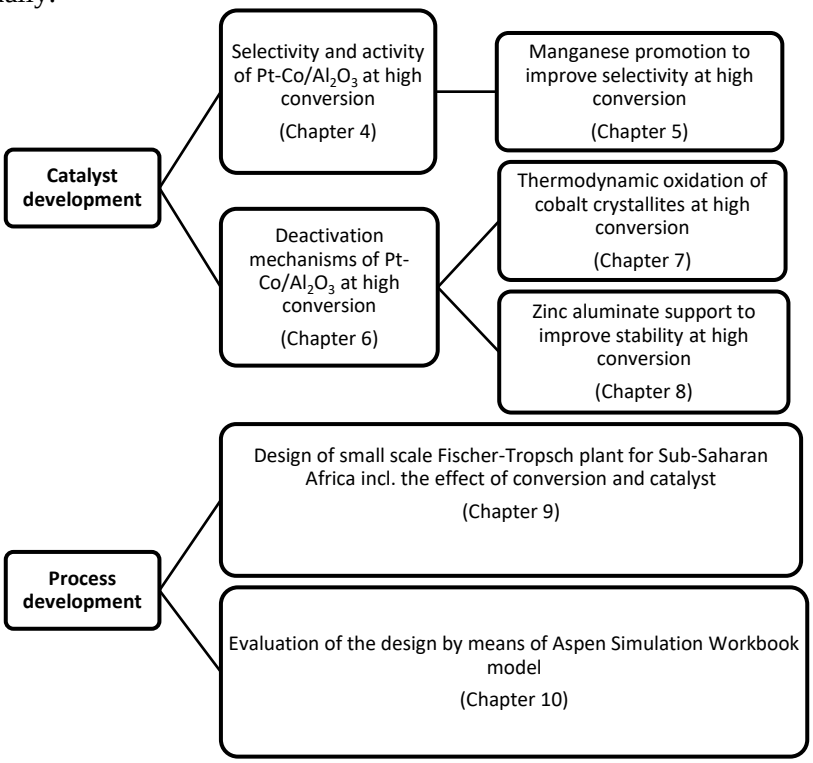

Figure 3-1: Framework of thesis chapters presented in terms of main sections and conceptual links

The catalyst development section (Chapters 4-8) focuses on the effect of high conversion conditions on the selectivity and stability of a typical industrial catalyst – Pt-Co/Al_2O_3 – including an investigation into the mechanisms that cause unfavourable performance. Thereafter, catalyst design improvements will be made to promote operation at high conversion conditions.

Chapter 4 evaluates how high conversion conditions effect the selectivity of undesired by-products such as methane and carbon dioxide as well as the fuel yield (C_{5+}) for a typical cobalt catalyst, Pt-Co/Al_2O_3. Potential explanations for the change observed at high conversion are proposed and tested.

Chapter 5 furthers the selectivity investigation by focusing on how to alter a cobalt catalyst to enhance the yield towards fuel and decrease the selectivity towards unwanted by-products. Manganese is added to the cobalt catalyst in varying concentrations as a promoter. The effect this has on the catalyst from low conversion to high conversion is analysed, and an optimal concentration of manganese is found. An explanation for the promotional effects is proposed based on literature.

Chapter 6 focuses on the effect that increasing conversion has on the stability of Pt-Co/Al_2O_3. This chapter provides a mechanistic understanding of some of the factors – cobalt oxidation, cobalt aluminate formation, and sintering - that impede on catalyst stability at high conversion conditions. This chapter also aims to mechanistically decouple the deactivation mechanisms at high conversion from the effect of water on the stability of Pt-Co/Al_2O_3.

Chapter 7 is a thermodynamic evaluation of one of the mechanisms discussed in Chapter 6 - cobalt oxidation. In order to fully explain the reversible loss of activity at very high conversions (X_{CO} > 90%) this chapter will analyse the thermodynamic effect of oxidation on a logarithmic distribution of cobalt crystallites to evaluate if a maximum conversion exists for a specific size distribution.

Chapter 8 evaluates the possibility of using zinc aluminate as an alternative support for cobalt, in order to decrease the level of deactivation at high conversion caused by the formation of cobalt aluminate.

Chapters 9 and 10 focus on using the catalyst information garnered in Chapters 4-8 as well as the design philosophy discussed in Section 1.6 to create a detailed design (Chapter 9) and an Aspen Simulation Workbook model (Chapter 10) for a small-scale biogas-to-fuel process (using biogas from the anaerobic digestion of waste as a raw material) operated at higher than typical conversion. This design will be contextualised within a Sub-Saharan African background, with fuel products that meet the needs of the region. The main focus of these chapters will be to evaluate how conversion and choice of catalyst

effect the production of fuels from waste, and to evaluate how much fuel can be generated from this system at an optimal conversion.

3.3. Novelty in research

The novelty of this investigation can be evaluated in the following three key sections.

3.3.1. Selectivity at high conversion

This investigation aims to provide an empirical explanation for unfavourable selectivities at high conversion. In the past this phenomenon has been theorized to be due to the formation of Co(II)O and $CoAl_2O_4$ [78] which is said to catalyse the methanation and water-gas shift reaction respectively. No study to date has provided evidence to substantiate this theory. In Chapter 4, this hypothesis is tested in order to provide an evidence-based understanding of selectivity at high conversion (X_{CO} > 75%)

In addition, manganese will be used as a promoter to counteract negative selectivities at high conversion. Whilst the use of manganese as a promoter for cobalt catalysts has been explored previously [129,140,141,144], no authors have to date researched the effects of manganese at conversions above X_{CO} = 60%.

3.3.2. Stability at high conversion

Whilst numerous studies have investigated the effect of hydrothermal conditions on cobalt catalysts [69,80,116,136], few studies have investigated the effect of high conversion on stability [69] nor has there been an attempt to mechanistically decouple the effects of high CO conversion and high partial pressures of water. Chapter 6 will provide evidence for the different mechanisms that occur in each case. In addition, Chapter 7 will establish a novel thermodynamic model that explains the oxidation behaviour at high conversion for a lognormal distribution of nano-sized cobalt crystallites. This thesis will, thereafter, investigate the use of $ZnAl_2O_4$ as a support material to decrease deactivation at high conversion, based on the phenomenon discussed in Chapters 6 and 7. The effect of $ZnAl_2O_4$ on stability of cobalt at high conversion has not been previously investigated.

3.3.3. Design of a once-through biogas-to-distillate plant

The concept of a combined biogas reformer / Fischer-Tropsch waste to fuel system is relatively new in the research sphere, albeit not entirely novel [59,152]. The studies that exist have conducted economic and life cycle analysis on such systems. However, none have considered the effect of conversion (and

thus syncrude composition) on the design. This investigation focuses on the consequence of both catalysts and conversion on the design strategy and modelling of this system. In addition, an ‘optimal’ conversion is reported for both standard industrial and promoted catalyst systems, where previously none existed.

Chapter 4

Activity and selectivity of Pt-Co/Al_2O_3 operating at high conversion

4.1. Justification for high conversion study

The viability of small-scale decentralized waste-to-liquid may be improved significantly by using a once-through configuration without an air separation unit as discussed in Section 1.6. In order to maintain high fuel yields with this configuration, the Fischer-Tropsch synthesis would have to operate at high conversion which implies exposing the Fischer-Tropsch catalyst to a high partial pressure of water and a low partial pressure carbon monoxide and hydrogen. These harsh conditions have been reported to have detrimental effects on the selectivity of desired FT products as described in Chapter 2 [78].

In particular, carbon dioxide selectivity has been reported to increase rapidly after a CO conversion level of ca. 80% [65,78]. A decrease in methane selectivity with increasing CO conversion has been reported for low conversions [65,67,68,78], whilst a significant increase in methane selectivity has been reported above X_{CO} = 80% in a slurry bed reactor [78].

This chapter aims to investigate the effects of high conversion on the selectivity and activity of an industrially relevant catalyst, Pt-Co/Al_2O_3, using conditions mimicking a synthesis gas obtained from air blown reforming (50% N_2 in the feed). In addition, experiments to determine the cause of this phenomena will be conducted.

4.2. Experimental

4.2.1. Catalyst preparation and characterisation

Cobalt supported on γ-Al_2O_3 was prepared by slurry impregnation [153] as described in Appendix B. The calcined catalyst contained 22 wt.-% Co and 0.05 wt.-% Pt as determined from elemental analysis using AAS-OES and ICP-OES.

BET surface area, pore volume and pore size (Micrometrics Tri-Star), hydrogen chemisorption (Micrometrics ASAP HP 2020C), X-ray diffraction (D8 Advance Bruker) and temperature programmed

reduction (Micrometrics Autochem HP II 2950) were used to characterise the catalyst. Detailed experimental procedures used for the analysis are described in Appendix B.

4.2.2. Reactor studies

4.2.2.1. Fischer-Tropsch slurry bed reactor

Four separate reactor tests were conducted at 220°C and 20 bar with reduction conditions and loading procedure as described in Appendix B.

Run 1, the primary investigative run, was performed to determine the effect of CO-conversion on the activity and selectivity in the Fischer-Tropsch synthesis over Pt-Co/Al_2O_3. The reduced catalyst (6.7 g) was loaded into the slurry bed reactor which was fed with gas containing H_2: CO: N_2 = 4:2:6 (to simulate air blown reforming). To assess the selectivity at each conversion level, the conversion of CO (X_{CO}) was increased from 43% to 97% by decreasing volumetric flow rates of all three species while keeping their relative ratio constant (see Fig. 4-1). After each conversion, the volumetric flow rate was increased to the standard level (1000 ml_n/min) to assess the reversibility of these effects.

Run 2 was performed to assess the effect of CO_2 on particularly the methane selectivity in the Fischer-Tropsch synthesis over Pt-Co/Al_2O_3. The reduced catalyst (5.2 g) was loaded in the slurry bed reactor and the conversion was increased in the same way as in Run 1. After steady state was reached at each conversion level, CO_2 was introduced while reducing the nitrogen content in the gas. As a result, the inlet gas composition was changed from H_2: CO: N_2: CO_2 = 4:2:6:0 to 4:2:3:3.

Run 3 was performed to assess the effect of the H_2/CO-ratio on particularly the methane selectivity in the Fischer-Tropsch synthesis over Pt-Co/Al_2O_3. The reduced catalyst (5.6 g) was loaded and excess H_2 was fed into the system so that the inlet H_2:CO:N_2 ratio was increased from 4:2:6 to 5:2:7, 6:2:8, 8:2:10 and 10:2:12. This corresponds to internal H_2:CO ratios of 2, 2.5, 3, 4 and 5 respectively with a constant inlet partial pressure of N_2 (10 bar) and overall pressure (20 bar). This procedure was conducted at various space velocities of CO in order to monitor the effect at various CO conversions.

Run 4 was performed to assess the effect of increasing water partial pressure on the selectivity of methane at low conversion (10%< X_{CO} < 30%) over Pt-Co/Al_2O_3. The reduced catalyst (3.15 g) was loaded in the slurry reactor with H_2: CO: N_2 = 4:2:6 at 220°C and a total flow rate of 1000 ml_n/min. Steam was then added to the feed, replacing N_2 and keeping the partial pressure of syngas in the feed constant (10 bar). The partial pressure of water in the feed was increased from 0 – 5 bar whilst the

nitrogen partial pressure was decreased from 10 – 5 bar. At each partial pressure (1, 2, 3, 4 and 5 bar) the water was removed to assess the effect of water-related deactivation on the selectivity.

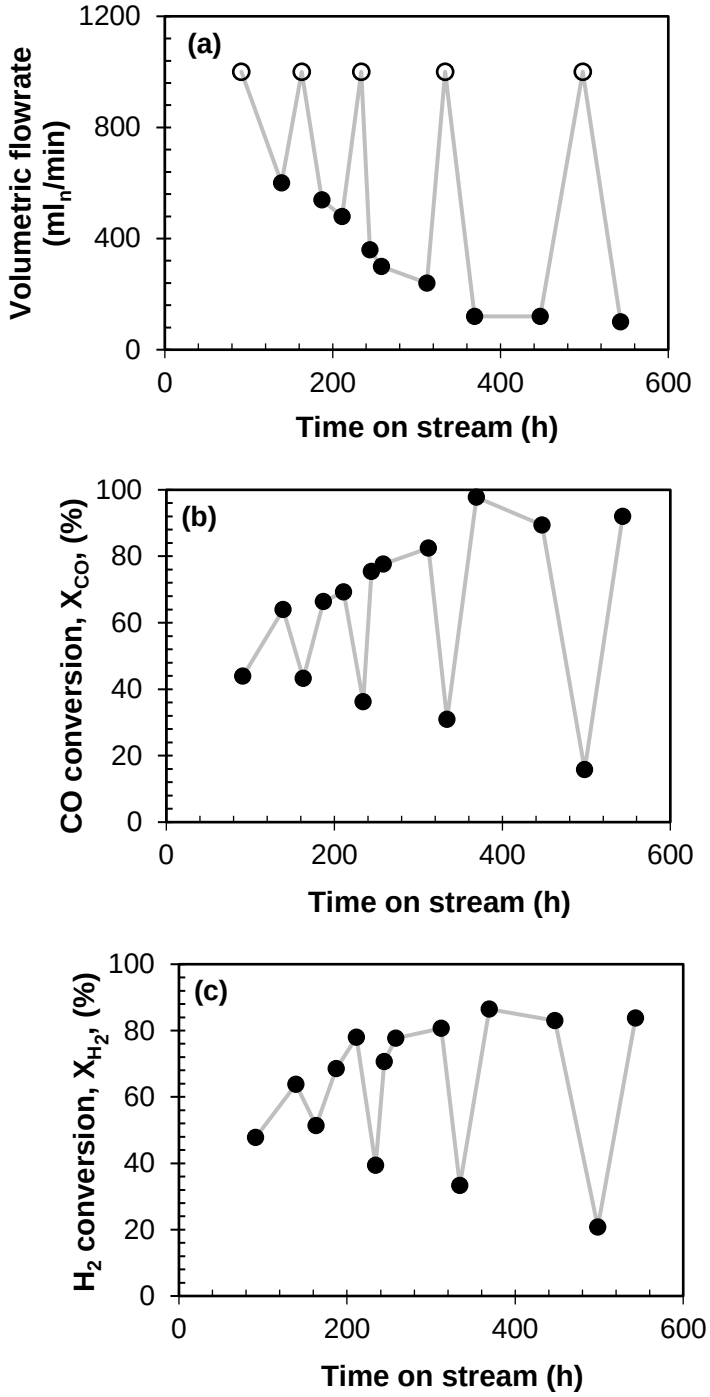

Figure 4-1: Obtaining different conversion levels in Run 1 ($m_{catalyst}$= 6.7 g; T = 220°C, p=20 bar; feed: H_2: CO: N_2 = 4:2:6 - open symbols (○) standard volumetric flow rate of 1000ml$_n$/min; closed symbols (●) variable volumetric flow rate.) (a) Total volumetric flow rate of gas mixture as a function of time on stream (b) CO-conversion as a function of time on stream (c) H_2 conversion as a function of time on stream.

5.2.2.2. Water-gas shift fixed bed reactor

The water-gas shift activity of various species was tested in a fixed bed reactor fed with water and carbon monoxide. This test was conducted for unreduced as well as increasingly reduced (for 2, 6, 12 and 16 hours) Pt-Co/Al_2O_3 to assess the effects of Co(II)O concentration on the water-gas shift activity. Additionally, the alumina support, Puralox SCCa 5/150, and pure cobalt aluminate were tested.

The catalyst/ support/ standard was diluted in a 1:3 ratio with silicone carbide and reduced in-situ at 350°C in pure hydrogen. The temperature was then decreased to atmospheric conditions. Carbon monoxide and water were fed to the reactor in a 1:1 ratio at a flow rate of 300 ml/min. The temperature was increased at a rate of 2°C/min between ambient and 400°C while the concentrations of CO, H_2 and CO_2 in the effluent were measured.

4.3. Results and Discussion

4.3.1. Catalyst characterisation

The physio-chemical characteristics of the calcined and reduced catalyst, Pt-Co/Al_2O_3, are shown in Table 4-1. Further characterisation is described in Appendix C.1.

Table 4-1: Physio-chemical characterization of the support and catalyst.

	calcined catalyst precursor				***Reduced catalyst (350°C, 16 hours)***			
	S_{BET} (m^2/g)	**V_{pore} (cm^3/g)**	**d_{pore} (nm)**	**$d_{Co_3O_4}$[1] (nm)**	**DOR[2]**	**S_{Me}[3] (m^2/g_{cat})**	**D_c[4] (%)**	**d_{Co}[5] (nm)**
Puralox	157	0.5	8.8					
Pt-Co/Al_2O_3	113	0.3	8.0	11	54%	13	16[6]	6.0[6]

[1]Diameter of Co_3O_4-crystallites as determined using XRD; [2]Degree of reduction; [3]Metal surface area as determined by H_2-chemisorption; [4]Cobalt dispersion; [5]Diameter of cobalt-crystallites estimated from H_2-chemisorption data; [6]Corrected for degree of reduction

4.3.2. Effect of conversion on activity

The rate of formation of hydrocarbons in the Fischer-Tropsch synthesis is a function of the partial pressure of the kinetically relevant compounds, and thus a function of the conversion. Increasing the CO-conversion will result in a decrease in the partial pressures of CO and H_2. Many different rate expressions have been proposed in the past [98,99,101,111] and according to these expressions a decrease in the partial pressures of CO and hydrogen will result in a decrease in the rate of formation of hydrocarbons

The reduced catalyst, Pt-Co/Al_2O_3, deactivated with time on stream (see Fig. 4-2), with more pronounced deactivation taking place after ca, 160 h on-line. The evaluation of the activity of a deactivating catalyst is non-trivial. In order to compare, the activity of the catalyst as a function of time on stream, the relative activity, *a*, was defined as the observed rate of reaction relative to the expected rate of reaction based on the rate described by the expression proposed by Botes et al. [103] (and the constants determined by fitting to data obtained at time on stream between 90 and 160 h):

$$a = \frac{-r_{CO+CO_2,measured}}{\left(\frac{A \cdot p_{H_2}^{0.75} \cdot p_{CO}^{0.5}}{\left(1+B \cdot p_{CO}^{0.5}\right)^2}\right)}$$ with A = 1.39 mmol/(min.g·$bar^{1.25}$) and B = 1.80 $bar^{-0.5}$

Figure 4-2 shows relative activity as a function of time on line. The relative activity as a function of time on line seems to drop significantly after ca. 200 h on line levelling off after ca. 400 h on line for both *Run 1* and *Run 2*. The relative activity as a function of time on line can be reasonably described by an empirical tanh-function.

The observed deactivation may have been affected by the range of conditions to which the catalyst was exposed seeing that the deactivation seems to be faster than previously reported [127]. Furthermore, it can be noted that the relative activity in Run 2 at ca. 600 h on line was much higher than expected. In this case, the catalyst had been exposed to extremely high CO-conversion of 97.5% (which was obtained after ca. 525 h on line). Since the Botes et al. [103] model was empirically derived at low conversion, it may be postulated that this increase is due to the theoretical model's under-prediction of activity at these conditions.

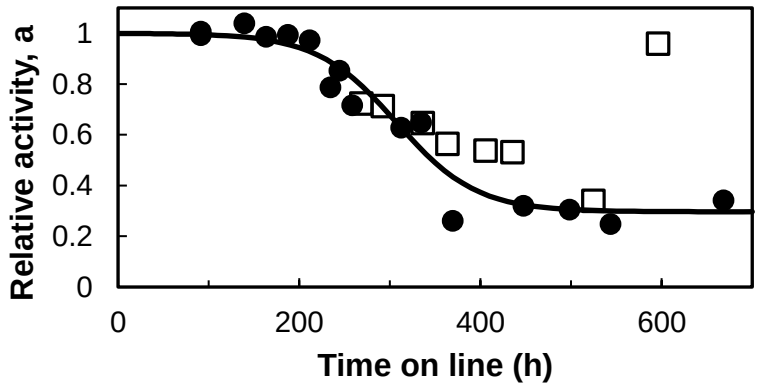

Figure 4-2: Relative activity (as defined in the text) as a function of time on line (Run 1: ● Run 2; □; solid line empirical fit of the relative activity as a function of time on line with $a = \frac{1-0.54 \cdot \tanh\left(\frac{t-88}{307}\right)}{1.54}$

4.3.3. CO_2 selectivity

The effect of increasing CO conversion from 15% to 97% on the selectivity of carbon dioxide is shown in Figure 4-3.

The CO_2 selectivity at low to moderate conversions increased very slightly up to X_{CO} = 70%, at which point the selectivity for CO_2 was 1.4 C-%. Increasing the CO-conversion beyond 75%, by decreasing the space velocity, resulted in a strong increase in the selectivity for CO_2 to 21 C-% at a CO conversion of 97%. This strong rise was also reported by Ma et al. [78] wherein the CO_2 selectivity increased to > 10 C-% at X_{CO} > 90%.

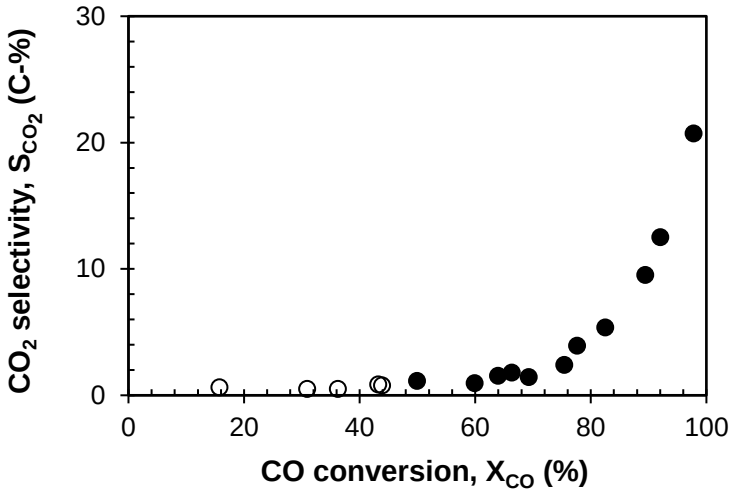

Figure 4-3: Selectivity towards CO_2 for Pt-Co/Al_2O_3 at 20 bar, 220°C, H_2: CO: N_2=4:2:6 (*Run 1*). Closed symbols (●) changing volumetric flow rate. Open symbols (○) standard volumetric flow rate (1000ml_n/min).

4.3.3.1. Cause of CO_2 elevation

Previously [154], the increase in the formation of CO_2 with increasing CO-conversion was attributed to the conversion of Co^0 to oxidised species such as Co(II)O and $CoAl_2O_4$ [65,67,78], which have been suggested to actively catalyse the water-gas shift reaction [65,78].

$CoAl_2O_4$ is thought to be irreducible under Fischer-Tropsch conditions [82,91]. This phase, if formed under Fischer-Tropsch conditions, will remain present after decreasing the conversion. This would increase the amount of the presumably catalytically active phase for the water-gas shift reaction, and,

as a result, an elevated selectivity towards CO_2 can be expected upon return to baseline conditions (low conversion, high space velocity). However, this was not observed in the current investigation. On increasing flow rate to baseline conditions, the CO_2 selectivity completely recovered. This indicates that either $CoAl_2O_4$ was not formed, or it is not water-gas shift active. In either case, the formation of $CoAl_2O_4$ is likely not the cause of the elevated CO_2 selectivity seen at high conversion.

The oxidation of metallic cobalt to Co(II)O may be considered to be the cause for a reversible increase in the CO_2 selectivity as this oxidation is both reversible and reported for cobalt-based catalysts [78,79,81,117,126]. This oxide may catalyse the water-gas shift reaction [155–162]. However, with few exceptions [41], significant water-gas shift activity using cobalt-based catalysts is reported only for temperatures above 250°C [155–160,162] (see Appendix A). In order to test the validity of the correlation between Co(II)O and water-gas shift activity, Pt-Co/Al_2O_3 in different stages of reduction was tested in a water-gas shift fixed bed reactor with a CO feed volumetric flow rate of 300 ml/min and a $CO:H_2O$ ratio of 1. This experiment was conducted for Pt-Co/Al_2O_3 with H_2 reduction (350°C) times of 0, 2, 6, 12 and 16 hours as well as pure cobalt aluminate and Puralox SCCa 5/150. The catalysts/supports were tested for water gas shift activity between 50°C and 400°C.

Figure 4-4 shows the effect of temperature and reduction time on the volumetric flow rate of CO, H_2 and CO exiting the water-gas shift reactor for Pt-Co/Al_2O_3 at reduction times of 0, 2 and 12 hours between 180°C and 300°C. Graphs for all reduction times and temperatures can be found in Appendix D. The unreduced Pt-Co/Al_2O_3 was found to be inactive for the water-gas shift reaction, producing no CO_2 and H_2 from CO and water. After reduction at 350°C for 2 hours, the water-gas shift activity of the catalyst increased to a conversion of 0.63% at 220°C based on the exiting H_2 volumetric flow rate flow. No CO_2 was detected at this point due to the detection limits of the GC. The CO conversion eventually increased to 11.5% at a temperature of 300°C. Reducing the catalyst for a longer period of time (12 hours) resulted in an increase in the amount of H_2 and CO_2 produced. Based on the amount of H_2 produced, the water-gas shift conversion could be calculated to be approximately 1.2 % at 220°C and 14.6% at 300°C. Pure alumina and cobalt aluminate were also tested (see Appendix D) and found to have no water-gas shift activity over the entire temperature range.

This experiment indicates that a greater level of cobalt reduction, and thus less Co(II)O and more Co^0, enhances the water-gas shift reaction, even at temperatures as low as 220°C, albeit far more at higher temperatures. This may suggest that Co^0 has a greater level of water-gas activity than Co(II)O or Co_3O_4. Thus, the increase in CO_2 at $X_{CO} > 75\%$ is likely be due to the kinetic enhancement of the water-gas shift reaction due to increased partial pressures of water at these conditions rather than a thermodynamic

transformation to Co(II)O. This explanation is theoretically consistent with the thermodynamic model by van Steen et al. [117] (Figure 2-7) which indicates that for a cobalt crystallite of 6 nm, a conversion of 93% is required to convert Co^0 to Co(II)O, whilst CO_2 formation is seen at far lower conversions.

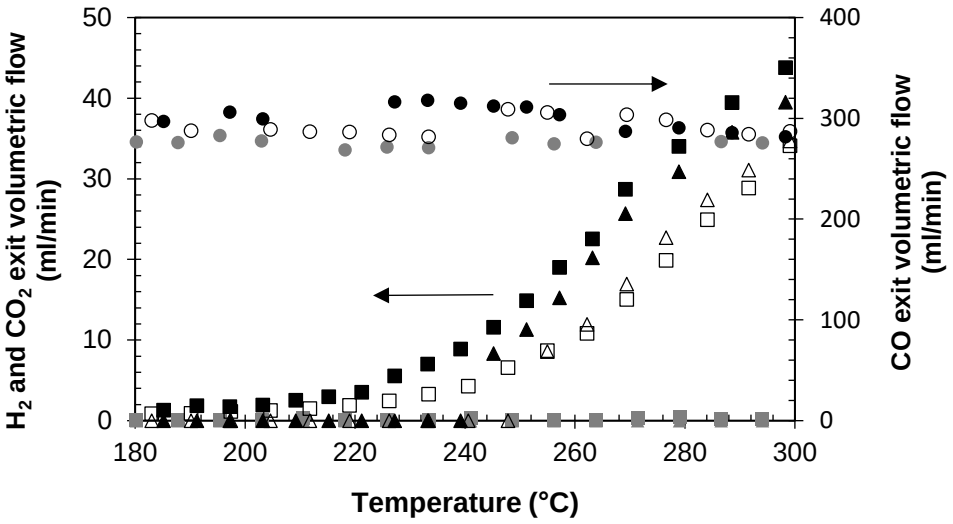

Figure 4-4: H_2 (■), CO_2 (▲)and CO (●) exit volumetric flow rate as a function of temperature for Pt-Co/Al_2O_3 reduced at 350°C for 0 h (▲,■,●), 2 h (△, □ , ○) and 12 h (▲,■,●) in a water-gas shift fixed bed reactor with feed CO:H_2O = 1:1, CO volumetric flow rate = 300 ml/min, cat weight = 0.5 g.

4.3.4. CH_4 selectivity

This study found that the effect of conversion on the methane selectivity could be divided into two distinct regimes across the conversion range (see Fig. 4-5).

Regime I, from a CO conversion of 20% to 75%, was characterized by a decrease in the methane selectivity with increasing conversion whilst Regime II, from 75% onwards, was characterized by a strong increase in methane selectivity (on a CO_2-free basis) to 57 C-% at a CO conversion of 97%. This trend confirmed the results presented by Ma et al. [78] wherein a strong increase in methane selectivity was also noted, although they reported a much lower methane selectivity at high conversion (14 C-%). The difference in results can be attributed to large amounts of N_2 in the feed (50 vol.%) for this study (chosen to simulate conditions after air-blown reforming), which effectively reduced the inlet partial pressure of reactants to 10 bar.

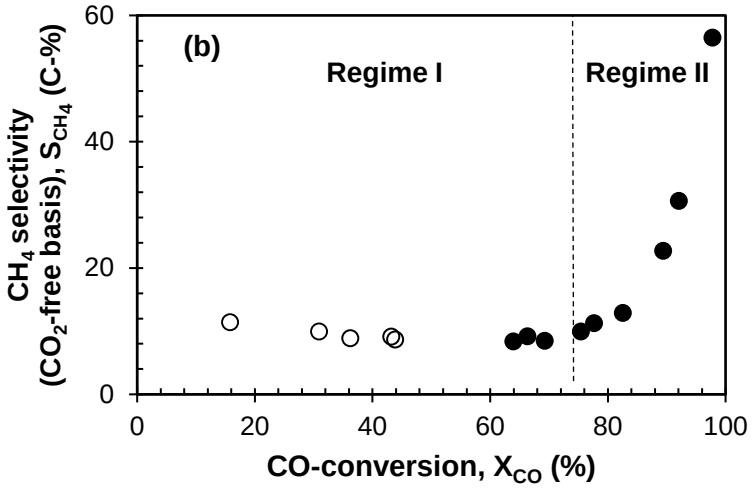

Figure 4-5: Selectivity towards methane (CO_2 free basis) (b) for Pt-Co/Al_2O_3 at 20 bar, 220°C, H_2: CO: N_2=4:2:6 (*Run 1*). Closed symbols (●) changing volumetric flow rate. Open symbols (○) standard volumetric flow rate 1000ml_n/min).

4.3.4.1. Cause of CH_4 elevation in regime II

4.3.4.1.1. Cobalt oxidation

The strong increase in methane selectivity has been previously attributed [78] to the formation of oxidized Co species or cobalt-support complexes such as $CoAl_2O_4$. It was suggested that such species may catalyse the methanation reaction [78]. As the conversion to $CoAl_2O_4$ is thought to be irreversible, upon return to baseline conditions from high conversion (which could have led to the formation of $CoAl_2O_4$) an increased selectivity towards methane should have been exhibited. However, this was not observed in this study. Therefore, the presence of $CoAl_2O_4$ is unlikely to be the cause of the increase in methane selectivity with increasing CO-conversion.

4.3.4.1.2. Hydrogenation of CO_2

Hydrogenation of carbon dioxide may be a potential cause of the high CH_4 selectivity at high conversion. Previous studies have reported that the addition of CO_2 to a CO/H_2 stream resulted in the hydrogenation of CO_2 to methane [163–165] at similar temperatures (190 – 210°C) and pressures (10 - 24 bar) to this study. Figure 4-6 illustrates the effect of conversion on the selectivity of methane with (●) and without (□, ○) co-feeding of CO_2 for Runs 1 and 2. In Run 2 the reactor feed was changed from H_2: CO: N_2: CO_2= 4:2:6:0 to H_2: CO: N_2: CO_2= 4:2:3:3 at various levels of CO-conversion. The amount of CO_2 added to the reactor was equivalent to approximately 8 times the maximum partial pressure of CO_2, which was observed at a CO conversion of 97% with a selectivity towards CO_2 of 21 C-%.

Figure 4-6 shows that there was no strong increase in methane selectivity upon replacing some of the nitrogen in the feed with CO_2. This was even true at X_{CO} = 92%, where the CO_2/CO ratio would have reached a maximum. This implies that CO_2 hydrogenation under the tested conditions was not the cause of the observed high methane selectivity at high conversion.

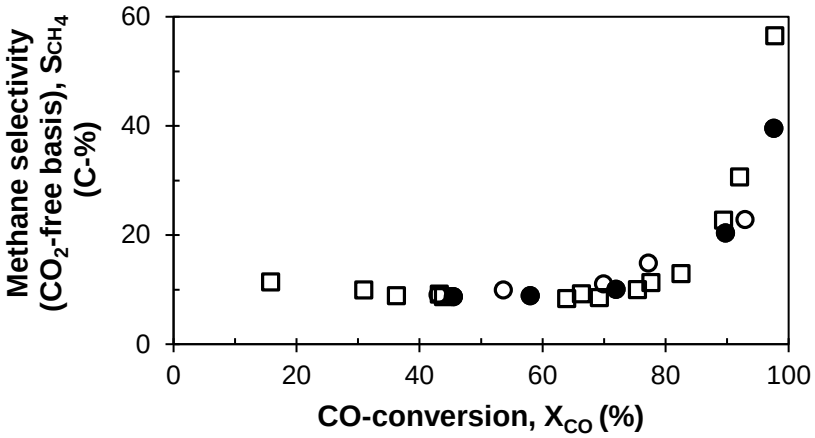

Figure 4-6: Methane selectivity on a CO_2-free basis as a function of CO-conversion over Pt-Co/Al_2O_3 at 20 bar, 220°C (*Run 1* (□) feed ratio H_2: CO: N_2: CO_2= 4:2:6:0; *Run 2* (●) feed ratio H_2: CO: N_2: CO_2= 4:2:3:3; *Run 2* (○) feed ratio H_2: CO: N_2: CO_2= 4:2:6:0)

4.3.4.1.3. H_2/CO ratio

An alternative explanation is that the increase in methane selectivity at high CO conversion can be attributed not to CO_2 but rather as a consequence of CO_2-formation. Independent of the route through which CO_2 is formed, the reaction of CO to CO_2 does not consume H_2. The formation of CO_2 would, thus, create an imbalance in the syngas ratio as the CO partial pressure decreases, and the H_2 partial pressure (in the case of WGS) increases. The formation of CO_2 will, thus, inherently increase the H_2/CO ratio within the slurry bed reactor.

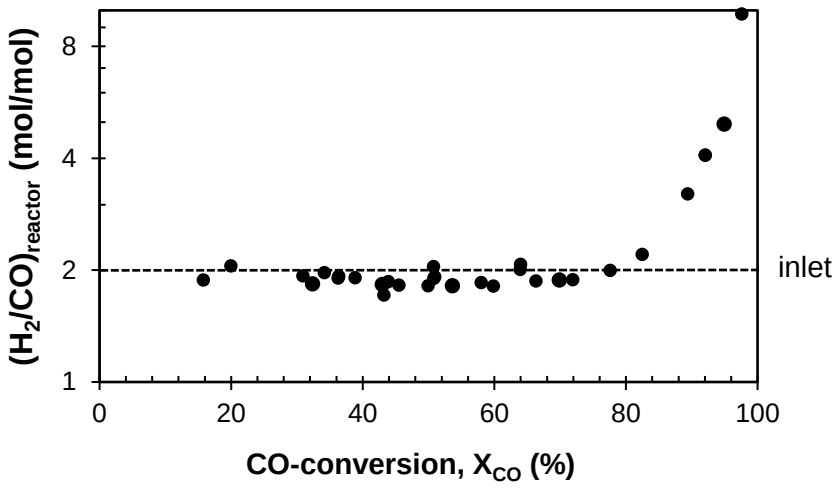

Figure 4-7: H_2/CO-ratio within the reactor as a function of CO-conversion over Pt-Co/Al_2O_3 at 20 bar, 220°C, H_2: CO: N_2 = 4:2:6 (*Run 1*)

Figure 4-7 shows that the measured H_2/CO ratio leaving the reactor was slightly below 2 at CO-conversion level between 20% and 75%. The exit H_2/CO ratio at these conditions was below the ratio in the feed (H_2/CO=2) since the usage ratio for cobalt-based Fischer-Tropsch synthesis was slightly larger than 2 [48]. The H_2/CO-ratio within the reactor increased strongly for CO-conversions larger than 80% and reached a maximum of 10 at X_{CO} = 97%. This can be attributed to the increased conversion of CO to CO_2, via the water-gas shift reaction, which effectively reduces the usage ratio [78].

The effect of H_2/CO ratio on the methane selectivity was tested by the addition of external H_2, keeping the inlet partial pressure of N_2 constant, to artificially increase the internal H_2/CO ratio; the CO-conversion was varied by changing the space velocity (see Fig. 4-8).

At an approximately constant CO conversion level of ca. 50%, the methane selectivity increased proportionally to the increase in the inlet H_2/CO-ratio (from 9.5 C-% for $(H_2/CO)_{inlet}$=2 to 26 C-% $(H_2/CO)_{inlet}$=4). The methane selectivity appeared to be dependent on the conversion of CO for all inlet H_2/CO-ratios. A similar trend (little change in the methane selectivity at low levels of CO-conversion and a strong increase in the methane selectivity going to high conversions), albeit at higher levels, was observed for the experiments performed with a higher inlet ratio of H_2/CO.

Methane formation is kinetically controlled in the Fischer-Tropsch synthesis and thus the partial pressures of the kinetically relevant components within the reactor are the determining factor. Changes in the internal partial pressures of H_2 and CO have two contributing properties that may affect the methane selectivity. At low to moderate conversion, the catalyst surface is covered primarily with CO.

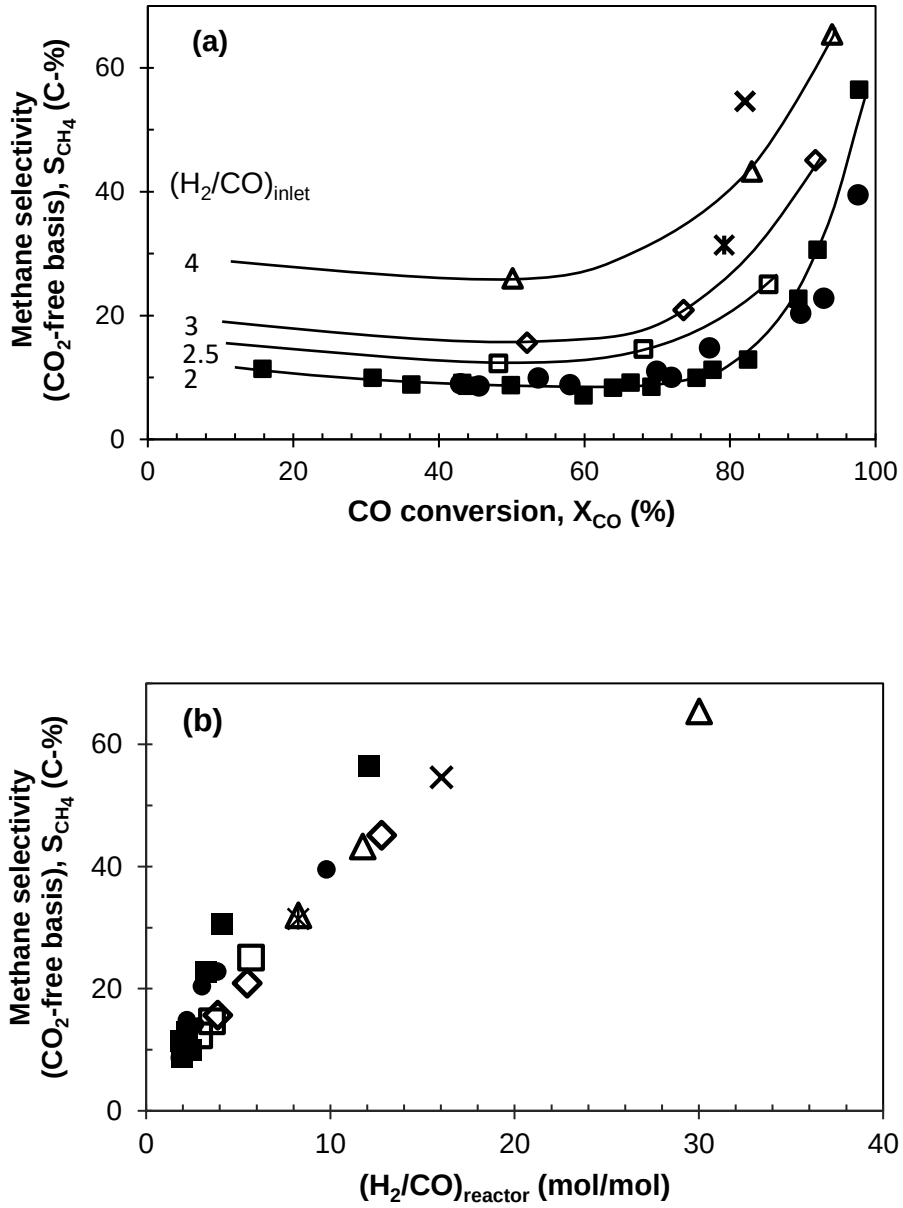

Figure 4-8: Methane selectivity as a function of (a) CO-conversion and (b) H_2/CO-ratio within the reactor over Pt-Co/Al_2O_3 at 220°C and 20 bar (inlet partial pressure of N_2: 10 bar; filled symbol $(H_2/CO)_{inlet}$=2: *Run 1* ■ and *Run 2* ●; *Run 3* $(H_2/CO)_{inlet}$=2.5: □, $(H_2/CO)_{inlet}$=3: ◊, $(H_2/CO)_{inlet}$=3.5: ✳, $(H_2/CO)_{inlet}$=4: Δ and $(H_2/CO)_{inlet}$=5: ✕)

However, at high conversion the CO surface concentration decreases and the H_2 coverage subsequently increases. This increased hydrogen availability on the surface favours desorption, leading to enhanced methane formation [50].

4.3.4.2. Cause of CH_4 decrease in regime I

4.3.4.2.1. Kinetic effects of water

At low to moderate levels of CO-conversion (15% - 60%, Regime I) the H_2/CO ratio within the reactor was approximately constant resulting in $(H_2/CO)_{reactor}$=1.9-2.2. Under these conditions, methane selectivity varied between 8.6 and 14.8 C-%. As shown in Fig. 4-5, in this region (Regime I) the methane selectivity decreased with increasing CO-conversion. This decrease in methane selectivity with conversion is consistent with earlier studies [65,68,78,79,116] and has been previously attributed to the increase in the partial pressure of water, which is intrinsically linked with CO-conversion in this study. Water is thought to inhibit secondary hydrogenation of olefins and chain termination, thus increasing the chain growth probability [68,78].

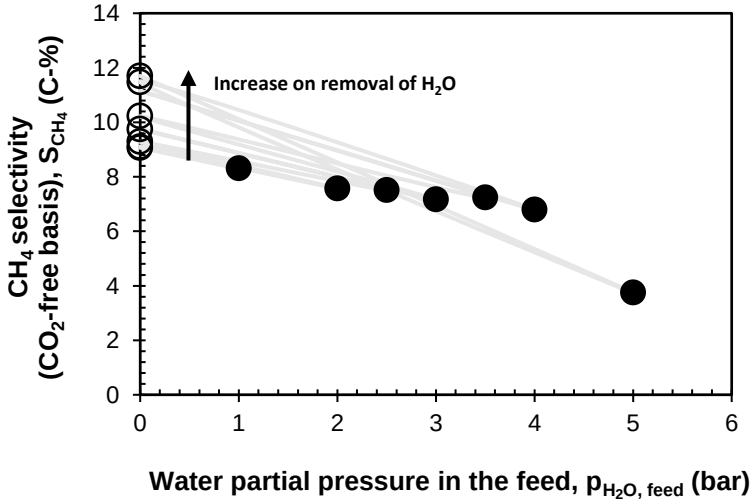

Figure 4-9: Methane selectivity as a function of the partial pressure of water in the feed keeping the partial pressure of synthesis gas in the feed constant (T=220°C, p=20 bar; feed $N_2:H_2:CO:H_2O$ = 6-x:4:2:x (x=0-3)). Closed symbols: with externally added water; Open symbols: water removed.

Decoupling the effect of conversion and water partial pressure on methane selectivity is not trivial. To assess the effect of high water partial pressure, Run 4 was conducted whereby water was co-fed into the reactor (replacing N_2 in the feed to keep the partial pressures of CO and H_2 in the feed constant). After introducing a feed containing water, the water was removed from the feed to assess the change in the catalyst behaviour after exposing the catalyst to a high water partial pressure.

Figure 4-9 illustrates the methane selectivity obtained over Pt-Co/Al_2O_3 as a function of water partial pressure in the feed (Run 4). The methane selectivity decreased upon increasing the water partial

pressure in the feed as reported previously [11-13, 51]. Water may affect carbon coverage on the surface [78,116] e.g. by facilitating CO dissociation [11,52,53], thus increasing the surface concentration of monomeric species. This would not only result in a decrease in the methane selectivity, but also in an increase the rate of the Fischer-Tropsch synthesis.

Upon increasing the conversion in the Fischer-Tropsch synthesis, the partial pressure of water will increase. Hence, a decrease in the methane selectivity is expected, as observed in Run 1 when the conversion was below 75%. It should, however, be noted that the methane selectivity in Run 1 in Regime I ($15\% < X_{CO} < 75\%$) was in the range 11.4 C-% - 8.5C-%. Yet for equivalent water addition (1 - 3 bar) the methane selectivity was 8.3 C-% – 7.1 C-%. The elevated methane selectivity in Run 1 may be related to the deactivation of the catalyst, or the 'catalyst age'. Carbon is expected to built-up over time [26], and hence methane selectivity is expected to increase. Appendix E contains further experimental evidence, and a discussion, on this phenomenon.

4.3.5. Chain growth probability

The chain growth probability (Run 1) in the C_3-C_8 range decreased with increasing level of CO-conversion as shown in Figure 4-10. This implies that with increasing CO-conversion the desorption reaction becomes more favoured compared to the chain growth reaction. This may be due to the increased hydrogen availability [50] lightening the inhibition of product desorption [49]. It should further be noted that the decrease in the chain growth probability as a function of the conversion of CO is more gradual than the increase in the methane selectivity, possibly caused by the observed decrease in the methane selectivity with increasing CO-conversion in Regime I.

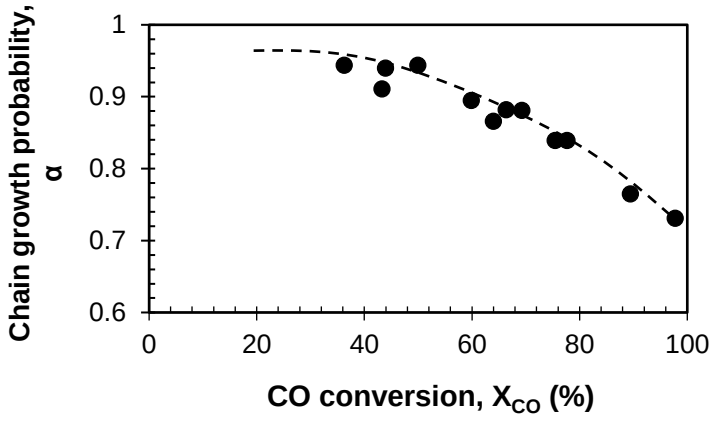

Figure 4-10: Chain growth probability (C_3-C_8) as a function of CO-conversion in *Run 1*.

4.3.6. Olefin content

The olefin content in the hydrocarbon fraction with a specific carbon number is dependent on CO-conversion and carbon number as previously reported [68,78,111]. Figure 4-11 shows a decrease in olefin content with increasing conversion for C_2, C_4 and C_6. This decrease appears to be stronger in Regime II, especially between X_{CO} = 75% and X_{CO} = 90%, albeit this appears to level off above X_{CO} = 90%. Various plausible explanations have been given for the decrease in olefin content with increasing conversion. One such explanation suggests that this phenomenon can be explained by competitive adsorption between CO and the alkenes [78]. Alternatively the observed decrease in the olefin content with increasing CO-conversion may be attributed to a reduction in CO-partial pressure thus favouring re-adsorption of olefins [78] and/or increased residence time with increasing CO-conversion (which was achieved by changing the space velocity) [68]. The stronger decrease in olefin content between X_{CO} = 75 – 90% may be attributed to increased H_2 availability which would facilitate secondary hydrogenation of primarily formed olefins to paraffins.

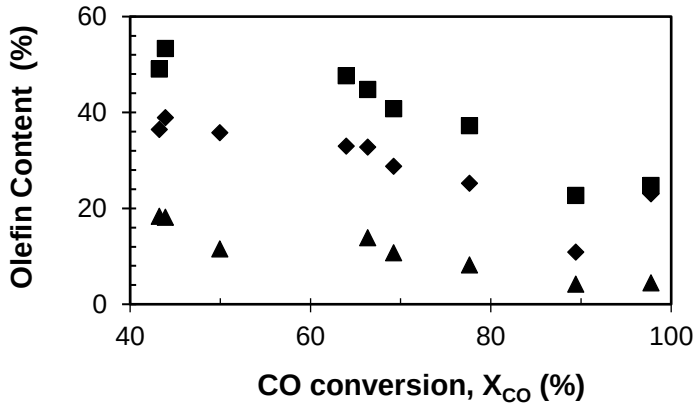

Figure 4-11: Olefin content as a function of CO-conversion (C_2: ▲; C_4: ■; C_6: ♦) in *Run 1*.

4.3.7. C_{5+} selectivity

The ultimate objective of the low temperature Fischer-Tropsch process is to convert synthesis gas as efficiently as possible into liquid hydrocarbons (C_{5+}). The C_{5+} selectivity is determined by a combination of several factors, such as the chain growth probability and methane selectivity. Figure 4-12 shows the effect of CO-conversion on the (a) C_{5+} selectivity and (b) C_{5+} yield.

At low conversions (X_{CO} = 38% to 60%) the C_{5+} selectivity (Figure 4-12 (a)) increased from 83 C-% to 91 C-%. The C_{5+} yield (Figure 4-12 (b)), consequently, increased strongly from 30 C-% to 67 C-% between X_{CO} = 36% and X_{CO} = 78%. The increase in C_{5+} selectivity and yield were accompanied with

the decrease in the methane selectivity, which may be associated with a change in the surface coverage with carbonaceous species [58].

The C_{5+} selectivity (Figure 4-12 (a)) started to decrease at X_{CO} = 75% , reaching a minimum of 50 C-% at X_{CO} = 97%. This resulted in the C_{5+} yield (Figure 4-12 (b)) levelling out at X_{CO} = 78% and decreasing significantly passed X_{CO} = 90%. The rapid decrease in C_{5+} selectivity and yield at high conversion was associated with the strong increase in methane selectivity, a decrease in chain growth probability, and an increase H_2/CO-ratio within the reactor. This may be attributed to a decrease in the number of monomers present on the surface thus reducing the rate of growth and resulting in an increase in methane selectivity (and thus a decrease in the C_{5+} selectivity) at high CO-conversion [58].

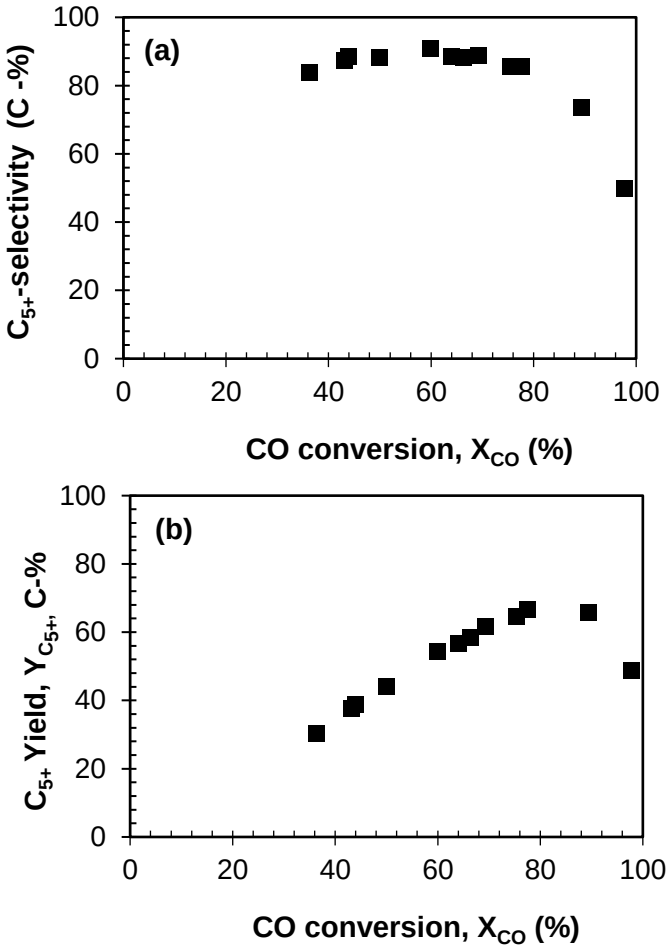

Figure 4-12: Selectivity (a) and yield (b) towards liquid hydrocarbons (C_{5+}) as a function of the conversion of CO over Pt-Co/Al_2O_3 at 220°C and 20 bar (feed: H_2: CO: N_2 = 4:2:6)

The prospect of having a WTL-process operating at high CO-conversion is seriously hampered by the observed decrease in C_{5+} yield and the increase in the methane selectivity over this Pt-Co/Al_2O_3 Fischer-

Tropsch catalyst. The prospect may be enhanced by shifting the maximum in the C_{5+}-yield, which for this catalyst is obtained at X_{CO} ~ 78%, towards higher CO-conversion. This may be achieved by the addition of a promoter strengthening CO-adsorption and favouring CO-dissociation [59], thus increasing the coverage of the surface with carbonaceous species, which may favour chain growth over termination even at high CO-conversion, i.e. low partial pressure of CO. This will be discussed further in Chapter 5.

4.4. Conclusion

The level of conversion has a remarkable effect on the performance and selectivity of a platinum promoted cobalt catalyst supported on alumina in a slurry bed reactor. Increasing conversion was found to decrease the rate of reaction due to the low partial pressures of reactants in the slurry bed reactor. The harsh conditions of high conversion adversely affected the selectivity obtained over Pt-Co/Al_2O_3. A strong increase in carbon dioxide selectivity at high conversion was noted which was attributed to kinetic enhancement of the water-gas shift reaction by an increase in water partial pressure. Methane selectivity decreased with increases in conversion until X_{CO} > 75% where a rapid rise in methane selectivity was detected. This rise can be attributed to an increase in the H_2/CO ratio within the slurry bed at high conversion, due to CO_2 formation which occurs without the depletion of H_2, rather than a transformation of cobalt as previously suggested.

The obtained minimum in the methane selectivity as a function of CO-conversion can be understood in terms of the coverage of the surface with carbonaceous species. If the surface coverage with carbonaceous species becomes too high (at low conversion or upon catalyst deactivation), the diffusion of surface species, and also the monomeric species, will be impeded thus reducing the chain growth probability. At high CO-conversion, the coverage with carbonaceous species is expected to be low due to the low partial pressure of CO, aggravated by the increase of the H_2/CO ratio in the reactor. This will reduce the surface coverage with monomeric species and thus favouring chain termination in the form of methane. Hence, increasing conversion was also found to decrease chain growth probability and the C_{5+} selectivity.

Chapter 5

Manganese promotion of Pt-Co/Al_2O_3 to improve selectivity at high conversion for single pass Fischer-Tropsch

5.1. Rational for manganese promotion

Operating at high conversion (X_{CO} > 75%) has been shown to negatively affect the activity and selectivity of Pt-Co/Al_2O_3 as described in Chapter 4. In particular, the selectivity towards C_{5+} is inhibited whilst selectivities towards unwanted by-products such as CH_4, and CO_2 improves. It may be possible to counteract these effects by the addition of a promoter. It has been reported that the addition of small amounts of manganese (Mn) to cobalt-based catalysts has led to an increased rate [141–143], an increased C_{5+} selectivity and a decrease in CH_4 selectivity [77,90,129,140,141,143]. Whilst manganese promotion has been well explored in literature, its effect at conversions higher than X_{CO} = 60% has not yet been established. Furthermore, the extent of promotion is reportedly dependent on the amount of Mn added - small concentrations of Mn reportedly improve rate whilst higher ratios decrease activity [142,145,146]. Thus, an optimal level of Mn promotion may be attainable.

Chapter 5 investigates the effect of adding incremental amounts of Mn to Pt-Co/Al_2O_3 to improve activity and C_{5+} selectivity whilst decreasing the selectivity towards unfavourable by-products such as CO_2 and CH_4 at conversions from X_{CO} = 40 to X_{CO} = 95%

5.2. Experimental

5.2.1. Catalyst synthesis

Six Mn- and Pt- promoted cobalt catalysts were prepared with varying levels of Mn promotion and supported on Puralox SCCa 5/150 as described in Appendix B. The ICP-OES for each of the 6 catalysts can be seen in Table 5-1. The catalysts range from mass Mn:Co ratio of 0 to 0.47. The Pt:Co ratio for all catalysts was kept constant and unchanged from the investigation in Chapter 4.

Table 5-1: Catalyst compositions as determined by ICP-OES.

	Mn:Co	*0.00*	*0.04*	*0.09*	*0.14*	*0.23*	*0.47*
ICP wt. %	Al	38	38	38	37	36	35
	Co	22	22	22	22	22	21
	Pt	0.04	0.04	0.03	0.03	0.03	0.03
	Mn	0	1	2	3	5	10

5.2.2. Catalyst characterization

X-ray diffraction (D8 Advance Bruker), hydrogen chemisorption (Micromeritics ASAP HP 2020C), physisorption (Micromeritics Tri-Star system), temperature programmed reduction (TPR), hydrogenation (TPH) (Micromeritics Autochem HP II 2950) and high resolution transmission electron microscopy (HR-TEM) (JEOL ARM 200F) were conducted to characterize the fresh and spent catalyst. Detailed experimental procedures can be found in Appendix B.

5.2.3. Slurry bed reactor studies

Catalysts were reduced and loaded as described in Appendix B. The catalysts were tested for activity and selectivity between X_{CO} = 40% and X_{CO} = 95% at 220°C, 20 bar and $(H_2{:}CO{:}N_2)_{inlet}$ = 2:1:3 (to simulate air blown reforming). Conversion was increased by decreasing space velocity. Each catalyst was initially left at a conversion between 40% and 50% for 100 hours to determine initial deactivation rates. Turnover frequencies were determined at low conversion (ca. X_{CO} = 40%) at 100 hours on stream.

5.3. Results and discussion

5.3.1. Catalyst characterization

The physio-chemical characteristics of calcined and reduced Mn-Pt-Co/Al_2O_3 prepared via slurry impregnation [153] are presented in Table 5-2. Key points for the characterisation of these catalysts will be discussed in this section whilst comprehensive characterisation is presented in Appendix C.2.

Table 5-2: Physio-chemical characterization of Puralox and Mn-Pt-Co/Al_2O_3.

		Calcined catalyst precursor				*Reduced catalyst (350°C, 16 hours)*	
	Mn:Co	**S_{BET} (m^2/g)**	**V_{pore} (cm^3/g)**	**d_{pore} (nm)**	**d_{Co3O4}[1] (nm)**	**H_2 uptake[2] (cm^3/g STP)**	**Metal surface area[3] (m^2/g sample)**
Puralox		157	0.5	8.8			
Pt-Co/Al_2O_3	0	113	0.3	8.0	11	4.3	13
Mn-Pt-Co/Al_2O_3	0.04	118	0.3	8.7	14	3.0	11
	0.09	122	0.3	8.3	15	3.1	9.6
	0.14	150	0.3	7.6	13	3.2	9.1
	0.23	100	0.2	7.3	12	2.4	6.9
	0.47	86	0.2	7.9	10	1.6	4.7

[1]Diameter of Co_3O_4-crystallites as determined using XRD; [2]H_2 uptake as determined by chemisorption; [3] Based on H_2 uptake

The XRD crystallite size of Co_3O_4 for Pt-Co/Al_2O_3 without manganese promotion was 11 nm. Promoting the catalyst with small amounts of manganese increased the apparent size of Co_3O_4 up to 15

nm (Mn:Co = 0.09). After this point the measured crystallite size decreased reaching a minimum of 10 nm (Mn:Co = 0.47). This trend is consistent with previous results [145,146].

The H_2 uptake (Table 5-2) decreased significantly with manganese addition from 4.6 cm^3/g to 1.8 cm^3/g for a Mn:Co ratio of 0 to 0.47 respectively. This may be explained by results from HR-TEM elemental mapping (see Fig. C-3, Appendix C.2.) which indicated that regions of high cobalt concentration are also dense in manganese, suggesting that manganese may be preferentially positioned close to cobalt. As manganese was co-impregnated in a secondary step, this may indicate that it was positioned on top of the cobalt species, blocking cobalt active sites. Temperature programmed reduction (see Figure C-2, Appendix C.2.) showed that increasing levels of manganese promotion resulted in more sluggish cobalt reduction behaviour. This may be due, in part, to manganese coverage of the metal which may be a contributing factor to the decrease in H_2 uptake measured by hydrogen chemisorption.

5.3.2. Rate of Mn-Pt-Co/Al_2O_3 over first 100 h

Figure 5-1 shows the change in rate with time on stream for Pt-Co/Al_2O_3 and Mn-Pt-Co/Al_2O_3 (Mn:Co = 0.04 - 0.47) over an initial 100 h period. Unpromoted Pt-Co/Al_2O_3 and Mn-Pt-Co/Al_2O_3 with the highest activity (Mn:Co = 0.14) are shown with filled in symbols for representational simplicity.

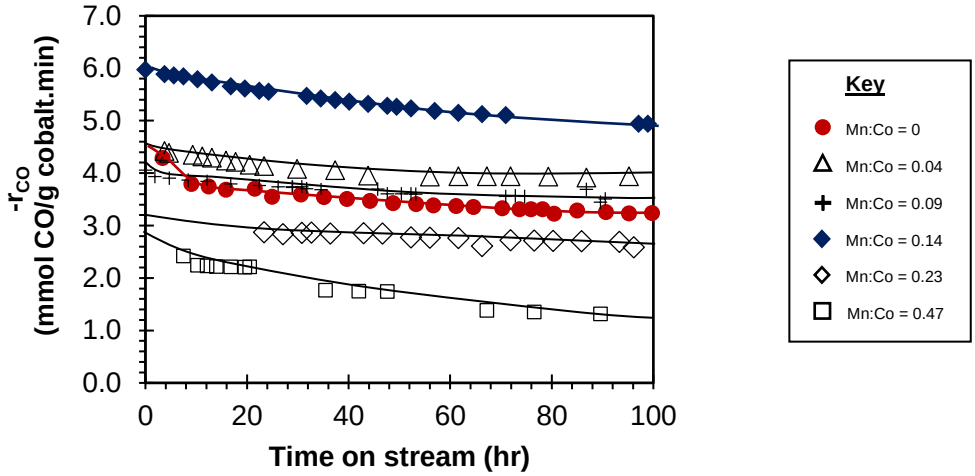

Figure 5-1: Rate of reaction as a function of time on stream during the initial 100 h period for Mn-Pt-Co/Al_2O_3 with Mn:Co = 0 - 0.47.

The industrial catalyst Pt-Co/Al_2O_3 started the run with a rate of 4.4 mmol/g_{cobalt}.min. However, the catalyst lost a significant amount of activity in the first 10 h after which the rate levelled out to between 4 – 3.2 mmol/g_{cobalt}.min. This catalyst experienced a total loss of rate of ca. 1.2 mmol/g_{cobalt}.min (27% of its initial rate) over the 100- h period.

Adding a manganese promoter to a level of Mn:Co = 0.04 and 0.09 resulted in a slightly higher rate (after the first 10 h) when compared to Pt-Co/Al_2O_3. In addition, the total loss of rate was significantly lower than Pt-Co/Al_2O_3 at 0.5 and 0.4 mmol/g_{cobalt}.min (11% and 10% of their initial rates) respectively over the 100- h period.

Increasing the manganese content further to a Mn:Co ratio = 0.14 significantly enhanced the rate, with a 53% increase at 100 h on stream when compared to Pt-Co/Al_2O_3. This catalyst, however, exhibited slightly enhanced deactivation characteristics in the first 100 hours, with a total loss of rate of 1.1 mmol/g_{cobalt}.min (18% of its initial rate) over the 100- h period.

Interestingly, high levels of manganese promotion (Mn:Co = 0.23 and 0.47) resulted in a lower rate throughout the first 100 h. This may be due to higher manganese loadings resulting in lower levels of reducibility, or manganese blocking the cobalt active sites, as discussed previously. High levels of manganese promotion also resulted in strong deactivation, with a total loss of rate of ca. 0.6 and 1.1 mmol/g_{cobalt}.min (19% and 46% of their initial rates) respectively over the 100- h period. Only the catalyst with a Mn:Co = 0.47 exhibited more significant deactivation than unmodified Pt-Co/Al_2O_3.

5.3.2.1. Loss of activity in the first 100 h

Small levels of Mn promotion (Mn:Co = 0.04 – 0.14) improved the rate of reaction as well as led to a decrease in deactivation between 0 h and 100 h when compared to unpromoted Pt-Co/Al_2O_3. The level of deactivation reached a minimum at a Mn:Co = 0.09, after which it increased, reaching a maximum deactivation rate for Mn:Co = 0.47. There are multiple reasons why cobalt deactivates, as discussed in Section 2.5. However, as this deactivation was measured at low conversion (mild hydrothermal conditions), the two most likely causes are carbon deposition or sintering, rather than cobalt oxidation.

It is tempting to attribute this phenomenon to carbon deposition as Mn promotion has been linked to enhanced CO adsorption [142,145] which, in theory, may enhance carbon coverage and thus, potentially, carbon deposition at high manganese concentrations. Contrary to this, an analysis of the spent Mn promoted samples shows a decrease in carbon on the surface of the catalyst with increasing Mn content (Fig C-5, Appendix C.3.). Additionally, carbon deposition is typically thought to occur over periods of time longer than 100 h [91].

A more realistic explanation for deactivation, and one that fits the time period in question (first 100 h), is the sintering of nanoparticles. Sintering is thought to be more pervasive for smaller crystallites [134,166], due to larger surface energy contributions. Both Pt-Co/Al_2O_3 and Mn-Pt-Co/Al_2O_3 with

Mn:Co = 0.47 had the smallest Co_3O_4 crystallites as shown by XRD (Table 5-2) of 11 nm and 10 nm respectively and exhibited the largest deactivation rates.

Figure 5-2 (a) shows the percentage of rate lost (loss of rate / initial rate) in the first 100 h and the Co_3O_4 crystallite size (as per Table 5-2) as a function of the Mn:Co loading for the six catalysts. It appears that the parabolic trend for Co_3O_4 crystallite size is consistent with the percentage of rate lost, signifying a potential correlation. In order to confirm this, the percentage rate loss for all six catalysts was plotted as a function of their crystallite sizes (Figure 5-2 (b)). As the Co_3O_4 crystallite size increased, the percentage of rate loss in the first 100- h period decreased, with the effect more prevalent for smaller Co_3O_4 crystallite sizes.

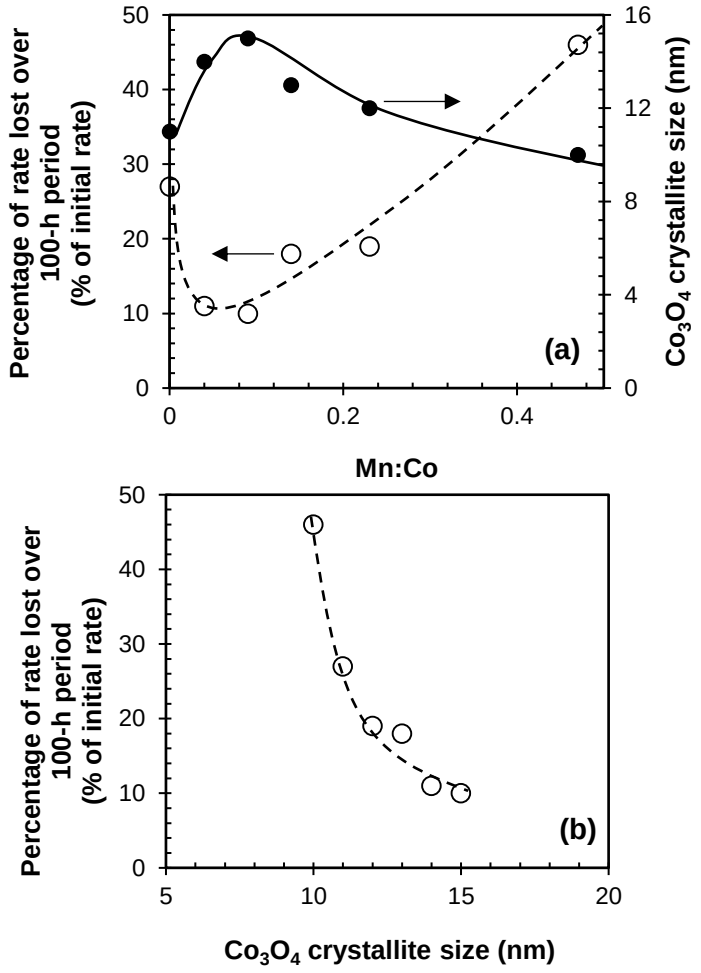

Figure 5-2: Percentage rate loss over the first 100 h period (○) and Co_3O_4 crystallite size (●) as (a) a function of Mn:Co ratio from 0 – 0.47 and (b) a function of Co_3O_4 crystallite size.

Figure 5-2 (a) and (b) indicate that the likely cause of deactivation in the first 100 h is sintering, and that this effect is enhanced for cobalt catalysts with no manganese promotion and high manganese loadings due to their relatively smaller cobalt crystallite sizes.

5.3.3. Turnover frequency at 100 h

The turnover frequency is a measure of the activity of a catalyst site. Thus, turnover frequency enables the Mn-Pt-Co/Al_2O_3 catalysts to be compared taking their varying metallic surface area into account. Figure 5-3 shows the turnover frequency as a function of Mn:Co ratio measured at 100 h on stream, at X_{CO} = 30 – 40%.

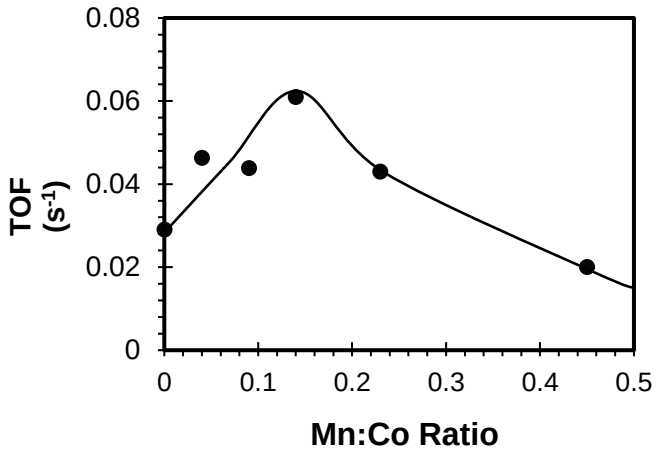

Figure 5-3: Turnover frequency for each catalyst as a function of Mn:Co ratio at ca. X_{CO} = 40% at 100 hours on stream.

The industrial catalyst, Pt-Co/Al_2O_3, had a TOF of 0.03 s^{-1}. This is typical for cobalt catalysts of this type under similar conditions [154]. Increasing the Mn:Co ratio resulted in up to a 100% increase in the turnover frequency, reaching a maximum of 0.06 s^{-1} at a Mn:Co ratio of 0.14, likely due to the chemical promotional effects of manganese discussed in 5.3.3.1. The addition of more manganese (Mn:Co = 0.23) resulted in a decrease in turnover frequency to 0.04 s^{-1}. At the highest level of Mn promotion investigated (Mn:Co = 0.47) a minimum TOF of 0.02 s^{-1} was reached, with poorer activity than unmodified Pt-Co/Al_2O_3.

5.3.3.1. Mechanism for activity improvement

The results shown in Figures 5-1 and 5-3 are consistent with previous accounts that Mn promotes the activity of cobalt catalysts in the Fischer-Tropsch synthesis [90,140,141]. Furthermore, these results

indicate an optimal level of Mn promotion – in this case found to be at a Mn:Co ratio equal to 0.14. This rate maximum has been reported previously to be at 0.05 [129,141] and 0.075 [144] at 1 bar and 0.125 [129,141] at 10 bar.

The increase in activity with manganese promotion up until this maximum has been attributed in the past to an improved dispersion of Co^0 [140]. This is a highly debated theory, as an increase in dispersion with manganese promotion is not always exhibited, or is exhibited for only some concentrations of Mn [90,142,145,146]. The increase in dispersion has not been seen for this investigation, using either H_2 chemisorption or HR-TEM elemental imaging (see Figure C-3, Appendix C.2.) despite the increase in activity.

The activity improvement may, however, be caused by chemical promotion rather than structural promotion. It has been proposed [142] that the improved rate is due to MnO (Mn^{2+} according to thermodynamic calculations, see Appendix F) increasing the activity of adjacent Co-sites through Lewis acid-base interactions. These interactions between Mn^{2+} cations located at the edges of MnO islands may increase the amount of weakly-bonded CO adsorbed onto the cobalt surface [77,140–142]. This is thought to increase the dissociation of CO and thus increase the rate. Another explanation by Johnson et al. [142] suggested that Mn promotion altered CO adsorption characteristics as identified using CO-TPD and analysing the CO desorption temperatures.

These explanations, however, do not explain the decrease in activity with 'too high' Mn concentrations (Mn:Co > 0.23). Dinse [141] attributed a rate maxima seen in their investigation to an interplay between the increased activity at Co sites due to the Lewis acid-base interactions, and the decreased number of Co sites (shown by H_2 uptake). The present investigation reports on a large loss of metallic surface area due to Mn blockage of Co sites during impregnation, as well as hindered reducibility (see Figure C-2, Appendix C.2.) with increasing Mn content. Both factors may lead to the decrease in rate seen at high Mn concentrations. However, the turnover frequency reported here also revealed a maxima at Mn:Co = 0.14. As TOF considers the loss of H_2 uptake with increasing Mn-content, it may be inferred that an additional mechanism may be present. It has been suggested previously [142] for cobalt supported on silica that, at very high Mn:Co ratios, Mn starts to deposit in onto the surface of the support as well as 'clumping' on the surface of the catalyst. This may physically block hydrogen spillover within the Fischer-Tropsch reaction, further impeding the activity and TOF. In addition, very low H:C ratios on the surface of the catalyst (caused by enhanced CO adsorption [142]) may hinder the rate.

It is important to note that a contributor to the change in turnover frequency, especially for unmodified Pt-Co/Al_2O_4 and Mn-Pt-Co/Al_2O_3 with a Mn:Co ratio = 0.47 with the smallest crystallite sizes, could be slight particle size effects as described by Bezemer et al. [82]. Whilst the mean crystallite sizes in both cases are roughly 6 nm [82], due to a lognormal distribution of crystallites, a small portion of cobalt crystallites in both catalysts may affected by this phenomenon which could decrease TOF.

5.3.4. Selectivity of Mn-Pt-Co/Al_2O_3

Addition of manganese to Pt-Co/Al_2O_3 appears to have a remarkable effect on the selectivity of the catalyst, albeit this seems to be dependent on the Mn:Co ratio. Figure 5-4 (a)-(e) shows the effect of increasing Mn content of Mn-Pt-Co/Al_2O_3 on the CO_2, CH_4, C_{5+} and C_4 olefin selectivity and chain growth probability across a conversion range of X_{CO} = 40% to X_{CO} = 95%.

Manganese promotion appears to decrease the selectivity towards CO_2, an effect that seems to be more prominent at high conversions and Mn:Co ratios > 0.04 (see Fig. 5-4 (a)). Initially, at conversions between X_{CO} = 40% and X_{CO} = 70%, increasing the Mn content from 0 to 0.47 decreased the CO_2 selectivity from ca. 1 C-% to ca. 0.1 C-% with low Mn loadings having a more limited effect. Above X_{CO} = 70%, however, the improvement with Mn addition was far more noticeable. At X_{CO} = 90% the addition of a small amount of Mn (Mn:Co = 0.04) decreased the CO_2 selectivity from ca. 10 C-% to ca. 3 C-%, whilst larger loadings (Mn:Co = 0.47) decreased the CO_2 selectivity even further to 2 C-%.

The change in CH_4 selectivity with Mn promotion appears to follow a similar trend to CO_2 selectivity, albeit the relationship with respect to increasing Mn:Co ratio may be slightly more complex. Increasing levels of Mn promotion decreased the selectivity towards CH_4 (see Fig 5-4 (b)), with the most significant effect at conversions above X_{CO} = 70%, and Mn:Co ratios of 0.14 and 0.23. At X_{CO} = 90%, increasing the ratio of Mn:Co from 0 to 0.14 decreased the CH_4 selectivity from ca. 22 C-% to ca. 10 C-%. This is within realistic levels for operation of a Fischer-Tropsch plant. The selectivity improvement towards CH_4, like activity, seems to have gone through a maximum. Very high levels of Mn promotion do not have as much of a positive effect, with a Mn:Co = 0.47 exhibiting a CH_4 selectivity of only ca. 15 C-% at X_{CO} = 90%.

Due to the significant effect that Mn promotion has on the selectivity of unwanted by-products, the selectivity towards C_{5+} could be improved substantially, especially at higher conversions. Figure 5-4 (c) shows that at conversions of X_{CO} = 40% and X_{CO} = 90%, C_{5+} selectivity was improved by 5 C-% (87 C-% to 92 C-%) and 14 C-% (73 C-% to 87 C-%) respectively for a Mn:Co ratio = 0.14. Low manganese loadings exhibited the same effect, albeit, to a lesser degree, whilst a Mn:Co = 0.47 exhibited no effect.

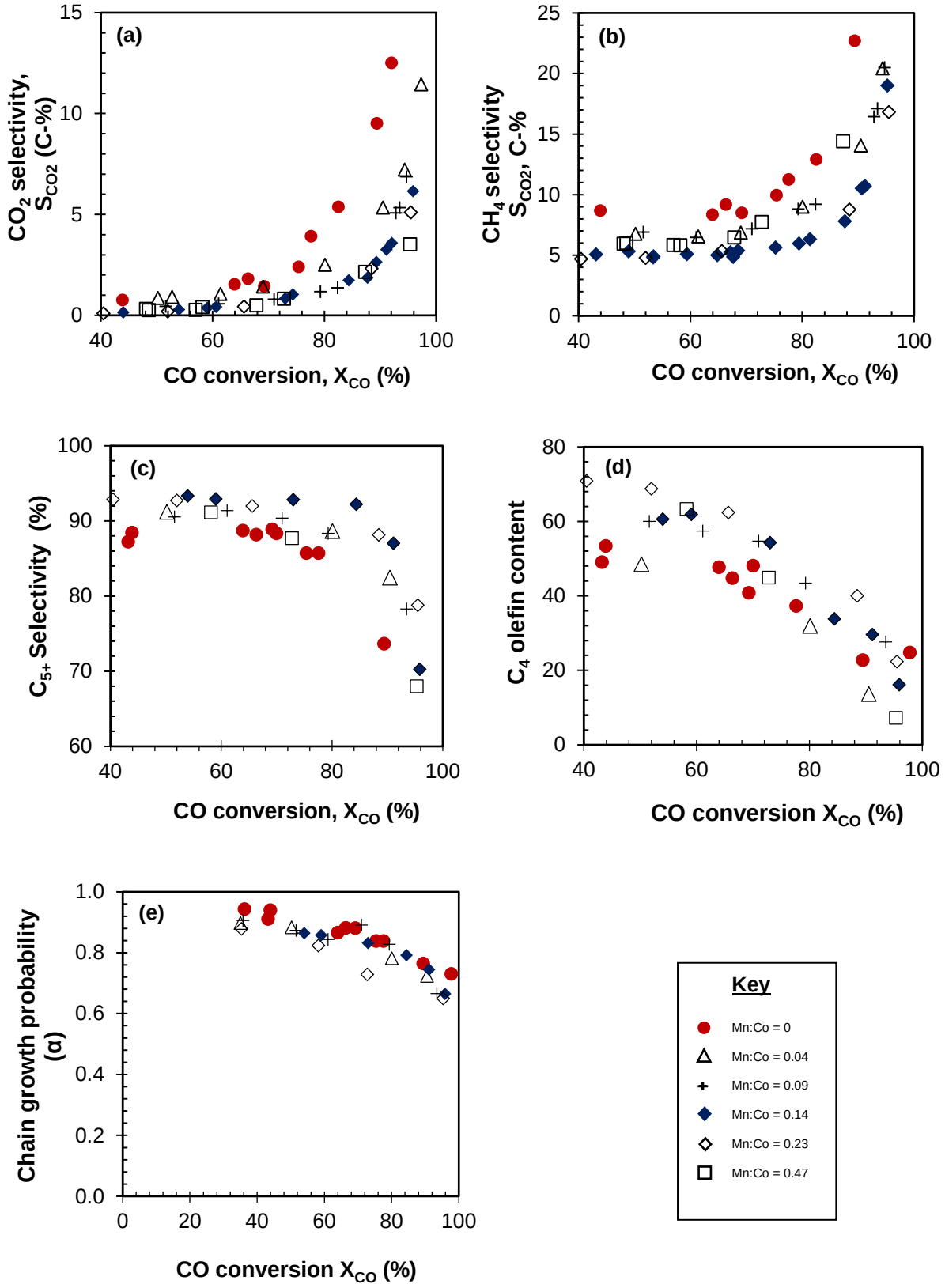

Figure 5-4: The selectivity of CO_2 (a), CH_4 (b) and C_{5+} (c), C_4 olefins content (d) and chain growth probability alpha value (e) as a function of CO conversion for Mn-Pt-Co/Al_2O_3 with Mn:Co = 0 – 0.47

Figure 5-4 (d) shows the effect of manganese on the by the C_4 olefin content across the range of conversions. The trend of C_4 olefin content with regards to increasing manganese content is not entirely clear. It appears that at lower conversions, manganese-promoted samples have a higher olefin content, albeit the downward linear trend has a stronger gradient resulting in lower olefin contents at high conversion. More apparent in this study was that all catalysts showed a decrease in olefin content with an increase in conversion – likely due to the longer residence times at lower space velocities.

Manganese appears to decrease the chain growth probability slightly with respect to the unmodified catalyst Pt-Co/Al_2O_3 with this effect more significant at very high conversions (X_{CO} > 95%) (see Fig 5-4 (e)). This will likely shift the product distribution towards lighter hydrocarbons (from distillate to naphtha range). However, the decrease in alpha value does not seem to entirely offset the significant effect that the improved CH_4 selectivity has on the C_{5+} selectivity.

5.3.4.1. Mechanism for CO_2 selectivity improvement

One of the most surprising results in this investigation is the decrease in CO_2 selectivity with addition of manganese. Whilst the effects of manganese on activity and CH_4 selectivity at low conversion are well known, very few authors suggest that CO_2 formation is suppressed and in some cases authors [145] suggest that MnO may catalyse the water-gas shift reaction at Fischer-Tropsch conditions. The results of the present study differ from this assertion.

One explanation for the decrease in CO_2 selectivity may be related to the sluggish reducibility of Mn-promoted cobalt catalysts (see Fig C-2, Appendix C.2.). As discussed in Chapter 4, a greater level of reduction (and thus more Co^0 and less Co(II)O and Co_3O_4) improves water-gas shift activity, and since the level of reduction decreases significantly with Mn addition, a lower rate of CO_2 production may be expected.

5.3.4.2. Mechanism for CH_4 selectivity improvement

This study reports on inhibited CH_4 selectivity with increasing manganese content, as well as a maximum level of promotion (Mn:Co = 0.23) after which the CH_4 suppression become less effective. The effect of Mn on CH_4 selectivity has been well documented in literature at low conversions [129,140,141,144] and discussed in detail in Section 2.6.1.

Johnson et al. [142] attributes the selectivity improvement to a change in the surface concentration of C* and H* due to enhanced CO adsorption by Mn (shown by increased CO desorption temperatures with Mn addition). Decreased H:C ratios at the surface would certainly decrease the methane selectivity, and one would expect this effect to be enhanced at high conversion, as seen in this study, where

increases in the H_2:CO ratio in the reactor cause the methane selectivity to spike. It may be plausible that the selectivity maximum in the improvement of methane selectivity is created due to the combination of enhanced adsorption and dissociation [142]. At low concentrations of Mn, CO adsorption is the controlling factor which enhances the surface concentration of C*, thus decreasing methane selectivity. At high concentrations of Mn, the contribution of dissociation becomes very high, which makes hydrogenation to CH_4 easier.

5.3.5. Relevance for high conversion

Two primary factors which impede operation of Pt-Co/Al_2O_3 at high conversion are a low rate due to the low partial pressures of reactants and a high selectivity towards CH_4 and CO_2 at X_{CO} > 75%. Both factors have been shown to be mitigated by Mn promotion in this study. Using the optimal Mn:Co ratio (0.14) the rate was improved by up to 53% (TOF by 100%) and selectivity towards CO_2 and CH_4 was decreased by 8 C-% and 12 C-% at X_{CO} = 90% respectively. This consequently improved the C_{5+} selectivity by 14 C-% at the same conversion.

These changes resulted in a significant improvement in the liquid fuel yield. Figure 5-5 shows that at a Mn:Co ratio of 0.14, the liquid fuel yield increased from ca. 66 C-% to ca. 80 C-% at X_{CO} = 90%. The maximum for liquid fuel yield also appears to have shifted from X_{CO} = 78% to 91% with moderate manganese addition. Unfortunately, further increases in the conversion swiftly decreased this yield. This means that whilst the conversion for once-through Fischer-Tropsch waste-to-liquid may be substantially increased with manganese promotion, an upper conversion limit of X_{CO} = 91% still exists. From a design perspective, this means that electricity generation will still be necessary to convert the last 10% of unreacted syngas. Based on these results, Mn promotion may be used as a promoter to counter-act the negative activity and selectivity seen at high conversion.

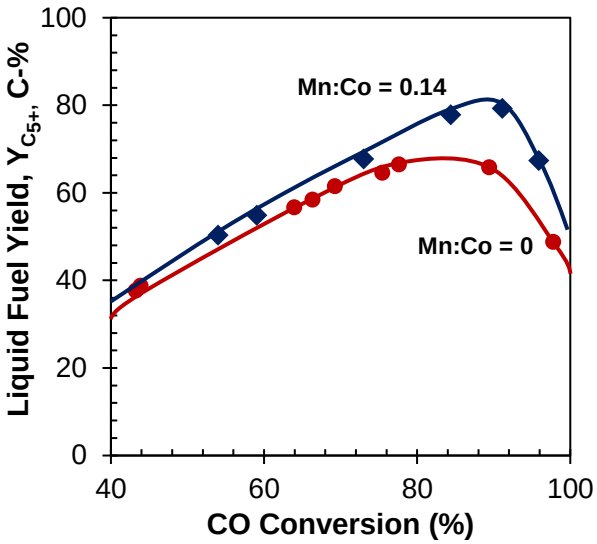

Figure 5-5: The yield of C_{5+} as a function of CO conversion for Mn-Pt-Co/Al_2O_3 with Mn:Co = 0 and 0.14.

5.4. Conclusion

Manganese promotion has been studied with regards to improving the activity and selectivity of Pt-Co/Al_2O_3 between X_{CO} = 40% and 95%. Increasing levels of Mn promotion were found to decrease dispersion, metal surface area and reducibility. Despite this, a moderate level of Mn promotion (Mn:Co = 0.14) was found to increase activity by ca. 53% and turnover frequency by ca. 100%. This can be attributed to the increase in CO adsorption and dissociation due to Lewis acid-base interactions. In addition, Mn promotion was found to decrease CO_2 and CH_4 selectivity significantly, attributed to a decrease in reducibility and an increase in the surface concentration of carbon respectively. Selectivity enhancement was found to be more significant at higher conversions, resulting in a shift of maximum fuel yield from X_{CO} = 78% to 91% for Mn-Pt-Co/Al_2O_3 with a Mn:Co ratio of 0.14.

Chapter 6

Deactivation mechanisms in a Pt-Co/Al_2O_3 Fischer-Tropsch catalyst operated at high conversion

6.1. Introduction

The harsh conditions of high conversion affect not only selectivity (Chapter 4, 5) but also the stability of cobalt-based catalysts as described in Chapter 2 [67,69]. Possible causes for the reduced catalyst stability include sintering of cobalt nanoparticles [69,80,124,125], carbon deposition, cobalt oxidation [69,80,117–119] and the formation of cobalt-support compounds [119–123]. Section 2.5 discusses each of these mechanisms with regards to high conversion.

The effect of hydrothermal conditions on the deactivation of cobalt-based catalysts has been well explored [66–69,80,116,119,124,139,167], but is typically investigated by the addition of water to the feed (often termed 'simulated' high conversion) to increase $p_{H_2O,}$ rather than decreasing space velocity to increase real CO conversion. Water produced in-situ, i.e. via the Fischer-Tropsch synthesis, may not have the same effect as water added to the feed at similar partial pressures. For instance, under real high conversion in addition to the higher water partial pressure, the partial pressures of CO and H_2 are considerably lower thus resulting in a low carbon coverage and enhanced p_{H2O} / p_{H_2} (which controls thermodynamic phase changes of metallic cobalt to oxidic cobalt [119]). An increase in conversion from 40% to 95% results in a change in p_{H2O} from ca. 1.7 bar - 4.5 bar and a change in p_{H2O} / p_{H_2} from 0.38 - 9.5 whilst the addition of 0 – 5 bar water at X_{CO} = 40% would only yield a p_{H2O} / p_{H_2} of 0.4 – 1.3.

This study presents the consequences of a high conversion on the stability of 0.05Pt - 22Co/Al_2O_3 within the Fischer-Tropsch synthesis. Furthermore, it will attempt to decouple the reversible and irreversible mechanisms associated with a loss of activity due to a high partial pressure of in-situ water coupled with a low partial pressure of CO and H_2 (high conversion) and a high partial pressure of externally added water with high partial pressures of CO and H_2 at low conversion ('simulated' high conversion).

6.2. Experimental

6.2.1. Catalyst and standards synthesis

Platinum-promoted cobalt supported on γ-alumina (0.05 Pt - 22Co/Al_2O_3) was prepared and characterized as detailed in Appendix B. The method for the preparation of the cobalt aluminate standard is described in Appendix B.3.1.

6.2.2. Catalyst characterisation

Fresh and spent catalysts were characterized by transmission electron microscopy (FEI TecnaiTM F_{20}), hydrogen chemisorption (Micromeritics ASAP HP 2020C), temperature programmed reduction (TPR) and hydrogenation (TPH) (Micromeritics Autochem HP II 2950). Detailed experimental procedures can be found in Appendix B.

6.2.3. Slurry bed reactor studies

For slurry bed reactor runs, the catalyst, Pt-Co/Al_2O_3 was reduced and loaded as per Appendix B

6.2.3.1. High conversion run

The high conversion run was conducted to understand the deactivation under decreasing space velocity/ increasing conversion conditions. Figure 6-1 illustrates the CO conversion (X_{CO}) over a period of 500 hours for Pt-Co/Al_2O_3 in the slurry bed reactor with a feed of N_2:H_2:CO = 3:2:1 at 220°C and 20 bar.

The space velocity of CO was initially held at a baseline condition of 1.73 mmol CO/min/g which resulted in an initial CO conversion of X_{CO} = 43%. The CO space velocity was subsequently decreased to 1.03, 0.94 - 0.83, 0.62 - 0.42 and 0.21 mmol CO/min/g (keeping the inlet feed ratios constant) to achieve CO conversions of 67%, 70% - 80%, 80%-90% and 90% - 97% respectively. At each conversion level the instantaneous deactivation (decrease in activity with time) was assessed. Between each conversion interval, the space velocity was increased to baseline conditions to assess irreversible deactivation (difference in activity before and after reaching a specific conversion).

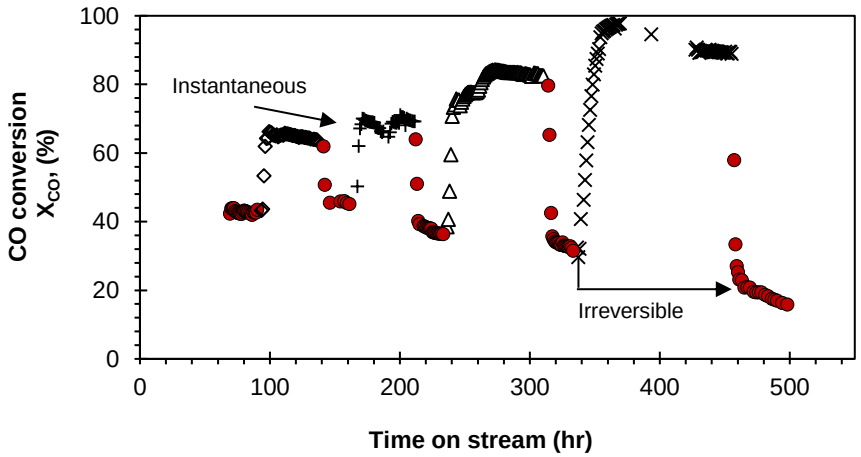

Figure 6-1: CO conversion as a function of time on stream with Pt-Co/Al_2O_3 in a slurry bed reactor at 220°C and 20 bar with a feed N_2:H_2:CO = 3:2:1. Space velocity of CO: ● 1.73 mmol CO/min/g, ◊ 1.03 mmol CO/min/g, + 0.94-0.83 mmol CO/min/g, Δ 0.62-0.42 mmol CO/min/g × 0.21 mmol CO/min/g.

6.2.3.2. 'Simulated' high conversion run

Similarly, to understand the deactivation of Pt-Co/Al_2O_3 in a hydrothermal environment at a constant partial pressure of CO and H_2 (i.e. 'simulated' high conversion), water was added to the feed, replacing N_2 such that the water partial in the feed was increased from 0 bar to 5 bar (slightly larger than the partial pressure of in-situ water produced at 100% conversion). Between each water addition, the water was removed entirely (0 bar) to a baseline condition to assess irreversible deactivation. Figure 6-2 shows the change in CO conversion as well as the partial pressure of water added throughout the run.

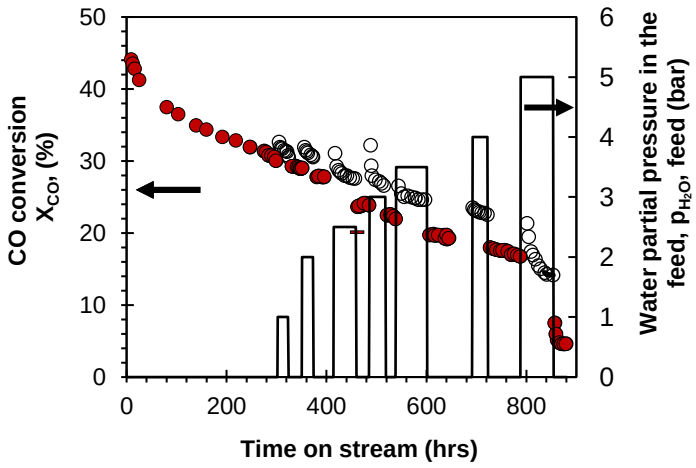

Figure 6-2: CO conversion, X_{CO}, and water partial pressure in the feed (bar) as a function of time on stream for a slurry bed run with constant partial pressure of synthesis gas in the feed (T = 220°C, p = 20 bar; feed N_2:H_2:CO:H_2O = 6-x:4:2:x (x = 0-3)).

6.2.4. Magnetometer

To study the sintering and reduction/oxidation characteristics of Pt-Co/Al_2O_3 at various conversion levels an in-situ magnetometer [168] at the University of Cape Town, South Africa was used. The measurement is based on the Weiss extraction method and uses a field-controlled electromagnet which provides a field strength between 0 and 2.0 T [124].

The reduction/oxidation of the catalyst was monitored by the saturation magnetization (M_{sat}), which is directly proportional to the amount of magnetic material in the sample. Cobalt metal, the active phase for the Fischer-Tropsch synthesis [79], is magnetic whilst cobalt oxide and cobalt aluminate are not. Thus, an increase in the saturation magnetization represents an increase in the amount of catalytically active material. The saturation magnetization which is reported to be independent of crystallite size [124,169] above 2 nm can, however, be affected by the presence of adsorbed species on the surface of the catalyst.

Information on sintering at each conversion level was obtained using the remnant magnetization (M_{rem}). Remnant magnetization is the magnetization that remains after the electromagnetic field has been decreased from 2 T to 0 T [169]. Only crystallites larger than the critical diameter, $D_{c,}$ (approximately 15-20 nm at room temperature [124,170,171]) remain in their magnetic state upon removal of the magnetic field. The mass fraction of cobalt that remains in magnetic, γ, can be taken as an indicator for sintering and is calculated as follows,

$$\gamma = \frac{2M_{rem}}{M_{sat}} \times 100\%. \qquad \textbf{7-2}$$

At the start of this run, 0.42 g of Pt-Co/Al_2O_3 was diluted with silicone carbide and loaded in a fixed bed reactor attached to the in-situ magnetometer. The catalyst was reduced in-situ in pure H_2 for 16 hours at 350°C. The temperature was then decreased to 180°C in argon and the pressure was increased to 11 bar abs. The feed was then changed to a mixture of H_2:CO = 2:1 with argon as a standard (10 vol-%). The temperature was then increased slowly to 220°C. The total space velocity was then decreased periodically to increase CO conversion from 0% to 98%.

6.3. Results

The physio-chemical characteristics of calcined and reduced Pt-Co/Al_2O_3 prepared via slurry impregnation are presented in Table 4-1 and further characterization is presented in Appendix C.1. The calcined catalysts contain crystalline Co_3O_4 with an average diameter of ca. 11 nm.

6.3.1. Instantaneous deactivation

Instantaneous deactivation ($-\frac{da}{dt}$) is defined as the decline in activity measured quantitatively by the rate of change of activity with time at a specific space velocity (see Fig. 6-1), where activity is defined as per Section 4.3.2 in Chapter 4.

Figure 6-3 shows the rate of change of activity with time ($\frac{da}{dt}$) as a function of partial pressure of water (H_2O) within the reactor for high conversion and 'simulated' high conversion scenarios. The corresponding initial conversion (high conversion run only) is also shown on a secondary horizonal axis. It must be noted, that as the change in activity with time is a function of both feed condition and time on stream, there is an inevitable multiple dependency with regards to quantifying this deactivation.

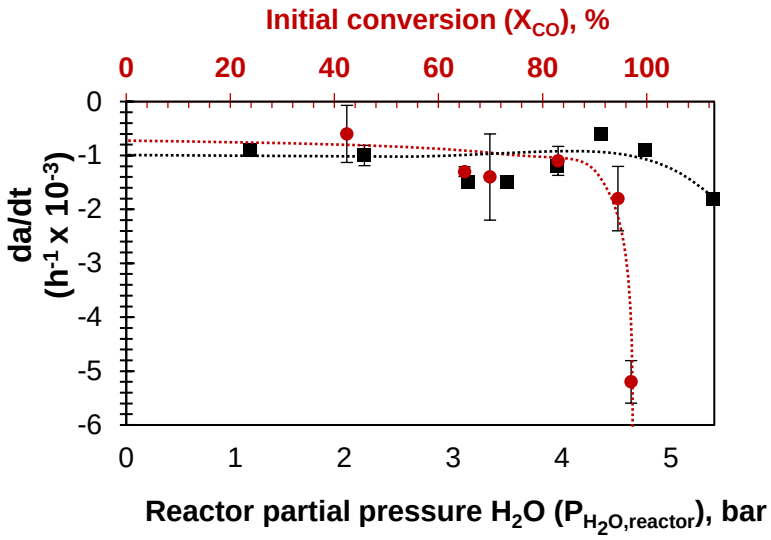

Figure 6-3: Rate of change of activity with time as a function of reactor partial pressure of water and conversion (for high conversion run only) for Pt-Co/Al_2O_3 in a slurry reactor (N_2:H_2:CO = 3:2:1, 220°C, 20 bar). Key: ● high conversion run, ■ 'simulated' high conversion run.

For the high conversion run, a baseline conversion of X_{CO} = 47% ($p_{H_2O,\ reactor}$ = 2 bar) resulted in a rate of instantaneous deactivation of $0.6 \cdot 10^{-3}$ hr^{-1}. As the conversion increases, the rate of instantaneous deactivation increased steadily to $1.1 \cdot 10^{-3}$ hr^{-1} at ca. X_{CO} = 82% ($p_{H_2O,\ reactor}$ = 3.9 bar) and $1.8 \cdot 10^{-3}$ hr^{-1} at X_{CO} = 94% ($p_{H_2O,\ reactor}$ = 4.6 bar). The strongest instantaneous deactivation occurred at an initial conversion of ca. X_{CO} = 97% for the high conversion run. This deactivation is visible on Figure 6-1 as the conversion decreases from X_{CO} = 97% to X_{CO} = 89%. This resulted in a rate of instantaneous deactivation of $5.0 \cdot 10^{-3}$ hr^{-1}.

For the 'simulated' high conversion case, the rate of instantaneous deactivation remained between $0.9 \cdot 10^{-3} hr^{-1}$ and $1.0 \cdot 10^{-3}$ hr^{-1} at a $p_{H2O,\ reactor}$ between 1-2 bar and increased to $1.5 \cdot 10^{-3}$ hr^{-1} between 3-4 bar. Interestingly, the instantaneous deactivation recovered slightly at a $p_{H2O,\ reactor}$ between 4 – 5 bar. Increasing the partial pressure of water in the feed further to 5 bar ($p_{H2O,reactor} = 5.4$) resulted in a strong instantaneous deactivation rate of $1.8 \cdot 10^{-3}$ hr^{-1}.

Both high conversion and 'simulated' high conversion runs exhibited an increase in instantaneous deactivation at ca. $p_{H2O,\ reactor} = 2.5 - 3$ bar ($X_{CO} = 65 - 70\%$ for the high conversion run) and to similar extents. The rate of instantaneous deactivation appeared to recover slightly in both cases after these conditions.

The severe instantaneous deactivation at $X_{CO} = 97\%$, which was not observed during the 'simulated' high conversion run, implies that strong instantaneous deactivation is not only a function of the partial pressure of water, but also governed by the low partial pressures of carbon monoxide and/or hydrogen in the reactor. The latter may suggest a thermodynamic change controlled by the p_{H2O}/p_{H2} ratio.

6.3.2. Irreversible deactivation

Irreversible deactivation is defined as the change in relative activity at baseline conditions before and after reaching a specific conversion or water partial pressure added to the feed (see Fig. 6-1). Figure 6-4 (a) and (b) show the relative activity changes after exposing Pt-Co/Al_2O_3 to increasing (a) CO conversion levels, and (b) p_{H2O} added to the feed, shown as a function of internal reactor water partial pressure ($p_{H2O,\ reactor}$). In addition, both figures represent the p_{H2O}/p_{H2} throughout the range.

When analyzing the irreversible deactivation, it must again be noted that there is a multiple dependency on both time on stream as well as feed conditions which cannot be ignored. In order to limit this, the reactor was held at each condition for similar (albeit not equal) times. There has been no attempt to adjust for, or normalize, this data for deactivation due to time on stream, but rather warn that this dependency exists.

For the high conversion run, shown in Figure 6-4 (a), the system starts at baseline conditions at $X_{CO} = 43\%$ (SV = 1.73 mmol CO/min/g, $p_{H2O}/p_{H2} = 0.4$, $p_{H2O,\ reactor} = 1.8$). Moving from baseline conditions to $X_{CO} = 65\%$ (SV = 1.03 mmol CO/min/g, $p_{H2O}/p_{H2} = 0.9$, $p_{H2O,\ reactor} = 2.7$ bar), and back resulted in a negligible loss of relative activity.

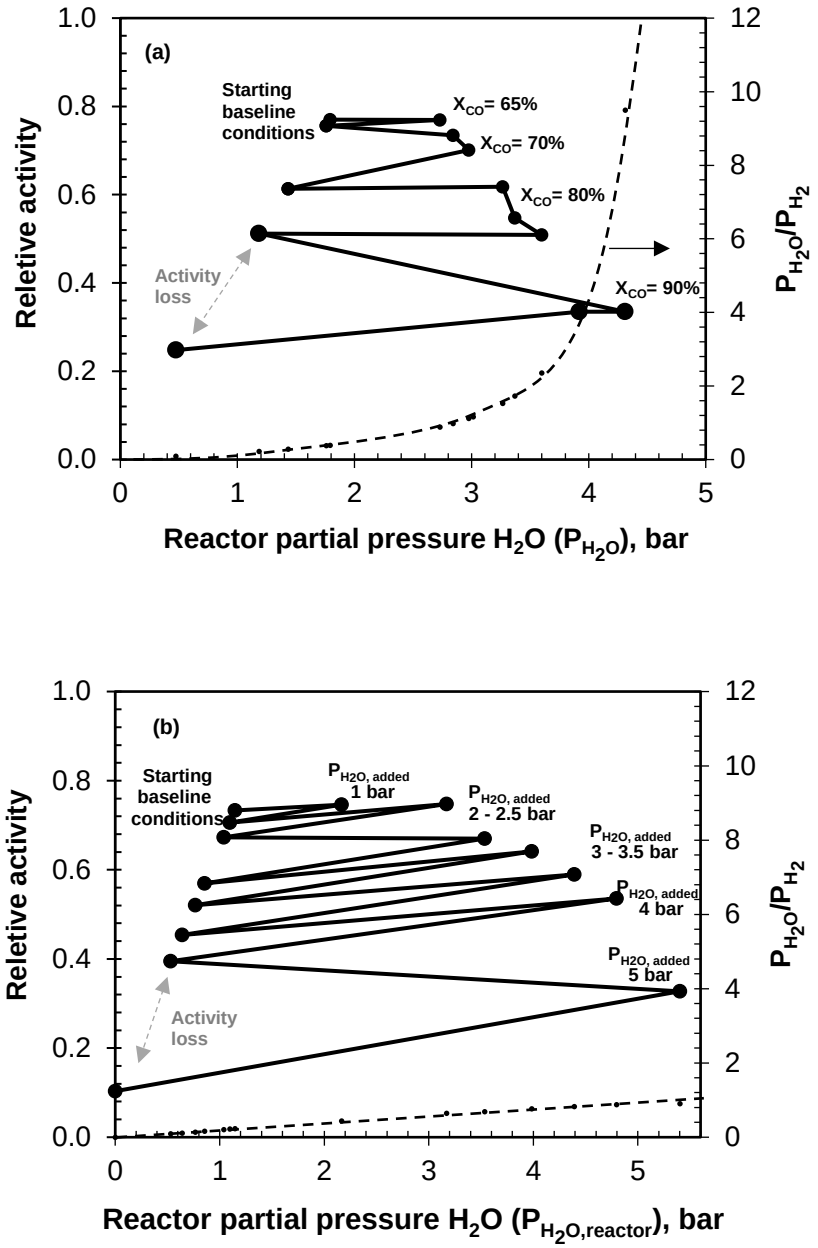

Figure 6-4: Irreversible activity loss after exposing the catalyst, Pt-Co/Al_2O_3, to (a) a conversion level of X_{CO} = 60%, 70%, 80% and 90% in a slurry reactor (N_2:H_2:CO = 3:2:1) and (b) externally added water to increase P_{H_2O} in the feed incrementally from 0 bar to 5 bar by replacing N_2 keeping H_2:CO = 2:1. Both experiments conducted at 220°C, 20 bar. Key: ● relative activity ; --- p_{H_2O}/p_{H_2}

Decreasing the space velocity further to achieve X_{CO} = 70% (SV = 0.94-0.83 mmol CO/min/g, p_{H2O}/p_{H2}= 0.11, $p_{H2O,\ reactor}$ = 3.0 bar) and X_{CO} = 82% (SV = 0.62-0.42 mmol CO/min/g, p_{H2O}/p_{H2} = 2.4, $p_{H2O,\ reactor}$ = 3.6 bar) resulted in an irreversible loss of relative activity of 15% and 10% respectively on return to baseline conditions. The irreversible deactivation after exposing the catalyst to X_{CO} = 70% was slightly greater than X_{CO} = 80% which is consistent with results for instantaneous deactivation.

Significant relative activity loss of 26%, was noted upon return to baseline after reaching X_{CO} = 97% (SV = 0.21 mmol CO/min/g , p_{H2O}/p_{H2} = 9.5, $p_{H2O,\ reactor}$ = 4.3 bar).

Figure 6-4 (b) shows the relative activity upon increasing the water partial pressure in the feed from 0 – 5 bar (resulting in a $p_{H2O,reactor}$ between ca. 1.1 and 5.4), but keeping the partial pressure of H_2 and CO in the feed fixed at 6.67 bar and 3.33 bar, respectively. Upon addition of 1 and 2 bar water to the feed (p_{H2O}/p_{H2} = 0.4 and 0.6), a slight increase in relative activity was observed, which was reversible upon removing water from the feed (also visible in Figure 6-2). Water is known to enhance the relative activity of the catalyst at these conditions [111,112,121,131,172]. This has been attributed to the promotion of CO activation by water [121] or the change in the relative concentration of active and inactive carbon on the surface of the catalyst [112].

Upon addition of 2.5 bar water to the feed (p_{H2O}/p_{H2} = 0.7), the first sign of significant irreversible deactivation was noted with an relative activity loss of 10%. The extent of irreversible deactivation decreases slightly for a partial pressure of water in the feed between 3 – 4 bar (p_{H2O}/p_{H2} = 0.8 - 0.85), with an irreversible relative activity loss between 4 % and 7%.

Upon addition of 5 bar water to the feed (p_{H2O}/p_{H2} = 0.9), the catalyst deactivated rapidly. On removal of this water the catalyst's relative activity decreased further indicating almost complete irreversible deactivation and an activity loss of 30%.

The increase in instantaneous and irreversible loss with increasing $p_{H2O,reactor}$ at high and 'simulated' high conversion confirms that hydrothermal environments do, as expected, deactivate Pt-Co/Al_2O_3 likely via a combination of sintering, cobalt aluminate formation or carbon deposition [80,116,123,169,173].

The difference in results for high and 'simulated' high conversion reveal where deactivation may be reliant on either only high $p_{H2O,\ reactor}$ or combined with a low p_{CO} and p_{H2}. For instance, at moderate $p_{H2O,\ reactor}$ (2.5 – 4), decreasing space velocity to induce an increase in conversion appears to result in a higher level of irreversible relative activity loss (10% - 15%) in comparison to the relative activity loss

between each consecutive addition of water (4% - 10%). This suggests that between X_{CO} = 70% and X_{CO} = 90%, low p_{H2} and/or p_{CO} contribute to enhanced deactivation. One explanation for this may be the strong increase in p_{H_2O}/p_{H_2} with increasing conversion (Fig. 6-4 (a)) which may favor the thermodynamic transformation to cobalt aluminate. The formation of cobalt aluminate has been reported[5,7,33] for p_{H_2O}/p_{H_2} greater than 1.5 and said to accelerate[21] at p_{H_2O}/p_{H_2} greater than 2.2. Whereas the addition of water at low conversion resulted in a p_{H_2O}/p_{H_2} consistently less than 1 (Fig. 6-4 (b)).

At high reactor water partial pressures ($p_{H_2O,reactor}$ > 4) the addition of water to the feed ('simulated' high conversion) resulted in more severe irreversible relative activity loss (30%) than very high conversions of X_{CO} > 90% (26%). This is inconsistent with results for instantaneous deactivation where very high conversions resulted in far more severe deactivation. This suggests that deactivation at very high conversion is partly reversible. It may be speculated, that at very high conversion conditions, the oxidation of Co(II)O (which is favored due to high p_{H_2O}/p_{H_2}) instantaneously deactivates the catalyst. As the conversion decreases due to deactivation so too does the production of indigenous water. This could lead to a re-reduction of cobalt and thus less irreversible deactivation. This may explain the leveling off in conversion seen for the high conversion run after deactivating from X_{CO} = 97% to X_{CO} = 89% (see Fig. 6-1).

6.3.3. Spent catalyst characterization

To decouple the differences in deactivation mechanism between the two scenarios – high conversion and 'simulated' high conversion the spent samples were extracted, dewaxed, characterized and compared to the fresh sample.

6.3.3.1. Sintering

Figure 6-5 shows the cumulative particle size distribution (based on 100 particles, see Appendix C.4.1 for TEM images) for the crystallites in both fresh (unreduced) and spent catalysts. The distributions can be fitted well with a lognormal distribution with an average crystallite size of 7.0 nm (in the fresh catalyst), 13.3 nm (in the spent catalyst after exposure to conditions prevalent at high conversion) and 13.0 nm (in the spent catalyst after exposure to a feed with a high water partial pressure). Noting the standard deviations of 1.5 nm, 1.7 nm and 1.6 nm, respectively, it must be concluded that the extent of sintering seems statistically similar after exposing the catalyst to conditions prevalent at high conversion and a feed with a high partial pressure of water.

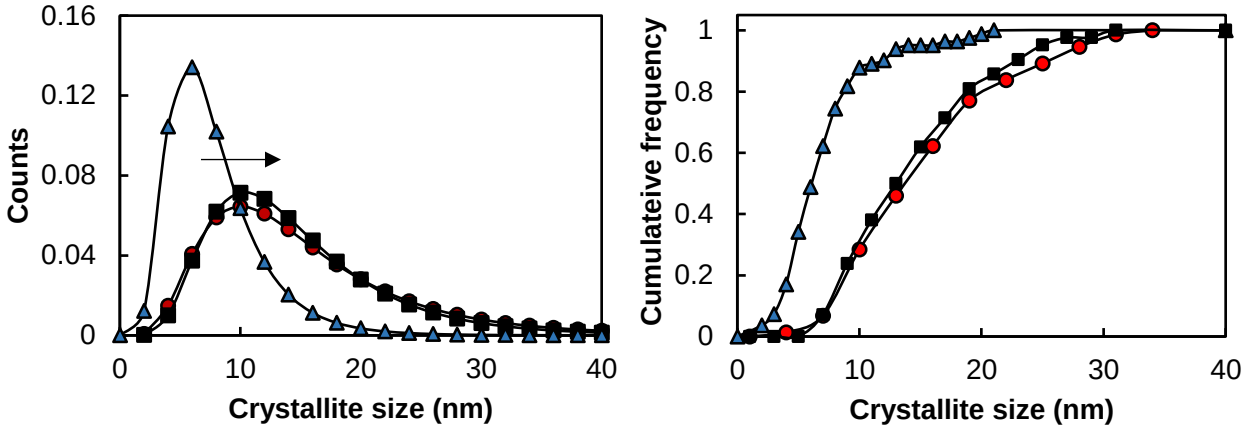

6.3.3.2. Carbon aluminate formation

Figure 6-5: Particle size distribution (left) and cumulative frequency curve for crystallite size distribution of fresh Pt-Co/Al_2O_3 (▲), high conversion spent Pt-Co/Al_2O_3 (●) 'simulated' high conversion spent Pt-Co/Al_2O_3 (■) based on TEM of 100 crystallites per catalyst.

Figure 6-6 shows the temperature programmed reduction (TPR) and temperature programmed hydrogenation (TPH) profiles for (a) fresh Pt-Co/Al_2O_3, (b) spent catalyst after exposing to conditions prevalent at high conversion, (c) the catalyst exposed to a feed with a high partial pressure of water ('simulated' high conversion) and (d) a standard for cobalt aluminate. The profiles were deconvoluted using Gaussian peaks with a peak assignment described by Nabaho [94] and Moodley [174] for platinum-promoted cobalt catalysts supported on alumina.

In the TPR profile, the fresh catalyst sample contains 3 reduction peaks which from low to high temperature have been assigned to the decomposition of cobalt nitrate, the reduction of Co_3O_4 to

Co(II)O and the reduction of Co(II)O to Co^0 [94]. The cobalt nitrate decomposition peak is absent from the TPR profile for both spent samples and the reduction of Co_3O_4 to Co^0 is seen by two overlapping peaks between 200°C and 650°C. Unlike the fresh samples, the TPR profile of the spent samples also exhibit a high temperature peak between 680°C and 880°C. This peak is typically ascribed to the reduction of difficult to reduce cobalt species such as cobalt in $CoAl_2O_4$. This peak also appears between the same temperature as the cobalt aluminate standard. It may thus be plausible that the amount of hydrogen consumed for this reduction process is an indication of the relative amount of $CoAl_2O_4$ formed in either run.

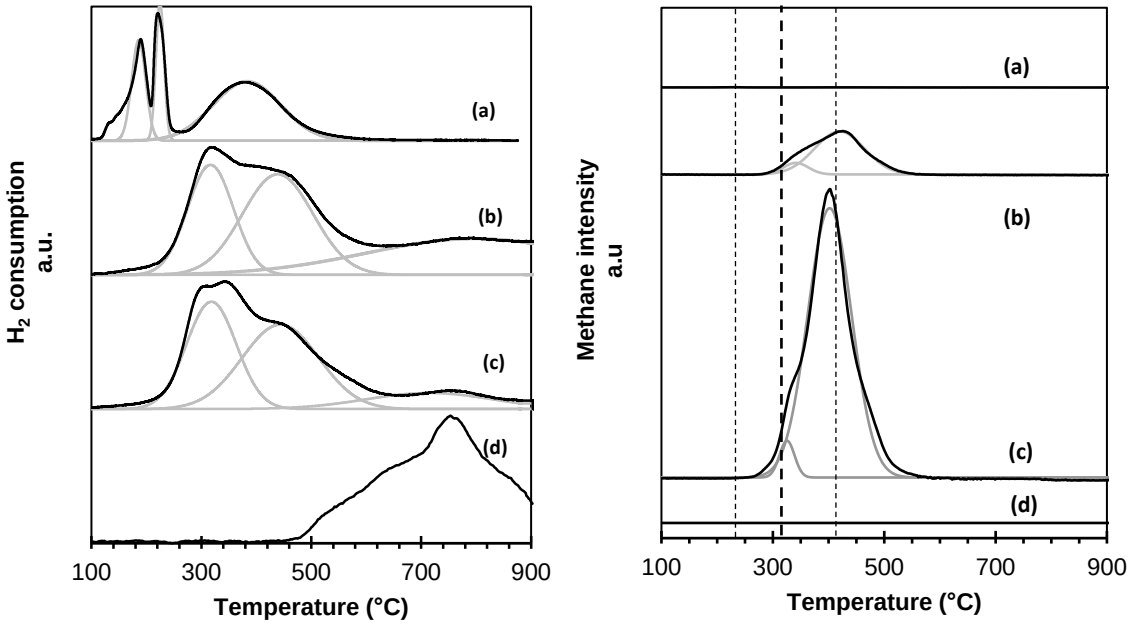

Figure 6-6: Normalized TPR spectra (left) and methane formation (right) during temperature programmed hydrogenation (TPH) for (a) fresh Pt-Co/Al_2O_3 (b) spent catalyst exposed to high X_{CO} (c) catalyst exposed to a feed containing water (d) $CoAl_2O_4$ reference.

The peak deconvolution of the TPR profile (see Table 6-1) shows a two-fold larger relative area for hydrogen consumption between 680°C and 880°C for the catalyst exposed to conditions prevalent at a high conversion than the 'simulated' high conversion case. More cobalt aluminate formed in the sample exposed to high conversion conditions could have been expected a priori, since increasing conversion from 40% to 95% results in a far stronger increase in p_{H_2O}/p_{H_2} (0.38 - 9.5) than increasing partial pressure of water in the feed (0.52 – 0.9). This result is consistent with irreversible deactivation in the slurry bed reactor study (see Fig. 7-4).

Table 6-1: Calculated hydrogen consumption (mmol/g_{cat}) for each deconvoluted peak in the TPR for the fresh catalyst, the sample exposed to high conversion conditions and the catalyst exposed to a feed containing water.

	Cobalt nitrate	***$Co_3O_4 \rightarrow CoO$***	***$CoO \rightarrow Co^0$***	***Cobalt aluminate***	***Fit error***
Temp (°C)	180	200-450	200-600	350-900	
	Hydrogen consumption (mmol/$g._{cat}$)				
Fresh	0.64	1.0	3.6	No peak	4.17%
High conversion	No peak	1.5	2.1	2.0	1.10%
'Simulated' high conversion	No peak	1.6	2.3	1.0	1.08%

6.3.3.3. Carbon deposition

The extent of carbon formation on the surface of the catalyst may be determined by means of TPH (see Appendix B for experimental details) where a GC-MS is attached to the exhaust during temperature programmed reduction. The amount of methane produced from the sample indicates the amount of material able to hydrogenate on the surface of the catalyst (i.e. wax, hydrocarbons and carbon).

The TPH profile is shown in Figure 6-6 and the relative peak areas are shown in Table 6-2. The fresh sample shows a flat profile indicating that it does not contain any material which hydrogenates to methane. The TPH profile of the spent samples, on the other hand, show peaks at 330°C and 440°C as identified by deconvolution. The peak at ca. 330°C can be ascribed to difficult to remove wax, presumably trapped within the pores [139]. The peak at 440°C can be ascribed to polymetric carbon [123,175] as described by Moodley [174]. Both spent samples show no methane peaks at 250°C, indicating that the Soxhlet extraction and drying was effective in removing wax on the surface.

Remarkably, the spent sample from the 'simulated' high conversion run contains more than 5-fold as much polymeric carbon as the sample exposed to conditions prevalent at high conversion, despite similar partial pressures of water within the system (albeit different p_{H_2O}/p_{H_2}). There are two primary factors that may affect the formation of inactive carbon – time on stream and the H_2/CO ratio within the reactor. The 'simulated' high conversion run was conducted at low to moderate conversions for over 600 h., whilst the high conversion run was conducted over 500 h. Thus, based on the time on stream one may have expected a slight increase in carbon deposition for the 'simulated' high conversion case. However, the significant difference may also be caused by the differences in p_{CO} and p_{H_2}. In the 'simulated' high conversion case a relatively high partial pressure of CO (2 - 3.2 bar) may have increased the tendency for carbon deposition on the catalyst.

Table 6-2: Relative peak areas for methane TPH-MS of fresh Pt-Co/Al_2O_3 spent catalyst high X_{CO} run spent catalyst externally added water run. Methane TPH-MS profile peak assignment as described by Moodley et al. [139]. Peaks relative to largest polymeric carbon peak.

	Residual wax/hydrocarbons	***Smaller chained polymetric carbon Residual wax in pores***	***Polymeric (amorphous) carbon***	***Fit error***
Temp (°C)	250	330	440	
Fresh	No peak	No peak	No peak	N/A
High conversion	No peak	0.02	0.18	0.8 %
'Simulated' high conversion	No peak	0.04	1	1.5 %

Going to actual high conversion reduces the partial pressure of CO (0.1 – 1.3 bar) whilst increasing the H_2/CO ratio [176]. This may lead to a lower C-availability and abundance of H-species which may hydrogenate active carbon on the surface of the catalyst [176]. Thus, it may be argued, that high conversion is a uniquely inhospitable environment for carbon deposition. One could thus speculate that operating the reactor at high conversion, with in-situ generated H_2/CO ratios of between 3 and 8 (see Chapter 4), and high p_{H_2O}/p_{H_2} ratios [176], minimizes the significance of carbon deposition as a deactivation mechanism.

6.4. Sintering and oxidation at high conversion: an in-situ study

To decouple the effect of cobalt oxide, cobalt aluminate formation and sintering at various conversions an in-situ magnetometer was used [168]. Figure 6-7 (a)-(b) shows the saturation magnetization, M_{sat}, and mass fraction of cobalt that remains magnetic upon removal of the magnetic field, γ, as a function of time on stream and conversion. Conversion was altered by decreasing the space velocity of N_2, H_2 then CO (in this order) while keeping their ratios constant, in the same manner as the high conversion slurry bed run.

A drop in the magnetization upon changing space velocity may indicate a transformation of metallic cobalt to Co(II)O whilst an irreversible loss of magnetization might be attributed to the formation of cobalt aluminate. It is important to note that the change-over of conditions may temporarily alter the magnetization of the sample by changing the concentration of adsorbed species [124]. The mass fraction of cobalt that remains in its magnetic state, γ, after the electro-magnetic field is removed represents the mass fraction of large cobalt crystallites. An increase in this value may, therefore, be taken as an indication of crystallite growth and therefore sintering.

The saturation magnetization (Fig. 6-7 (a)) increases with increasing conversion from X_{CO} = 3% - 59%. This may be attributed to further reduction of the catalyst in the presence of CO and H_2 since the initial

degree of reduction was only 54%. Alternatively, this may be due to the increase in magnetization via adsorbed O and OH groups [124].

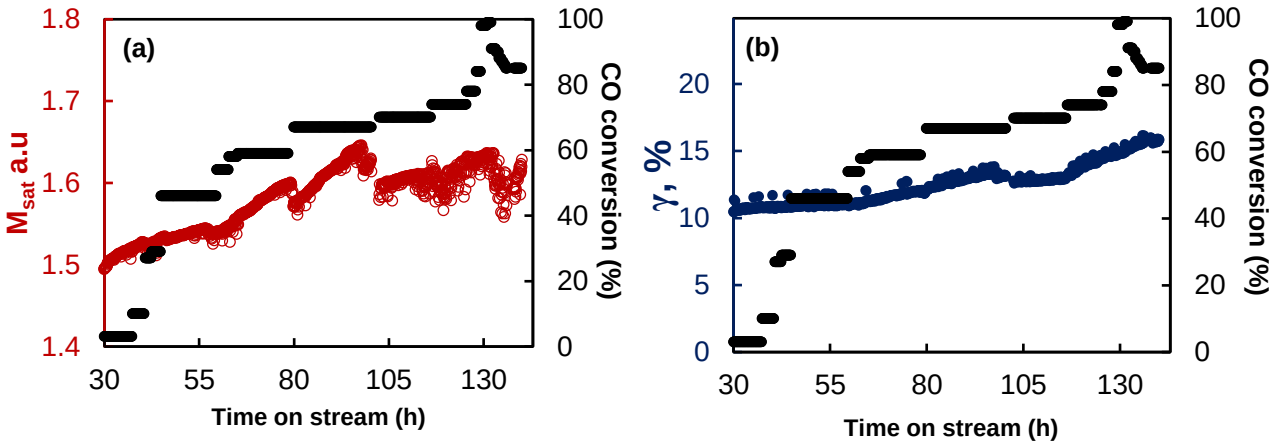

Figure 6-7: Saturation magnetization, M_{sat} (a), and mass fraction of cobalt that remains magnetic upon removal of the magnetic field, γ (b), as a function of time on stream and conversion, X_{CO}, for Pt-Co/Al_2O_3 with an average crystallite size of 6 nm.

On increasing the conversion from 59% to 67%, a temporary loss of magnetization occurs followed by an immediate increase in magnetization. This may be due to oxidation, however considering the large increase in conversion it is more likely due to the change-over of conditions. A CO rich environment may have been temporarily created leading to a change in the adsorbed species concentration (decrease in H* and increase in C*), leading to a decrease in M_{sat} [124].

Upon increasing the CO-conversion to X_{CO} = 70%, a permanent decrease in magnetization is observed. This may be due to the start of formation of irreducible compounds such as cobalt aluminate. This result is in accordance with the findings from the slurry bed reactor run where significant irreversible relative activity was exhibited at 70% conversion, and the spent catalyst characterization which revealed cobalt aluminate formation for the sample exposed to high conversion conditions.

Interestingly, this appears to be the only time where an irreversible loss of magnetization is noted. At these conditions, only crystallites under 5 nm in size will oxidize [117], which may imply that crystallites above 5 nm may not convert to irreducible compounds such as cobalt aluminate. It may be speculated that smaller crystallites are more likely to form irreducible compounds, possibly due to increased susceptibility to support encroachment which decreases the diffusion length for cobalt into the alumina structure. The higher surface energy contribution of smaller crystallites will also increase the driving force for the formation of cobalt aluminate. This may be the cause of greater irreversible deactivation between X_{CO} = 70% - 80% in relation to X_{CO} = 80% - 90% in the slurry bed reactor test.

Upon increasing the conversion further, the rate of change of magnetization decreases slightly, possibly due to lower partial pressures of CO and H_2 which would hinder reduction. As a conversion of 98% is reached, M_{sat} decreases quickly accompanied by a loss in activity and a consequential decrease in conversion from 98% to 85%. As the conversion decreases, the saturation magnetization begins to recover, almost fully regaining its magnetization. This phenomenon may be attributed to a reversible transformation of metallic cobalt to Co(II)O associated with the changing p_{H_2O}/p_{H_2} as a function of conversion. The formation of Co(II)O from metallic cobalt may reduce the active metal surface area resulting in a loss of activity that consequently reduces the conversion. The decrease in conversion results in a reduced p_{H_2O}/p_{H_2}, which may result in the re-reduction of Co(II)O, thus, increasing the magnetization. This result seems to be in accordance with the results obtained at high conversion (see Fig. 6-1), where a change in the space velocity from baseline conditions to 0.21 mmol CO/min/g resulted in a strong irreversible deactivation leading to a decrease in conversion from X_{CO} = 97% to X_{CO} = 89%. This ultimately resulted in only a marginal change in the obtained conversion with decreasing space velocity. This may suggest that a maximum conversion exists for a specific crystallite size distribution due to the formation Co(II)O.

Figure 6-7 (b) shows the mass fraction of cobalt that remains in magnetic state upon removal of the magnetic field, γ, for Pt-Co/Al_2O_3 as a function of time on stream at different levels of conversion. For conversions up to 54% there is very little increase in γ. Increasing the CO-conversion from 54% to 67% resulted in a small increase in γ from 11 to 13.5%, providing some evidence for sintering at these conversions. Since larger crystallites are easier to reduce, this also explains the increased positive gradient in the saturation magnetization at these conditions.

At a CO-conversion level of 70%, there is a slight drop in γ, that coincides with an irreversible decrease in M_{sat}. This result is surprising as an increase in γ is expected with preferential "loss" of small crystallites. It may be speculated that rapid formation of cobalt aluminate on the exterior surface of cobalt crystallites may result in a (slightly) smaller cobalt crystallite covered in cobalt aluminate and thus a smaller magnetic domain and reduced γ.

Once the conversion goes beyond X_{CO} = 74%, γ increases at a rapid rate, indicating a greater prevalence of sintering due to the hydrothermal environment [124]. The extent of sintering continues to increase upon increasing the conversion to X_{CO} = 98%, possibly explaining why the CO-conversion does not increase upon re-reduction of Co(II)O.

From the in-situ magnetometer study, it may be deduced that the various deactivation mechanisms are conversion dependent and that for crystallites of 6 nm, increasing conversion past 70% may lead to the formation of both Co(II)O and $CoAl_2O_4$ as well as enhanced sintering behavior.

6.5. Conclusion

A 500-h slurry bed study of Pt-Co/Al_2O_3 revealed that significant irreversible deactivation starts from as early as X_{CO} = 70% and reaches a maximum at X_{CO} > 90%. Using spent catalyst characterization and an in-situ magnetometer and to evaluate the mechanisms, deactivation at high conversion was linked to a combination of sintering and the formation of cobalt oxide and cobalt aluminate. These results suggest that industrial operation of a once-through Fischer-Tropsch process operated at high conversion is not feasible for a standard industrial catalyst, Pt-Co/Al_2O_3, and that improvements need to be made to the catalyst in order to facilitate operation under these conditions.

Deactivation mechanisms associated with high conversion were compared to deactivation under low-conversion, high water partial pressure environments ('simulated' high conversion) and found to be remarkably different. The low partial pressure of CO at high conversion dramatically reduces the extent of carbon deposition compared to hydrothermal environments at relatively high partial pressure of CO, as confirmed by a TPH study of the spent catalysts. Furthermore, cobalt aluminate formation is favored at high conversion due to low H_2 partial pressures which result in enhanced p_{H_2O}/p_{H_2} ratios of up to 9.5.

Interestingly, the formation of irreducible oxides seems to occur only between 70% and 80% conversion. This may be attributed to the susceptibility of small crystallites to the formation of metal-support oxides due to lowered diffusion lengths and increased surface energies. The reversible formation of Co(II)O at very high conversion X_{CO} > 90% is speculated to impose a thermodynamic conversion limit based on crystallite size.

Chapter 7

Thermodynamic analysis of the oxidation and re-reduction of a lognormal size distribution of cobalt crystallites

7.1. Introduction

Chapter 6 showed that significant instantaneous activity loss is possible at very high conversions, X_{CO} = 97% (p_{H_2O}/p_{H_2} = 9.5). Using an in-situ magnetometer, it was shown that this activity loss was accompanied by a reversible loss of magnetization. This indicates that at these very high conversions, Co(II)O is formed, which causes a subsequent loss of activity, leading to a decrease in conversion. This decrease in conversion would cause a decrease in p_{H_2O}/p_{H_2} and, subsequently, a reformation of Co^0 which may increase, or stabilize, conversion.

Typically the oxidation of cobalt at Fischer-Tropsch conditions is explained by the presence of cobalt nanoparticles, as discussed in Chapter 2 [77,117,118]. Whilst the formation of cobalt oxide from bulk metallic cobalt requires very high p_{H_2O}/p_{H_2} ratios [117], the formation of cobalt oxide from smaller cobalt crystallites requires far less extreme conditions. This is due to the contributions of surface energy, which makes nanosized crystals less resistant to oxidation.

Useful thermodynamic calculations have been previously performed [117], which aimed to predict the p_{H_2O}/p_{H_2} limit at which discreet Co^0 crystallites of specific sizes would convert to Co(II)O. However, industrial Fischer-Tropsch catalysts do not have uniform and discreet cobalt crystallite sizes. These catalysts have a characteristic distribution which can more accurately be modelled as a lognormal distribution. This means that at any specific p_{H_2O}/p_{H_2} ratio, whilst cobalt crystallites with a discreet size corresponding to the thermodynamic limit (see Figure 2-7) will convert to Co(II)O, so too will every cobalt crystallite of a smaller size.

Here, we report on a novel thermodynamic model for the oxidation and re-reduction of a lognormal distribution of cobalt crystallites to calculate the maximum possible conversion achievable in the Fischer-Tropsch synthesis considering the loss of activity from formation of Co(II)O.

7.2. Mathematical methodology

For a continuous slurry bed reactor, the design equation can be described as:

$$-r_A = \frac{F_{CO_0} X}{w} \quad \textbf{7-1}$$

where F_{CO_0} is the molar flow rate of CO into the reactor, X is the CO conversion and w is the weight of catalyst.

The rate of reaction, and therefore conversion, is dependent on the amount of active metal – in this case metallic cobalt. The design equation and stoichiometric relationship is, therefore, reliant on the assumption that the amount of active material is constant across the entire conversion range. This assumption is not necessarily true due to the phenomenon of catalyst oxidation.

7.2.1. Rate dependency on surface area

Rate of reaction is in principal proportional to the metal surface area. For a catalyst with a crystallite size distribution (taking the rate of reaction per unit surface area independent of particle size), the rate of reaction per unit mass is given by:

$$-r_{CO,w} = \int_{d_{Co}=0}^{d_{Co}=\infty} \left(-r_{CO,A}\right) \cdot SA(d_{Co}) \cdot Me \cdot w(d_{Co}) \cdot dd_{Co} \quad \textbf{7-2}$$

where $\left(-r_{CO,A}\right)$ is the rate of reaction per unit surface area, $SA(d_{Co})$ is the surface area of the particle per gram of active metal when the crystallite size of the active material is d_{Co}, $w(d_{Co})$ is the weight fraction of crystallite size d_{Co} in the total weight of active material and Me is the metal loading in the whole catalyst.

The surface area of cobalt, assuming spherical crystallites is given as a function of the area of a sphere over its mass which simplifies to:

$$SA(d_{Co}) = \frac{6000}{\rho_{active\ metal} \cdot d_{Co}} \quad \textbf{7-3}$$

The mass or weight fraction is related to the particle size distribution ($psd(d_{Co})$) by the following equation:

$$w(d_{Co}) = \frac{m(d_{Co}) \cdot psd(d_{Co})}{\int_{d_{Co}=0}^{d_{Co}=\infty} m(d_{Co}) \cdot psd(d_{Co}) \cdot dd_{Co}} = \frac{\rho_{active\ metal} \frac{\pi}{6} \cdot d_{Co}^3 \cdot psd(d_{CO})}{\int_{d_{Co}=0}^{d_{Co}=\infty} \rho_{active\ metal} \frac{\pi}{6} \cdot d_{Co}^3 \cdot psd(d_{CO}) \cdot dd_{Co}} = \frac{d_{Co}^3 \cdot psd(d_{CO})}{\int_{d_{Co}=0}^{d_{Co}=\infty} d_{Co}^3 \cdot psd(d_{CO}) \cdot dd_{CO}} \quad \textbf{7-4}$$

Thus, the rate of reaction for the non-deactivated particle is given by:

$$-r_{CO,w} = \frac{Me \cdot 6000 \cdot (-r_{CO,A})}{\rho_{active\ metal}} \cdot \int_{d_{Co}=0}^{d_{Co}=\infty} \frac{d_{Co}^2 \cdot psd(d_{Co})}{\int_{d_{Co}=0}^{d_{Co}=\infty} d_{Co}^3 \cdot psd(d_{Co}) \cdot dd_{Co}} \cdot dd_{Co} \quad \textbf{7-5}$$

$$-r_{CO,w} = \frac{Me \cdot 6000 \cdot (-r_{CO,A})}{\rho_{active\ metal}} \cdot \frac{\int_{d_{Co}=0}^{d_{Co}=\infty} d_{Co}^2 \cdot psd(d_{Co}) \cdot dd_{Co}}{\int_{d_{Co}=0}^{d_{Co}=\infty} d_{Co}^3 \cdot psd(d_{Co}) \cdot dd_{Co}} \quad \textbf{7-6}$$

The rate of reaction depends on the area average diameter (so-called Sauter-diameter) of the size distribution. In a deactivated catalyst, only the activity of particles with a size larger that $d_{Co,min}$ will contribute to the activity, thus:

$$-r_{CO,w,deactivated} = \frac{Me \cdot 6000 \cdot (-r_{CO,A})}{\rho_{active\ metal}} \cdot \frac{\int_{d_{Co}=d_{Co,min}}^{d_{Co}=\infty} d_{Co}^2 \cdot psd(d_{Co}) \cdot dd_{Co}}{\int_{d_{Co}=0}^{d_{Co}=\infty} d_{Co}^3 \cdot psd(d_{Co}) \cdot dd_{Co}} \quad \textbf{7-7}$$

Hence, the deactivation factor (D_F) may be given by:

$$D_F = \frac{-r_{CO,w,deactivated}}{-r_{CO,w,fresh}} = \frac{\int_{d_{Co}=d_{Co_{min}}}^{d_{Co}=\infty} d_{Co}^2 \cdot psd(d_{Co}) \cdot dd_{Co}}{\int_{d_{Co}=0}^{d_{Co}=\infty} d_{Co}^2 \cdot psd(d_{Co}) \cdot dd_{Co}} \quad \textbf{7-8}$$

Combining D_F in terms of our design equation the following equation can be derived:

$$D_F = \frac{-r_{CO,w,deactivated}}{-r_{CO,w,fresh}} = \frac{\frac{F_{CO_0} X_{deactivated}}{w}}{\frac{F_{CO_0} X_{fresh}}{w}} = \frac{X_{deactivated}}{X_{fresh}} \quad \textbf{7-9}$$

7.2.2. Particle size distribution

The relationship between rate and surface area requires an equation to describe the particle size distribution. Cobalt crystallite sizes typically present as a lognormal distribution. The general equation for a lognormal distribution can be written as follows

$$f(d_{Co}) = \frac{1}{d_{Co}\sigma\sqrt{2\pi}} e^{-\frac{(ln(d_{Co})-\mu)^2}{2\sigma^2}} \quad \textbf{7-10}$$

where d_{Co} is the cobalt crystallite size and σ and μ are parameters relating to the mean and the variance according to the following correlations.

$$median = e^{\mu} \quad \textbf{7-11}$$

$$mean = e^{\mu+\frac{\sigma^2}{2}} \quad \textbf{7-12}$$

$$variance = (e^{\sigma^2} - 1).(e^{2\mu+\sigma^2}) \quad \textbf{7-13}$$

Figure 7-1 illustrates a typical normal distribution for an industrial cobalt catalyst [177]. Under ideal circumstances (well dispersed catalyst with no oxidation) all cobalt crystallites that are on the surface of will contribute to the rate. However, if the partial pressure of water is increased within the reaction system to an extent that p_{H_2O}/p_{H_2} ratio is high enough to oxidize a certain crystallite size – all crystallites below that size ($d_{Co,min}$) will lose activity through a transformation to Co(II)O (see shaded area).

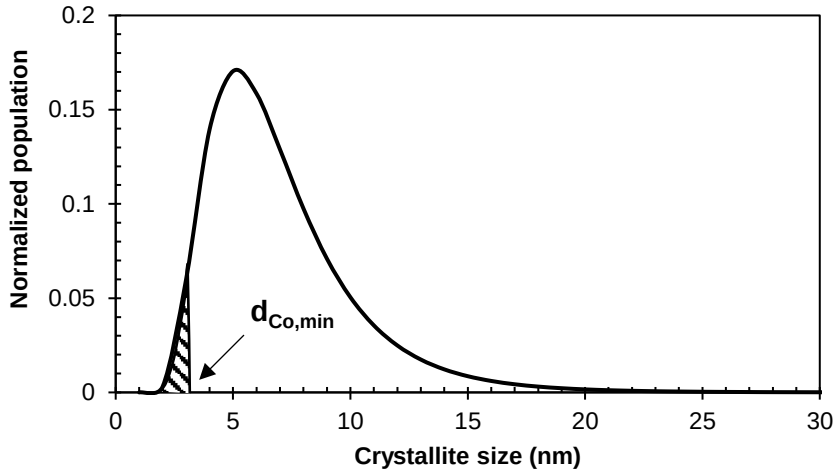

Figure 7-1: Log normal distribution of a typical cobalt catalyst with a median of 5 nm, mean of 6 nm and a standard deviation of 3.2 (σ = 0.5).

7.2.3. Minimum diameter ($d_{Co,min}$)

The relationship between crystallite size and stability has been presented previously [117]. For a spherical crystallite, the thermodynamic limit for $\beta - Co$ (fcc) and water to convert to Co(II)O crystals and hydrogen lies along a boundary that can be described as per

$$\mu^0_{CoO(s)} + \mu^0_{H_2(g)} - \mu^0_{Co(s)} - \mu^0_{H_2O(g)} + RTln\left(\frac{p_{H_2}}{p_{H_2O}}\right) + \frac{6\gamma_{Co}}{\rho_{Co}d_{Co}}\left(\frac{\gamma_{CoO}}{\gamma_{Co}}\left(\frac{\rho_{Co}}{\rho_{CoO}}\right)^{\frac{2}{3}} - 1\right) = 0 \quad \textbf{7-14}$$

where $\mu^0$is the chemical potential of species i at temperature T and 1.013 bar, γ is the surface energy, d_{Co} is the diameter of cobalt crystallites and ρ is molar density. In addition, the ratio of the surface energies may described as per [117] (equation 7-15) due to Co(II)O being a weak function of crystal morphology.

$$\frac{\gamma_{CoO}}{\gamma_{\beta-Co}} = 0.2167 + \frac{0.011}{d_{Co}} - \frac{0.064}{d_{Co}^2} \qquad \textbf{7-15}$$

As $d_{Co,min}$ would be the diameter at this thermodynamic limit and conversion is a function of P_{H_2O}/P_{H_2}, a correlation between conversion and $d_{Co,min}$ for a spherical shaped $\beta - Co$ (fcc) and Co(II)O crystals may be calculated as shown in Figure 7-2.

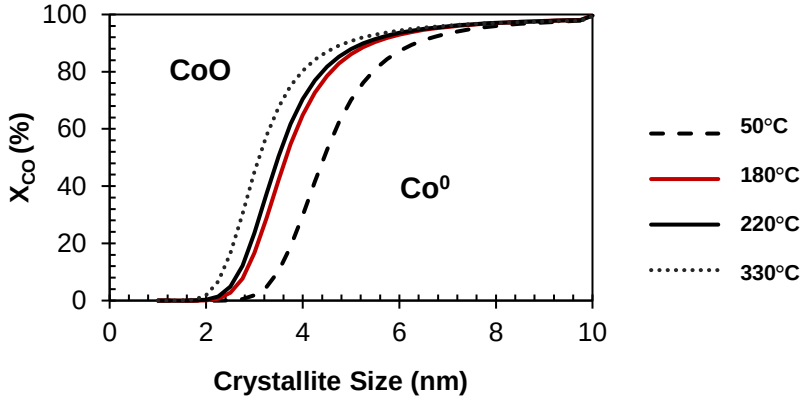

Figure 7-2: Phase diagram for cobalt transformation to cobalt oxide at 220°C for different crystallite sizes based on data provided by Knacke (1977) [128]. These curves represent $d_{Co,min}$ across a range of temperatures. Methodology based on [117].

7.2.4. Deactivation factor, D_F

Thus, the general relationship between the deactivation factor and particle size distribution may be derived by substituting the general equation for a lognormal particle size distribution (equation 7-10) into the equation for the deactivation factor (equation 7-9) where $d_{Co,min}$ is given as a function of conversion using the thermodynamic stability limit for $\beta - Co$ (fcc).

$$D_F = \frac{-r_{CO,w,deactivated}}{-r_{CO,w,fresh}} = \frac{\int_{d_{Co}=d_{Co\,min}}^{d_{Co}=\infty} d_{Co} \cdot \frac{1}{\sigma\sqrt{2\pi}} e^{-\frac{(\ln(d_{CO})-\mu)^2}{2\sigma^2}} \cdot dd_{Co}}{\int_{d_{Co}=0}^{d_{Co}=\infty} d_{Co} \cdot \frac{1}{\sigma\sqrt{2\pi}} e^{-\frac{(\ln(d_{CO})-\mu)^2}{2\sigma^2}} \cdot dd_{Co}} \qquad \textbf{7-16}$$

Thereafter, equation 7-16 can be integrated analytically or numerically as described in Appendix G.

7.3. Results

7.3.1. Instantaneous and system deactivation factor

This model can be used to calculate a deactivation factor for a given crystallite size distribution (with a given mean and variance) at any temperature. The deactivation factor calculation (equation 7-16) must be iterated with respect to conversion and $d_{Co,min}$ in order to accurately model the maximum achievable conversion. The deactivation factor calculated without iteration can be referred to as the 'instantaneous deactivation factor'. Instantaneous deactivation factors represent the deactivation that occurs directly after the flowrate has been decreased (conversion increased) to target. At this point, the system would theoretically reach the target conversion for an instant before reversible deactivation via oxidation causes all crystallites below $d_{Co,min}$ to become inactive. This oxidation causes a decrease in conversion and water partial pressure in the system. Once this occurs, a portion of the Co(II)O converts back to Co^0, which then increases the conversion and water partial pressure which then re-oxidizes the cobalt. This cycle continues until the system converges.

Figure 7-3 shows the deactivation factor calculated over 9 iterations for a lognormal crystallite size distribution with a mean of 2 nm and a σ of 0.5 at 220°C for various conversions. The first iteration reveals that the instantaneous deactivation factor is the largest deactivation in the range for all conversions. By 8 iterations, all conversion levels appear to have converged on a 'system deactivation factor' when the system has reached a steady state.

The importance of the iterative calculation process is shown by Figure 7-4, where the deactivation factor is calculated using numerical and analytical methods (see Appendix G) for 1 iteration ('instantaneous deactivation factor') and at convergence ('system deactivation factor'). At very low conversions, this iterative process does not change the deactivation factor to a significant extent. However, on increasing the conversion, the instantaneous and system deactivation factors increasingly diverge. For small crystallite sizes, this effect is more significant. For instance, for a lognormal crystallite size distribution with a mean of 2 nm and σ of 0.5, there is a 0.29 difference in deactivation factor at X_{CO} = 90%, whilst for a mean of 6 nm and σ of 0.5 the difference is only 0.06.

The system deactivation factor decreases with increasing conversion and decreasing crystallite size. As the deactivation factor represents the ratio of the rate of the deactivated catalyst over the fresh catalyst this shows, as predicted, that increasingly hydrothermal environments and cobalt catalysts with small mean crystallite sizes are more susceptible to deactivation and a decrease in rate due to oxidation of Co^0 to Co(II)O.

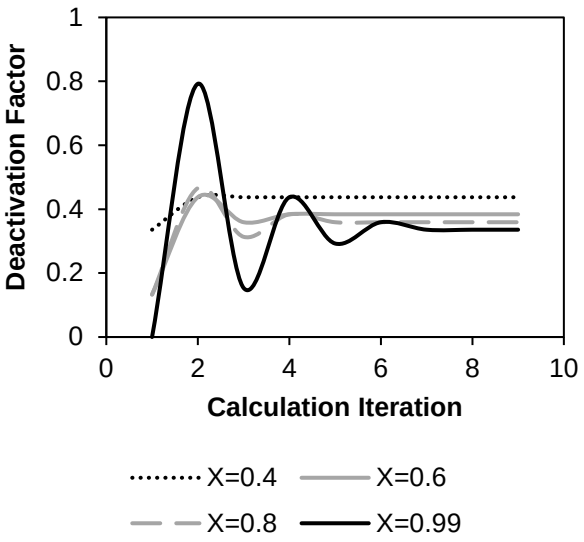

Figure 7-3: The effect of calculative iterations of equation 20 on the deactivation factor for a lognormal particle size distribution with a mean of 2 nm and a standard with σ = 0.5 at 220°C

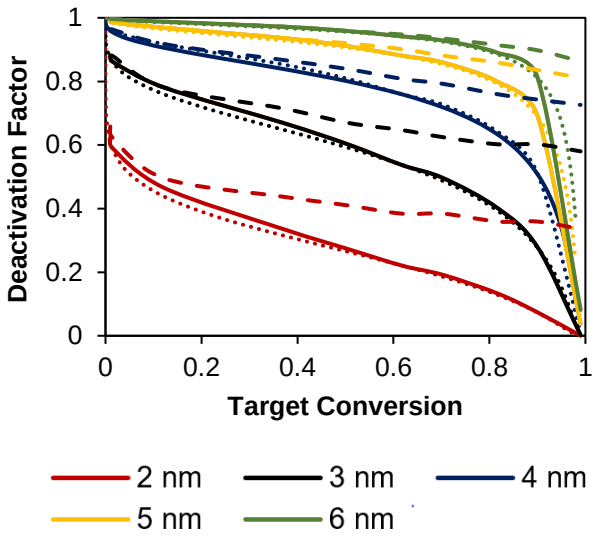

Figure 7-4: Instantaneous deactivation factors calculated numerically (—) and analytically (⋯) as well as the system deactivation factor (---) for various mean lognormal crystallite sizes with σ = 0.5 at 220°C.

7.3.2. The effect of mean size on achievable conversion

This model may be used to calculate the thermodynamic feasibility of achieving a specific conversion for various crystallite size distributions. Here, we refer to a 'target conversion' (the specific conversion targeted when decreasing the space velocity) and the 'achievable conversion' (the conversion of the system after the oxidation/re-reduction process has converged).

Figure 7-6 shows the effect of the mean crystallite size (shown in Figure 7-5) on the thermodynamically achievable conversions across the range of target conversions at a standard Fischer-Tropsch temperature of 220°C. The chosen distributions include mean crystallite sizes from 2 nm – 10 nm with σ = 0.5. The effect of the variance parameter (σ value) and temperature on the achievable conversion is shown in Appendix H.

For small mean crystallite sizes, large surface energy contributions (which facilitate oxidation) have a remarkable effect on thermodynamically achievable conversions, which remain lower than target conversions across the range. For instance, a system targeting X_{CO} = 60%, with mean cobalt crystallite sizes of 2, 3 and 4 nm will only reach conversions of X_{CO} = 24 %, 40 % and 50 % respectively. This effect is even more pronounced at higher target conversions, with maximum achievable conversions

(target X_{CO} = 100%) of 33%, 57% and 72% respectively. According to this model, conversions of X_{CO} > 80% are simply unattainable for lognormal crystallite size distributions with an average crystallite size of less than 4 nm.

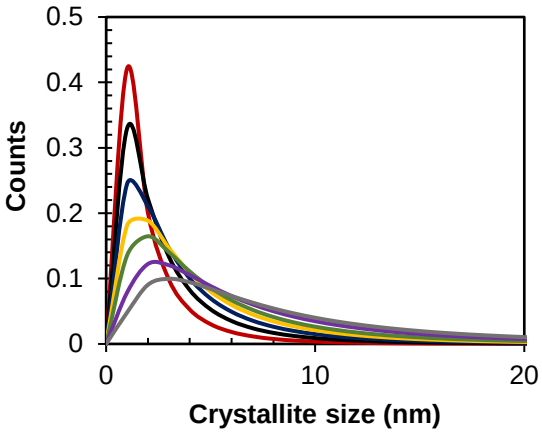

Figure 7-5: Lognormal distribution for various mean crystallite sizes with σ = 0.5

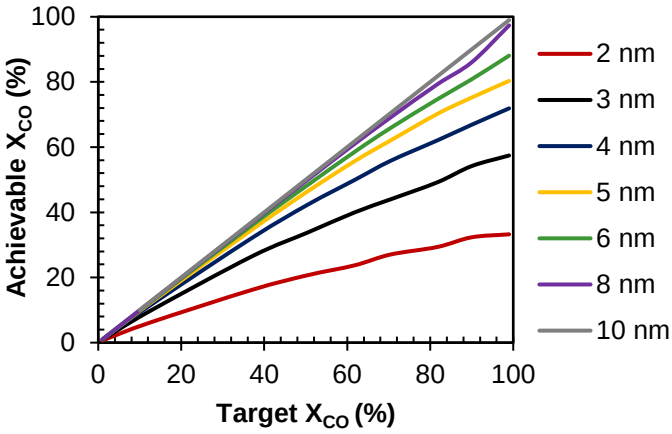

Figure 7-6: Maximum achievable conversions for various mean crystallite sizes with σ = 0.5 at 220°C.

The thermodynamic model for discreet crystallite sizes [117] estimates the maximum achievable conversions for crystallite sizes of 2, 3 and 4 nm at X_{CO} = 0.02 %, 12 % and 61% respectively. Thus, for small crystallite sizes, the model presented here for a lognormal distribution estimates that less deactivation will occur than what is given by the discreet model. This is due to the lognormal distribution model considering larger crystallites within the distribution which do not oxidize. This model indicates that significantly less deactivation will realistically occur for small ranges of crystallite sizes than one would predict with a thermodynamic model that only takes discreet sizes into account.

At more industrially realistic mean crystallite sizes of 5 and 6 nm, there is little difference between the achievable and target conversion below X_{CO} = 60%. Past this point however, the difference is more significant, reaching maximum achievable conversions (target X_{CO} = 100%) of only 80% and 88% respectively. For discreet crystallites of 5 and 6 nm the maximum achievable conversions [117] are estimated to be 85% and 93 % respectively. This indicates that for moderately sized cobalt crystallites, once the lognormal size distributions are considered, the extent of deactivation via oxidation is more severe than previously estimated and, thus, may have greater implications for industrial operation at high conversion.

For the deactivation study in Chapter 6, a Pt-Co/Al_2O_3 catalyst with an estimated Co^0 size of 6 nm (based on theoretical shrinkage and degree of reduction) was used. On increasing the conversion to X_{CO} = 97% in the slurry bed reactor, a sharp decrease in conversion to X_{CO} = 89% was exhibited. In the fixed bed magnetometer, an increase to a target conversion of X_{CO} = 98% yielded an immediate decrease to X_{CO} = 85%. Both results appear to correlate with our results for this model (maximum achievable conversion X_{CO} = 88%), albeit showing a slight discrepancy. This may be due to the Co^0 size being underestimated for Chapter 6, or an underestimation of the variance parameter (σ = 0.5) in this chapter. Results shown in Appendix H shows that an increase in variance from 0.5 to 0.9 changes the maximum achievable conversion from 88% to 91%.

At a mean crystallite size distribution of > 8 nm, there is very little effect of oxidation on the ability to achieve any specific conversion, with a maximum achievable conversion of X_{CO} = 98%. This suggests, perhaps, that by controlling the size of the cobalt crystallites to a minimum of 8 nm, it may be possible to avoid instantaneous deactivation at very high conversions.

7.4. Conclusion

Operation at high conversion results in a strong increase in the partial pressure of water. It is postulated that this water will reversibly deactivate all crystallites under a specific size threshold due to oxidation of Co^0 to Co(II)O [117]. The potential for oxidation is controlled by both the size of cobalt crystallites and the distribution of these sizes within a catalyst. A thermodynamic model was developed to account for the lognormal distribution of cobalt crystallites to more accurately predict deactivation via oxidation and to discover if a maximum achievable conversion exists.

At an industrially relevant mean crystallite sizes of 6 nm with a variance parameter value of 0.5 (based on the distribution presented in Chapter 6 and [177]) the oxidation of Co(II)O decreases the maximum achievable conversion to 88%. This appears to correspond with experimental results in Chapter 6 which showed that for both slurry and in-situ magnetometer work (fixed bed) almost immediate deactivation occurred at conversions above X_{CO} = 97%, which decreased conversions to a plateau of X_{CO} = 89% and 85% respectively. Based on this model, mean cobalt crystallite sizes above 8 nm are estimated to inhibit oxidation at high conversion, thus effectively eliminating the maximum conversion limitation.

Chapter 8

Zinc aluminate as a support for cobalt to improve stability at high conversion

8.1. Justification for zinc aluminate as a support

There are three mechanisms that cause strong deactivation at high conversion: cobalt oxidation to Co(II)O, the formation of cobalt aluminate and sintering. Carbon deposition is less significant at high conversion due to high hydrogen availability (as discussed in Chapter 6). Co(II)O formation is reversible and is thought to thermodynamically limit conversions to $X_{CO} < 90\%$ (as discussed in Chapter 7). Sintering and cobalt aluminate formation occur at $X_{CO} > 70\%$ and can cause irreversible deactivation for industrial sized nano crystallites of Pt-Co/Al_2O_3. Thus, to operate the Fischer-Tropsch process at higher conversion than typically seen in industry, the stability of Pt-Co/Al_2O_3 under these conditions must be improved.

One way to achieve this may be to change the support material. Alumina has very strong metal support interactions, which may decrease the size of cobalt crystallites, which promotes sintering, cobalt oxidation (as shown in Chapter 7) and, thus, the indirect formation of cobalt aluminate during the Fischer-Tropsch synthesis. A support with weaker metal support interactions may lead to increased cobalt crystallite size and thus improved stability. In addition, it may be possible to thermodynamically limit the formation of cobalt aluminate (direct and indirect) by changing the support. Mixed metal oxides do not form irreducible compounds with cobalt, thereby effectively eliminating the possibility of irreversible deactivation via cobalt-aluminate formation [77]. Of the mixed metal oxides available, zinc aluminate is particularly promising as it is low-cost and hydrothermally stable [148,149].

Figure 8-1 illustrates the Gibbs free energy of reaction for the formation of $CoAl_2O_4$ from Co(II)O and Al_2O_3, SiO_2 and $ZnAl_2O_4$ respectively. Whilst the formation of $CoAl_2O_4$ from Co(II)O and Al_2O_3 or SiO_2 is thermodynamically favoured (negative $\Delta G°_{rxn}$) over the whole the temperature range, the formation of $CoAl_2O_4$ from Co(II)O and $ZnAl_2O_4$ is not thermodynamically feasible.

Chapter 8 will evaluate the effect of using zinc aluminate as a support on the stability of a platinum-promoted cobalt catalyst and compare this to the results discussed in Chapter 6 for Pt-Co/Al_2O_3.

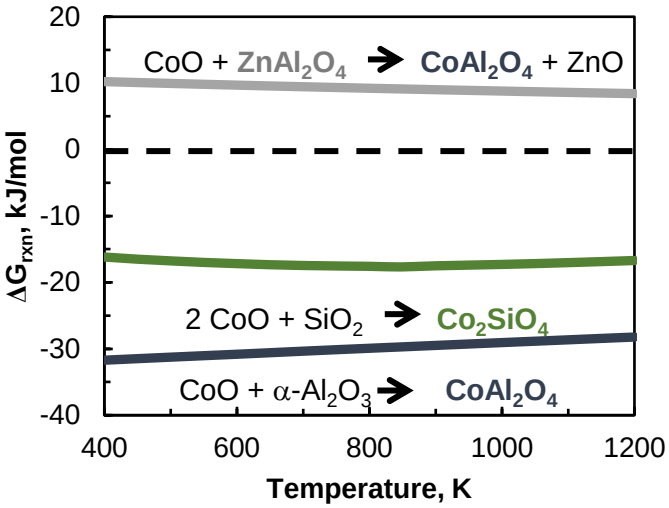

Figure 8-1: Gibbs free energy of reaction for the formation of cobalt aluminate from Co(II)O and Al_2O_3, SiO_2 and $ZnAl_2O_4$

8.2. Experimental techniques

8.2.1. Catalyst and support preparation

Zinc aluminate was prepared via sol-gel [178] and co-precipitation [179] methods whilst the catalysts, Pt-Co/Al_2O_3 and Pt-Co/$ZnAl_2O_3$, were prepared via slurry impregnation as described in Appendix B. The calcined catalysts contained 22 wt.-% and 23 wt.-% Co and 0.05 wt.-% and 0.04 wt.-% Pt respectively as determined from elemental analysis using AAS-OES and ICP-OES.

8.2.2. Catalyst characterisation

The zinc aluminate support material was characterised via BET surface area, pore volume and pore size (Micromeritics Tri-Star system) as well as scanning electron microscopy (LEO 1450 SEM), particle size distribution (Mastersizer 2000) and X-ray diffraction (D8 Advance Bruker). The catalysts were characterised via hydrogen chemisorption (Micromeritics ASAP HP 2020C), temperature programmed reduction (TPR) (Micromeritics Autochem HP II 2950). Detailed experimental procedures can be found in Appendix B.

8.2.3. Slurry bed reactor study

The catalysts were reduced and loaded in the slurry bed reactor as per Appendix B and tested in the same manner as described in Chapter 6, Section 6.2.3. Initially, each catalyst was held at a space velocity of CO of 1.73 mmol/min/g_{cat} (baseline conditions) which resulted in a conversion of X_{CO} = 42% and X_{CO} = 35% for Pt-Co/Al_2O_3 and Pt-Co/$ZnAl_2O_4$ respectively. The space velocity was then systematically decreased to increase conversion to ca. X_{CO} = 60%, 70%, 80% and 90%. Between each

conversion the space velocity was decreased to baseline conditions to assess irreversible deactivation. Different space velocities were required for each catalyst to reach these conditions due to differing activities. For Pt-Co/Al_2O_3, CO space velocities of 1.73, 1.03, 0.94 - 0.83, 0.62 - 0.42 and 0.21 mmol CO/min/g were used, whilst for Pt-Co/$ZnAl_2O_4$, space velocities of 1.73, 0.65, 0.45, 0.31 and 0.22 - 0.17 mmol CO/min/g were used.

8.3. Results and discussion

8.3.1. Characterising $ZnAl_2O_4$

The two samples of $ZnAl_2O_4$ formed via co-precipitation [179] and sol-gel [178] methods were characterised in terms of their crystallography, topography, particle size distribution, BET surface area, pore volume and pore radius as described in Appendix B. The full characterisation, and description of choice support, can be found in Appendix C.5.

Both preparation methods yielded zinc aluminate with similar crystallite size (8.61 and 9.89 nm), an irregular shape and particle sizes between 10 μm – 300 μm (median = 17 and 22 μm). Irregular shaped supports may shatter in industrial-sized slurry bed reactors and, thus, get carried out of the reactor. Therefore, for industrial purposes, spray drying of this support may be necessary.

Zinc aluminate prepared via sol gel method and calcined at 600°C was found to have the most favourable combination of physisorption features including a large pore size, comparable to that of γ-Al_2O_3, which will limit unfavourable mass transfer limitations. Thus, $ZnAl_2O_{4,\ sol\ gel}$ was used for studying the effect of deactivation in a slurry bed reactor.

8.3.2. Catalyst characterisation

The physio-chemical characteristics of calcined and reduced Pt-Co/Al_2O_3 and Pt-Co/$ZnAl_2O_{4,\ sol\text{-}gel}$ are shown in Table 8-1, further characterisation is given in Appendix C.1. and C.5. The surface area and pore volume were decreased for Pt-Co/$ZnAl_2O_4$. However, the pores size was not significantly altered which ensures favourable mass transfer. The crystallite size of Co_3O_4 in Pt-Co/Al_2O_3 was smaller (ca. 11 nm) than in Pt-Co/$ZnAl_2O_4$ (ca. 15 nm). This may be attributed to weaker metal-support interactions and correlates with the TPR of Co/Al_2O_3 and Co/$ZnAl_2O_4$ (Figure C-12, Appendix C.5) which shows a greater level of reducibility for the latter. The H_2-uptake measured via chemisorption for reduced Pt-Co/$ZnAl_2O_4$ (2.3 cm^3/g) was significantly lower than that for Pt-Co/Al_2O_3 (4.6 cm^3/g). This may be due to the reduced surface area or a lower level of dispersion of cobalt over the support surface.

Table 8-1: Physisorption and chemisorption results for Pt-Co/Al_2O_3 and Pt-Co/$ZnAl_2O_4$.

	Calcined catalyst precursor				*Reduced catalyst (350°C, 16 hours)*		
	S_{BET} (m^2/g)	V_{pore} (cm^3/g)	d_{pore} (nm)	d_{Co3O4}[1] (nm)	H_2 uptake[2] (cm^3/g STP)	Metal surface area[3] (m^2/g sample)	TOF s^{-1}
Puralox	157	0.5	8.8				
$ZnAl_2O_4$	64	0.2	8.1				
Pt-Co/Al_2O_3	113	0.30	8.0	11	4.6	13	0.03
Pt-Co/$ZnAl_2O_4$	63	0.13	7.2	15	2.3	7.3	0.05

8.3.3. Reactor study

Figure 8-2 shows the change in conversion as a function of time on stream for the deactivation slurry bed reactor runs for (a) Pt-Co/Al_2O_3 and (b) Pt-Co/$ZnAl_2O_4$, sol gel at 220°C and 20 bar with a feed N_2:H_2:CO = 3:2:1. Figure 8-2 (a) was also shown in Chapter 6 (Figure 6-1) and repeated here for ease of comparison. Both catalysts were initially held at baseline conditions of 1.73 mmol CO/min/g for ca. 100 h before their relative space velocities were decreased to increase conversion from ca. X_{CO} = 40 to X_{CO} > 90. Between each cycle the catalysts were returned to baseline conditions to assess irreversible deactivation. The red lines on Figure 8-2 indicate the general trend of irreversible deactivation for both catalysts.

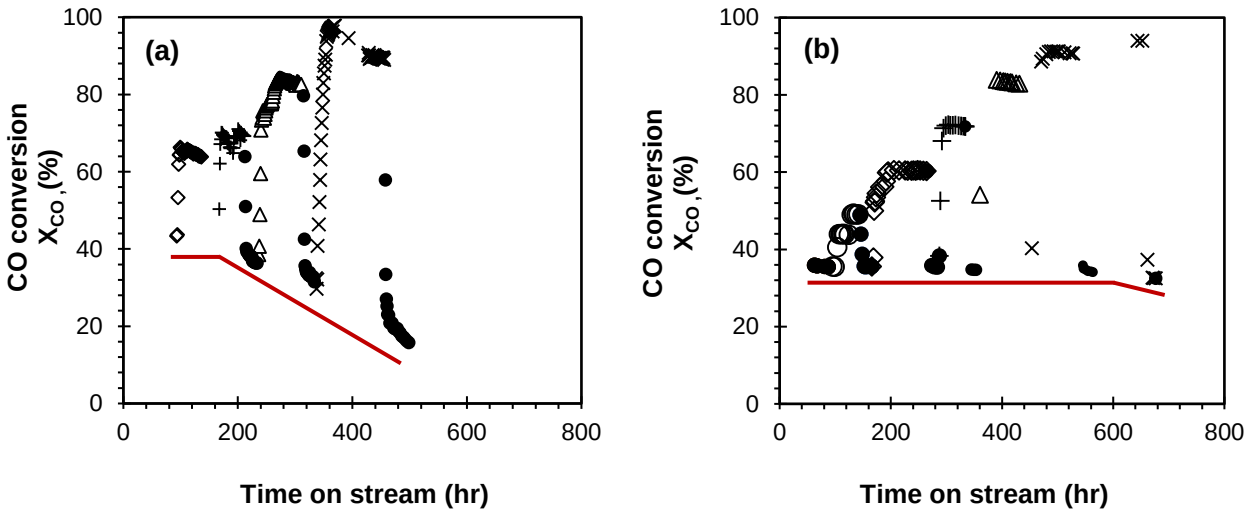

Figure 8-2: CO conversion as a function of time on stream for (a) Pt-Co/Al_2O_3 and (b) Pt-Co/$ZnAl_2O_4$ in a slurry reactor at 220°C and 20 bar with a feed N_2:H_2:CO = 3:2:1. Space velocity of CO for (a) and (b): ● 1.73 mmol CO/min/g, ○ N/A and 1.4 – 1.1, ◊ 1.03 and 0.65 mmol CO/min/g, + 0.94 - 0.83 and 0.45 mmol CO/min/g, Δ 0.62-0.42 and 0.31 mmol CO/min/g × 0.21 and 0.22-0.17 mmol CO/min/g respectively. Note: red lines are a graphical aid and do not represent actual data points.

8.3.3.1. Turnover frequency

The baseline conversions (at 1.73 mmol CO/min/g) of Pt-Co/Al_2O_3 and Pt-Co/$ZnAl_2O_4$, shown in Figure 8-2, were X_{CO} = 35% (88 h on stream) and X_{CO} = 43% (90 h on stream) respectively. This corresponds to baseline rates of CO consumption of 0.74 mmol/g_{cat}.min and 0.63 mmol/g_{cat}.min respectively. This result seems to suggest that the zinc aluminate supported cobalt catalyst is less active at baseline conditions. However, once H_2 uptake was considered (Table 8-1), the turnover frequency for Pt-Co/Al_2O_3 and Pt-Co/$ZnAl_2O_4$ were calculated to be 0.03 s^{-1} and 0.05 s^{-1} respectively (Table 8-1).

Interestingly, despite a decreased rate at baseline conditions, the site activity for Pt-Co/$ZnAl_2O_4$ appears to be higher. This is quite a startling result as there is no evidence of $ZnAl_2O_4$ acting as an promoter for cobalt catalysts in the Fischer-Tropsch synthesis, albeit there have been reports of increased Fischer-Tropsch activity associated with zinc promotion [151,180–183]. In one study [151], zinc was introduced into the alumina support via co-precipitation, which increased the Fischer-Tropsch reaction rate by 14%, despite similar support pore structures and surface areas. This was attributed to zinc improving the reduction of CoO to Co^0 (also noted in this study - see Figure C-12, Appendix C) and improving dispersion.

Another possibility is that the increase in turnover frequency seen when changing the support to $ZnAl_2O_4$ is a function of the crystallite size distribution. The Pt-Co/Al_2O_3 catalyst used in this study has a mean crystallite size of Co^0 of 6 nm, which, based on a lognormal distribution of crystallites, suggests that a portion of Co^0 crystallites are < 6 nm, and thus susceptible to particle size effects as described by Bezemer et al. [82]. The mean crystallite size for cobalt in Pt-Co/$ZnAl_2O_4$ is larger, thus less likely to be affected by this phenomenon.

8.3.3.2. Instantaneous deactivation

Figure 8-3 shows the effect of conversion on the rate of change of activity with time ($\frac{da}{dt}$) for Pt-Co/Al_2O_3 and Pt-Co/$ZnAl_2O_4$. The rate of instantaneous deactivation ($-\frac{da}{dt}$) of Pt-Co/Al_2O_3 increased with increasing conversion (between $0.6 \cdot 10^{-3}$ $hr^{-1}$and $1.8 \cdot 10^{-3}$ hr^{-1}), with a very strong increase at very high conversion (X_{CO} > 94%) to $5.4 \cdot 10^{-3}$ hr^{-1}. Pt-Co/$ZnAl_2O_4$, on the other hand, maintained a constant rate of instantaneous deactivation between $0.08 \cdot 10^{-3}$ hr^{-1} and $0.5 \cdot 10^{-3}$ hr^{-1} with the highest rate of instantaneous deactivation equal to the baseline condition for Pt-Co/Al_2O_3.

The lack of a strong increase in instantaneous deactivation at very high conversion is likely due to the larger crystallite size of Co_3O_4, possibly due to weaker metal-support interactions. In Chapter 7, it was shown that for a Co^0 crystallite size distribution mean above 8 nm, the deactivation factor at very high conversions is minimal due to lower surface energy contributions inhibiting oxidation.

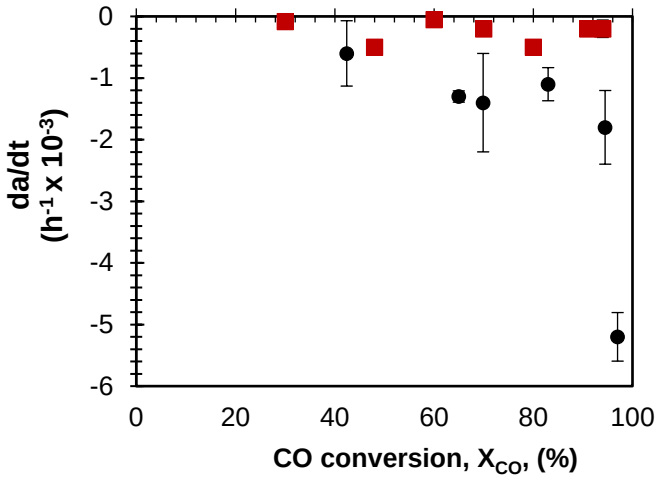

Figure 8-3: Rate of change of activity with time as a function of conversion for ● Pt-Co/Al_2O_3 and ■ Pt-Co/$ZnAl_2O_4$.

8.3.3.3. Irreversible deactivation

Irreversible deactivation was assessed at baseline conditions before and after reaching a specific conversion level. Figure 8-2 (a) and (b) show the change in conversion for both catalysts as a function of time-on-stream. For Pt-Co/Al_2O_3, over a 500- h period, the CO conversion at baseline conditions decreased from X_{CO} = 42% to 16%, a total loss of conversion of 26%. For Pt-Co/$ZnAl_2O_4$, over a 670-h period, the conversion decreased from X_{CO} = 36% to 32%, a total loss of only 4%. Half of the total deactivation for the latter case occurred at X_{CO} > 90% .

Figure 8-4 shows the rate of CO consumption at each conversion level and at baseline conditions for (a) Pt-Co/Al_2O_3 and (b) Pt-Co/$ZnAl_2O_4$. The change in rate between higher conversion conditions and the baseline is a relative indication of the irreversible deactivation, albeit not shown as an activity as there is currently no accurate model with which to predict the rate of the novel catalyst Pt-Co/$ZnAl_2O_4$ at various conversions.

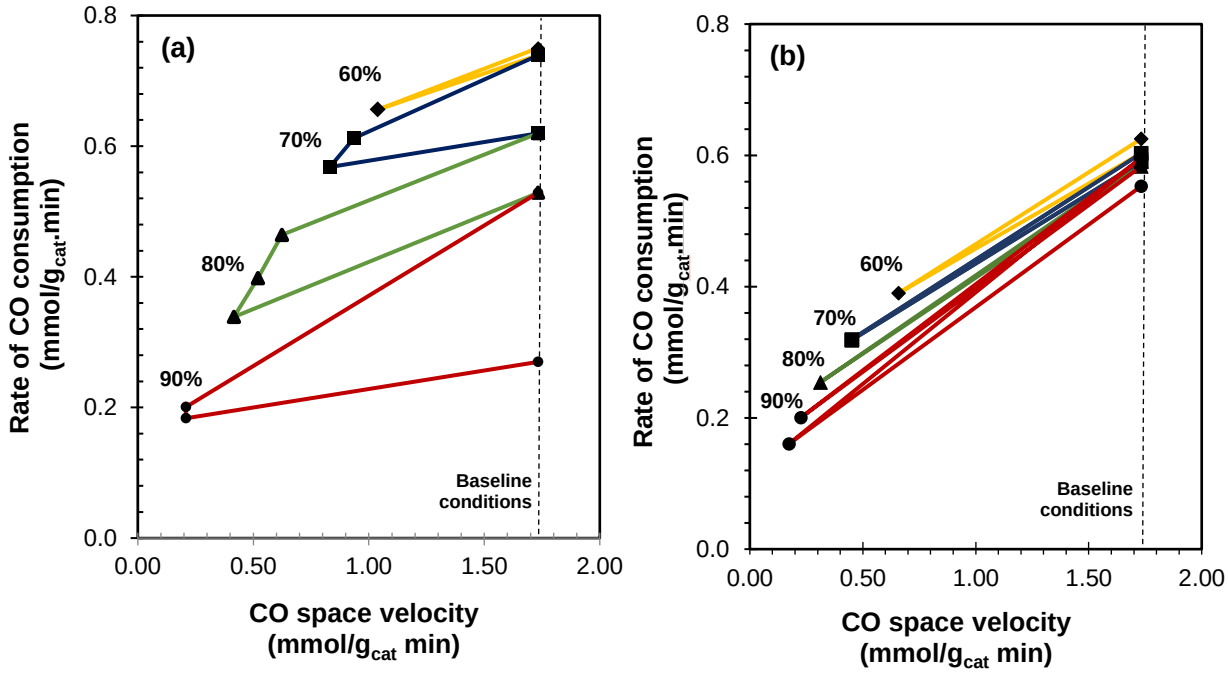

Figure 8-4: Irreversible change in the rate of CO consumption exposing the catalysts (a) Pt-Co/Al_2O_3 and (b) Pt-Co/$ZnAl_2O_4$, to a conversion level of X_{CO} = ♦ 60%, ■ 70%, ▲ 80% and ● 90% in a slurry reactor (N_2:H_2:CO = 3:2:1) at 220°C, 20 bar.

For Pt-Co/Al_2O_3 (Figure 8-4 (a)), deactivation from X_{CO} = 60% was minimal whilst on return to baseline conditions from X_{CO} = 70%, X_{CO} = 80% and X_{CO} = 90% the rate of CO consumption decreased by 0.12, 0.09 and 0.26 mmol /min/g respectively. A negative change in the total rate of CO consumption of 0.47 mmol /min/g was exhibited throughout this run. The enhanced loss of rate at X_{CO} = 70% as opposed to X_{CO} = 80% is attributed to the proclivity of the smallest cobalt nano-crystallites to form cobalt aluminate at these conditions (as discussed in Chapter 6).

The Pt-Co/$ZnAl_2O_4$ sample (Figure 8-4 (b)), on the other hand, exhibited significantly less irreversible deactivation. On returning to baseline conditions from X_{CO} = 60%, X_{CO} = 70%, X_{CO} = 80% and X_{CO} = 90%, the negative change in the rate of CO consumption was only 0.02, 0.01, 0.01 and < 0.005 mmol /min/g respectively. The highest level of irreversible deactivation was exhibited on return from X_{CO} = 94% with a negative change in rate of 0.04 is mmol /min/g. A total loss of rate of CO consumption of 0.08 mmol /min/g was exhibited throughout the 670- h run.

As the formation of cobalt aluminate is not feasible with a zinc aluminate support, and the fact that carbon deposition is unlikely at the conditions for high conversion (see Chapter 6, Section 6.3.3.3), it

is speculated that the irreversible deactivation is entirely due to sintering which may be enhanced above X_{CO} = 90%.

8.3.3.4. Selectivity

Chapters 4 and 5 showed that conversion has a significant negative effect on the selectivity (CO_2, CH_4 and C_{5+}) of Pt-Co/Al_2O_3. Whilst Mn can, in the right concentration, be used to alleviate this problem (see Chapter 5), it is critical to ensure that changing the support from γ-Al_2O_3 to $ZnAl_2O_4$ does not negatively affect selectivities across the conversion range.

Figure 8-5 shows the effect of conversion on the (a) CO_2, (b) CH_4 and (c) C_{5+} selectivity for Pt-Co/Al_2O_3 and Pt-Co/$ZnAl_2O_4$. Increasing conversion from X_{CO} = 30% to 92% results in a strong increase in the selectivity of CO_2 and CH_4 for both catalysts, for reasons discussed in Chapter 4.

Zinc aluminate does not seem to significantly affect the selectivity across the range, albeit minor deviations exist between the two catalysts. For instance, at very high conversion (X_{CO} > 90%) there is a slightly lower level of CO_2 selectivity in the case of the zinc aluminate supported catalyst. This may be due to the difference in reducibility or metallic surface area, as CO_2 production appears to be linked to the amount of metallic Co^0 in the catalyst, as shown in Chapter 4.

It is also, however, possible that this result may be due to interference in the TCD spectra at low space velocities or an interference with the valve switching peak which may have created a greater level of error on the CO_2 selectivity. This is suspected specifically as the CH_4 selectivity, which is a function of water gas shift activity due to shifts in the H_2/CO ratio (see Chapter 4), follows the exact trend as Pt-Co/Al_2O_3. Additionally, there is a slight deviation in the CH_4 selectivity that occurs at ca. X_{CO} = 30% where the methane selectivity for Pt-Co/$ZnAl_2O_4$ is slightly lower than for Pt-Co/Al_2O_3. Interestingly, these points reflect the CH_4 selectivity on return to baseline conditions.

The C_{5+} selectivity (Figure 8-5 (c)) is similar for both catalysts, with a decrease between X_{CO} = 40% and X_{CO} = 80% from ca. 90 C-% and 80 C-%. Past this conversion, there is an equally strong decrease for both catalysts resulting in a C_{5+} selectivity of ca. 70 C-% at X_{CO} = 90%.

Despite the minor deviations, these results indicate that altering the support material from γ-Al_2O_3 to $ZnAl_2O_4$ does not significantly affect the selectivity of the catalyst, and thus is suitable for operation at high conversion.

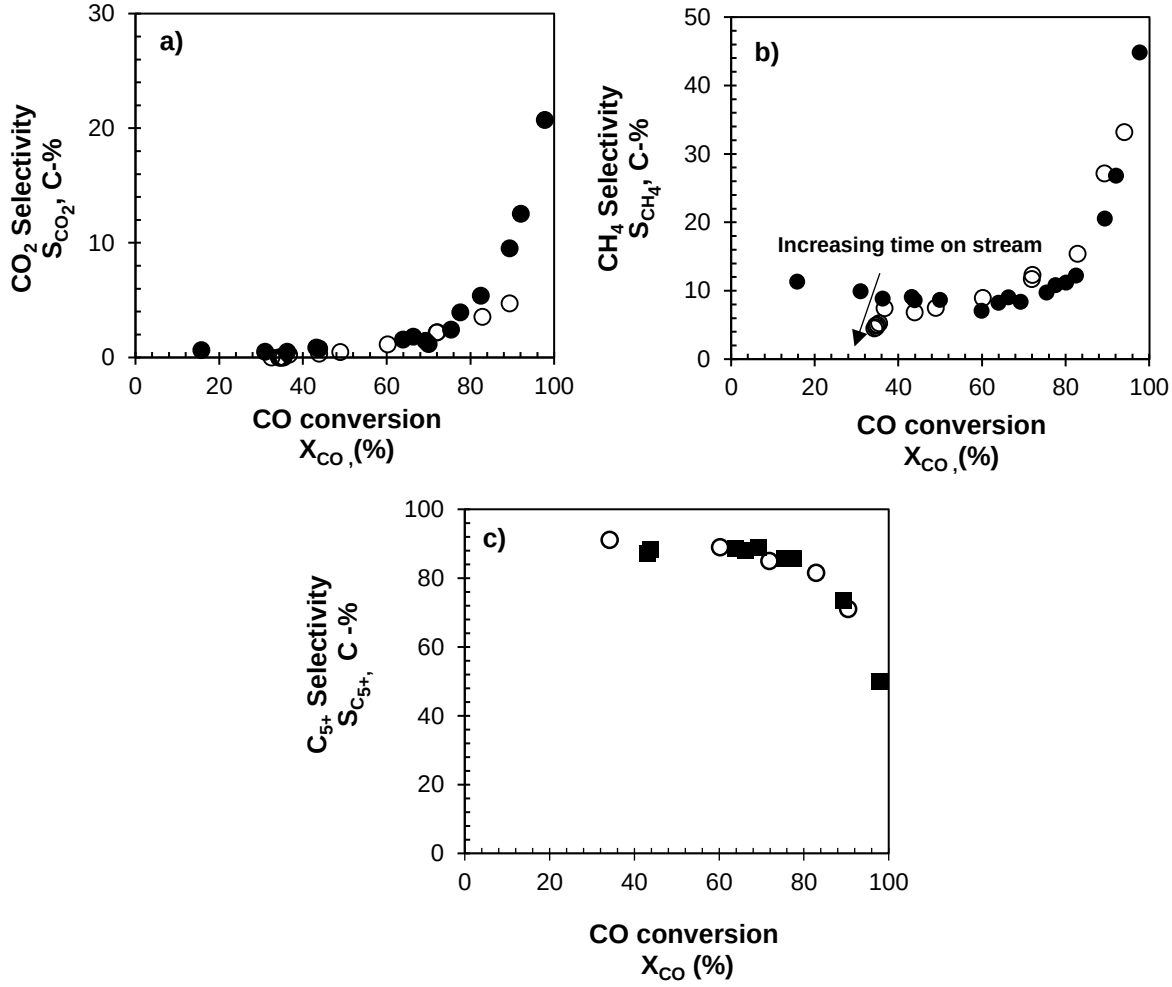

Figure 8-5: Effect of conversion on the selectivity of (a) CO_2, (b) CH_4, (b) C_{5+} for Pt-Co/Al_2O_3 (closed symbols) and Pt-Co/$ZnAl_2O_4$ (open symbols).

8.4. Conclusion

The effect of changing the support from γ-Al_2O_3 to $ZnAl_2O_4$ on the stability of a platinum-promoted cobalt catalyst is discussed. Chapter 6 showed that the cause of significant deactivation at high conversion conditions is sintering, the formation of cobalt aluminate and the formation of Co(II)O. Replacing γ-Al_2O_3 with $ZnAl_2O_4$ as a support material for cobalt was hypothesised to reduce the level of deactivation due to weaker metal-support interactions which should promote larger crystallite sizes as well as the thermodynamic limitation for Co^0 or CoO to react with $ZnAl_2O_4$ to form $CoAl_2O_4$.

Replacing Al_2O_4 with $ZnAl_2O_4$ for a platinum-supported cobalt catalyst was found to increase the crystallite size of Co_3O_4 from 11 nm to 15 nm. The H_2 uptake via chemisorption was found to be

significantly lower for Pt-Co/$ZnAl_2O_4$. However, the initial turnover frequency for Pt-Co/$ZnAl_2O_4$ (0.05 s^{-1}) was found to be significantly larger than for Pt-Co/Al_2O_3 (0.03 s^{-1}).

Instantaneous and irreversible deactivation across the entire range of conversions (X_{CO} = 34% to 94%) was inhibited. A total change of rate of 0.08 mmol /min/g (in relation to 0.48 mmol /min/g for Pt-Co/Al_2O_3) was exhibited for Pt-Co/$ZnAl_2O_4$ of which 50% was noted on return from very high conversion (X_{CO} = 94%), where the extreme partial pressures of H_2O may promote sintering. The zinc aluminate supported catalyst was also found to have similar selectivity towards CO_2, CH_4 and C_{5+}.

This study indicates that with a relatively inexpensive zinc aluminate support it is possible to avoid irreversible deactivation and realistically shift the conversion to X_{CO} = 90%, thus making operation of a once-through Fischer-Tropsch waste-to-liquid plant potentially viable.

Chapter 9

Detailed process design of a once-through Fischer-Tropsch waste-to-liquid plant for remote diesel and electricity production

9.1. Context and scope

Small-scale, decentralized waste to fuel production is an appealing concept to provide a local supply of fuels and electricity in Sub-Saharan Africa. The technology steps involved in this process are well known and consist of synthesis gas generation and cleaning, Fischer-Tropsch synthesis, separation and refining. However, current implementation of these process steps in waste or biomass-based facilities have all had access to utilities and technical services (Table 1-1). Design of a smaller scale facility in a remote setting, requires a different approach.

Section 1.6 discussed the design philosophy for a remote plant located in Sub-Saharan Africa, of which the main design changes from a typical Fischer-Tropsch BTL and WTL plant are as follows:

- Biogas reforming, rather than typical gasification, will be used to produce syngas.
- The design will operate in a once-through configuration, without recycle.
- The design must be entirely off-grid and provide its own electricity. Thus, any tail gas and excess reactants or unwanted products from the Fischer-Tropsch reactor will be used to generate electricity in a gas fired power plant.

Essential to these changes is the operation at a higher-than-usual Fischer-Tropsch conversion and the choice of catalyst. Throughout Chapters 4-8, catalyst improvements have been made to ensure that conversions up to ca. X_{CO} = 90% (as opposed to a maximum of X_{CO} = 70%) are plausible in terms of activity, selectivity and stability.

Chapter 9 will discuss key design decisions for the development of a small-scale decentralized waste-to-liquid plant with a particular focus on how the design may change based on the chosen Fischer-Tropsch conversion. The design will use data from the Fischer-Tropsch catalysts discussed in Chapters 4-8 with selectivities obtained from Pt-Co/Al_2O_3 and Mn-Pt-Co/Al_2O_3 (Mn:Co = 0.14).

In addition to the design philosophy, the following scope is considered:

- Anerobic digestion and gas cleanup are not discussed as the output of these processes using various feedstock are well documented [18,61,62]. The feed to the plant will consist of clean biogas with a composition of 75% CH_4 and 25% CO_2. This relatively optimistic composition will be used for the base case; lower methane concentrations would result in more diluent gas and lower overall carbon yields.
- Due to the size and Sub-Saharan African context, diesel and electricity are the only products desired. Diesel, in particular, accounts for the majority of Sub-Saharan Africa's transportation fuel consumption [5,6] as well as up to 10% of its electricity generation capacity [184].

9.2. Design overview

Taking the design philosophy discussed in Section 1.6 into account, the overall block flow diagram for the biogas-to-diesel plant may be illustrated as per Figure 9-1. The design consists of 4 distinct segments – syngas generation, syngas conversion, fuel separation and refining and power generation.

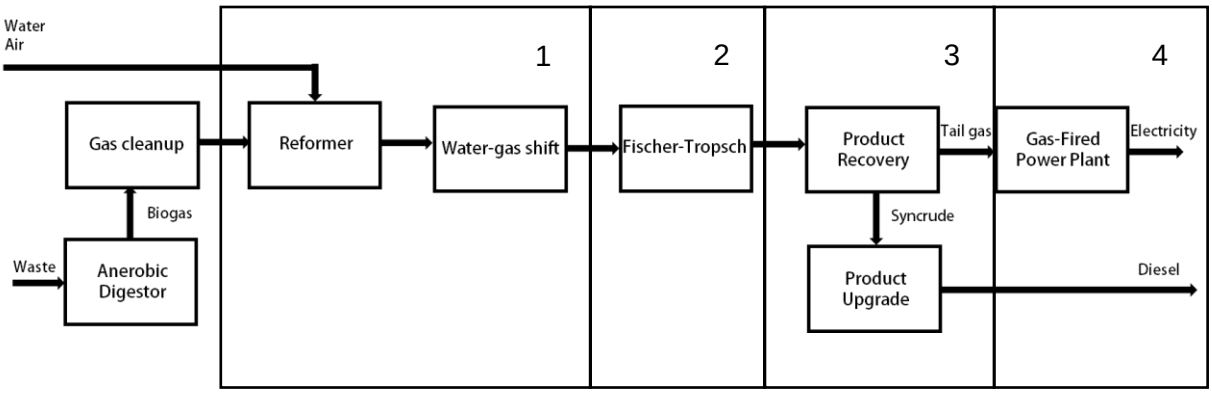

Figure 9-1: Schematic of small-scale biogas-to-diesel Fischer-Tropsch design including design segmentation

Clean (sweet) biogas is reformed to syngas and the ratio of H_2/CO adjusted by a water-gas shift unit. The syngas is then reacted in the Fischer-Tropsch reactor, at a conversion to be evaluated in Chapter 10. The Fischer-Tropsch products are subsequently separated and upgraded to produce diesel, light gasses and wax. The light gases (tail gas) are combined with air, combusted and used to generate electricity via a gas fed power plant. Wax is hydrocracked to improve diesel yield.

9.3. Syngas generation and cleaning

9.3.1. Type of biogas reforming

There are multiple routes by which methane can be converted to syngas [57,185–187], some of which are applicable to biogas conversion (see Table 9-1).

Table 9-1 : Types of reforming, the associated chemical equations and reaction enthalpies [57,187].

Dry Reforming	$CH_4 + CO_2 \leftrightarrow 2CO + 2H_2$	ΔH^0 = 247 kJ/mol
	$CO_2 + H_2 \leftrightarrow CO + H_2O$	ΔH^0 = 41 kJ/mol
Steam Reforming	$CH_4 + H_2O \leftrightarrow CO + 3H_2$	ΔH^0 = 206 kJ/mol
Bi-Reforming	$CH_4 + H_2O \leftrightarrow CO + 3H_2$	ΔH^0 = 220 kJ/mol
	$3CH_4 + CO_2 + 2H_2O \leftrightarrow 4CO + 8H_2$	
Oxy-CO_2 Reforming	$3CH_4 + CO_2 + O_2 \leftrightarrow 4CO + 6H_2$	ΔH^0 = 58 kJ/mol
Tri-Reforming	$CH_4 + CO_2 \leftrightarrow 2CO + 2H_2$	ΔH^0 = 247 kJ/mol
	$CH_4 + H_2O \leftrightarrow CO + 3H_2$	ΔH^0 = 206 kJ/mol
	$CH_4 + ½\ O_2 \leftrightarrow CO + 2H_2$	ΔH^0 = - 36 kJ/mol
	$CO + H_2O \leftrightarrow CO_2 + H_2$	ΔH^0 = - 41 kJ/mol

Dry reforming involves the conversion of CH_4 and CO_2 to CO and H_2. The reverse water-gas shift reaction also occurs in this process, resulting in high conversions of CO_2 [57]. Due to the process being highly endothermic, a large external energy input is required.

Steam reforming is commonly used in industry to convert CH_4 to syngas or hydrogen in the presence of water. However, the reaction does not account for conversion of CO_2. Bi-reforming, on the other hand, involves the conversion of CO_2, CH_4 and H_2O to syngas or hydrogen. This, too, requires external heating to satisfy its very large endothermic requirements [186].

Oxy-CO_2 reforming is autothermic [186], making it an attractive, low energy-intensive process. However, safety concerns regarding the process limit its industrial prevalence [188]. Tri-reforming, by contrast, involves the conversion of biogas, water and oxygen into syngas [57] with fewer safety issues. The presence of water allows for greater control of the H_2/CO ratio based on the feed composition whilst the oxygen in the system reduces the energy duty, allowing for autothermal operation if high enough oxygen flow rates are used [57,186,187].

The choice of reformer is by no means trivial and typically depends on the product requirements, location and scale. Table 9-2 shows a comparison of the main viable routes for converting biogas to syngas (dry reforming, bi-reforming and tri-reforming). Of particular importance to the choice of

reformer is the method of heat addition, syngas product specifications, probability of coking and carbon utilization.

Table 9-2: Comparison of types of biogas reforming [189].

	Dry reforming	*Steam reforming*	*Tri-Reforming*
Heat addition	External	External	Autothermal
Typical H_2/CO	1	3-4	2
Typical catalyst	Ni	Ni	Ni
Coking probability	High	Low	Low
CH_4 utilisation	High	High	High
CO_2 utilisation	High	Medium	Low

9.3.1.1. Autothermal vs externally heated biogas reforming

Reforming is an endothermic process; thus, heat needs to be provided. This can be achieved in two ways. Either, heat can be generated internally by the addition of oxygen (tri-reforming) or heat can be added externally (dry reforming and bi-reforming) via an external hot furnace with the combustion of raw biogas [53].

This choice is analogous to that between autothermal and allothermal gasification for which there are implemented WTL and BTL examples of both (Table 1-1). For instance, CHOREN, Enerkem and Total operate their gasifier autothermally, whilst Fulcrum and Red Rock biofuels opt for allothermal operation – typically due to the benefit of the removal of the air separation unit.

Autothermal operation allows for a simpler reactor design with no heat transfer area, thus decreasing capital costs [190]. No exterior furnace (high capital cost) is required for autothermal operation. For a small-scale, remote location low complexity is a major benefit. In addition, if a catalyst can be used that can operate at high conversion, the air separation unit can be removed irrespective of choice of reformer.

However, autothermal operation without air separation, necessitates large inert flows throughout the system. This can increase the size of not only the reformer but also equipment downstream, as well as decreasing reaction rates for the Fischer-Tropsch reactor by decreasing reactant partial pressures (discussed in detail in Section 2.3, Chapter 2). Excess nitrogen in the tail gas would also decrease the heating value of the gas combusted for the power plant. According to equilibrium calculations for a feed composition (mol%) 50% CH_4, 35% CO_2, 3% O_2, 13% N_2, a tri-reformer operating at 750°C is able to decrease its energy requirements from > 25 kW/ kmol to autothermal conditions with a O_2/C ratio just under 0.3 (see Figure 9-2). This is equivalent to roughly 40 vol. % nitrogen in the outgoing stream. This additional inert gas could, however, allow for heat control in the Fischer-Tropsch reaction, which is highly exothermic.

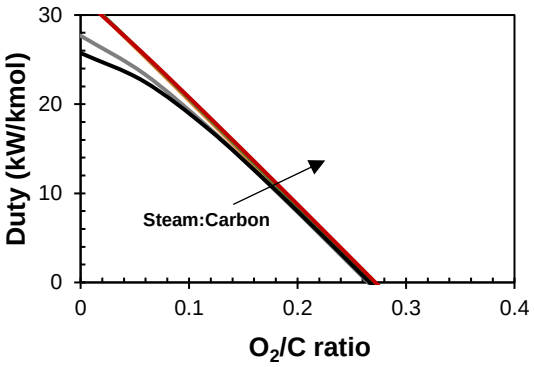

Figure 9-2: Effect of O_2/C ratio on the duty of the tri-reformer per kmol biogas with the following composition (mol%) 50% CH_4, 35% CO_2, 3% O_2, 13% N_2.

9.3.1.2. H_2/CO ratio

Low temperature cobalt-catalysed Fischer-Tropsch synthesis requires a syngas product with a H_2/CO ratio of 2. Dry-reforming can typically only reach H_2/CO ratios between 0.5 – 1.5 [191,192] due to the lack of steam addition, which controls hydrogen production. This requires extensive water-gas shift activity to further correct for the H_2/CO ratio. Bi-reforming produces syngas in high H_2/CO ratios between 3 and 4 making it ideal for hydrogen production, but less so for syngas production. This may be tuned, albeit to the detriment of biogas conversions. Tri-reforming typically produces syngas in a H_2/CO ratio of 2 - ideal for Fischer-Tropsch synthesis.

9.3.1.3. Coking

Dry reforming results in high levels of carbon deposition (coking) [61]. This means that the catalyst needs to be regenerated online in order to avoid constant replacement and downtime. Bi- and tri-reforming use steam as a feedstock, which results in far less coking, and thus no need for an extra regeneration unit.

9.3.1.4. Carbon utilisation

Dry reforming is by far the most ideal process from a carbon utilization perspective, with high conversions of both CH_4 and CO_2 into CO and H_2. The reverse water-gas shift reaction occurs within dry-reforming and as no steam is fed into the process, CO_2 utilization can be increased substantially by kinetic and equilibrium enhancement. Both bi- and tri- reforming have lower CO_2 conversions due to the presence of steam. Unfortunately, tri-reforming typically results in very low and sometimes negative CO_2 conversions (net CO_2 formation) due to the presence of both steam and oxygen.

9.3.1.5. Reformer choice

For the purpose of remote Fischer-Tropsch applications, tri-reforming appears to be the most suitable choice. This is due to the increased simplicity in the design of the reformer, the low coking risk and a product with an ideal H_2/CO ratio for the Fischer-Tropsch synthesis.

9.3.2. Removal of water-gas shift unit

Tri-reforming has the benefit of tuning the H_2/CO ratio with relative ease with low steam/carbon (S/C) ratios, in relation to bi-reforming. At a temperature of ca. 750°C a S/C ratio above 0.3 could ensure a H_2/CO ratio of 2, adequate for the Fischer-Tropsch synthesis [56]. Depending on the hydrogen requirements of the hydrocracker downstream, slightly more steam may need to be added in addition to this.

The effect of altering the S/C ratio on the H_2/CO ratio is so significant that, if properly tuned, can leave the water-gas shift reactor downstream redundant. The inclusion of a water-gas shift (WGS) unit, however, improves the robustness of the system, allowing for a greater controllability by either the WGS temperature or additional steam addition. This may be essential if the composition of the waste stream or the requirements in the hydrocracker (hydrogen: hydrocarbon feed ratio) change over time. Depending on the context and location, this may be invaluable for the insignificant cost of the unit itself.

9.3.3. Compressor configuration

The Fischer-Tropsch reactor is required to operate at pressure – typically 20 bar – to decrease the size of the reactor and to increase the rate of reaction. This means the compression of biogas is required, which has major capital and operating cost implications for the plant.

At a compression ratio of 2.7 a multistage compressor system with 3 compressors is required – to 2.7 bar (C_1), 7.3 bar (C_2) and 20 bar (C_3). The location of these compressors will affect the compression duty, cost and the operation of the reformer. Figure 9-3 shows the effect of the location of each compressor (before or after reforming) on the duty and relative capital cost of the compression system. As tri-reforming results in an increase in the volume of gas (by ca. 20%) as well as a vaporous water phase (water could be pumped, rather than compressed, at ambient conditions before the reformer), compressing after the reforming step results in an increase in compressor duty and capital cost.

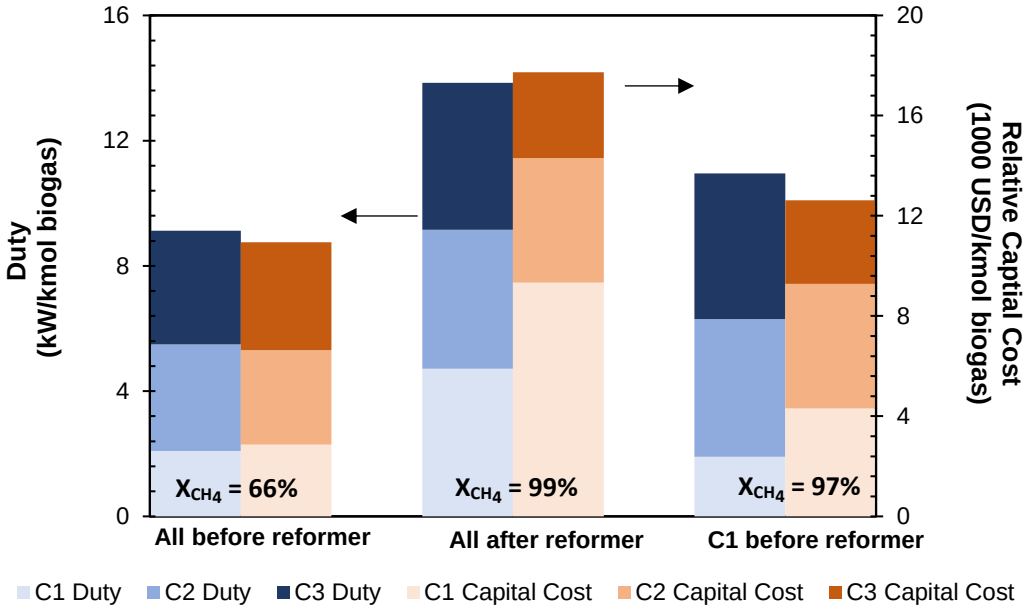

Figure 9-3: The effect of compressor location on the duty and relative capital cost of compression calculated based on Aspen model of syngas generation section.

However, compressing before the reformer has its own challenges. An increase in pressure negatively affects conversion of CH_4 in the tri-reformer. Increasing pressure from 1 bar to 20 bar results in a CH_4 conversion drop from 99% to 66% for a tri-reformer operating autothermally at 750˚C. This loss of carbon yield may be counteracted by splitting compression across the plant, i.e. by compressing to 2.7 bar before the reformer, resulting in a methane conversion of 97%, and further compressing at a later point. This minimizes the capital cost without a significant negative effect on the equilibrium conversion in the tri-reformer.

9.3.4. Carbon dioxide removal

Boerrigter et al. [37] estimated that, for a biomass-to-liquid plant, the cost of CO_2 removal is ca. 22% of the total equipment cost of the plant. If recycled, CO_2 builds up in the process making its removal a necessity. However, this design operates without a recycle. Under once-through operation CO_2 acts as an inert [176] throughout the process and takes up only about 8% of the stream. Whilst this does increase the Fischer-Tropsch diluent factor, this is mild in comparison to the diluent effect of N_2. The only point at which CO_2 may convert is in the hydrocracker downstream (to CH_4) which may necessitate a once-through hydrocracker.

9.3.5. Hydrogen separation technology

Pressurized hydrogen is required as a feed for downstream hydrocracking. To achieve this, hydrogen needs to be separated prior to entering the Fischer-Tropsch reactor. For this application, pressure swing adsorption, cryogenic separation or membrane technology may be used, each with individual technological and economic advantages. Alqaheem et al. [193] presented a comparison between these technological options, as shown in Table 9-3.

Cryogenic distillation is a low temperature separation method that uses the different boiling points to separate out a feed. Whilst this method is appropriate in terms of the feed compositions of H_2 and purity, the reliability of cryogenic distillation is low and it requires significant maintenance and supervision [193]. Cryogenic distillation is also only economically viable at a very large scale, above 10,000 Nm^3/h

Table 9-3: Comparison between hydrogen separation technologies adapted from [193,194].

	Cryogenic separation	*Pressure swing adsorption*	*Membrane*
Feed composition (H_2 mol%)	30—75	75-90	30-90
Product purity (H_2 mol %)	90-98	>99	90-98
Product volume (Nm^3/hr)	>10,000	1000-10,000	<30,000
Recompression required	No	No	Yes
Reliability	Poor	95%	100%

Pressure swing adsorption (PSA) technology is the most extensively used process to separate hydrogen in industry and is attractive for processes that require a very pure product [193]. However, PSA technology is reportedly difficult to scale down economically [195] and requires a hydrogen feed composition significantly higher (75 mol. %) than in the air-fed Fischer-Tropsch process (33 mol.% H_2, 16 mol.% CO, 40 mol.% N_2, 8 mol.% CO_2).

Membrane technology, on the other hand, is typically regarded as advantageous for smaller scale applications. This is due to the lack of moving parts and greater level of stability and control [193] due to its continuous (rather than cyclical) operation. Membranes require minimal supervision [193], have long operating lives and are reliable [194]. However, as membranes are driven by pressure, any hydrogen produced would need to be recompressed.

Due to the enhanced reliability, low supervision requirements and scalability, a membrane has been chosen as the hydrogen separation method for this application. The choice of membrane is typically based on the performance (selectivity and permeability) as well as cost and operating conditions. For this process a membrane with moderate selectivity and permeability is favoured. Very pure hydrogen is not required, and the amount of hydrogen required in the hydrocracker is typically far lower than the space velocity to the Fischer-Tropsch reactor. Most importantly, the cost should be low to moderate.

Table 9-4 shows a comparison of the different membrane technologies applicable for these applications, along with their characteristics.

Table 9-4: Comparison of different membrane technology

	Metallic	*Polymeric*	*Micro/nano porous*	*Ref*
Composition	Palladium, palladium alloys	Polyimide, cellulose acetate	Silica, zeolites, metal organic framework, carbon	[195,196]
Driving force	Partial pressure	Partial pressure	Partial pressure	[196]
Rel. permeability	Low	Low-moderate	Moderate-high	[196]
Rel. selectivity	Very high	Moderate	Low-moderate	[196]
Relative cost	Moderate-high	Low	Low - moderate	[195–197]
T range	300-600	<100	200-900	[197]
Mechanical stability	Phase transitions	Swelling and compaction	Brittle	[197]

Membranes are typically separated into three categories – metallic, polymeric and micro/nano porous. Metallic membranes have a very high selectivity towards hydrogen, and can be used at high temperatures however are high cost and have low permeability [196]. These membranes are typically used for applications where small flow rates of high purity hydrogen are required.

Micro/nano porous membranes consist of a very wide range of oxide, zeolite, metal organic framework and carbon membranes. These membranes can typically operate under a very wide range of temperatures, and with good stability in hydrothermal conditions (so could be placed after the Fischer-Tropsch reactor) [196]. They have moderate costs, and typically acceptable permeabilities. Many of these types of membranes have ideal stability for hydrogen separation from syngas. However, the commercialization of these types of membranes is typically slow, and those that are well developed (silica) have low selectivities towards hydrogen.

In contrast, polymeric membranes are low cost with moderate permeability [196]. Advantages of the polymeric type include a good scalability and the ability to cope with variable pressure drops [197]. These membranes are well investigated and commercialized, but also have a lower selectivity and are only useful at low temperatures. Polymeric membranes meet the requirements for this process, however, there are a few disadvantages. The low temperature requirement means that the polymeric membrane may require cooling post compression, which implies reheating before the Fischer-Tropsch synthesis. In addition, glassy polymer membranes cannot be placed after the Fischer-Tropsch reactor as hydrocarbons can cause swelling and damage to glassy polymers [198].

9.3.6. Proposed syngas generation technology

The proposed design based on these key design decisions can be seen in Figure 9-4. Sweet biogas and air are combined and pressurized to 2.7 bar. Water is pumped to the same pressure and combined to feed the pre-heater to the reformer. The feed is heated to 220°C in a heat exchanger to decrease the amount of air required for heating purposes (higher temperatures may require a furnace which increases cost significantly). The feed is fed into the tri-reformer that operates at X_{CH_4} = 97%. The product from the reformer is cooled and combined with extra water (when applicable) and fed to the water-gas shift reactor - used to correct the H_2/CO ratio as desired. The WGS product is cooled and fed into a compressor system with inter-stage water knock-out. Hydrogen is subsequently removed via polymeric membrane from the pressurized Fischer-Tropsch feed for use in the hydrocracker.

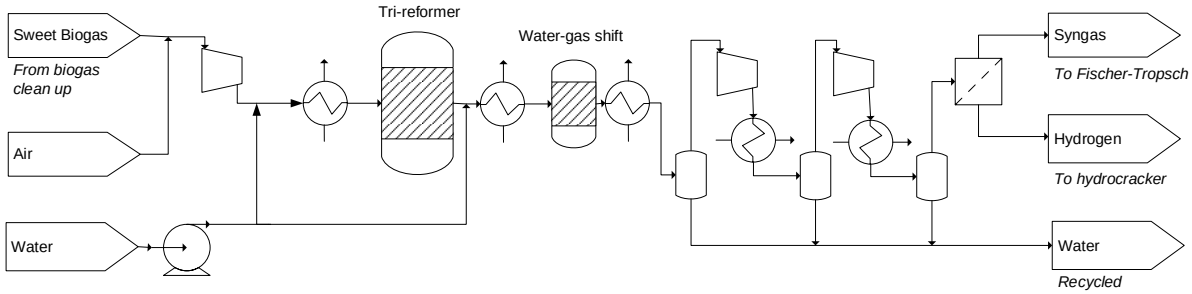

Figure 9-4: Schematic of proposed synthesis gas generation design

9.4. Fischer-Tropsch reactor

Based on the selectivity models and chain growth probabilities discussed for Pt-Co/Al_2O_3 and Mn-Pt-Co/Al_2O_3 (Mn:Co = 0.14) in a slurry bed reactor at various conversions (Chapter 4 and 5), it is possible to extrapolate a Fischer-Tropsch product carbon distribution (see Appendix I for details). The carbon distributions for both catalysts between X_{CO} =60 and X_{CO} = 90% are shown in Figure 9-5.

At a conversion of X_{CO} = 60%, the carbon distribution is wide for both catalysts and evenly distributed over the C_5-C_{15} range, with a significant concentration of waxes (C_{22+}). Increasing the conversion to X_{CO} = 70% and X_{CO} = 80%, decreases the width of the carbon range, as well as shifting the distribution towards lighter hydrocarbons, due to lower chain growth probabilities. This shift is even more prominent at 90% conversion, where almost no C_{30+} hydrocarbons appear to be formed. Changing the catalyst from Pt-Co/Al_2O_3 to Mn-Pt-Co/Al_2O_3 appears to have little effect at lower conversions, however, it significantly increases the number of hydrocarbons within the naphtha and diesel range for X_{CO} > 70%.

The carbon distribution shown as a function of conversion allows for greater understanding of the refining and upgrading requirements for the small-scale model at various conversions. As higher conversions result in less wax production (C_{22+}), one may hypothesise that a hydrocracker may not be necessary to enhance diesel yields at these conditions, whilst hydrocracking may be critical for systems operating at low conversion.

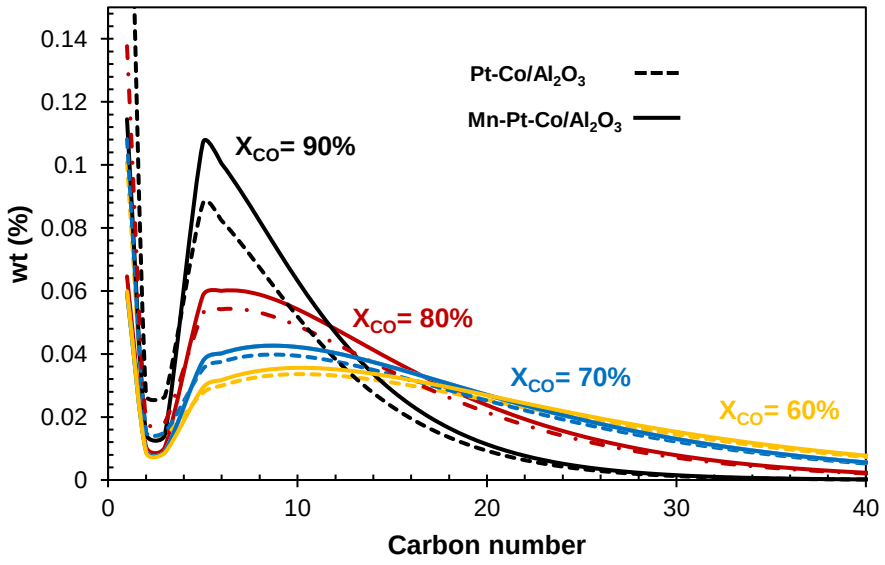

Figure 9-5: Carbon number distribution for Pt-Co/Al_2O_3 and Mn-Pt-Co/Al_2O_3 in a slurry bed reactor at various conversions based on data from Chapters 4 and 5.

9.5. Refinery design

The mixture of hydrocarbons produced in the Fischer-Tropsch synthesis is typically termed 'syncrude' or synthetic crude oil (depicted by the carbon distribution in Figure 9-5). Like natural crude oil, syncrude is a mixture of hydrocarbons that cannot be used directly as a transportation fuel, but rather needs to be refined to final products – diesel, naphtha etc. To further complicate matters, the products of the Fischer-Tropsch synthesis consist of multiple phases – gaseous, organic liquid, aqueous liquid and solid which need to be separated out before refining can occur [54,199,200].

9.5.1. Refine or upgrade?

The debate regarding whether Fischer-Tropsch syncrude should be refined to final product onsite, or simply upgraded and sold to central refineries is ongoing. There are multiple options for syncrude post-processing, and the choice often depends on the size, economics and market location of the individual plant.

Calemma et al. [200] describes the four business cases for syncrude post-processing as follows.

- Syncrude product. This entails selling syncrude as a primary product, analogous to crude oil production.
- Upgrading. The purpose of upgrading is to produce a higher quality fuel that can be transported and sold to refineries.
- Partial refining. Specific parts of syncrude are refined to fuels, with other parts sent to central refineries as blending material.
- Refining. Total refining of syncrude to final products.

In order to sell the syncrude product, one must have a centralized refinery that is willing to purchase and refine to final products. For the purposes of decentralized fuel production in Sub-Saharan Africa this may be impractical as few refineries are located in the region (as discussed in Chapter 1), and there are even fewer that have the technical capabilities to process syncrude (multiple phases and different carbon distribution to crude oil). Moreover, processing in a centralized refinery would require transportation of syncrude, which becomes impractical for low temperature Fischer-Tropsch products which contain waxes that are solid at ambient temperature.

The latter problem may be solved by upgrading the syncrude to a liquid product [54]. Wax hydrocracking is the most common technique used to convert solid heavy hydrocarbons such as wax to easily transported liquid hydrocarbons. Hydrocracking is a combination of catalytic cracking and hydrogenation with a reaction pathway including multiple chemical steps namely dehydrogenation, protonation, isomerisation, cracking, deprotonation and hydrogenation. Mild hydrocracking is typically used in the Fischer-Tropsch process to achieve higher liquid fuel yields [201]. Unfortunately, even with a hydrocracking step, transportation of the upgraded fuel to a central facility is challenging. Due to the lack of pipelines in the region, the upgraded syncrude needs to be transported with oil trucks which may increase the logistics and operating cost of the process substantially.

This leaves the option of partial or complete refining. Complete refining would entail trying to separate out all possible products (distillate, kerosene, naphtha etc.) and process via multiple reactions including oligomerization, hydroisomerisation, aromatisation and hydrotreating to produce multiple drop-in fuels such as diesel, petrol, jet fuel as well as chemicals [200]. This approach is typically not used in modern Fischer-Tropsch plants due to the complexity and cost of each fuel refining step.

Partial refining, however, focuses on refining a subset of wanted products to either blending materials or final products and selling the rest to refineries as upgraded material [200]. Many Fischer-Tropsch

facilities (including larger scale facilities like Oryx in Qatar and Shell SMDS in Bintulu) make use of partial refining on-site.

9.5.2. Industrial partial refining designs

The design of a partial refining step varies based on how many products are desired and the business case. For instance, Shell's SMDS facility in Bintulu, which is designed to produce fuels, blending material and chemicals, splits the Fischer-Tropsch product into two portions which are fed into either a hydrocracker or hydrotreater as shown in Figure 9-6. The hydrocracker (which is used for alkene hydrogenation, hydroisomerisation, hydrodeoxygenation and hydrocracking) produces a mixture that contains unrefined lights, naphtha, kerosene, distillate and waxes (all meant as blending material) which are further separated using a distillation column [54]. The hydrotreater is used for alkene hydrogenation and hydrodeoxygenation and produces a linear n-alkane rich chemical products that can be used as solvents, detergents and fire retardants [199].

Sasol's Oryx Plant in Qatar (Figure 9-7), on the other hand, focuses solely on the production of fuel intermediates as well as LPG [54]. In this case, the syncrude is initially separated and cleaned before the wax and cold condensate are fed into the hydrocracker which operates to hydrotreat, hydroisomerize and hydrocrack the mixture [54]. The hydrocracker product is then separated, to remove and recycle hydrogen, and fed into two separate distillation columns that separate out three main products - LPG, naphtha and distillate.

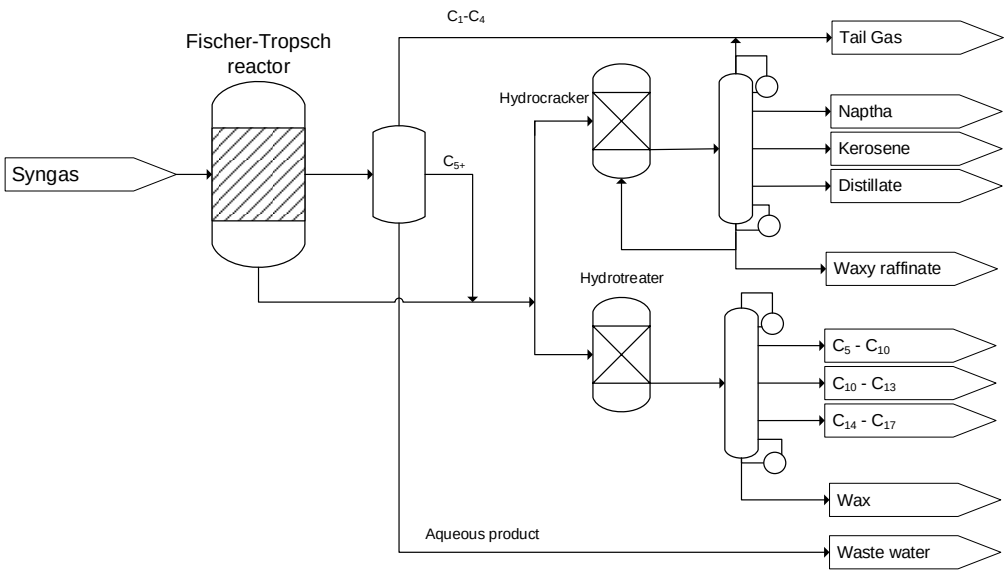

Figure 9-6: Fischer-Tropsch partial refinery at Shell Bintulu SMDS facility, taken from [54].

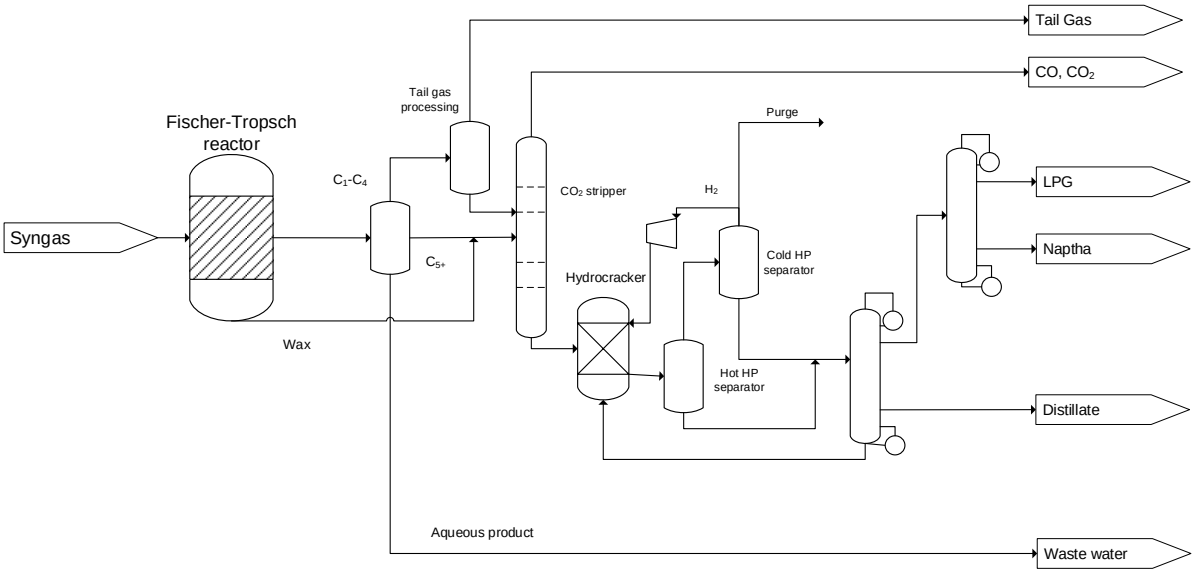

Figure 9-7: Fischer-Tropsch partial refinery at Sasol Oryx facility, Qatar, taken from [54].

9.5.3. Distillate vs diesel

At this point it is important to note the difference between the term distillate (produced by both Shell Bintulu SMDS and Sasol Qatar Oryx facilities) and diesel. Literature commonly, and incorrectly, interchanges these terms which has led to largely misleading perceptions about the ability to produce diesel directly from the Fischer-Tropsch syncrude [199]. Distillate is a mixture of roughly C_{10}-C_{22} straight-chain hydrocarbons, whilst diesel is a distillate that meets region-legislated specifications of cetane number, density, sulphur content, boiling point and distillation range, etc. [54,199,200].

Table 9-5 shows the regional fuel specifications for the United States (ASTM D975:15b), European Union (EN 590:2014 and EN 15940:2016), African Union (AFRI-5 2016) and South Africa (SANS 342:2016). These specifications change with time and are updated regularly. For instance, the Clean Fuels regulations in South Africa led to a decrease in the sulphur content from 500 ppm to 10 ppm. The EU has two diesel specifications – one for crude-oil based fuels (EN 590:2014) and one for XTL (Fischer-Tropsch) derived fuels (EN 15940:2016).

Fischer-Tropsch LTFT distillate has a very low sulphur and aromatic content and a high cetane number in relation to typical crude-oil derived diesel [71], thus, these specifications are easily met by FT derived fuels. The content of impurities such as water may be easily altered by additional separation steps, as may the distillation profile.

Table 9-5: Regional diesel specifications for the US, EU, Africa and South Africa

	Diesel specifications				
	ASTM D975: 15b (US)	**EN 590:2014 (EU)**	**EN 15940:2016 (EU)**	**AFRI-5 2016 (AU)**	**SANS 342:2016 (ZA)**
Diesel density at 15°C	-[a]	820	765-800	820-880	805-850
Sulphur, ppm	<15	<10.0	<5.9	50	10[b]
Polycyclic aromatic hydrocarbons (max mass %)	- [a]	- [a]	8	- [a]	8
Water, ppm	500	200	< 200	- [a]	250
Cetane number min	49	51	70	49	51
Viscosity at 40°C mm^2/s	1.9 - 4.1	2.0 - 4.5	2.0-4.5	-[a]	2.2-5.3
Flash Point, °C	55	55	55	-[a]	
Cloud Point, °C					
Winter	-5 to - 34	-10 to -34	-10 to -34	-[a]	+6
Summer					-[a]
Distillation					
T_{95}	370	360	360	-[a]	362
T_{90}	338				360
	[202]	[202]	[199,202]	[203]	[204]

[a] No limit specified

[b] Based on low sulphur diesel. Standard diesel is rated at 500 mg/kg.

A potential issue for LTFT diesel is the cloud point – which represents the temperature at which diesel forms a cloudy appearance due to the waxy hydrocarbons beginning to solidify. This specification is set to avoid blockages in fuel filters and engine injectors. It is inherently based on the minimum temperatures within a region. This specification can vary significantly between 6°C (South Africa) and -34°C (lowest in EU and US). Africa has no cloud point specification. As Fischer-Tropsch LTFT fuels have a typically high cloud point (at 0°C [199]) fuels may need to undergo isomerization for EU and US diesel, however for Sub-Saharan Africa this may not be necessary.

The specification that LTFT distillate often cannot meet is density. The distillate product from LTFT and hydrocracking typically has a density below 780 kg/m^3 which does not fall within the EU (EN 590), African (AFRI-5) or South African (SANS 342:2016) specifications [199]. The reason for the density specification is the way in which the density affects the air-fuel ratio, which is set for specific compression-ignition engines. As the amount of fuel is volumetrically measured, a change in density changes mass of fuel injected. Whilst an engine can operate with lower density fuels, it may change the emission specifications provided by engine manufacturers [199]. Thus, depending on the region, the distillate produced from hydrocracking may require blending with crude oil derivatives, or higher density blending material, in order to be legally sold on the diesel market [202].

However, the United States of America (ASTM D975) has no such specification, and the EU released new specifications in 2016 with a lower the density limit, that take Fischer-Tropsch based fuels into account [54,199].

9.5.4. Partial refining design for decentralized distillate production

For the purposes of a remote small-scale decentralized waste-to-liquid plant in Sub-Saharan Africa, the only products desired are distillate and electricity. Although refining of the naphtha products is possible, the complexity required to refine to motor gasoline is severe and, thus, impractical for such applications. Therefore, partial refining to a distillate-only product is favoured.

The design of a partial refining section for decentralized distillate production has certain requirements that differ from the Oryx and SMDS facilities. Firstly, no naphtha is required as a liquid product and any naphtha formed will be combusted to generate steam for electricity. This means that the design must aim to avoid over-cracking to naphtha range products in the hydrocracker and losing valuable distillate yield. In addition, no secondary distillation to naphtha and LPG is required.

Secondly, as the ideal product would be diesel, the distillate from the refining section must meet all the specifications of AFRI-5 2016 and SANS 342:2016, with the exception of the density specification such that if blended with on-spec crude oil based diesel, the fuel would classify as a drop-in transportation fuel.

9.5.4.1. Phase separation

The first step in refining Fischer-Tropsch syncrude to diesel is to separate out the four-phase system. Figure 9-8 shows the proposed schematic of the phase separation section.

Depending on reactor technology used, the phase separation may start in the Fischer-Tropsch reactor itself or outside of the reactor (so long as the temperature is not decreased below 100°C, the congealing point of wax [54]). For slurry bed technology, it is common for this separation to occur within the reactor (as is true for Sasol Oryx facility), where the liquid wax phase is separated from a gaseous phase at 20 bar and 220°C.

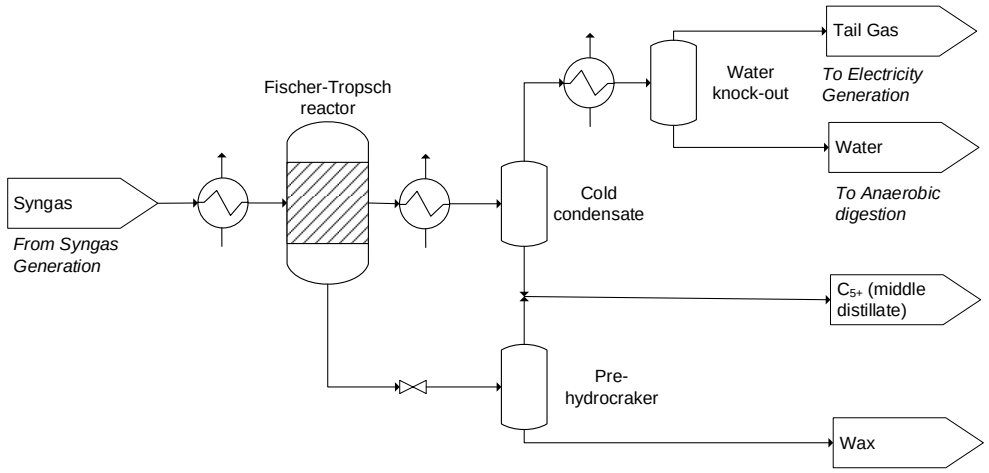

Figure 9-8: Schematic of proposed phase separation section

The gaseous Fischer-Tropsch product contains natural gasses (CO, H_2, CH_4, CO_2, N_2), an aqueous phase (with dissolved oxygenates) and an organic phase. Initially, the hydrocarbon organic phase is separated out in a flash tank, termed the cold condensate. Tuning the temperature of the cold condensate is a vital optimization step in achieving maximum distillate yield.

The gaseous product from the cold condensate will be further flashed at a lower temperature to yield an aqueous and a tail gas stream. The aqueous stream cannot be directly recycled as it contains a small percentage of alcohols which could build up in the process. A waste-water treatment system would thus be required. In the past, anaerobic digestion has been used to process Fischer-Tropsch wastewater (as is true of the PetroSA's Mossgas facility [54]). Therefore, it may be possible to recycle the wastewater back to the first step of the process, thus combining the functions of both biogas digestor and waste-water treatment. This is, however, speculative and would require detailed planning to confirm the microbial consistency.

The liquid wax phase from the Fischer-Trospch reactor contains entrained distillate range hydrocarbons. Thus, a flash separator may be necessary to remove distillate before the hydrocracker as this would result in over-cracking and a loss of valuable distillate yield. Flashing the liquid phase can be done either by heating the system, or by dropping the pressure to allow for hydrocarbon evaporation. As the system is already at 220°C, further heating would require a furnace which would increase the complexity and cost of the design. Alternatively, decreasing the pressure necessitates recompression of liquid wax via pumping as the hydrocracker typically operates at > 30 bar (hydrocracking at 20 bar may be possible [205,206], albeit a different catalyst may be required). As pumps are typically less expensive than furnaces, a pressure change may be more suitable for this flash.

9.5.4.2. Hydrocracking

A hydrocracking unit may be required for wax-heavy product streams in order to improve the distillate yield. The hydrocracker also works to hydrotreat and hydroisomerize the mixture, in a similar manner to the Oryx facility, to ensure high paraffin yields. Mild hydrocracking typically takes place at high pressures (between 30 and 75 bar) and at temperatures between 300°C and 350°C (isobarically and isothermally) [201,207] with high hydrogen : hydrocarbon (H_2:HC) ratios. This is done to allow the catalyst to operate close to "ideal" hydrocracking conditions, which improves the ability of the catalyst to operate at quasi-equilibrium between the alkanes and alkenes which facilitates a limitation of secondary cracking reactions [54]. This means that the feed must be heated and pressurized before entering the reactor. This necessitates a pump for the liquid wax, a compressor for the hydrogen post-membrane and a furnace to increase the temperature above 300°C (as this exceeds the limit for high pressure steam). Furthermore, post hydrocracking, the system requires separation of the excess hydrogen, wax and lighter hydrocarbons. This can be done in a two-step flash separation similar to the configuration used at the Oryx facility (see Figure 9-7).

A hydrocracking system can therefore be a significant cost, involving (potentially) multiple compressors, a furnace and membrane separation upstream. It is thus important to evaluate the necessity of this step. As mentioned previously, with respect to Figure 9-5, at lower conversions the wide carbon distribution results in the production of a significant portion of C_{22+}, thus necessitating a hydrocracker to recover distillate yield. At higher conversions (X_{CO} > 70%) however, the portion of hydrocarbons in the wax fraction decreases meaning that hydrocracking may not be necessary for this purpose (albeit wax removal may be needed to improve the cloud point). The removal of the hydrocracking unit from the refinery design may have significant implications on the capital cost and complexity of design – with the compressors in the system contributing up to 20% of the compression cost (calculated using the Aspen model in Chapter 10).

Unfortunately, as the hydrocracker also acts as a hydrotreater to convert alkenes (olefins) to alkanes (paraffins) it is important to consider whether or not the products need to be hydrogenated. This may be required to meet regional diesel specifications, or to ensure no gumming occurs during storage (alkenes are less resistant to oxidation by O_2 radicals which may result in poly/oligomerization) [208]. The former is more of a problem when it comes to producing gasoline for which there is a limit on the amount of alkenes [54]. As alkenes a have lower cetane number [209] than alkanes, this may affect the ability to meet diesel cetane specifications. Luckily, Fischer-Tropsch syncrude naturally has a very high cetane number and the olefin:paraffin ratio decreases with increasing conversion (see Section 4.3.6), so for the conversion ranges where removal of the hydrocracking system becomes viable, it is likely that the number of alkenes is sufficiently low to avoid hydrotreating. It must be noted, however, that

manganese promoted cobalt catalysts yield a higher olefin/paraffin ratio (see Figure 5-4 (d)) than their un-modified counterpart, and, thus, considerations must be made with regards to hydrotreating products from this catalyst to ensure specifications are met and storage-related manageability is ensured.

In addition, as the hydrocracker operates to isomerize Fischer-Tropsch syncrude, the removal of the hydrocracking step may only be possible for regions where the cloud point specification is sufficiently high (i.e. in warm climates). Luckily, this is the case for Sub-Saharan Africa where the cloud point specification either is not listed or is listed at a low of 6°C (see Table 9-5).

9.5.4.3. Hydrogen and wax recycle

The hydrogen and wax left over after the hydrocracker must be separated out from the distillate. Thereafter they can either be recycled back to the hydrocracker or sent to tail-gas and storage respectively. Recycle streams inherently add complexity to a system, especially in terms of start-up. Furthermore, due to pressure drop across the flash, hydrogen will require recompression if it is to be recycled.

As the hydrocracker require a large hydrogen:hydrocarbon (H_2:HC) ratio, it is typical (and seen in the design of the Oryx partial refinery - see Figure 9-7) for hydrogen to be recycled. However, as this design prioritizes pre-hydrocracking separation, the flows to the hydrocracker are ultimately relatively small. Even at high H_2/HC ratios of 500, 1000 and 1400 m^3/m^3 the amount of H_2 required in the hydrocracker from the syngas stream is only 2%, 5% and 7% of the hydrogen produced in the reforming process respectively.

Furthermore, adding a recycle necessitates the addition of another compressor and a purge for dissolved impurities. Most membranes, even with high selectivity towards H_2, have a small selectivity towards N_2 and significant selectivities towards CO_2. Whilst N_2 is an inert in the recycle, CO_2 will be hydrogenated to CH_4 in the hydrocracker, thus providing another inert in the loop. This may result in a gas build up which may further increase as the membrane degrades over time. In addition, this will add a level of additional concentration control that may not be plausible for a remote setting with little access to laboratory services. Therefore, the hydrogen recycle will not be included in the design.

Wax, by contrast, is less of a problem to recycle as it is liquid so can be pumped back into the hydrocracker and can be heated with the rest of the feed. For the purpose of this investigation, which focuses on a once-through system and the subsequent Aspen model, this recycle will not be included. However, from a purely engineering perspective this could be easily implemented.

9.5.4.4. Atmospheric distillation

Once the four phases have been separated, the liquid product from the cold condensate, vapour product from the pre-hydrocracker flash and the liquid product from the hydrocracker (less H_2) need to be refined via atmospheric distillation in order to meet regional specifications. Figure 9-9 shows the specified distillation profile for SANS 342:2016, and the composition of Fischer-Tropsch products produced at various conversions for Pt-Co/Al_2O_3. All Fischer-Tropsch conversions from X_{CO} = 60% to 90% require a decrease in the number of light components in order to sharpen the distillation profile and ensure that the flash point of the distillate is not too low. As both light (naphtha) and heavy (wax)

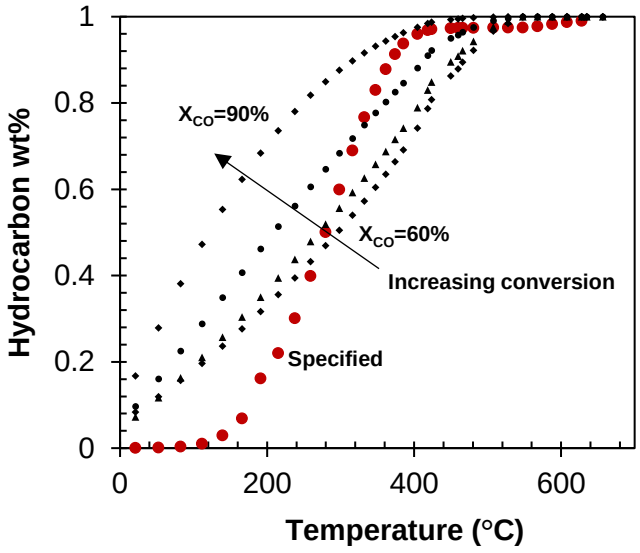

Figure 9-9: Distillation profile of Fischer-Tropsch products at various conversions compared to the specified distillation profiles as per SANS 342:2016

components need to be removed for conversions lower than X_{CO} = 90% (see Figure 9-9), an atmospheric distillation column with a side stream may employed. This allows for the separation of three component mixtures – waxes, distillate and light tail gas – in a similar way to the atmospheric distillation at the Sasol Oryx facility [54].

9.5.5. Proposed partial refinery design

The proposed design for the Fischer-Tropsch partial refinery is shown in Figure 9-10. Syngas from the syngas generation plant is heated to 220°C before being fed into the Fischer-Tropsch reactor. The Fischer-Tropsch product and hydrocarbon distribution are dependent on the CO conversion (as discussed in Chapter 4), thus the partial refining section is too.

For lower conversion ranges (where wax is a significant product), Fischer-Tropsch wax is fed into a pre-hydrocracker flash to remove any distillate range hydrocarbons then pumped to 35 bar and

combined with compressed hydrogen from the hydrogen separation membrane. The combined stream is then fed into the hydrocracker where the distillate and paraffinic yield is improved. The excess hydrogen is then separated from the hydrocracker product through a series of two flash tanks.

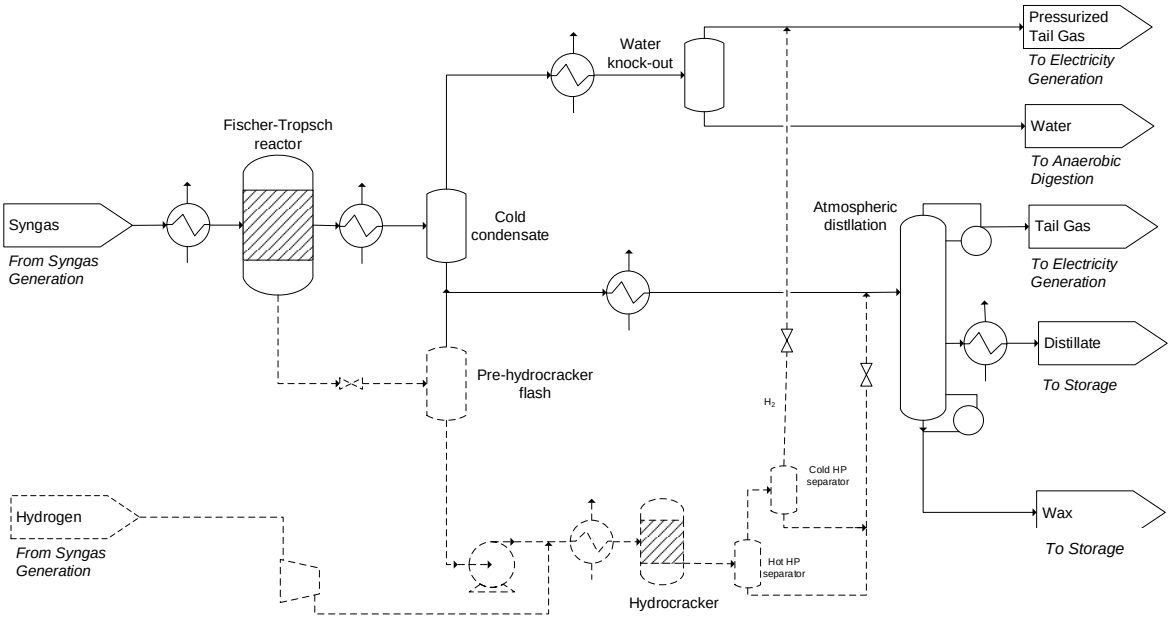

Figure 9-10: Proposed partial refining design showing streams (---) that are only required for conversions with significant wax product.

For all conversion ranges, the Fischer-Tropsch lighter products are flashed at high pressure to remove light gasses such as CO, H_2, N_2 and CH_4. These light gasses (termed pressurized tail gas) are further flashed to remove process water, and then fed to the gas turbine to produce power. The heavier product (post decompression to 1 bar) is combined with the vapour from the pre-hydrocracker flash (where applicable) and fed into an atmospheric distillation column with a side distillate stream. All light and naphtha products are removed through the top of the column and sent to the power plant. The distillate is taken off via a side stream whilst any excess heavy waxes are removed via a liquid bottom stream.

9.6. Power plant design

9.6.1. Combined cycle vs steam turbine

Producing electricity from Fischer-Tropsch gaseous products and unconverted reactants (containing C_1-C_4, CO_2, CO and H_2) can be achieved using either a steam or gas turbine.

Steam turbine technology is thermodynamically based on the non-ideal Rankine cycle which operates with closed-circuit pressurized steam. Water in the closed circuit is pumped to high pressures and fed into a boiler (heated by the combustion of the gaseous exhaust from the Fischer-Tropsch reactor) where it is vaporised and superheated. The superheated, pressurized steam is then fed into a turbine, where pressure is decreased through driving the blades of a rotor, creating work. The steam is then condensed before being fed back to the pump.

Steam turbines have high operating efficiency and reliability [210]. This process typically operates with steam at temperatures lower than gas turbines, meaning that the material costs are not as high. However, due to the amount of components required [210] (boiler, cooling tower etc.) high equipment costs typically make the technology reliant on large scale operation (500-1000 MWe) [211]. Small-scale operation (less than 100 MWe) typically requires equipment modifications to decrease capital cost. These modifications often decrease efficiency [211].

Gas turbines, on the other hand, operate via the Brayton cycle. Compressed air is fed into a combustion chamber where fuel is injected and combusted at temperatures between ca. 650°C and 1200°C [211,212]. This produces a high pressure, high temperature gas which drives a turbine, creating work for inlet compressors and power via a generator.

Gas turbines require far fewer components than steam turbines making them more attractive for small-scale operation [210]. They are also more dynamic in terms of producing variable amounts of energy. However, high temperatures also require specialised materials and higher levels of maintenance and have low adaptability to different types of fuels [212]. Compressed air is required to enable combustion in a gas turbine. However, compressing this air reportedly uses up to two-thirds of the generated power of gas turbines [210].

Combined cycles are a way to maximize the process efficiency of power generation – combining the advantages of both gas and steam turbine. In this system, high pressure gas is used to drive a turbine. The exhaust gas from this turbine is then combusted with low pressure air and used to superheat steam and drive a steam turbine, thus producing extra power [212].

9.6.2. Proposed power plant design

A combined cycle is used to generate power from the tail gas of the refining section (see Figure 9-11). This includes two streams, a high pressure (18-19 bar) stream from the product separation flash tanks and a low pressure (1.1 bar) stream from the atmospheric distillation column. The high-pressure tail gas is pre-heated before being fed into a gas turbine which generates power through decreasing the pressure to slightly above atmospheric. The off gas from the turbine is then combined with tail gas from the

Fischer-Tropsch synthesis and air. The mixture is combusted in a furnace and used to heat up high pressure water which is subsequently fed into a steam turbine to generate the bulk of power for the plant. All heat exchanges on the power plant are integrated to ensure no excess utilities are required.

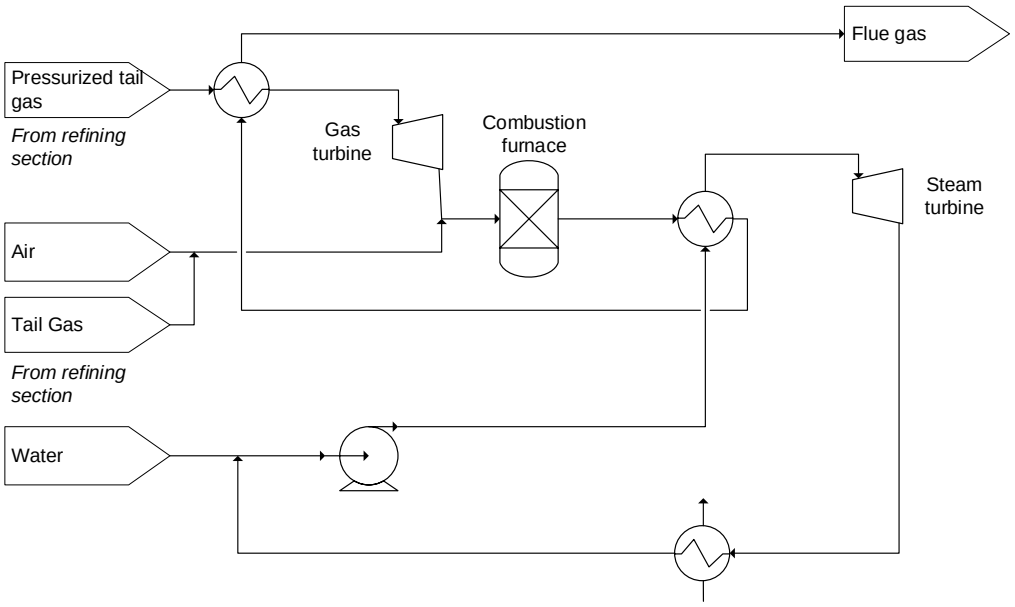

Figure 9-11: Proposed combined cycle power plant

9.7. Conclusion

Chapter 9 has explored the key design decisions made in the process of developing a design for a once-through biogas-to-distillate plant. Figure 9-12 shows the overall process flow diagram developed as a result of these decisions. A tri-reformer was chosen as the syngas generation step due to the favourable H_2:CO ratio, simple reactor design and low levels of catalyst coking, despite the unfavourable CO_2 utilisation and potential dilution affect from air. The tri-reformer is set to operate at 2.7 bar, in order to optimise compression costs across the plant. The tri-reformer product is fed into a water-gas shift unit, which is used to adjust for changes in the feed or requirements in the hydrocracker. The syngas is then compressed to 20 bar with inter-stage water knockout and passed through a polymeric membrane (chosen based on reliability, low supervision requirements, scalability and relatively low cost) to separate off hydrogen for the hydrocracker.

The resulting syngas is fed into the Fischer-Tropsch reactor. Depending on the conversion at which the Fischer-Tropsch reactor operates, the range of hydrocarbons produced differs significantly. At lower conversions a highly waxy product is formed, which requires hydrocracking to improve distillate yields. At higher conversions hydrocracking is unnecessary due to the shift towards lighter products. Thus, the resulting product separation and partial refining section is conversion dependant.

For lower conversions, the Fischer-Tropsch wax product is fed into a pre-hydrocracker flash to separate any entrained naphtha fraction, before being fed into the hydrocracker and resulting separation. For higher conversions, wax from the Fischer-Tropsch reactor may be fed directly into the atmospheric distillation column.

For all conversions, light Fischer-Tropsch products and syngas are fed into a cold condensate flash tank which removes the distillate fraction from the light gasses. The light gasses are then passed through a water-knock out, whilst the resulting distillate is fed into the atmospheric distillation column. The atmospheric distillation column has 3 product streams, a top stream which removes tail gas, a side stream for distillate and a bottom stream for waxes. The tail gas from the distillation column and pressurised tail gas from the water-knock out are fed into a combined cycle power plant.

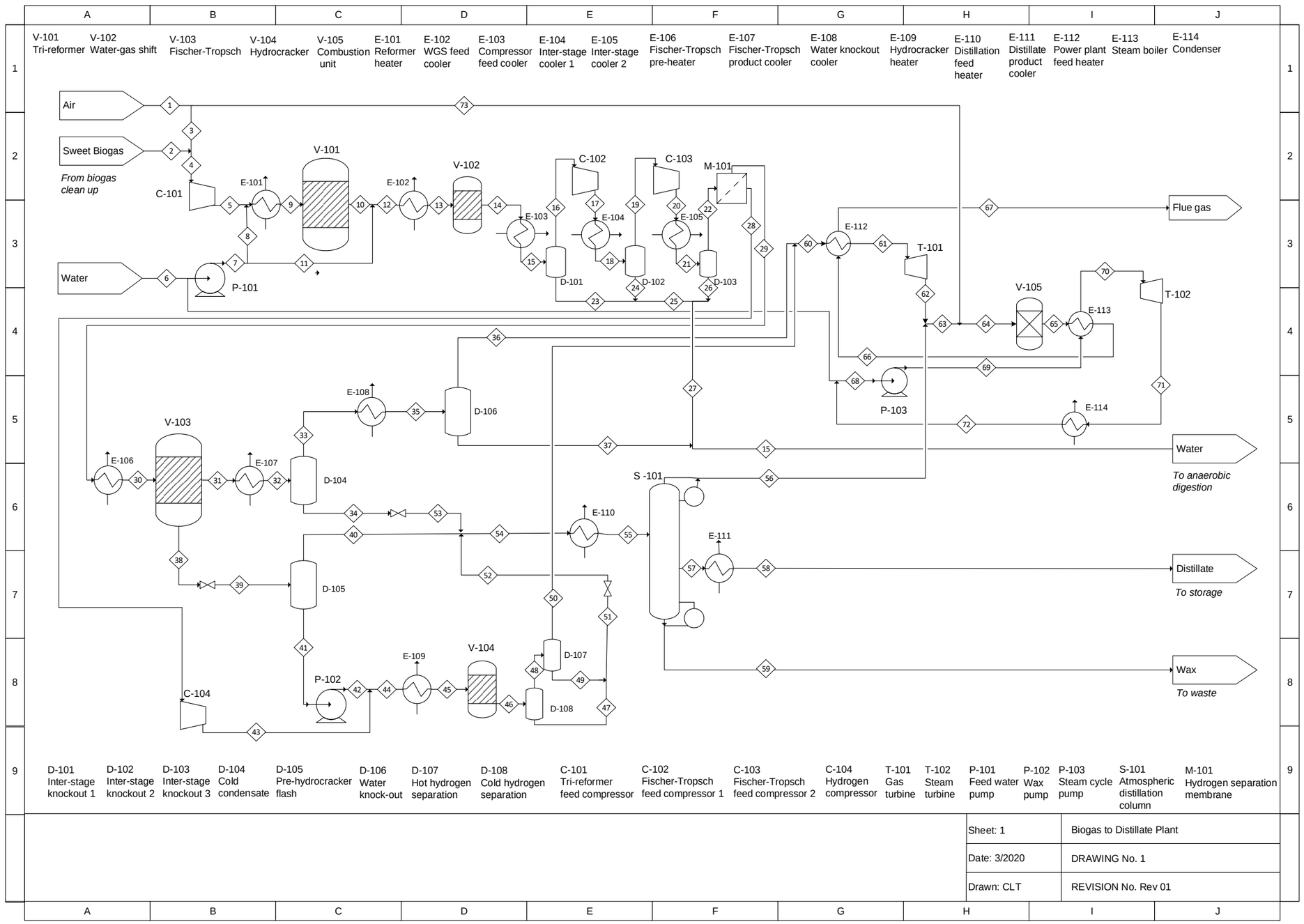

Figure 9-12: Proposed once-through biogas-to-distillate Fischer-Tropsch plant

Chapter 10

Evaluation of a single pass reactor configuration for a Fischer-Tropsch biogas-to-distillate process

10.1. Introduction

Liquid fuel security in Sub-Saharan Africa may be improved substantially by small-scale decentralized production of fuels from organic waste via the Fischer-Tropsch process. A design philosophy and detailed process design for this system were discussed in Chapters 1 and 9 respectively with the aim of developing a system that prioritizes simplification, capital cost reduction and utility self-sufficiency for remote applications. Due to the size and context of the plant, distillate (low density diesel) and electricity are the only desired products.

Chapter 10 discusses the modelling of the once-through biogas-to-distillate design discussed in Chapter 9. The feed to the plant consists of 400 kmol/ h clean biogas with a composition of 75% CH_4 and 25% CO_2. This is equivalent to biogas produced from 400 t/day of organic municipal solid waste which is roughly equal to the amount of organic waste produced in Sub-Saharan cities with populations between 200,000 [213] and 900,000 [10] (region and income level dependent). These populations are equivalent to well-known cities such as Gaborone, Botswana (232,000) and Kigali, Rwanda (860,000), respectively.

The aim of this chapter is to determine the optimal Fischer-Tropsch conversion, catalyst and refining configuration at which to operate in order to produce the highest yield of on-spec distillate. A total of 16 cases will be tested including: four different levels of conversion in the Fischer-Tropsch synthesis (60%, 70%, 80% and 90%), two different cobalt-based Fischer-Tropsch catalysts (Pt-Co/Al_2O_3 and Mn-Co/Al_2O_3) and a partial refining plant with and without hydrocracking. For the purposes of representing the design via mol balances and sensitivity analyses, a base case will be used: a once-through system operating with a Pt-Co/Al_2O_3 catalyst in the Fischer-Tropsch synthesis (operated at X_{CO} = 60%) and a partial refining section that includes a hydrocracker .

10.2. Model Development

The following assumptions were made in the development of the once-through biogas-to-distillate Aspen Plus ® model.

- The feedstock to the model was sweet biogas (post-desulphurization). Anerobic digestion and gas cleanup were not modelled as the output from these processes using various feedstocks are well documented [18,61,62].
- Only paraffinic compounds were used for vapour-liquid equilibrium calculations. Olefins were included for hydrotreating, hydrocracking and Fischer-Tropsch mass and energy balance calculations.
- The Peng-Robinson equation of state was used for vapour-liquid equilibrium calculations [214] since the refinery stream contains mainly apolar components.
- The products from the Fischer-Tropsch synthesis were determined from an empirical model using experimental data obtained over the two catalysts: industrial Pt-Co/Al_2O_3 and Mn-Pt-Co/Al_2O_3 (Mn:Co = 0.14). The ASF model was used to extrapolate to high carbon numbers (C_{80}) using the conversion-dependent chain growth probabilities discussed in Chapter 4 and 5.
- Carbon numbers C_1-C_{45} were used for vapour-liquid equilibrium calculations in the refining section, as experimental data for the two Fischer-Tropsch catalysts (Figure 9-5) show low molar levels of C_{45+} across the conversion range of interest, and these components will remain mainly in the liquid phase under the conditions considered.
- The formation of oxygenates (~1.4%), branched compounds (~1.2%) and aromatics (<0.1%) were ignored for vapour-liquid equilibrium calculations. These are low enough to ignore in the Fischer-Tropsch LTFT stream (although they are more significant in HTFT streams) [54]. Oxygenates were assumed to leave via the aqueous stream and would need to be removed in waste-water treatment or fed back to the reformer.
- The hydrocracker was modeled using yields reported by Leckel and Liwanga-Ehumbu [215]. Ideal separation of hydrocracker product from hydrogen was assumed.

10.2.1. Overall design

The once-through biogas-to-distillate plant was modelled using three Aspen Plus ® simulations – syngas cleaning and compression, separations and refining and power production. The hydrogen separation membrane [216], Fischer-Tropsch reaction [176] and hydrocracker [215] were modelled on Excel using empirical data. The Excel and Aspen models were then combined and run simultaneously through Aspen Simulation Workbook.

The molar feed flow rates to the process are shown in Table 10-1. The biogas composition was based on a methane-rich stream from the anaerobic digestion of organic waste [61]. The chosen ranges for oxygen and water vapour flow rate were based on similar studies used for autothermal reforming, steam reforming and tri-reforming [187,188,217]. The nitrogen flow rate was calculated according to the oxygen flow rate and the standard composition of air.

Table 10-1: Inputs to model of components based on the anaerobic digestion of 400 tonnes municipal solid waste (MSW) per day.

Component	*Molar flow (kmol/hr)*
Methane (CH_4)	300
Carbon Dioxide (CO_2)	100
Oxygen (O_2)	0-250
Water Vapour (H_2O)	0-400
N_2	0 – 940

10.2.2. Syngas generation and compression

The syngas generation and compression section comprise a tri-reformer, water gas shift reactor, compression system and hydrogen separation (split ratio defined by requirements in the hydrocracker on the Aspen Simulation Workbook). Figure 10-1 shows the Aspen Plus ® simulation of the section whilst Table 10-2 shows stream table belonging to the base case (i.e. the Fischer-Tropsch section operating at a conversion of 60% with a Pt-Co/Al_2O_3 catalyst and a partial refining section including a hydrocracker).

In the Aspen simulation, air and biogas are compressed to 2.7 bar and combined with water pumped to the same conditions. The air, water and biogas feed are preheated to 220˚C (HEATERX) before being fed into the tri-reformer. The tri-reformer was modelled using an RGIBBS reactor, with calculations driven by minimization of Gibbs free energies [62,185]. Whilst in practice equilibrium may not be achieved, modern reforming catalysts [218–221] are reported to operate relatively close to equilibrium exit concentrations [62,222,223], especially at high temperatures [222]. Thermodynamic models driven by equilibrium have been shown to satisfactorily estimate the O_2 consumption [218] and H_2/CO ratios at temperatures above 750˚C [224]. It must be noted that CH_4 conversions and CO_2 conversions may deviate slightly from equilibrium at temperatures lower than 750˚C due to inaccuracies in the modelling of coke formation [152].

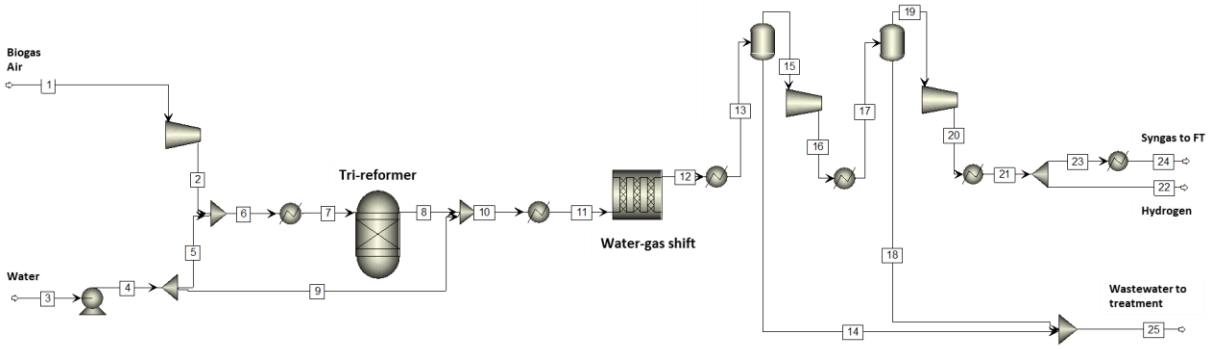

Figure 10-1: Aspen model for syngas generation and compression with a clean biogas feed.

Table 10-2: Base case stream table for the syngas generation system using the Aspen model.

Stream	*1*	*3*	*7*	*8*	*9*	*11*	*12*	*24*	*22*
Stream	**Biogas feed**	**Water feed**	**Tri-reformer feed**	**Tri-reformer product**	**Water addition to WGS**	**WGS feed**	**WGS product**	**Syngas product**	**H_2 product**
T (°C)	25	25	220	750	25	280	300	220	50
P (bar)	1	1	2.7	2.7	2.7	2.7	2.7	20	10
					Molar flow rate (kmol/hr)				
CO_2	100	0	100	125	0	125	144	141	2.5
CH_4	300	0	300	9.07	0	9.07	9.07	9.07	0.00
CO	0	0	0	266	0	266	247	247	0.31
H_2O	0	140	120	184	20	204	185	11.7	0
O_2	190	0	190	0	0	0	0	0	0
H_2	0	0	0	518	0	518	537	501	36.3
N_2	714	0	714	714	0	714	714	714	0.38

An adiabatic RPLUG reactor was used for modelling the water-gas shift (WGS) reaction, using an empirical power law (Equation 10-1) with parameters for the noble metal catalyst, 0.5%Pt/TiO_2, as described by [225]. The catalyst, 0.5%Pt/TiO_2, was used due to its relatively high water-gas shift activity at low-to-medium temperatures, which facilitates single stage operation rather than the more classical two-stage water-gas shift process [226].

$$r = k_0 e_a^{-\frac{E}{RT}} p_{CO}^a p_{H_2O}^b p_{CO_2}^c p_{H_2}^d (1-\beta) \qquad 10\text{-}1$$

$$\beta = \frac{p_{CO_2} p_{H_2}}{K_{Eq} p_{CO} p_{H_2O}} \qquad 10\text{-}2$$

In Equation 10-1, r is the kinetic rate ($mols^{-1}g_{cat}^{-1}$), k the rate constant, p_i the partial pressure of each species (atm) and a, b, c and d are reaction orders 0.5, 1, 0, -0.7. The constants k_0 = 0.31 $mol{\cdot}s^{-1}{\cdot}g_{cat}^{-}$

$^{1.}atm^{-0.8}$ and E_a = 10.8 kcal/mol. The term β is defined as the approach to equilibrium [225] and is calculated as per Equation 10-2, where K_{eq} is the equilibrium constant. The tri-reformer was designed to deliver a H_2/CO ratio sufficient for the Fischer-Tropsch reactor, whilst the water-gas shift unit was designed to provide excess hydrogen needed for the hydrocracker (as determined by the H_2:HC ratio requirements). The WGS conversion and exit H_2/CO ratio were determined by excess steam addition and inlet temperature (determined by the exit temperature of the feed cooler – HEATERX).

In the simulation, the water-gas shift reactor product stream is cooled to 35˚C and water is knocked out before entering the 2-stage compressor system (compression ratio = 2.7) with inter-stage cooling. Water is knocked out at each stage. After the final compressor, a stream of hydrogen is separated off from the Fischer-Tropsch feed stream to be used in the hydrocracker. To achieve this, a hydrogen selective polymeric membrane was used. The flux of various species through the membrane was calculated using

$$N_i = \frac{P_{M_i}}{l_M}(\Delta P) \qquad 10\text{-}3$$

where N_i is the molar trans-membrane flux of species (cm^3(STP)/(cm^2·s), P_{Mi} is the permeability of species i (cm^3 (STP)·cm/(cm^2·s·cm Hg)), l_M is the membrane thickness (cm) and ΔP is the pressure difference across the membrane (cm Hg). Table 10-3 shows the permeability and selectivity of H_2, CO_2, CO, N_2 and CH_4 for various polymeric membranes.

Table 10-3: Polymeric hydrogen separation membranes including the permeabilities and selectivities toward components of syngas [216,227–232].

Membrane type	***Permeability Barrer****					***Ideal selectivity***			***Exp. conditions***	***Ref.***
	H_2	CO_2	N_2	CO	CH_4	H_2/N_2	H_2/CO_2	H_2/CO	T˚C	
Polyimide Matrimid	23.9	6.1	0.19	0.44	-	133.9	4.0	54.8	30	[216]
P84/ND	6.7	1.61			0.022	-	4.1	-		[227]
6FDA-TTM/Si-H	62.6	29.7	-	-	0.39	-	2.1	-		[227]
PI/MWCNT@GONRS	42.5	25.2	-	-	2.3	-	1.7	-		[227]
PIM-EA(H_2)-TB	1630	1380	62.8	-	1380	25.9	-	-		[228]
Cellulose acetate	2.63	6.3	0.21	-	0.21	-	0.41	-	80	[229]
Poly (p-phenylene oxide)	113	75.8	3.81	-	11	-	1.49	-	210	[229]
Ethyl Cellulose	87	26.5	8.4	-	19	-	3.33	-	43	[229,230]
Polydimethylsiloxane	550	2700	250	-	800	-		-	-123	[229]
Polystyrene	23.8	10.4	-	-	-	-	2.29	-	30	[196]

*1 Barrer = 10^{-10} cm^3 (STP).cm/cm^2.s.cmHg)

Polyimide Matrimid® is a commercially available and well tested glassy polymer membrane with a good trade-off between the permeability and H_2/CO_2 and H_2/N_2 selectivity [216]. Permeability and selectivity values for the syngas components through Matrimid® have been well established (see Table 10-3) [216,231–233]. Both raffinate and permeate concentrations were calculated based on these permeabilities reported by David et al. [216]. The flux through the Matrimid® membrane can be controlled by permeate pressure and membrane area [195]. In this case, the lower boundary for permeate pressure was set at ca. 8.8 bar, in order to make sure that the hydrogen can be recompressed for the hydrocracker in 1 stage with a compression ratio less than 4.

10.2.3. Fischer-Tropsch modelling

In the model, the raffinate from the hydrogen separation membrane is directed to the Fischer-Tropsch reactor, which was modelled using the empirical selectivity data taken from Chapter 4 ($Pt\text{-}Co/Al_2O_3$) and Chapter 5 ($Mn\text{-}Pt\text{-}Co/Al_2O_3$, mass Mn:Co = 0.14) and rate data based on [101]. The Fischer-Tropsch reactor was modelled entirely in Excel and linked to the simulation via Aspen Simulation Workbook.

The empirical data was fitted to exponential functions ($a \cdot e^{b.x} + c$) for computational simplicity, with constants determined using least squares regression. The constants for both catalysts are presented in Appendix I. The fitting of this data can be seen in Figure 10-2. Using a standard ASF distribution, a model was derived for selectivity of C_5-C_{80} as a function of conversion, for which products from selected conversions are shown in Figure 9-5.

The olefin/paraffin ratio for each catalyst and each carbon number was calculated separately. For C_2-C_{11}, the olefin content is reportedly [54,176] not only significant (between 65% and 10%) but also largely dependent on conversion. For this carbon range, where the olefin content was determined for each carbon number, constants were calculated for an empirical model with respect to conversion. For C_{11}-C_{22} it has been estimated [54] that olefins are approximately 5% of total carbons. Thus, this was used as a constant value across the range. The amount of C_{22+} olefins are reportedly negligible [54], and thus were ignored in this range.

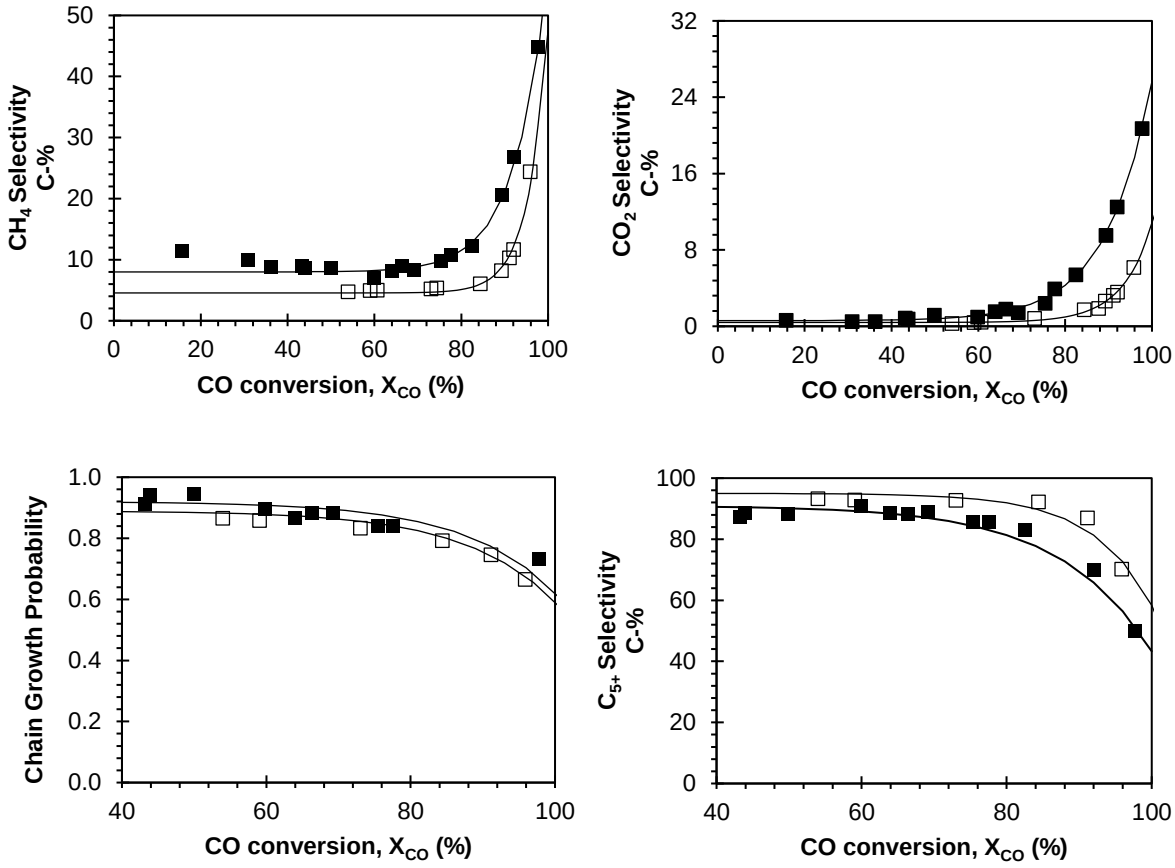

Figure 10-2: Empirical modelling of the Fischer-Tropsch products as a function of conversion based on selectivity data from Chapters 4 and 5 for Pt-Co/Al_2O_3 (closed symbols) and Mn-Pt-Co/Al_2O_3 with a mass ratio of Mn:Co = 0.14 (open symbols).

10.2.4. Separation and refining

Wax, distillate, water (incl. aqueous products) and tail gas (a mixture of H_2, CO, CO_2, CH_4, N_2 and C_2-C_{10}), are separated out in the effluent of the Fischer-Tropsch synthesis and the distillate is refined to meet all diesel specifications, with the exception of density. Table 10-4 shows the stream table obtained from the Aspen simulation over the separation and refining section with a hydrocracker (see Figure 10-3) for a Fischer-Tropsch conversion of X_{CO} = 60%.

In reality, the first separation occurs in the Fischer-Tropsch reactor itself. Therefore, the first flash tank (Fischer-Tropsch VLE in Figure 10-3) was used to model the vapour-liquid equilibrium within the Fischer-Tropsch reactor at 220°C and 20 bar.

In the model, the vapour from the Fischer-Tropsch reactor (modelled as a flash tank) is fed into a pressurized cold condensate flash tank where distillate is separated off from the water and tail gas. The

subsequent flash tank knocks out Fischer-Tropsch product water. The pressurized tail gas is then fed to the combined cycle power plant.

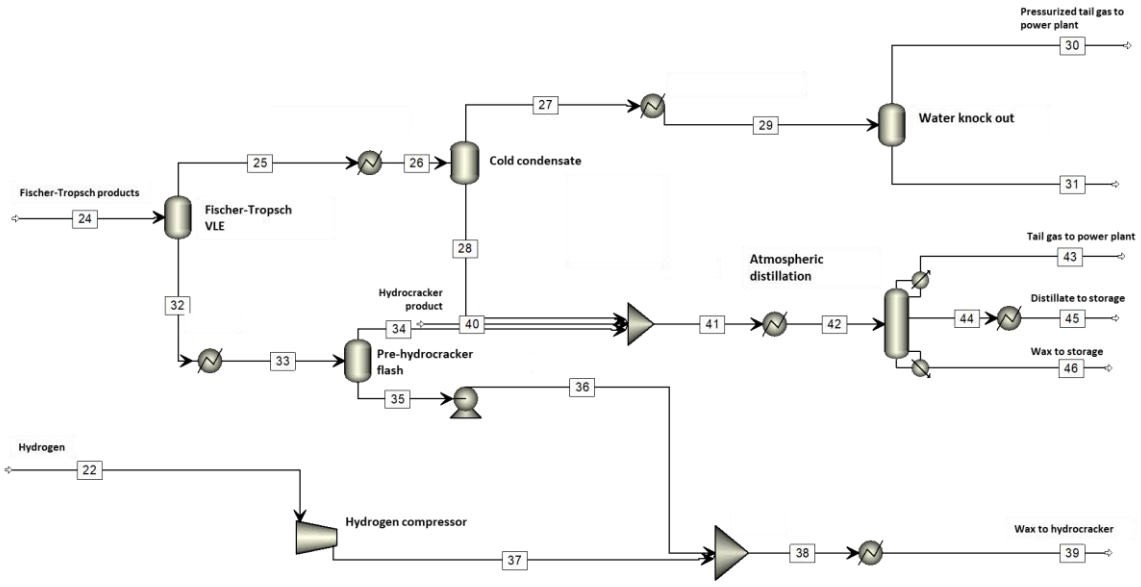

Figure 10-3: Aspen model for Fischer-Tropsch product separation and distillate refining.

The liquid Fischer-Tropsch product is flashed to remove any entrained C_{10}-C_{20} product to avoid over-cracking in the hydrocracker (Figure 10-3). The liquid products from this flash are then combined with hydrogen and fed to the hydrocracker. The hydrocracker was modelled in Excel using empirical selectivity data reported by reported by Leckel and Liwanga-Ehumbu [215] at a conversion of the feed of 81%. Hydrotreating was modelled within the hydrocracker – which allows for the adiabatic conversion of olefins to paraffins. The feed to the hydrocracker model was determined by the output of Stream 39 (Figure 10-3), whilst the hydrocracker product (excl. hydrogen) was fed into the Aspen Plus ® simulation via Stream 40.

The liquid product from the hot condensate, vapour from the pre-hydrocracker flash and the liquid products from the hydrocracker are combined (Stream 42) and undergo a final atmospheric distillation to purify the distillate. The atmospheric distillation column (with a side distillate stream) was modelled using an equilibrium trayed RADFRAC column with condenser and kettle reboiler.

The separations section was modelled both with and without the hydrocracking section. In the case without a hydrocracker, the hydrocracking conversion was set to zero such that the wax product from the Fischer-Tropsch flash is fed directly into the atmospheric distillation column.

Table 10-4: Base case stream table for the separation and refining section for the product of a Pt-Co/Al_2O_3 catalyst at a Fischer Tropsch conversion X_{CO} = 60% with a hydrocracker using the Aspen model.

Stream	*24*	*25*	*27*	*28*	*30*	*31*	*32*	*34*	*35*	*40*	*42*	*43*	*45*	*46*
Description	**FT product**	**FT product vapour**	**Cold cond. vapour**	**Cold cond. liquid**	**Pressurized tail gas**	**Water knock out liquid**	**FT product liquid**	**Pre-hydrocrack. vapour**	**Pre-hydrocrack. liquid**	**Hydrocrack. product**	**Atm. dist. feed**	**Tail gas**	**Distillate**	**Wax**
P (bar)	19	19	19	19	19	19	19	1	1	34	1.1	1	1	1
T (°C)	20	220	50	50	35	35	220	220	220	370	180	150	300	356
CO_2	143	143	143	0.2	143	0.0	0.0	0.0	0.0	0.0	0.2	0.2	0.0	0.0
CH_4	21	21	21	0.0	21.3	0.0	0.0	0.0	0.0	2.5	2.5	2.5	0.0	0.0
CO	99	99	99	0.0	99	0.0	0.0	0.0	0.0	0.0	0.0	0.0	0.0	0.0
H_2O	156	156	152	3.8	15.2	137	0.0	0.0	0.0	0.0	3.8	3.8	0.0	0.0
H_2	210	210	210	0.0	210	0.0	0.0	0.0	0.0	0.0	0.0	0.0	0.0	0.0
N_2	714	714	713	0.1	713	0.0	0.0	0.0	0.0	0.0	0.1	0.1	0.0	0.0
C_2-C_4	2.3	2.3	2.3	0.0	2.3	0.0	0.0	0.0	0.0	0.3	0.3	0.3	0.0	0.0
C_5-C_9	3.4	3.4	2.4	1.0	2.4	0.0	0.0	0.0	0.0	1.4	2.4	2.3	0.1	0.0
C_{10}-C_{22}	3.9	3.3	0.1	3.2	0.1	0.0	0.6	0.0	0.6	1.9	5.0	0.7	3.7	0.6
C_{22+}	1.6	0.2	0.0	0.3	0.0	0.0	1.4	0.0	1.4	0.4	0.7	0.0	0.1	0.6

10.2.5. Combined cycle power plant

In the model, tail-gas from the partial refinery is fed to a combined cycle power generation unit (see Figure 10-4 and Table 10-5). Two tail gas streams exist, the high-pressure stream from cold condensate and water separator and the depressurized stream from the atmospheric distillation column. The pressurized tail gas is fed first through a gas turbine to generate power. Due to the large pressure drop, the gas needs to be preheated, which was achieved via integration with the gases from the steam turbine. The two atmospheric tail gas streams are then combined with air at atmospheric pressure and combusted. The combustion was modelled using an RGIBBS unit using Gibbs free energy minimization. The combusted material heats up pressurized water, which is subsequently fed to a steam turbine, thereby generating the bulk of power for the plant.

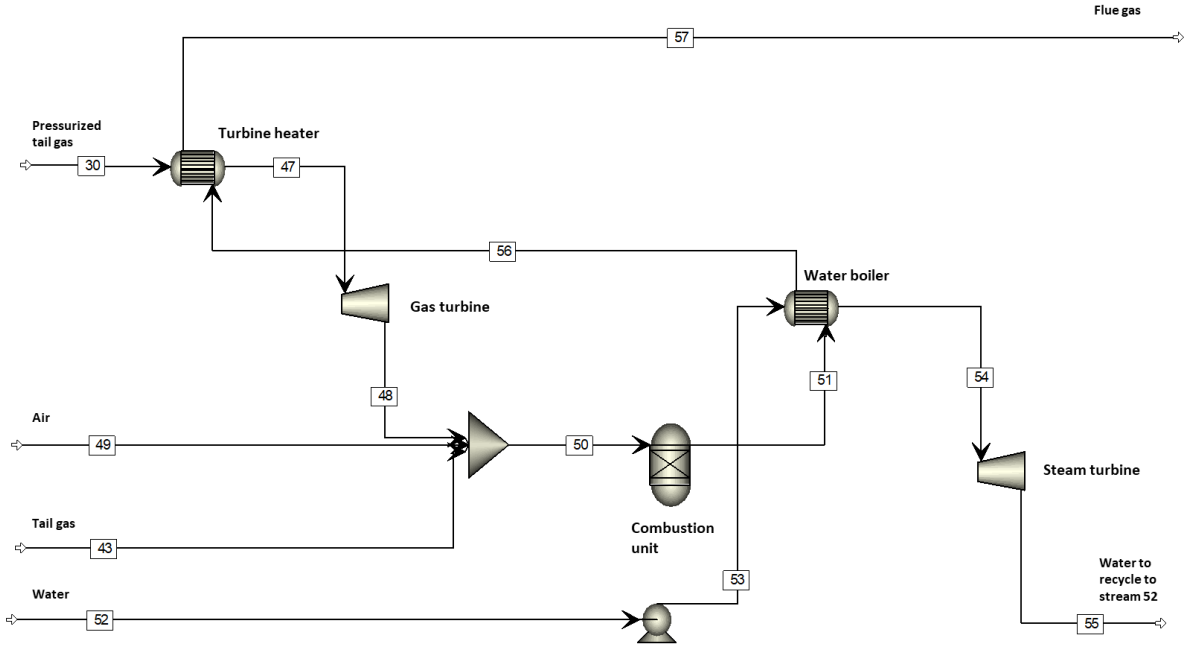

Figure 10-4: Aspen model for the combined cycle power plant.

Table 10-5: Base case stream table for the combined cycle power plant for a feed from FT reactor operating at X_{CO} = 60%.

Stream	*30*	*43*	*48*	*49*	*50*	*51*	*52*	*54*	*55*	*56*
Stream	**Pressurized tail gas**	**Tail gas**	**Gas turbine product**	**Air feed**	**Combined tail gas**	**Combustion unit product**	**Water feed**	**Boiler steam**	**Steam turbine product**	**Boiler flue gas**
T (°C)	35	150	137	35	140	1278	27	620	102	650
P (bar)	19	1	1	1.1	1	1	100	100	1.1	1
						Molar flow rate (kmol/hr)				
CO_2	143	0.2	143	0	143	314	0	0	0	314
CH_4	21	2.5	21	0	23.5	0	0	0	0	0
CO	99	0.0	99	0	99	0.02	0	0	0	0.02
H_2O	15.2	3.8	15.2	0	19	326	1074	1074	1074	326
O_2	0	0	0	400	0	128	0	0	0	128
H_2	210	0	210	0	210	0.01	0	0	0	0.01
N_2	713	0.1	713	1504	713	2217	0	0	0	2217
C_2-C_4	2.3	0.3	2.3	0	2.6	0	0	0	0	0
C_5-C_9	2.4	2.3	2.4	0	4.7	0	0	0	0	0
C_{10}-C_{22}	0.1	0.7	0.1	0	0.8	0	0	0	0	0
C_{22+}	0.0	0.0	0.0	0	0	0	0	0	0	0

10.2.6. Distillate specifications

In order to meet the legal specifications of diesel, the cetane number, flash point, distillation profile and cloud point must be within the limits set by a regional governing body. Although it would be preferable to meet the density specifications, this was not feasible (see Section 9.5.3). In order to ensure the relevant specifications were met, the following product characteristics were calculated:

- Flash point
- Cetane number
- Cloud point
- Distillation curve

Flash points were calculated using the Pensky-Martens flash point estimation as implemented in Aspen Plus. The cetane number of the diesel from the atmospheric distillation column was calculated using the correlation from Ghosh and Jaffe [209]:

$$CN = \frac{\sum v_i \beta_i CN_i}{\sum v_i \beta_i} \qquad 10\text{-}4$$

where CN represents the cetane number of the mixture, β is a correlation factor based on a blend value that differs for n-paraffins and olefins, v_i is the volume fraction of molecule i in the fuel, whilst CN_i is the lumped cetane number of compound i as described by [209].

Cloud points were calculated using the correlation described in [234].

$$CP = -267.5332 \cdot SG + 0.1315 \cdot T_{10\%} + 0.7837 \cdot T_{50\%} - 0.4301 \cdot T_{90\%}\% + 89.1003 \qquad 10\text{-}5$$

where CP is the cloud point in ºC, SG is the specific gravity of the distillate, and $T_{10\%}$, $T_{50\%}$ and $T_{90\%}$ are points on the cumulative distribution distillation curve which was modelled using the atmospheric equivalent boiling points of paraffins [235].

10.3. Sensitivity analysis

10.3.1. Tri-reformer

The choice of feed composition (oxygen- and steam-to-carbon ratios) and reactor temperature affect the product composition, yields and conversions of the tri-reformer. For the context of small-scale

decentralized applications, it was critical that the tri-reformer operate adiabatically. Thus, the feed needed enough oxygen to enhance the exothermic combustion reaction.

Figure 10-5 illustrates the effect of the steam-to-carbon (S/C) ratio and temperature on the conversion of CH_4 and CO_2, the CO and H_2 yield and the H_2/CO ratio for an adiabatic tri-reformer with an air feed adjusted to ensure a net duty of zero.

The CH_4 conversion (Figure 10-5 (a)) increased rapidly with increasing temperature. At 500°C, X_{CH_4} lay between 20% and 40% whilst at temperatures above 800°C, X_{CH_4} was close to 100%. Unfortunately, in order to reach these high temperatures, more oxygen was required, and thus air, which increased the diluent factor for the Fischer-Tropsch synthesis. An increase in the steam-to-carbon (S/C) ratio further increased the conversion, with a noticeable effect at temperatures below 800°C.

Unfortunately, whilst a high CH_4 conversion is likely, a high conversion of CO_2 is less likely (Figure 10-5 (b)), due to the combustion and water-gas shift reactions. Mostly negative conversions were found throughout the temperature range, with the exception of a steam-to-carbon ratio of 0 at high temperatures [57]. Operating with oxygen but no steam (oxy-CO_2 reforming) is not feasible due to safety concerns [188] as discussed in Chapter 9. Increasing in the steam-to-carbon ratio above 0 unfortunately decreased the CO_2 conversion significantly.

Figures 10-5 (c) and (d) show the effect of temperature and steam-to-carbon ratio on the yield of H_2 (H-%) and CO respectively (C-%). Hydrogen yield was defined as the amount of hydrogen produced, considering the amount of atomic hydrogen contained in feed CH_4 and H_2O. CO yield was defined as the carbon yield from CO_2 and CH_4. Increasing temperatures favoured higher yields of CO and H_2, although the H_2 yield reached a maximum between 700°C and 800°C. Increasing steam-to-carbon ratio and temperature at low temperatures increased the H_2 yield, however this trend reversed at high temperatures, which may be due to contributions from the reverse water-gas shift reaction. Increasing the steam-to-carbon ratio decreased the CO yield across the entire range of temperature, with a more significant effect at 750°C.

Figure 10-5 (e) shows the effect of the steam-to-carbon ratio and the reformer temperature on the syngas (CO and H_2) partial pressure exiting the tri-reformer. The syngas partial pressure increased with increasing temperature until a point between 700ºC and 850ºC (depending on the steam-to-carbon ratio), after which it started to decrease. The increase in syngas partial pressure between ca. 500ºC and 700ºC can be attributed to the increase in CO and H_2 yield with increasing temperatures in the same range.

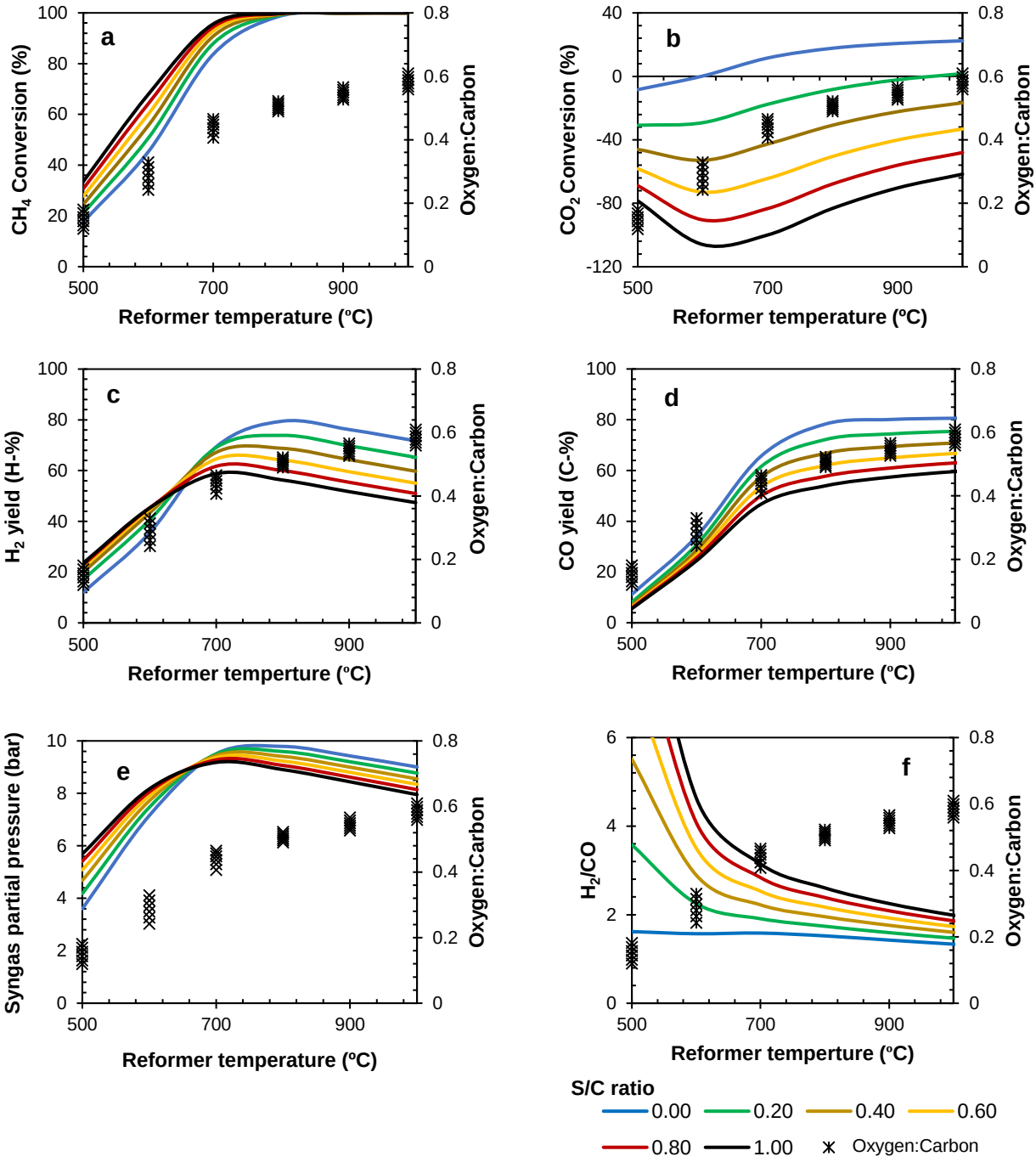

Figure 10-5: The effect of temperature and steam-to-carbon ratio on the (a) CH_4 conversion, (b) CO_2 conversion, (c) H_2 yield, (d) CO yield and (e) syngas partial pressure and (e) product H_2:CO ratio. The oxygen-to-carbon ratio required to maintain adiabatic conditions, at different steam-to-carbon ratios is shown on the secondary axis.

The decrease in the syngas partial pressure above ca. 700ºC can be attributed to the H_2 yield decreasing at a similar point, as well as the influence of the increasing concentration of inert N_2 (more air is required for adiabatic operation with increasing temperatures). Increasing the steam-to-carbon ratio improved

the partial pressure of syngas in the tri-reformer product at low temperatures and decreased it at high temperatures. This is similar to the trend for H_2 yield.

An increase in temperature had a strong negative effect on the H_2/CO ratio (Figure 10-5 (f)) for all steam-to-carbon ratios. At a S/C = 0.4, a temperature increase from 500°C to 700°C decreased the H_2/CO ratio from 5.5 to 2.2. Above 700°C the effect of temperature had a weaker effect. At a S/C = 0.4, an increase in temperature from 700°C to 900°C resulted in a decrease from 2.2 to 1.8. Increasing the S/C improved the H_2/CO ratio significantly, especially at low temperatures. Interestingly, this data suggests that at temperatures as low at 750°C, a S/C ratio of less than 0.3 may be used to achieve a H_2/CO ratio appropriate for the Fischer-Tropsch synthesis

10.3.2. Water-gas shift reactor

Figure 10-6 shows the sensitivity analysis for the water-gas shift reactor, including the change in exit H_2/CO ratio with (a) additional steam addition (S/C ratio) and (b) catalyst weight, at different feed temperatures, for a feed consistent with the base case (Stream 8, Table 10-2) for the product of a tri-reformer operating adiabatically at 750°C with a S/C ratio of 0.3 and an O_2/C ratio of 0.475. The additional S/C ratio in the x-axis of Figure 10-6 refers to the water entering the WGS unit from Stream 9 (Table 10-2, Figure 10-1), rather than the water left over after the tri-reformer. Figure 10-6 (a) is calculated for a catalyst weight of 0.03 kg whilst Figure 10-6 (b) is calculated for an additional steam-to-carbon ratio of 0.2.

Increasing the water-gas shift temperature and additional S/C ratio increased the exit H_2/CO ratio to varying extents (Figure 10-6 (a)). Without any additional water, the H_2/CO ratio could be shifted from under 2 to 2.3 by increasing the inlet temperature from 210°C to 310°C due to an enhanced rate of reaction per gram catalyst (Equation 10-1). As the temperature in the water-gas shift unit is controlled by a cooler after the tri-reformer, the exit H_2/CO ratio could be controlled by the coolant flow rate without the need for excess water addition. This is a benefit as it decreases the requirements of the water knock out pots and compressors downstream.

Figure 10-6 (a) further shows that increasing the S/C ratio increased the H_2:CO ratio with a more significant effect at higher temperatures. Luckily, in order to satisfy the requirements of the hydrocracker, even at extremely high H_2:HC ratios (4000 m_n^3/m^3), a H_2/CO ratio of less than 2.4 is required. Thus, the inlet temperature need not be increased above 310ºC.

Figure 10-6 (b) shows the change in H_2:CO ratio with increasing catalyst (Pt/TiO_2) weight for an additional S/C ratio of 0.2. Increasing the catalyst weight between 0 to 0.04 kg increased the exit H_2:CO ratio, with larger gradients at higher temperatures. A catalyst weight between 0.03 and 0.04 kg would easily be able to meet the requirements of this process (H_2:CO ratio between 2 and 2.4).

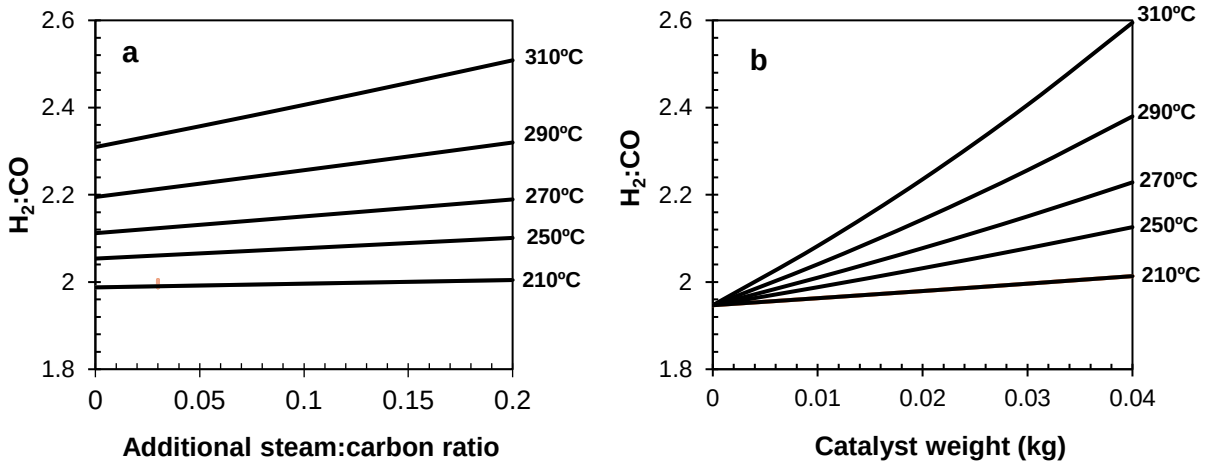

Figure 10-6: Sensitivity analysis of the water gas shift reactor showing the change in exit H_2/CO ratio with (a) extra steam addition for 0.03 kg of catalyst and (b) catalyst weight at an additional S/C ratio of 0.2. Feed and inlet conditions as presented in the base case stream table (Stream 8, Table 10-3).

10.3.3. Optimal conditions for tri-reformer / water-gas shift

Choosing optimal conditions for the tri-reformer requires the balancing of two objectives: optimising the carbon yield and ensuring that the desired H_2:CO ratio is attained after the water-gas shift unit. In theory, this appears to be a simple task of optimising the carbon yield of the tri-reformer (low steam-to-carbon ratio and a high temperature) and using the water-gas shift reactor to adjust the H_2:CO ratio (which decreases with temperature). However, as the water-gas shift unit converts CO into CO_2, the carbon yield decreases significantly in this step.

Figure 10-7 shows the CO yield of the reformer product and the water-gas shift product for the case where an H_2:CO ratio of 2 (no hydrocracking) and 2.4 (hydrocracking with extremely high H_2:HC ratio) is required. This analysis is based on a reformer (at a range of temperatures) operating adiabatically with a S/C ratio of 0.3 and an O_2/C ratio of 0.475 (as per the base case stream table presented in Table 10-2). The water-gas shift is operating at 280ºC with an additional S/C ratio of 0.2. The catalyst weight in the water-gas shift reactor is increased from 0.01 to 0.1 in each case such that the desired H_2:CO ratio

(2 or 2.4) may be attained. Figure 10-7 also shows the corresponding H_2:CO ratios for each case (in red).

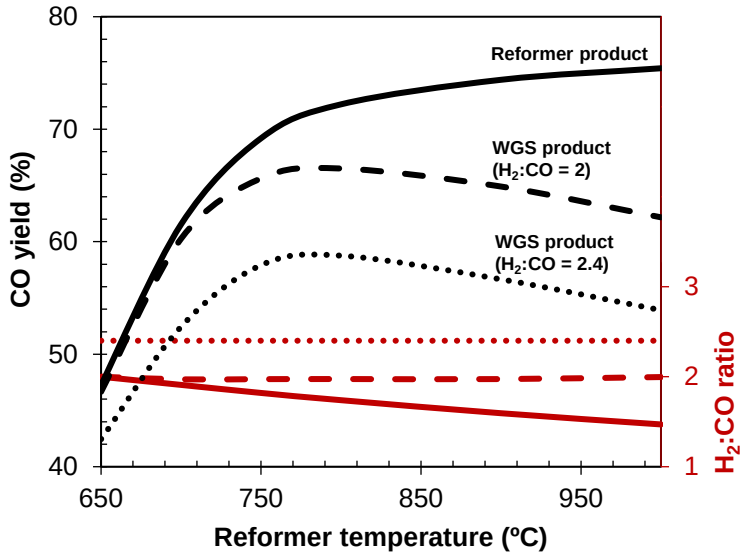

Figure 10-7: The CO yield (●) and H_2:CO ratio (●) for the reformer product (—) and the water-gas shift product after shifting the H_2:CO ratio to 2 (---) and 2.4 (···) for various reformer temperatures. Reformer S/C ratio = 0.3 and O_2/C ratio = 0.475. Water gas shift S/C ratio = 0.2 and T = 280ºC. Water-gas shift catalyst weight adjusted between 0.01 and 0.1 to attain desired H_2:CO ratio.

The CO yield after the reformer increased from < 50% to 75% between 650ºC and 1000ºC, as shown in both Figure 10-7 and Figure 10-5 (d). Over the same range, the reformer product H_2:CO ratio decreased from 2 to 1.5 (Figure 10-7 and Figure 10-5 (f)). Thus, increasing the reformer temperature increases the CO yield but also increases the requirement on the water-gas shift unit.

Once the reformer product is fed through the water-gas shift unit in order to correct the H_2:CO ratio (to between 2 and 2.4), the shape of the overall CO yield curve changes to a parabolic-type trend. At high temperatures, whilst the reformer has a high CO yield, the H_2:CO ratio is so low that, in shifting it, the CO yield decreases significantly. An optimal CO yield for the syngas generation system was found at a reformer temperature between 750ºC and 800ºC.

10.3.4. Cold condensate

The first separation of Fischer-Tropsch products is done at 20 bar and 220°C in the Fischer-Tropsch reactor itself, where a liquid stream and vapour stream leave the reactor. The cold condensate, thereafter, is separated off from the light gasses (CH_4, CO, CO_2, H_2, N_2, C_2-C_{10}) in the vapour stream. Figures 10-

8 (a) and (b) show the effect of the cold condensate temperature and pressure on the amount and distribution of products (C_2-C_{40}) recovered in the liquid phase. For Figure 10-8 (a), the pressure is constant at 19 bar, whilst for Figure 10-8 (b), the temperature is kept constant at 50°C. The arrow indicates the change that is required from Fischer-Tropsch conditions. The hydrocarbon distribution of the Fischer-Tropsch synthesis products is shown in both cases (red dotted line).

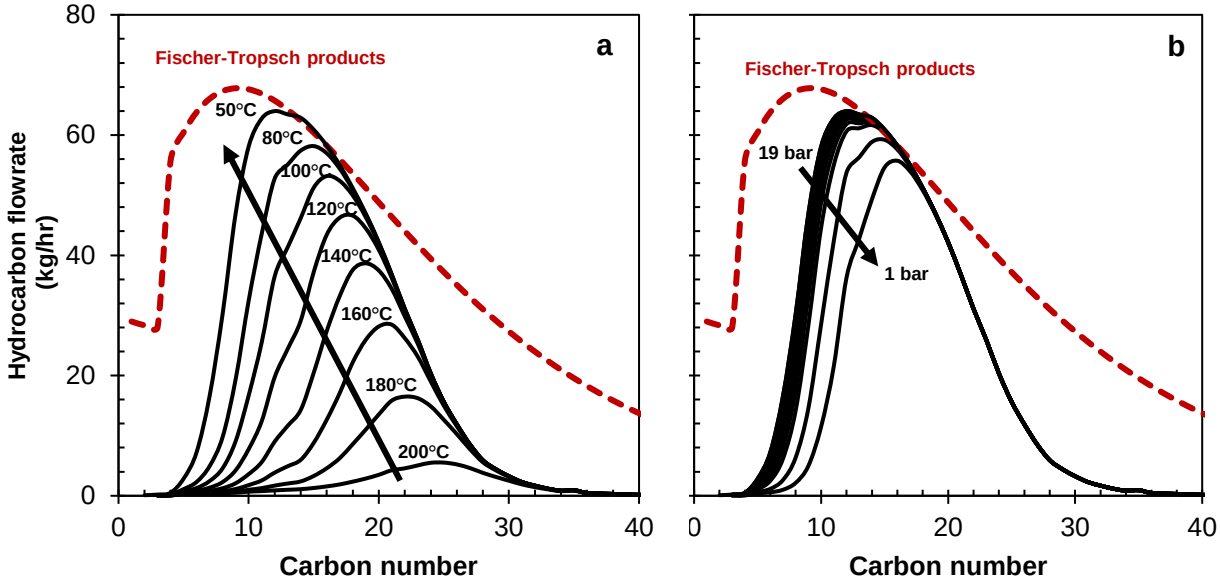

Figure 10-8: Sensitivity analysis of the cold condensate flash showing the effect of (a) temperature at 19 bar and (b) pressure at 50°C on the product distribution recovered as liquid cold condensate from the vapour stream leaving the Fischer-Tropsch reactor.

At temperatures close to Fischer-Tropsch conditions (200°C), the flash was relatively inefficient in ensuring high yields of distillate (C_{10}-C_{22}) in the liquid product. Instead, only C_{22+} remained as a liquid. Decreasing the temperature increased the total flow of liquid product and the yield of distillate which will be fed into the atmospheric distillation column. The temperature needed to be lowered quite substantially in order to minimize losses to the tail gas. A temperature of approximately 50°C appeared to maximize distillate yield, with only minor losses of C_{10}. Lower temperatures may have improved yield slightly more. However, this would require an enhanced cooling system for the downstream water knock out (limited to 35°C with cooling water).

By decreasing the pressure from 19 bar to 1 bar (Fig. 10-8 (b)), the amount of distillate in the liquid phase decreased, and a significant portion of C_{10}-C_{15} was lost. Thus, maintaining as high a pressure and as low a temperature as possible ensures the best distillate yield.

10.3.5. Pre-hydrocracker flash

The Fischer-Tropsch liquid wax product contains small amounts of distillate (increasing with conversion), which can be over-cracked in the hydrocracker as discussed in Chapter 9. Thus, depending on the composition of the Fischer-Tropsch wax, a pre-hydrocracker flash may be needed to separate off distillate from wax before it enters the hydrocracker. Figure 10-9 (a) and (b) show the effect of the temperature (at 1 bar) and pressure (at 370°C) of the pre-hydrocracker flash on the product distribution of liquid wax entering the hydrocracker for a Fischer-Tropsch system operated at X_{CO}=60%.

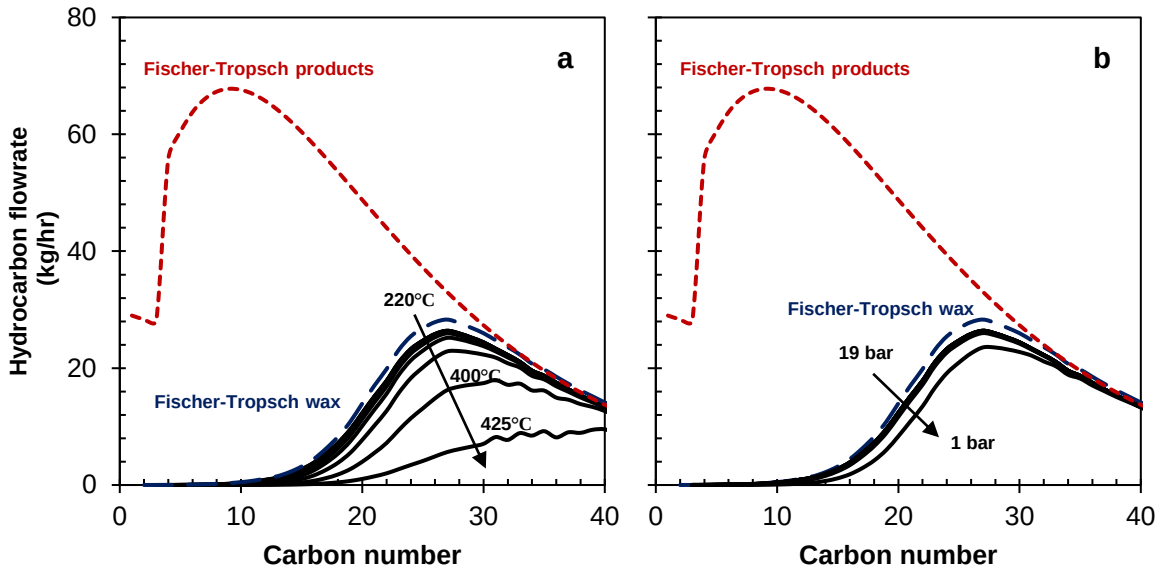

Figure 10-9: Sensitivity analysis of the pre-hydrocracker flash showing the Fischer-Tropsch products (--), the Fischer-Tropsch wax products (--) and the resulting liquid products of the pre-hydrocracker flash (-) at different (a) temperatures at 1 bar and (b) pressures at 370°C.

By increasing the temperature, and decreasing the pressure, more distillate could be removed via the gas phase, thus avoiding over-cracking in the hydrocracker. However, at this Fischer-Tropsch conversion (X_{CO} = 60%) very extreme conditions (425°C and 1 bar) were required to separate off most of the distillate at the expense of heavier wax fractions that could be converted in the hydrocracker. Temperatures as high as 425°C would likely result in the thermal cracking of hydrocarbons. Thus, at a Fischer-Tropsch conversion of X_{CO} = 60%, the pre-hydrocracker flash does not appear to be practical. At higher Fischer-Tropsch conversions, the Fischer-Tropsch product distribution tends towards lighter products, thus the flash, operating at a lower temperature, may be useful to improve overall distillate yield.

10.3.6. Hydrocracker

The hydrocracker selectivity and conversion were estimated based on experimental data reported by Leckel and Liwanga-Ehumbu [215] at 370°C and 35 bar for a hydrogen-to-wax ratio of 1200 m^3/m^3. The hydrocracker was fed with Fischer-Tropsch wax (ideally C_{22+}), which was hydrocracked to lighter hydrocarbons, increasing the distillate yield. This increase in distillate yield may be shown by comparing the hydrocarbon distribution of the Fischer-Tropsch products before and after hydrocracking.

Figure 10-10 shows the hydrocarbon distribution of the (—) Fischer-Tropsch products (Stream 24, Figure 10-3) and the (---) combined liquid products fed to the distillation column after separation and hydrocracking (Stream 42, Figure 10-3). Stream 42 contains the products from the hydrocracker, the cold condensate flash and the pre-hydrocracker flash. This analysis was conducted for a feed generated by the Fischer-Trospch synthesis operating at a conversion of X_{CO} = 60, 70, 80 and 90% .

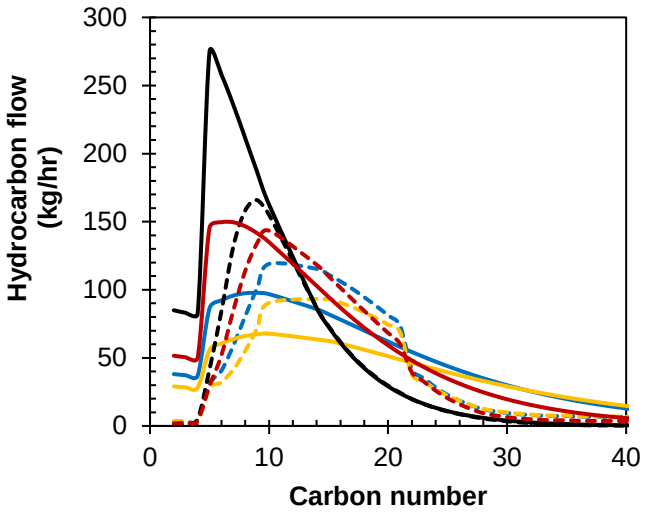

Figure 10-10: The hydrocarbon distribution of the Fischer-Tropsch synthesis products in Stream 24 (—) and the hydrocarbon distribution of the feed to the atmospheric distillation column in Stream 42 incl. the hydrocracking product (---) for a feed generated by operating the Fischer-Tropsch synthesis at a conversion of ● 60%, ● 70%, ● 80%, ● 90%

Figure 10-10 shows that hydrocracking the Fischer-Tropsch wax resulted in an increased distillate flow rate and decreased heavy hydrocarbons flow rate (C_{22+}). The decrease in light components of the Fischer-Tropsch product (—) was due to separation in the cold condensate, rather than hydrocracking.

Increasing conversion, as discussed in Chapter 9, shifted the product distribution towards lighter hydrocarbons. This meant that for higher Fischer-Tropsch conversions, there was less wax to hydrocrack. As there was a decrease in Fischer-Tropsch wax products with increasing conversion (due to decreasing alpha values), the improvement of the distillate yield after hydrocracking decreased accordingly. For a Fischer-Tropsch conversion of X_{CO} = 60%, 70%, 80% and 90% the C_{10} - C_{22} distillate yield was improved by 40%, 28%, 12% and 0.6% due to hydrocracking respectively. This clearly demonstrates that, based on the improvement of the yield, the hydrocracker can only be justified if the conversion of CO in the Fischer-Trospch synthesis is limited.

10.3.7. Atmospheric distillation

The atmospheric distillation column is central to the separation and refining section. To minimize the equipment in this plant, a single distillation column was utilized with the distillate being pulled out as a side stream as shown in Figure 10-11. The column was designed with 8 stages. The feed was fed to the column on stage 2 whilst the distillate side stream was pulled off from stage 7. These column specifications were based on the sensitivity analysis presented in Appendix J.

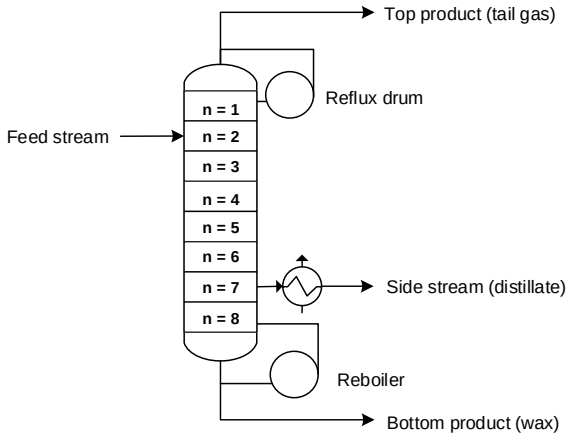

Figure 10-11: Atmospheric distillation column showing the number of stages as well as the feed stage and the side stream product stage based on the sensitivity analysis in Appendix J.

The main objective of the distillation column is to maximize the overall carbon yield of distillate, whilst producing a distillate that meets the regional specifications of diesel (see Section 9.5.3). The amount of product drawn out of the side stream, whilst maintaining the column within its operation limits, determines the distillate yield. However, the yield is limited by two distillate specifications: the flash point temperature limit, controlled by the number of light hydrocarbons, and the upper distillation temperatures (T_{90} and T_{95}), controlled by the number of heavy hydrocarbons.

This means that the distillation column conditions need to be optimised to maximise distillate side stream flow whilst also trying to minimise the fraction of light and heavy hydrocarbons. Figure 10-12 shows the effect of the (a) distillate side stream flowrate, (b) column feed temperature, (c) reboiler duty and (d) reflux ratio on the distribution of distillate in the side stream. The column feed (⋯) is also shown, based on the base case scenario (Stream 42 in Table 10-4).

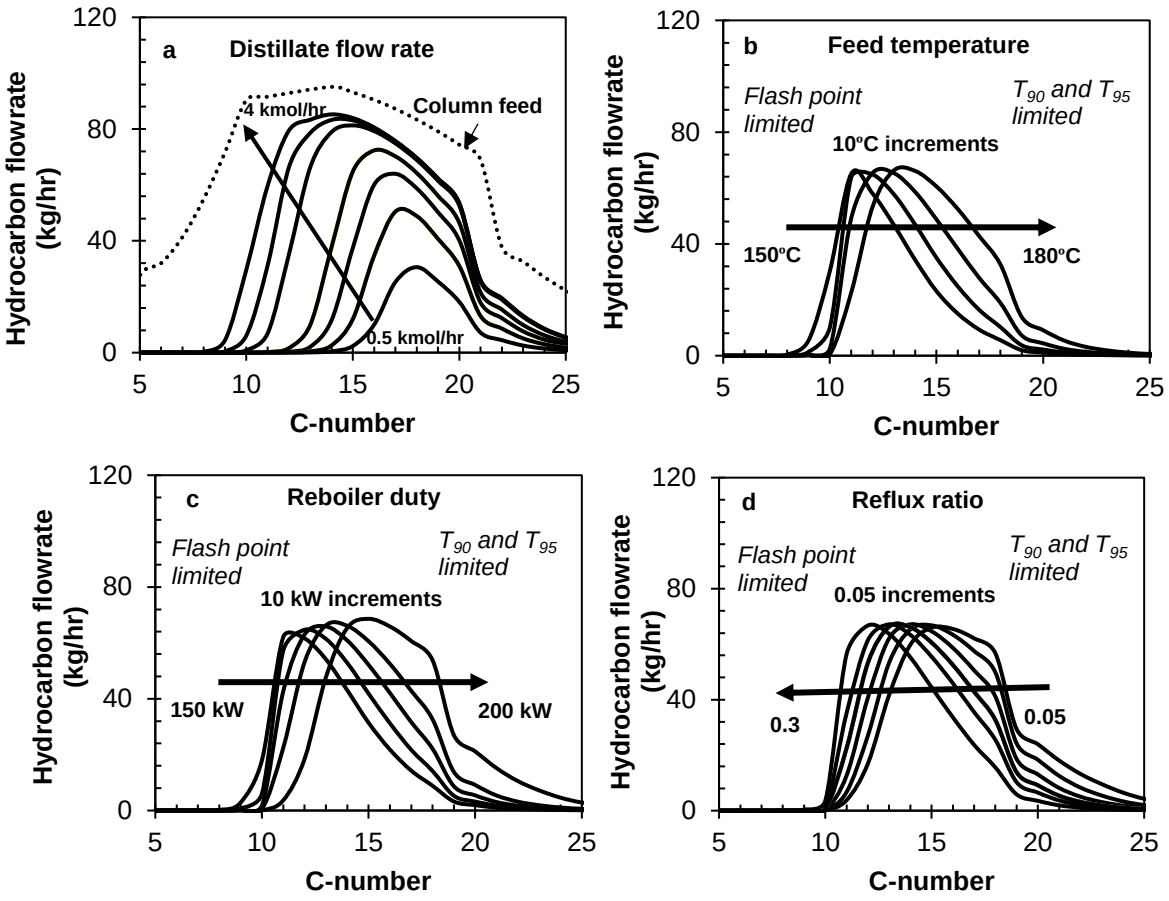

Figure 10-12: Sensitivity analysis of the atmospheric distillation column showing the change in the side stream distillate hydrocarbon distribution as a function of (a) side stream flow rate, (b) inlet temperature, (c) reboiler duty and (d) reflux ratio.

Figure 10-12 (a) shows the effect of increasing the flow rate of the distillate pulled off the side stream (Stream 44, Figure 10-3) on the hydrocarbon distribution of that stream for a column feed temperature of 180ºC, a reflux ratio of 0.2 and a reboiler duty of 180 kW. Increasing the distillate flow rate increased the size and width of the distillate hydrocarbon distribution, with a more significant effect towards the light range of hydrocarbons. The distillate side stream flow rate can be maximised by moving as close to the column feed distribution (⋯) as possible without breaching the flash point and T_{90} T_{95} limits.

In order to achieve this maximum, a certain level of flexibility is required to shift the distillate distribution towards the light and heavy range, so as to stay within the region that satisfies both specifications. This flexibility may be achieved by adjusting the column feed temperature, reboiler duty or reflux ratio. The effect of the feed temperature on the resulting distillate distribution is shown in Figure 10-12 (b), for a reboiler duty of 180 kW and a reflux ratio of 0.2. Increasing the inlet temperature shifted the product distribution towards higher carbon numbers, without significantly changing the shape of the distribution. The reboiler duty had a similar effect (Figure 10-12 (c)). By increasing the reboiler duty from 150 kW to 200 kW (keeping the feed temperature constant at 180ºC and the reflux ratio at 0.2), the product distribution was shifted towards the heavier products. The reflux ratio had the opposite effect. Figure 10-12 (d) shows the effect of increasing the reflux ratio from 0.05 to 0.3 at a constant feed temperature of 180ºC and a reboiler duty of 180 kW. By increasing the reflux ratio, the distribution was shifted towards lighter hydrocarbons.

Lower Fischer-Tropsch conversions (e.g. X_{CO} = 60) result in a larger fraction of heavy hydrocarbons, thus lower feed temperatures, lower reboiler duties and/or higher reflux ratios may be required. Operating without a hydrocracker would also increase the fraction of heavy hydrocarbons in the column feed, thus requiring similar conditions.

10.3.8. Steam turbine

The only variables that could be adjusted on the turbine section were the feed rate of water to the boiler, the feed rate of air to the combustion unit, and the exit pressure of the pump. Since the feed rate of water was a manipulated variable in the control of the exit temperature of the boiler (set to 620ºC), only the latter two variables were used for sensitivity and optimization.

Figure 10-13 shows the effect of the oxygen: feed (O:F) molar ratio on the power generated by the steam turbine. As the flow rate of air, and thus oxygen, was increased so too was the power generated by the steam turbine up to an O:F ratio of 0.32. This can be attributed to oxygen acting as a reactant in the exothermic combustion reaction. Oxygen increased the amount of energy produced in the exothermic reaction, which in turn increased the temperature of the gas leaving the combustion unit and thus the amount of heat that could be transferred to water to produce high pressure steam. As the amount of water was adjusted to ensure an exit temperature from the boiler of 620°C; an increase in the temperature of the combustion gas resulted in more water that was turned into steam and thus a greater turbine output. Above an O:F ratio of 0.32 oxygen and nitrogen were simply acting as inert gasses, decreasing the temperature of the combustion products and thus decreasing the power produced by the turbine. Thus, an O:F ratio of 0.32 appears to be an optimal feed ratio for power production.

Figure 10-14 shows the effect of the water pump exit pressure on the power generated by the steam turbine. Steam turbines can typically operate at pressures from as low as 2 bar up to super critical steam pressures of 250 bar [236]. Increasing the pressure of pumped water increased the power generated by the steam turbine, albeit more significantly up to 60 bar (5.7 MW), after which the rate of improvement decreased slightly, with only 1 MW extra (6.7 MW) being generated between 60 bar and 250 bar. The power required to pump the water increases linearly between 0 MW and 0.3 MW within the range. Whilst this is not significant enough to create a maximum in terms of the net power production, operation above 100 bar appears to be the point at which the increase levels out and, thus, an optimal operating condition.

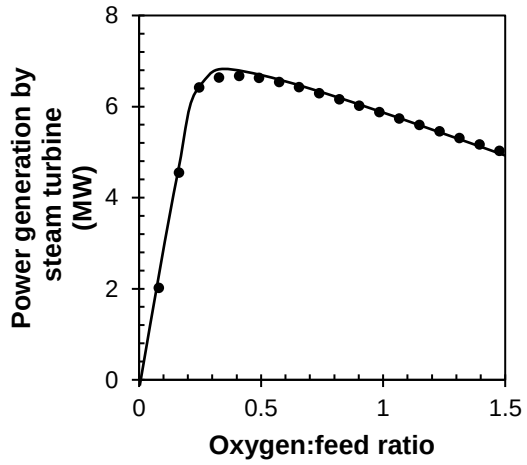

Figure 10-13: Effect of the oxygen: feed ratio to the combustion unit on the power generation by the steam turbine at a pump exit pressure of 100 bar.

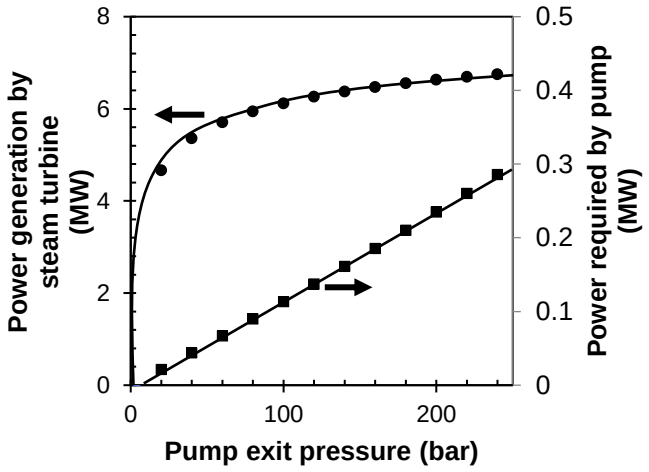

Figure 10-14: Effect of pump exit pressure on power generation of the steam turbine (left axis) and power required for the pump (right axis) at an oxygen:feed ratio of 0.5.

10.4. Optimised carbon flow for base case

Using the biogas-to-distillate plant model and the results from the sensitivity analysis, an optimised base case (Fischer-Tropsch conversion of X_{CO} = 60%, using Pt-Co/Al_2O_3 with a hydrocracker) was created. Figure 10-15 shows the carbon flow diagram for the optimised base case, indicating how carbon from the biogas was converted into various products across the plant. The variables used in each section of the optimised case are shown in Table 10-6.

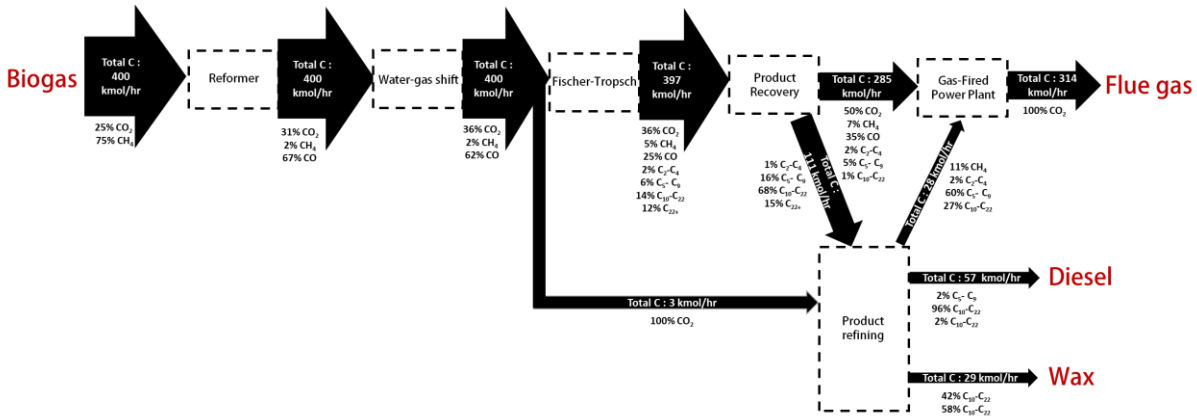

Figure 10-15: Carbon flow diagram of the Fischer-Tropsch plant operating at X_{CO} = 60% showing the distribution of carbon throughout the plant, including the distribution of carbon in (C-%) of different species in each section.

The overall feed to the plant was 400 kmol/ h biogas, with a composition of 25% CO_2 and 75% CH_4. The biogas was fed into the tri-reformer operated at 750ºC and 2.7 bar, which achieved a CH_4 conversion of 97%. Unfortunately, the CO_2 conversion remained low in this step (see Figure 10-5 (b)). The resulting syngas was reacted further in the water-gas shift unit, which converted CO and H_2O into CO_2 and H_2 in order to adjust the H_2:CO ratio. Just before entering the Fischer-Tropsch reactor, residual CO_2 was removed from the stream through the H_2 membrane.

The syngas stream then entered the Fischer-Tropsch reactor, which converted CO (at a conversion of X_{CO} = 60%) into longer-chain hydrocarbons. The stream exiting the Fischer-Tropsch reactor contained 36 C-% CO_2, 5 C-% CH_4, 25 C-% CO, 2 C-% C_2-C_4, 6 C-% C_5-C_9, 14 C-% C_{10}-C_{22} and 12% C_{22+}. The overall carbon yield to distillate range hydrocarbons (C_{10}-C_{22}) at this point was only 14-C%. The product recovery section split the Fischer-Tropsch products into tail gas (286 kmol carbon/hr, 1 C-% C_{10}-C_{22}) and liquid products (111 kmol carbon/hr, 67 C-% C_{10}-C_{22}) with minimal distillate losses. The hydrocracker in this section improved the distillate yield such that the overall carbon yield of C_{10}-C_{22} in the feed to the refining section was 19 C-%.

Table 10-6: Summary of key unit operations and the Aspen Plus block or modelling algorithm used in the development of the once-through biogas-to-distillate plant.

Unit label (Chapter 9)	*Unit operation*	*Aspen Plus Block or Modelling Algorithm*	*Input conditions*
Syngas generation			
V-101	Tri-reformer	RGibbs	T=750°C/ P = 2.7 bar / Selectivities calculated at equilibrium
V-102	Water-gas shift reactor	RPlug	Adiabatic/ T_0=280°C/P = 2.7 bar / Rate calculated according to [225]
C-101	Biogas and air compressor	Compr	P = 2.71 bar
P-101	Feed water pump	Pump	P = 2.71 bar
E-103	Compressor feed cooler	Compr	P= 2.71 / T = 35°C
C-102, C-103, D-101, D-102, D-103, 104, E-105	Fischer-Tropsch feed compressor with inter-stage cooling and water knockout	Compr/ Flash/ Heater	P_1=7.3 bar / P_2=20 bar / inter-stage cooling = 35°C / inter-stage water knockout/ isentropic efficiency = 76%
M-101	Membrane	Modelled using equation 10-1 and data from [216]	Selectivity and permeability based on [216]
Fischer-Tropsch synthesis			
V-103	Fischer-Tropsch reactor	Modelled using experimental data from [176]	X_{CO} = 60, 70, 80 and 90%
E-106	Fischer-Tropsch feed heater	Heater	P = 20 bar / T = 220°C
Separation and refining			
C-104	Hydrogen compressor	Compr	P_{exit} = 35 bar
D-104	Cold condensate	Flash	P= 19.5 bar/ T = 50°C
D-105	Pre-hydrocracker flash	Flash	P=1 bar/ T = 370°C
D-106	Water flash	Flash	P = 19 bar / T = 35°C
P-102	Hydrocracker pump	Pump	P_{exit} = 35 bar
S-101	Atmospheric distillation	RadFrac	P= 1 bar/ T= 150°C – 200°C / Reboiler duty = 90 kW – 210 kW / Partial condenser/ Reflux ratio = 0.2 /8 stages / Feed stage = 2 / Split stage = 7
V-104	Hydrocracker	Modelled using experimental data from [215]	Conversion = 81%, P = 35 bar, T = 370°C
E-107	Fischer-Tropsch product cooler	Heater	P= 19.5 bar/ T = 50°C
E-108	Water knockout cooler	Heater	P = 19 bar / T = 35°C
E-109	Hydrocracker heater	Heater	P = 35 bar/ T = 370°C
E-110	Distillation feed heater	Heater	P = 1 bar/ T= 150°C – 200°C
Power generation	*Power generation*		
T-101	Gas turbine	Compr (turbine)	P_{exit}= 1 bar/ isentropic efficiency = 38%
T-102	Steam turbine	Compr (steam)	$P_{exit=}$ 1 bar / isentropic efficiency = 76%
V-105	Combustion unit	RGibbs	Adiabatic, P = 1 bar
E-112	Power plant feed heater	HeatX	Counter-current, $T_{cold,out}$ = 390°C, ΔT = 10°C
E-113	Steam boiler	HeatX	Counter-current, $T_{cold,out}$ = 620°C, ΔT = 10°C
E-114	Condenser	HeatX	Counter-current, $T_{cold,out}$ = 50°C, ΔT = 10°C
P-103	Water pump	Pump	P_{exit} = 100 bar

In order to meet the legal specifications of diesel, excluding density, the distillate was refined in an atmospheric distillation column into tail gas, distillate and wax. This is where the largest losses of C_{10}-C_{22} hydrocarbons were found. The wax stream had a carbon flow rate of 29 kmol carbon/ h of which 42% was C_{10} - C_{22}. This does not necessarily represent lost distillate as this wax stream could be recycled back to the hydrocracker (see Section 9.5.4.3) albeit this has not been implemented at this stage of the once-through design. A total of 57 kmol carbon/ h on-spec distillate was produced via the side stream, of which 96% was C_{10}-C_{22}. The overall carbon yield of C_{10}-C_{22} in the final on-spec distillate stream from the atmospheric distillation column was 14 C-% .

The remaining light hydrocarbons were combined with the pressurized tail gas which contained all the remaining CO_2, CH_4 and CO. This was combusted in the power plant resulting in a product stream of 314 kmol/ h of CO_2 and a gross power production of 8.5 MW.

10.5. Plant evaluation

The biogas-to-distillate plant was evaluated based on 16 optimised scenarios including Fischer-Tropsch conversions of X_{CO} = 60%, 70%, 80% and 90%, a choice of catalyst between Pt-Co/Al_2O_3 and Mn-Pt-Co/Al_2O_3 and the presence or absence of a hydrocracker. In each case, two main criteria were analysed: the amount of on-spec distillate produced and the gross and net power production (MW) from the power plant.

The fixed variables for all conversions in this evaluation are shown in Table 10-6. Variables that were altered in each scenario include the temperatures of the flash tanks in the product recovery and refining section as well as the reboiler duty, distillation column feed temperature and side stream flowrate.

10.5.1. Optimized product distribution at different conversions

Figure 10-16 shows the optimised distillate product distribution (withdrawn from the side stream of the atmospheric distillation column) for a Fischer-Tropsch conversion of (a) 60%, (b) 70%, (c) 80% and (d) 90% using Pt-Co/Al_2O_3 with hydrocracking. The Fischer-Tropsch distribution before separation and refining is shown in black, albeit CH_4 has been removed for scaling purposes.

Increasing the Fischer-Tropsch conversion level from 60% to 90% resulted in a narrower product distribution shifted to lower carbon numbers. The optimised distillate distributions were calculated such that the distillate flowrate was maximized whilst remaining within the specifications set by AFRI-5 and SANS 342 and, where no other specification exists, EN 590:2014. The distillate had a much narrower

product distribution. However, the product flow rate in the range C_{10}-C_{16} in the distillate stream is larger than the flow rate of these compounds leaving the Fischer-Tropsch reactor for a CO-conversion in the Fischer-Tropsch synthesis is 60% or 70%, showing the benefit of the hydrocracker to improve the yield of distillate for lower conversions (see Figure 10-10).

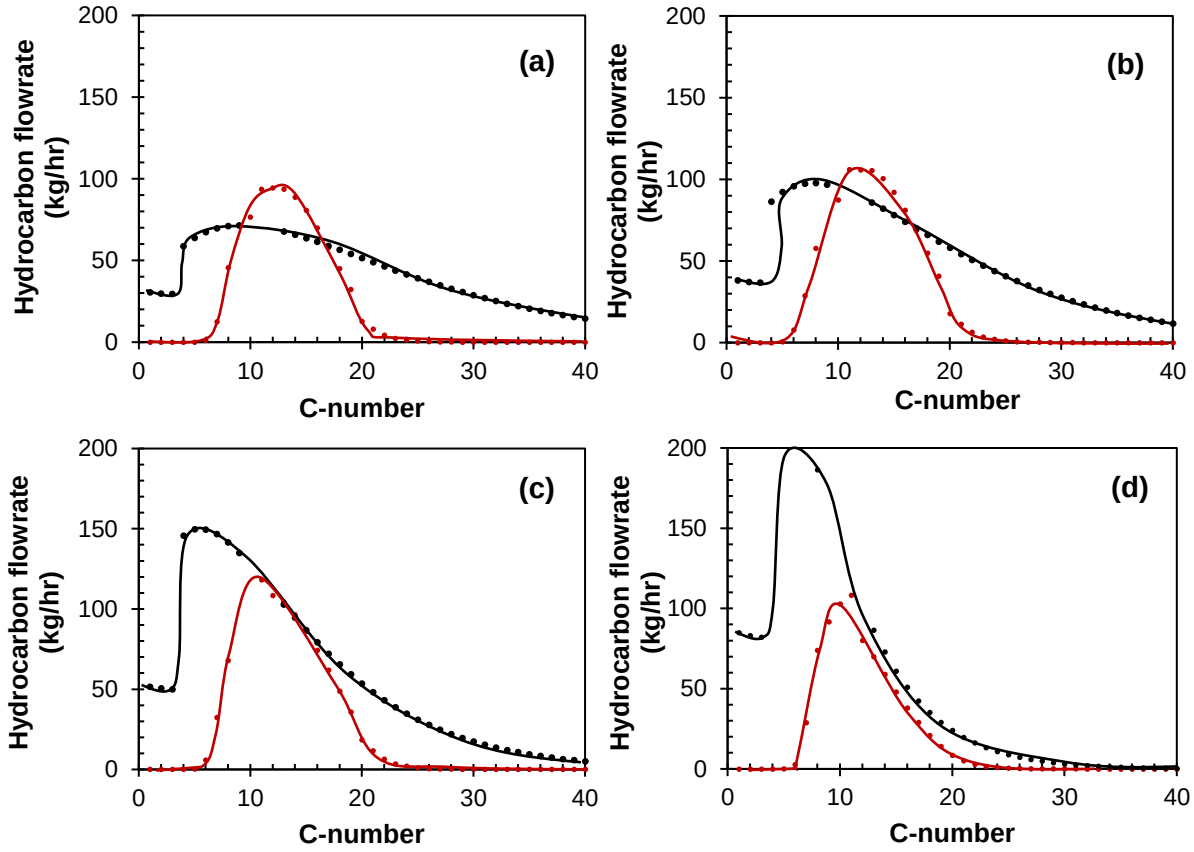

Figure 10-16: Mass hydrocarbon distribution C_2 to C_{40} product compounds for ─ Fischer-Tropsch products and ─ side stream distillate (distillate product) for X_{CO} = (a) 60%, (b) 70%, (c) 80% and (d) 90% for Pt-Co/Al_2O_3 for the case with a hydrocracker.

The specifications of the fuel produced (side stream distillate) in the optimised cases for X_{CO} from 60% to 90% for Pt-Co/Al_2O_3 are shown in Table 10-7 (all 16 cases are shown in Appendix K). For each case, the yield was optimised whilst trying to stay within the limits of the specifications. The optimised distillate distribution was limited by the flash point on the lighter end and the distillation profile on the heavier end. For each case, all specifications except the density were adhered to.

Table 10-7: Specifications of fuel produced in the optimised case for Pt-Co/Al_2O_3 with a hydrocracker.

				Conversion			
	EN 590:2014 (EU)	**AFRI-5 2016 (AU)**	**SANS 342:2016 (ZA)**	60%	70%	80%	90%
Diesel Density at 15°C	820	820-880	805-850	743	741	740	741
Water, ppm	200	- [a]	250	3	52	24	9.6
Cetane number min	51	49	51	91	90	90	89
Flash Point, °C	55	-[a]	-[a]	67	60	60	67
Cloud Point, °C	-10 to -34	-[a]	+6	-26	-17	-30	-21
Distillation							
T_{95}	360	-[a]	362	350	355	360	350
T_{90}			360	335	337	337	330
	[202]	[203]	[204]				

[a] No limit specified

10.5.2. Optimal conversion

The optimised product distribution for on-spec distillate was calculated for each of the 16 cases including 4 conversions (X_{CO} = 60% to 90%), 2 catalysts (Pt-Co/Al_2O_3 and Mn-Pt-Co/Al_2O_3) and cases with and without hydrocracking. From each of these optimised scenarios, the overall fuel production was calculated and shown in Figure 10-17, with yields shown in Table 10-8.

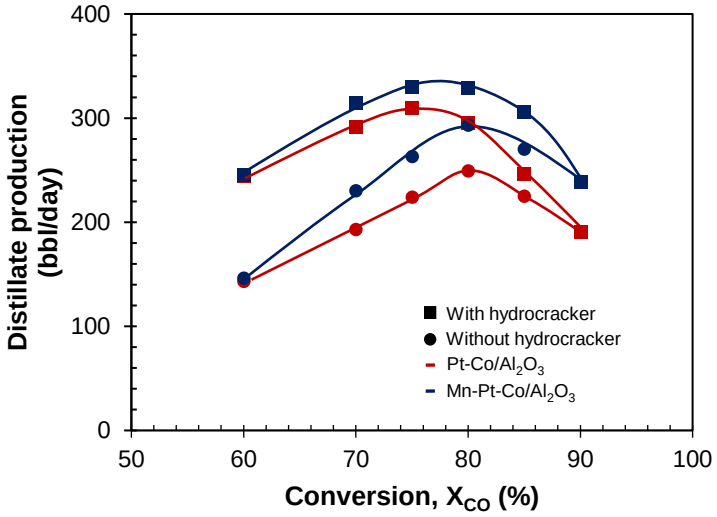

Figure 10-17: Distillate production as a function of conversion for Pt-Co/Al_2O_3 and Mn-Pt-Co/Al_2O_3 with and without hydrocracking.

Table 10-8: Refining and overall yield of distillate range product for the optimised version of each case.

		Conversion			
Catalyst		60%	70%	80%	90%
		Overall carbon yield of distillate from biogas (C-%)			
Pt-Co/Al_2O_3	With hydrocracker	14	16	16	11
	Without hydrocracker	8	10	14	11
Mn-Pt-Co/Al_2O_3	With hydrocracker	14	17	18	13
	Without hydrocracker	8	12	16	13

For a Pt-Co/Al_2O_3 catalyst with hydrocracking (base case) a Fischer-Tropsch conversion of X_{CO} = 60% resulted in a production of distillate of 244 bbl/day. Increasing the conversion increased the distillate production up to a maximum of 310 bbl/day at ca. X_{CO} = 75%. The distillate production then dropped off sharply as the conversion was increased to X_{CO} = 90%, obtaining only 190 bbl/day.

Operating a Pt-Co/Al_2O_3 catalyst without a hydrocracker resulted in significantly less distillate production. This effect was most significant at X_{CO} = 60% (143 bbl/day). The maximum conversion for this case was shifted from X_{CO} = 75% to X_{CO} = 80% with a production of only 249 bbl/day. Past the maximum there was also a strong decrease in productivity, reaching a minimum of 190 bbl/day, equal to the case of Pt-Co/Al_2O_3 with a hydrocracker. This confirmed that, for very high conversions, a hydrocracker may be redundant.

The manganese-promoted catalyst Mn-Pt-Co/Al_2O_3 seemed to produce roughly equal amounts of distillate as its unmodified counterpart for the lower conversion of X_{CO} = 60% (245 bbl/day and 146 bbl/day for case with and without hydrocracking respectively). On increasing the conversion, however, Mn promotion seemed to have a progressively more significant effect on distillate production. At Fischer-Tropsch conversions of 70%, 80% and 90%, the distillate production was 314, 329 and 239 bbl/day respectively which represented a relative improvement over the unmodified Pt-Co/Al_2O_3 of 8%, 12% and 25% respectively for the case with a hydrocracker. Additionally, the productivity seen over the Mn- promoted catalyst was less influenced by the change in conversion than the unmodified catalyst. As a result, this system would be less sensitive to shifts in conversion due to external disturbances.

Operating Mn-Pt-Co/Al_2O_3 in a system without a hydrocracker, decreased the distillate production significantly at low conversion, with an insignificant effect when moving to X_{CO} = 90%. Nevertheless, it seems advisable to operate the manganese promoted catalyst at a conversion of X_{CO} = 80% in combination with a hydrocracker to maximise the diesel yield (18 C-%) and production (329 bbl/dday).

It is important to note, that the maximum distillate production for both Pt-Co/Al_2O_3 and Mn-Pt-Co/Al_2O_3 require conversions above X_{CO} = 70%. These conditions have been shown to lead to

significant irreversible deactivation via sintering and the formation of cobalt aluminate (Chapter 6), without a change in support material (Chapter 8).

All cases resulted in low overall carbon yields (defined as ratio of carbon in the distillate to the carbon in CO_2 and CH_4 in the biogas) as shown in Table 10-8. Carbon yields range from 8 C-% to 18 C-%, which is consistent with the carbon flow diagram for the base case shown in Figure 10-15. There are several explanations for the low carbon yields seen in this study. Firstly, the very low (net negative) conversion of CO_2 in the tri-reformer resulted in a loss of yield of approximately 25 C-% at the start of the process. Secondly, even with an improved catalyst, the Fischer-Tropsch reactor only produced a fraction within the distillate carbon range, with significant amounts of carbon lost into the wax and naphtha fractions. Finally, a portion of the distillate is lost through the bottoms of the atmospheric distillation column. In reality, the latter could be solved by a liquid recycle from the bottoms of the atmospheric distillation column to the hydrocracker, which was not modelled in this study (see Section 9.5.4.2 for more details).

The low carbon yield is partially attributed to the formation of CO_2 in the anaerobic digestion of municipal waste and the lack of CO_2 conversion in the tri-reformer therefore the yield could be substantially improved by pre-removal of CO_2 from the biogas. Additionally, increasing the Fischer-Tropsch reactor pressure to shift the product distribution to higher carbon numbers (see Table 2-5) may increase the carbon fraction of distillate substantially, especially at higher conversions.

Figure 10-18 shows the effect of conversion on the gross and net power generation for Pt-Co/Al_2O_3 and Mn-Pt-Co/Al_2O_3 with and without hydrocracking. The net power generation was calculated after accounting for the power required to run the three compressors in the syngas generation section as well as the hydrogen compressor (only for scenarios with hydrocracking) and the water pumps (pressures as per Table 10-6).

Conversion, rather than the type of catalyst or the presence or absence of a hydrocracker had the most significant effect on the amount of power generated. At a lower conversion of X_{CO} = 60% the gross power generated ranged from 7.9 MW to 8.5 MW, with Pt-Co/Al_2O_3 producing only slightly more. The net power generation at this conversion was between 2.4 and 3 MW. As the conversion increases, the amount of power generated decreased in all cases, reaching a minimum at X_{CO} = 80%. The gross and net power production increased significantly at X_{CO} = 90% to 8.7 – 9.6 MW and 3.2 - 4.2 MW respectively in all cases. Pt-Co/Al_2O_3 appeared to produce more power across the conversion range, especially at high conversion where the difference between the catalysts was more substantial.

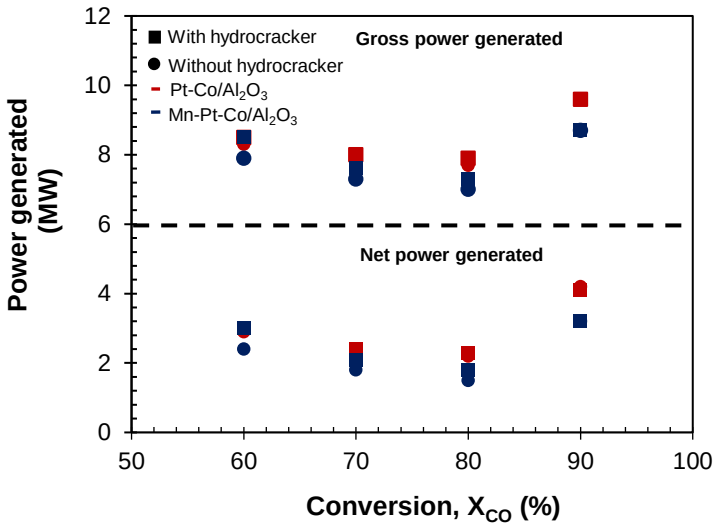

Figure 10-18: Power generated as a function of conversion for Pt-Co/Al_2O_3 and Mn-Pt-Co/Al_2O_3 with and without hydrocracking.

10.5.3. Energy efficiency

The overall energy efficiency of the once-through reactor system and power plant was assessed by analysing the lower heating values (LHV) of the reactants and products as well as the power production in the combined cycle (LHV used rather than HHV as water is emitted as steam in the power generation section). Figure 10-19 shows an illustration of the energy flow throughout the system for the base case of X_{CO} = 60% with a hydrocracker.

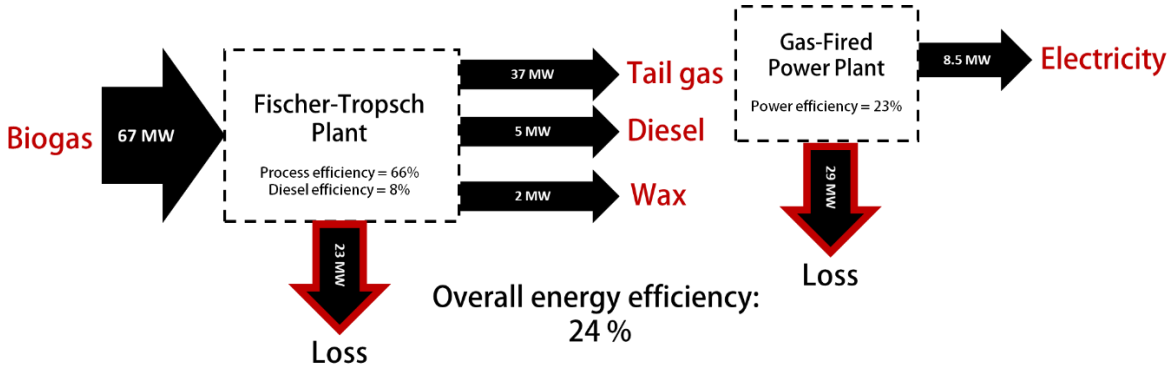

Figure 10-19: Energy balance for base case design X_{CO} = 60% for Pt-Co/Al_2O_3 showing the lower heating values of reactants and products as well as the power generated from the plant with a feed of 400 kmol/h biogas.

The LHV of 400 kmol/h of biogas with composition 75% CH_4 and 25% CO_2 is ca. 67 MW. Throughout the Fischer-Tropsch plant (including reformer, water-gas shift unit, Fischer-Tropsch reactor and refining section) 23 MW is lost to emissions and cooling water etc. At a moderate conversion of X_{CO} =

60%, most of the energy leaves the system as tail gas (37 MW) to the power plant whilst only 5 MW and 2 MW are contained in the distillate and wax respectively. Considering all of the product streams, the overall thermal efficiency of the Fischer-Tropsch process (calculated by the LHV products relative to LHV of biogas) is 66%. The distillate efficiency is only 8%. For a conversion of X_{CO} = 60%, the gas fired power plant has an efficiency of 23%, producing only 8.5 MW (gross) from 37 MW of tail gas with a loss of 29 MW. This is significantly lower than the expected efficiency of ca. 30 – 40 % for steam turbines, showing that design improvements are certainly possible.

Table 10-9 shows the LHV for the reactants and products for conversions 60 % - 90% as well as the gross power generated. The LHV of the tail gas, distillate and wax ranges from 33 - 39 MW, 5.3 – 9.1 MW and 0.6 – 2.1 MW. The difference in the LHV of products is a function of the amount of each product formed rather than the energy density, with X_{CO} = 80% having the highest LHV for distillate and X_{CO} = 90% having the highest LHV for tail gas (with thus translates to the highest electricity generated).

Table 10-9: Lower heating values of reactants and products (MW) as well as power generated as a function of conversion.

CO conversion (%)	*Lower heating value reactants (MW)*	*Lower heating value of products (MW)*			*Power generated (gross)*
		Tail gas	Distillate	Wax	
60	67	36	5.3	2.1	8.5
70	67	34	8.4	1.5	8
80	67	33	9.1	1.5	7.9
90	67	39	6.3	0.6	9.6

Table 10-10 shows the subsequent energy efficiencies of the Fischer-Tropsch process, power plant and overall, for each conversion. The efficiencies don't change significantly with conversion, ranging from 66% - 69% (Fischer-Tropsch process), 23 – 25% for power plant (gross power generated) and 24 – 28% overall. If net power generated is considered (i.e. after power used for compressors and pumps are accounted for) thus satisfying the off-grid requirement, the net efficiency of the overall process is between 16 - 19%.

Table 10-10: Energy efficiencies of the tri-reforming / Fischer-Tropsch process, power plant and overall process.

CO conversion (%)	*Energy efficiency (%)*			
	Fischer-Tropsch process[1]	Power plant (gross)[2]	Overall (gross) [3]	Overall (net) [4]
60	66	23	24	16
70	66	23	27	18
80	65	24	28	19
90	69	25	25	17

[1] LHV of tail gas, distillate and wax relative to LHV of biogas
[2] Gross power generated relative to LHV of tail gas
[3] LHV of distillate and wax as well as power generated (gross) (MW) relative to LHV of biogas
[3] LHV of distillate and wax as well as power generated (net) (MW) relative to LHV of biogas

10.6. Conclusion

A once-through Fischer-Tropsch biogas-to-distillate plant for the production of on-spec distillate from 400 kmol/ h of biogas (75% CH_4/25% CO_2), which can be obtained from municipal waste in Sub-Saharan cities with a population between 200 0000 and 900 000, was evaluated using Aspen Simulation Workbook. Initially, a base case was chosen that consisted of a system operating with a Fischer-Tropsch process operating at X_{CO} = 60% with a Pt-Co/Al_2O_3 catalyst and a partial refining section that included a hydrocracker. This base case was used to analyze the sensitivity of the overall plant design and provide a detailed molar and carbon balance.

In the syngas generation section, the tri-reformer and water-gas shift reactor were tested for their sensitivity to temperature and water feed flow rates. The tri-reformer, modelled according to equilibrium, was found to have very high CH_4 conversions above 750°C, with almost 100% conversion above 800°C. The CO_2 conversions, however, were found to be very low and in most cases negative due to the contributions of the reverse water-gas shift. Yields of both H_2 and CO were found to be high at 750°C. The yield of H_2 decreased at higher temperatures due to the reverse water-gas shift whilst H_2:CO ratios increased with increasing steam-to-carbon ratios and decreased with increasing temperature. The water-gas shift reactor was able to shift the H_2:CO ratio with relative ease by increasing the additional steam input as well as temperature. The optimal reformer temperature (750ºC) was chosen based on the overall CO yield and the outlet H_2:CO ratio after the water-gas shift reactor.

The removal of cold condensate from the vapour stream coming off the Fischer-Tropsch reactor should be done at low temperatures (50°C) and high pressures (19 bar). Furthermore, a flash before the hydrocracker operating at high temperatures (> 220°C) and low pressures (1 bar) may improve distillate

yields. However, this flash is ineffective for Fischer-Tropsch products generated at lower (60%) conversions, due to low concentrations of entrained distillate in the wax product. The effectiveness of the hydrocracker was found to be dependent on the level of conversion in the Fischer-Tropsch synthesis, with improved distillate yields of 40% and 28% for conversions of X_{CO} = 60% and 70%, but only 12% and 0.6% for conversions of X_{CO} = 80% and 90% respectively.

The required conditions in the atmospheric distillation column were also dependent on the level of conversion obtained in the Fischer-Tropsch synthesis. The products generated by the Fischer-Tropsch synthesis operated at lower conversions may require a lower reboiler duty and feed temperature or a higher reflux ratio in order to maximize on-spec distillate yields.

The power output from the steam turbine was controlled by the oxygen:feed ratio and the water pump exit pressure. An optimum oxygen:feed ratio of 0.32 was found, whilst increasing the water exit pressure led to a strong increase in power produced, which started to level off after ca. 100 bar.

The evaluation of the plant design consisted of testing 16 scenarios, including four Fischer-Tropsch conversions (60%, 70%, 80% and 90%), two Fischer-Tropsch catalysts (Pt-Co/Al_2O_3 and Mn-Co/Al_2O_3) and a partial refining plant with and without hydrocracking. Overall carbon yields for the on-spec distillate were found to be low in all cases (between 8 C-% and 18 C-%). This was due to low CO_2 conversions in the tri-reformer, low yields to C_{10}-C_{12} in the Fischer-Tropsch reactor and a loss of distillate into the wax fraction of the distillation column.

The optimal case was found to be a Mn-Co/Al_2O_3 operated at a conversion level of X_{CO} = 80%, with an on-spec overall distillate yield of 18 C-%, and a production rate of 329 bbl/day. This is a production rate of 12% higher than the Pt-Co/Al_2O_3 case at the same conversion. Operating without a hydrocracker was found to only have similar production levels at X_{CO} = 90%.

An important aspect to note is that the production level of the Mn-Co/Al_2O_3 was found to be far more stable with regard to Fischer-Tropsch conversion, with relatively similar production from conversions of X_{CO} = 70 to 85%. This means that the system will be far more robust and less sensitive to external disturbances that may affect ongoing conversion levels.

Chapter 11

Concluding remarks

This study sought to develop a low cost, utility self-sufficient and relatively simple Fischer-Tropsch process that could convert organic waste to diesel for remote fuel production in Sub-Saharan Africa. Central to the design of such a process was operating in a once-through Fischer-Tropsch configuration, which necessitates the development of a catalyst that could withstand the less favourable conditions of high conversion.

The first part of this study was an investigation into the effects of high conversion on the activity, selectivity and stability of a cobalt-based catalyst, including a more mechanistic understanding of the phenomenon that cause unfavourable performance under these conditions, and an evaluation of the effectiveness of changing various catalyst aspects – promotors and support material – on improving this performance. The second section used these catalytic results to develop the design of a once-through biogas-to-distillate (low density diesel) process, and to evaluate the effectiveness of operating at an optimal conversion and with the improved catalyst on the overall yield of distillate produced.

11.1. Selectivity at high conversion

A platinum promoted cobalt catalyst (0.05Pt-22Co/Al_2O_3) was used as a base case industrial-type catalyst for this investigation. Using a slurry bed reactor (T = 220°C, P = 20 bar, H_2: CO: N_2= 4:2:6) space velocity was decreased to increase conversion and evaluate how the activity, selectivity towards CO_2, CH_4, O/P and C_{5+} and the stability of the catalyst was affected when moving towards high conversion (X_{CO} = 40% to 97%).

This investigation found that a conversion of ca. X_{CO} = 75% formed a transition point from normal industrial selectivities to a high conversion regime, at which the selectivity towards unwanted by-products such as CO_2 and CH_4 increased strongly whilst the fuel product selectivity (C_{5+}) decreased. Previous understanding of this phenomenon attributed these changes in selectivity to a thermodynamic transformation of Co^0 to Co(II)O or $CoAl_2O_4$. In contrast, this study showed that the water-gas shift reaction was favoured under high conversion (hydrothermal) conditions thus increasing the production of CO_2 from Co^0. As a consequence of the production of CO_2, the internal reactor H_2:CO ratio increased, which was the reason for a strong increase in CH_4 and a decrease in C_{5+} selectivity at high conversion.

To improve selectivities of 0.05Pt-22Co/Al_2O_3 at high conversion, manganese was introduced as a promoter. The optimal level of Mn promotion was found to be at a Mn:Co mass ratio of 0.14, which led to a large improvement in C_{5+} -selectivity from 73 C-% to 87 C-% at X_{CO} = 90%. Hence, the maximum yield for the C_{5+}-fuel was obtained at X_{CO} = 91% due to the presence of manganese. The addition of the optimal amount of manganese seems to double the turn over frequency. This meant that, from a selectivity and activity perspective, conversions up to X_{CO} = 91% will be viable in terms of the design of a once-through Fischer-Tropsch plant.

11.2. Stability at high conversion

The stability of 0.05Pt-22Co/Al_2O_3 appears to be significantly affected above a Fischer-Tropsch conversion of ca. X_{CO} = 70%. After this point, significant irreversible deactivation was observed, with half the activity lost going to a conversion of X_{CO} > 90. This was shown to be due to enhanced cobalt aluminate formation and sintering (as shown via an in-situ magnetometer). Carbon deposition was found to be minimal at high conversion due to high hydrogen availability.

On increasing the conversion to a regime of very high conversion conditions (X_{CO} > 90%) for 0.05Pt-22Co/Al_2O_3, strong instantaneous deactivation was observed causing an immediate decrease in conversion which appeared to settle at X_{CO} = 89%. This was shown, using an in-situ magnetometer, to be accompanied by a reversible loss of magnetisation, which has been interpreted as the reversible oxidation and re-reduction of Co^0 to Co(II)O. It was speculated that a thermodynamic conversion limit exists due to reversible cobalt oxidation. This was further substantiated using a novel thermodynamic model for the oxidation of cobalt crystallites with a lognormal distribution, based on an existing thermodynamic model for discreet cobalt crystallites. Using this model, it was shown that whilst discreet cobalt crystallites of a typical industrial size of 5 and 6 nm have a maximum conversion limit of X_{CO} = 85% and 93% respectively, a more realistic lognormal distribution of the same sizes have a conversion limit of only X_{CO} = 80% and 88%, which correlates with results from the slurry bed reactor study presented here. This result indicates that once crystallite size distributions are accounted for, the extent of deactivation via Co(II)O formation is more severe than previously estimated. In addition, the model showed that for mean crystallite sizes of > 8 nm, the conversion is only slightly limited due to oxidation and a conversion of up to X_{CO} = 98% can be attained.

In order to improve the stability at high conversion, a novel support, $ZnAl_2O_4$, was introduced to replace Al_2O_3. The formation of cobalt aluminate is thermodynamically not feasible when zinc aluminate is used as a support and hence the level of irreversible and reversible deactivation could be decreased significantly. The catalysts 0.04Pt-23Co/$ZnAl_2O_4$ exhibited minimal deactivation in comparison to

0.05Pt-22Co/Al_2O_3. In addition, the support material was shown to have no visible effect on selectivity across the conversion range. Zinc aluminate may, thus, be expected to be a feasible alternative to alumina as a support for a cobalt Fischer-Tropsch catalyst operating under high conversion conditions.

11.3. Designing a biogas-to-distillate plant

With these catalyst improvements, conversion levels up to ca. X_{CO} = 90% are feasible, thus increasing the viability of a once-through Fischer-Tropsch design processing 400 kmol of biogas (75% CH_4 and 25% CO_2). The design developed in this study uses a tri-reformer to generate syngas from biogas, a once-through Fischer-Tropsch reactor, a partial refining section and a combined cycle power plant.

A set of 16 scenarios were evaluated including four Fischer-Tropsch conversions (X_{CO} = 60%, 70%, 80% and 90%), two Fischer-Tropsch catalysts (Pt-Co/Al_2O_3 and Mn-Co/Al_2O_3) and a partial refining plant with and without hydrocracking. The results of this study showed that Mn-Co/Al_2O_3 (Mn:Co = 0.14 mass/mass) produced more distillate across the range of conversions above X_{CO} = 70% when compared to Pt-Co/Al_2O_3. It appeared that Mn-Co/Al_2O_3 was also less sensitive to changes in conversion. Hydrocracking was found to improve the yield of distillate significantly below X_{CO} = 90% for both catalysts. At X_{CO} = 90%, hydrocracking was shown to be unnecessary.

An optimal conversion was found at X_{CO} = 80% for Mn-Co/Al_2O_3, with a distillate production of 329 bbl/day. The significance of the optimal conversion being above X_{CO} = 70% is that this is within a regime wherein significant irreversible deactivation occurs. Hence, the performance could be further improved by using zinc aluminate as a support rather than alumina.

The maximum production of 329 bbl/day represents an on-spec overall distillate yield (from biogas) of only 18 C-%. The reasons for the low yield include a low conversion of CO_2 in the tri-reformer, a low yield of distillate (C_{10}-C_{22}) range hydrocarbons in the Fischer-Tropsch synthesis, and a loss of distillate in the wax bottoms of the atmospheric distillation column. Carbon losses via the distillation column could be decreased significantly with a liquid recycle from the bottoms of the column to the hydrocracker, whilst, carbon losses in the Fischer-Tropsch synthesis could be decreased by increasing the reactor pressure to improve the chain growth probability of the catalysts at high conversion.

The tail gas from the biogas-to-distillate plant was used to generate power with a gross generation of between 7.9 MW and 8.7 MW and a net generation (after compressors and pumps) of between 2.4 MW and 3.2 MW for Mn-Co/Al_2O_3. The amount of power generated was strongly affected by conversion,

whilst the type of Fischer-Tropsch catalyst and presence or absence of a hydrocracker had only a small effect.

This study shows that a once-through Fischer-Tropsch biogas-to-distillate plant that is self-sustaining is feasible from a process and catalytic perspective, albeit improvements can be made to the overall carbon yields of the process. Catalyst improvements via manganese promotion were shown to improve fuel production significantly whilst the addition of zinc aluminate as a support was shown to stabilize the cobalt catalyst in order to reach optimal conversion.

11.4. Recommendations

This study reports on the activity, selectivity and stability of platinum-promoted cobalt catalysts within a slurry bed reactor. Slurry bed systems operate at homogeneous exit concentrations, thus, the effects of internal changes to the partial pressures of CO, H_2 and H_2O are at a maximum (i.e. worst case scenario). Fixed bed reactors operate with concentration gradients, thus are expected to behave better under high conversion conditions, albeit issues with regards to temperature control and mass transfer limitations may be more significant. Further analysis of the effect of high conversion on cobalt catalysts in a fixed bed reactor is therefore recommended. An optimal conversion may be significantly different within a fixed bed reactor and, thus, certain catalyst improvements may prove unnecessary.

It is further proposed that an investigation into the productivity of a Mn-Pt-Co/$ZnAl_2O_4$ catalyst held at X_{CO} = 80% be performed to confirm long-term stability and selectivity.

From a process design perspective, overall carbon yields of the biogas-to-distillate system remain low despite Fischer-Tropsch catalyst improvements. This is partly due to the low chain growth probability of both catalysts at higher conversion. It is therefore recommended that a further experimental study be performed looking at higher reactor pressures in order to increase the chain growth probability and enhance the yield of distillate. In theory, the Fischer-Tropsch synthesis in this process could be operated up a pressure of ca. 40 bar without the need for an additional compressor (compression ratio of 3.4), albeit with a greater power requirement.

As this study focused on the production of distillate (low density diesel) further investigation into blending material is required in order to meet Sub-Saharan Africa diesel requirements by increasing the density of this fuel.

Furthermore, whilst a full cost analysis of this plant falls out of the scope of this project, it is evident that the sale of remaining electricity may be important to provide extra income to offset the typically high capital costs of Fischer-Tropsch projects. A locational study on cost benefit of selling both distillate and electricity is thus recommended.

11.5. Contributions made

In conclusion, whilst previous studies have noted the effects of high conversion on industrial Fischer-Tropsch catalysts, no mechanistic understanding of the unfavourable changes to activity, selectivity and stability had been provided. Moreover, no attempt had been made to design a catalyst for high conversion conditions which may enable a single pass Fischer-Tropsch configuration.

This investigation provides a holistic view of both the consequences of high Fischer-Tropsch conversions and the mechanisms that can be associated with these harsh conditions. In addition, this study evaluates catalyst modifications that allow for operation of cobalt catalysts at conversions above X_{CO} = 70% that would otherwise be unattainable due to strong deactivation and unfavourable selectivities. Furthermore, this study provides a possible design for a once-through Fischer-Tropsch waste-to-liquid process, and reports on optimal conversion levels, where none existed previously, for the production of distillate from cobalt based catalysts.

References

[1] W.G. Matthews, Opportunities and challenges for petroleum and LPG markets in Sub-Saharan Africa, *Energy Policy*. **64** (2014) 78–86.

[2] R. Bacon, M. Adib, The vulnerability of African countries to oil price shocks: Major factors and policy options, The International Bank of Reconstruction, 2005, 1–76.

[3] C. Kaufffman, Policy Insights: Energy and poverty in Africa, OECD Development Centre, 2004.

[4] British Petroleum, BP statistical review of world energy, 2019, 1-45.

[5] W. Matthews, F. Sexsmith, Petroleum markets in Sub-Saharan Africa, Extractive Industries for Development Series, The World Bank, 2010, pp 1-64.

[6] Y. Mulugetta, Evaluating the economics of biodiesel in Africa, *Renew. Sustain. Energy Rev.* **13** (2009) 1592–1598.

[7] A.S. Ba, The energy policy of the Republic of Senegal: Evaluation and Perspectives, 2018, 10-31.

[8] C. Ewbank, S. Gupta, B.T. Stewart, A.L. Kushner, A. Charles, A systematic review of oil tanker truck disasters: Identifying prevention targets, *Burns.* **45** (2019) 905–913.

[9] M. Singh, Economics of biofuels for the transport sector in South Africa, *Energy Sustain. Dev.* **10** (2006) 40–47.

[10] D. Hoornweg, B. Perinaz, What a waste: A global review of solid waste management, Urban Development Series: Waste Generation, World Bank, 2012.

[11] M. He, Z. Hu, B. Xiao, J. Li, X. Guo, S. Luo, F. Yang, Y. Feng, G. Yang, S. Liu, Hydrogen-rich gas from catalytic steam gasification of municipal solid waste (MSW): Influence of catalyst and temperature on yield and product composition, *Int. J. Hydrogen Energy* **34** (2014) 195–203.

[12] U. Arena, Process and technological aspects of municipal solid waste gasification . A review, *Waste Manag*. **32** (2015) 625–639.

[13] C.S. Psomopoulos, A. Bourka, N.J. Themelis, Waste-to-energy: A review of the status and benefits in USA, *Waste Manag*. ***29*** (2009) 1718–1724.

[14] X. Zhang, R.C. Brown, Introduction to thermochemical processing of biomass into fuels, chemicals a and power in "Thermochemical Processing of Biomass: Conversion Into Fuels, Chemicals and Power", R.C. Brown (Eds.), John Wiley & Sons, 2011: pp. 1-14.

[15] F. Ferrara, A. Orsini, A. Plaisant, A. Pettinau, Pyrolysis of coal, biomass and their blends: Performance assessment by thermogravimetric analysis, *Bioresour. Technol.* **171** (2014) 433–441.

[16] A. V. Bridgwater, Renewable fuels and chemicals by thermal processing of biomass, *Chem. Eng. J.* **91** (2003) 87–102.

[17] R. Mawhood, E. Gazis, S. De Jong, R. Hoefnagels, R. Slade, Production pathways for renewable jet fuel: a review of commercialization status and future prospects, *Biofuels, Bioprod. Bioref.* **10** (2016) 462-484.

[18] A. Hilkiah Igoni, M.J. Ayotamuno, C.L. Eze, S.O.T. Ogaji, S.D. Probert, Designs of anaerobic digesters for producing biogas from municipal solid-waste, *Appl. Energy*. **85** (2008) 430–438.

[19] F. AL-Zuhairi, Combined use of anaerobic digestion and Fischer-Tropsch reaction to convert organic wastes into biodiesel, PhD Thesis, Univeristy of Naples, Italy, 2017.

[20] G. Liu, E.D. Larson, R.H. Williams, T.G. Kreutz, X. Guo, Making Fischer−Tropsch fuels and electricity from coal and biomass: Performance and cost analysis, *Energy & Fuels*. **25** (2011) 415–437.

[21] S.S. Ail, S. Dasappa, Biomass to liquid transportation fuel via Fischer Tropsch synthesis - Technology review and current scenario, *Renew. Sustain. Energy Rev.* **58** (2016) 267-286. [22]

[22] Arup URS Consonrtium, Advanced biofuel feedstocks – An assessment of sustainability, Prepared for E4tech Ltd., United Kingdom, 2014, https://www.e4tech.com/resources/

106-advanced-biofuel-feedstocks-an-assessment-of-sustainability.php?page_number=9 (accessed Jan. 2019)

[23] M. Rudloff, The CHOREN BTL process status – progress – future prospects, CHOREN, 2008, http://www.renew-fuel.com/fs_documents.php (accessed Jan 2019)

[24] ETIP Bioenergy, Discontinued BtL Projects, 2017. http://www.etipbioenergy.eu (accessed Dec. 2019)

[25] S.R. Deshmukh, S.C. LeViness, H.J. Robota, M. Davis, Commercializing an advanced Fischer-Tropsch synthesis technology in "Fischer-Tropsch Synthesis, Catalysts, and Catalysis Advances and Applications", B.H. Davis, M.L Occelli (Eds.), CRC Press, Taylor & Francis Group, 2016: pp. 361–377.

[26] H. Kennedy, Red Rock Biofuels facility breaks ground in Lakeview, Biofuels Dig. http://www.biofuelsdigest.com/bdigest/2018/07/29/red-rock-biofuels-facility-breaks-ground-in-lakeview (accessed Oct. 2019)

[27] Velocys, Biorefineries, https://www.velocys.com/our-biorefineries (accessed Oct. 2019)

[28] Neville Hargreaves, Plans submitted for the first waste to jet plant in the UK and Europe, 2019, https://www.velocys.com/2019/08/20/plans-submitted-for-the-first-waste-to-jet-fuel-plant-in-the-uk-and-europe (accessed October 2019)

[29] Fulcrum Bioenergy, "Fulcrum targets Northwest Indiana for the location of its next waste-to-fuel plant"http://fulcrum-bioenergy.com/wp-content/uploads/2018/12/2018-12-13-Fulcrum Centerpoint-Announcement-FINAL.pdf (accessed Dec. 2019).

[30] Petroleum Economist, Choren completes biomass biofuel plant, https://www.petroleum-economist.com/articles/low-carbon-energy/renewables/2008/choren-completes-biomass-biofuels-plant, (accessed Oct. 2019)

[31] H. Kittelmann, Carbo-V® Biomass Gasification Technology: Status after Application of Sound Engineering Practices, IAE Workshop, 2014.

[32] K. Thommes,V. Strezov, Fischer-Tropsch synthesis from biosyngas in "Biomass Processing

Technologies", V. Strezov, T. Evans (Eds.) CRC Press, 2014: pp 309-357.

[33] Biofuels International, BA waste-to-jet fuel project fails to take off. https://biofuels-news.com/news/ba-waste-to-jet-fuel-project-fails-to-take-off (accessed Oct. 2019).

[34] Total, BIOTFUEL: Developing second-generation biofuels. https://www.total.com/en/energy-expertise/projects/bioenergies/biotfuel-converting-plant-wastes-into-fuel (accessed Oct. 2019).

[35] R. Zennaro, Fischer-Tropsch process economics in "Greener Fischer-Tropsch Process for Fuels and Feedstocks", P.M. Maitlis, A. de Klerk (Eds.), Wiley-VCH Verlag GmbH & Co. KGaA. 2013, pp. 149–169.

[36] A. de Klerk, Small-scale Fischer-Tropsch gas-to-liquid facilities in "Fischer-Tropsch Synthesis, Catalysts, and Catalysis", B.H. Davis, M.L Occelli (Eds.), CRC Press, Taylor & Francis Group, 2016, pp. 379–399.

[37] H. Boerrigter, Economy of biomass-to-liquids (BTL) plants An engineering assessment, Energy research centre of the Netherlands, Report ECN-C-06-019, 2006.

[38] B. Reddall, Cost of delayed Chevron Nigeria plant now $8.4 bln, Reuters, 2011, https://www.reuters.com/article/chevron/cost-of-delayed-chevron-nigeria-plant-now-8-4-bln-idUSN2428474120110225 (accessed Jul. 2018).

[39] S. Webb, Sasol Chevron stands by Qatar GTL plans, costs up, Reuters, 2007, https://www.reuters.com/article/gtl-qatar-sasolchevron/sasolchevron-stands-by-qatar-gtl-plans-costs-up-idUSL0655136620070306 (accessed Jul. 2018).

[40] E. Rytter, A. Holmen, Deactivation and regeneration of commercial type Fischer-Tropsch cobalt catalysts—A mini-review, *Catalysts.* **5** (2015) 478–499.

[41] J.R. Rostrup-Nielson, New aspects of syngas production and use, *Catal. Today*. **63** (2000) 159–164.

[42] A. Jess, R. Popp, K. Hedden, Production of diesel oil and wax by Fischer-Tropsch-synthesis using a nitrogen-rich synthesis gas - Investigations on a semi-technical scale, *Erdoel Erdgas Kohle.* **113** (1997) 531–540.

[43] J.R. Rostrup-Nielson, Syngas in perspective, *Catal. Today*. **71** (2002) 243–247.

[44] D.J. Wilhelm, D.R. Simbeck, A.D. Karp, D. R.L, Syngas production for gas-to-liquid applications: technologies, issues and outlook, *Fuel Process. Technol.* **71** (2001) 139–148.

[45] K. Aasberg-Petersen, B.H. J.H, I. Dybkjaer, T.S. Christensen, P.S. Christensen, C. Stub Nielsen, S.E.L. Winter-Madsen, J.R. Rostrup-Nielson, Technologies for large-scale gas conversion, *Appl. Catal. A Gen.* **221** (2001) 379–387.

[46] A. Jess, R. Popp, K. Hedden, Fischer-Tropsch synthesis with nitrogen-rich syngas. Fundementals and reactor design aspects, *Appl. Catal. A Gen.* **186** (1999) 321–342.

[47] Q. Bernical, X. Joulia, I. Noirot-Le Borgne, P. Floquet, P. Baurens, G. Boissonnet, Sustainability assessment of an integrated high temperature steam electrolysis-enhanced biomass to liquid fuel process, *Ind. Eng. Chem. Res.* **52** (2013) 7189–7195.

[48] C.N. Hamelinck, Outlook for advanced biofuels, PhD Thesis, Utrecht University, Neatherlands, 2004.

[49] M.J.A. Tijmensen, A.P.C. Faaij, C.N. Hamelinck, M.R.M. van Hardeveld, Exploration of the possibilities for production of Fischer Tropsch liquids and power via biomass gasification, *Biomass and Bioenergy.* **23** (2002) 129–152.

[50] F. Trippe, M. Fröhling, F. Schultmann, R. Stahl, E. Henrich, A. Dalai, Comprehensive techno-economic assessment of dimethyl ether (DME) synthesis and Fischer-Tropsch synthesis as alternative process steps within biomass-to-liquid production, *Fuel Process. Technol.* **106** (2013) 577–586.

[51] K.S. Ng, J. Sadhukhan, Techno-economic performance analysis of bio-oil based Fischer-Tropsch and CHP synthesis platform, *Biomass and Bioenergy.* **35** (2011) 3218–3234.

[52] V. Shah, N.J Kuehn, M.J Turner, Cost and performance baseline for fossil energy plants, Volume 4: Coal-to-liquids via Fischer-Tropsch synthesis, United States, 2014. https://www.netl.doe.gov/energy-analysis/details?id=736 (accessed June 2017).

[53] L. Fagernäs, J. Brammer, C. Wilén, M. Lauer, F. Verhoeff, Drying of biomass for second

generation synfuel production, *Biomass and Bioenergy.* **34** (2010) 1267–1277.

[54] A. de. Klerk, Fischer-Tropsch refining, John Wiley & Sons, 2012, pp. 1-601

[55] H. Hofbauer, R. Rauch, Biomass to liquid (BTL) fuels in "Energy from Organic Materials (Biomass)", M. Kaltschmitt (Eds.), Springer, 2017, pp. 1047–1063.

[56] G. Herz, E. Reichelt, M. Jahn, Design and evaluation of a Fischer-Tropsch process for the production of waxes from biogas, *Energy*. **132** (2017) 370–381.

[57] J. Requies, J.F. Cambra, M.B. Güemez, U. Izquierdo, P.L. Arias, V.L. Barrio, Tri-reforming: A new biogas process for synthesis gas and hydrogen production, *Int. J. Hydrogen Energy*. **38** (2012) 7623–7631.

[58] X. Zhao, A. Naqi, D.M. Walker, T. Roberge, M. Kastelic, B. Joseph, J.N. Kuhn, Conversion of landfill gas to liquid fuels through a TriFTS (tri-reforming and Fischer-Tropsch synthesis) process: A feasibility study, *Sustain. Energy Fuels.* **3** (2019) 539–549.

[59] Z. Navas-Anguita, P.L. Cruz, M. Martín-Gamboa, D. Iribarren, J. Dufour, Simulation and life cycle assessment of synthetic fuels produced via biogas dry reforming and Fischer-Tropsch synthesis, *Fuel.* **235** (2019) 1492–1500.

[60] D. Deublein, A. Steinhauser, Biogas in "Biogas from Waste and Renewable Resources", WILEY-VCH Verlag GmbH & Co. KGaA, 2008, pp. 49-56.

[61] S.A. Chattanathan, S. Adhikari, M. McVey, O. Fasina, Hydrogen production from biogas reforming and the effect of H2S on CH4 conversion, *Int. J. Hydrogen Energy*. **39** (2014) 19905–19911.

[62] A. Naqi, Conversion of biomass to liquid hydrocarbon fuels via anaerobic digestion: A feasibility study, MSc Thesis, University of South Florida, USA, 2018.

[63] A.M. Mshandete, W. Parawira, Biogas technology research in selected sub-saharan African countries - A review, *African J. Biotechnol.* **8** (2009) 116–125.

[64] J. Yao, M. Kraussler, F. Benedikt, H. Hofbauer, Techno-economic assessment of hydrogen

production based on dual fluidized bed biomass steam gasification, biogas steam reforming, and alkaline water electrolysis processes, *Energy Convers. Manag.* **145** (2017) 278–292.

[65] D.B. Bukur, Z. Pan, W. Ma, G. Jacobs, B.H. Davis, Effect of CO conversion on the product distribution of a Co/Al_2O_3 Fischer–Tropsch synthesis catalyst using a fixed bed reactor, *Catal. Lett*. **142** (2012) 1382–1387.

[66] D. Schanke, A.M. Hilmen, E. Bergene, K. Kinnari, E. Rytter, E. Adnanes, A. Holmen, Study of the deactivation mechanism of Al_2O_3-supported cobalt Fischer-Tropsch catalysts, *Catal. Letters.* **34** (1995) 269–284.

[67] J. Li, X. Zhan, Y. Zhang, G. Jacobs, T. Das, B.H. Davis, Fischer–Tropsch synthesis: effect of water on the deactivation of Pt promoted Co/Al_2O_3 catalysts, *Appl. Catal. A Gen.* **228** (2002) 203–212.

[68] S. Storsæter, Ø. Borg, E. Blekkan, A. Holmen, Study of the effect of water on Fischer–Tropsch synthesis over supported cobalt catalysts, *J. Catal.* **231** (2005) 405–419.

[69] G. Kiss, C.E. Kliewer, G.J. DeMartin, C.C. Culross, J.E. Baumgartner, Hydrothermal deactivation of silica-supported cobalt catalysts in Fischer-Tropsch synthesis, *J. Catal.* **217** (2003) 127–140.

[70] W. Ma, G. Jacobs, D.E. Sparks, R.L. Spicer, B.H. Davis, J.L.S. Klettlinger, C.H. Yen, Fischer-Tropsch synthesis: Kinetics and water effect study over $25\%Co/Al_2O_3$ catalysts, *Catal. Today.* **228** (2014) 158–166.

[71] M.E. Dry, High quality diesel via the Fischer-Tropsch process - A review, *J. Chem. Technol. Biotechnol.* **77** (2002) 43–50.

[72] R.M. de Deugd, Fischer-Tropsch synthesis revisited; Efficiency and selectivity benefits from imposing temporal and/or spatial structure in the reactor, PhD Thesis, Delft University, 2004.

[73] M.E. Dry, The Fischer-Tropsch process: 1950-2000, *Catal. Today.* **71** (2002) 227–241.

[74] A. Steynberg, Introduction to Fischer-Tropsch technology in "Fischer-Tropsch Technology", A. Steynberg, M.E. Dry (Eds.), *Stud. Surf. Sci. Catal*. **152**, 2004, pp. 1-63.

[75] E. van Steen, M. Claeys, Fischer-Tropsch catalysts for the biomass-to-liquid (BTL)-process, *Chem. Eng. Technol.* **31** (2008)

[76] D. Stewart, D.D. Hsu, Chemicool Periodic Table, 2016, http://www.chemicool.com. (accessed May 2016)

[77] A.Y. Khodakov, W. Chu, P. Fongarland, Advances in the development of novel cobalt Fischer-Tropsch catalysts for synthesis of long-chain hydrocarbons and clean fuels, *Chem Rev.* **107** (2007) 1692–1744.

[78] W. Ma, G. Jacobs, Y. Ji, T. Bhatelia, D.B. Bukur, S. Khalid, B.H. Davis, Fischer–Tropsch synthesis: Influence of CO conversion on selectivities, H_2/CO usage ratios, and catalyst stability for a Ru promoted Co/Al_2O_3 Catalyst Using a Slurry Phase Reactor, *Top. Catal.* **54** (2011) 757–767.

[79] E. Iglesia, Design, synthesis, and use of cobalt-based Fischer-Tropsch synthesis catalysts, *Appl. Catal. A Gen.* **161** (1997) 59–78

[80] N.E. Tsakoumis, M. Rønning, Ø. Borg, E. Rytter, A. Holmen, Deactivation of cobalt based Fischer–Tropsch catalysts: A review, *Catal. Today.* **154** (2010) 162–182.

[81] N. Fischer, E. van Steen, M. Claeys, Structure sensitivity of the Fischer–Tropsch activity and selectivity on alumina supported cobalt catalysts, *J. Catal.* **299** (2013) 67–80.

[82] G.L. Bezemer, J.H. Bitter, H.P. Kuipers, H. Oosterbeek, J.E. Holewijn, X. Xu, F. Kapteijn, A.J. van Dillen, K.P. de Jong, Cobalt particle size effects in the Fischer-Tropsch reaction studied with carbon nanofiber supported catalysts, *J Am Chem Soc.* **128** (2006) 3956–3964.

[83] XQ. Zhang, R.A van Santen, E.J.M. Hensen. Carbon-induced surface transformations of cobalt, *ACS Catal.* **5** (2015) 596–601

[84] G.L. Bezemer, P.B. Radstake, V. Koot, A.J. van Dillen, J.W. Geus, K.P. de Jong, Preparation of Fischer-Tropsch cobalt catalysts supported on carbon nanofibers and silica using homogeneous deposition-precipitation, *J. Catal.* **237** (2006) 291–302.

[85] M. Trépanier, A. Tavasoli, A.K. Dalai, N. Abatzoglou, Co, Ru and K loadings effects on the

activity and selectivity of carbon nanotubes supported cobalt catalyst in Fischer-Tropsch synthesis, *Appl. Catal. A Gen.* **353** (2009) 193–202.

[86] M. Lualdi, Fischer-Tropsch synthesis over cobalt-based catalysts for BTL applications, PhD Thesis, KTH School of Chemical Science and Engineering, Sweden, 2012.

[87] G. Jacobs, T.K. Das, Y. Zhang, J. Li, G. Racoillet, B. Davis, Fischer–Tropsch synthesis: support, loading, and promoter effects on the reducibility of cobalt catalysts, *Appl. Catal. A Gen.* 233 (2002) 263–281.

[88] C. Reuel, C. Bartholomew, Effects of support and dispersion on the CO hydrogenation activity/selectivity properties of cobalt , *J. Catal.* **85**, (1984) 78-88.

[89] R. Oukaci, A.H. Singleton, J.G. Goodwin Jr, Comparison of patented Co F–T catalysts using fixed-bed and slurry bubble column reactors, *Appl. Catal. A Gen.* **186** (1999) 129–144.

[90] G.L. Bezemer, P.B. Radstake, U. Falke, H. Oosterbeek, H.P.C.E. Kuipers, A.J. van Dillen, K.P. de Jong, Investigation of promoter effects of manganese oxide on carbon nanofiber-supported cobalt catalysts for Fischer-Tropsch synthesis, *J. Catal.* **237** (2006) 152–161.

[91] A.M. Saib, D.J. Moodley, I.M. Ciobîc, M.M. Hauman, B.H. Sigwebela, C.J. Weststrate, J.W. Niemantsverdriet, J. van de Loosdrecht, Fundamental understanding of deactivation and regeneration of cobalt Fischer-Tropsch synthesis catalysts, *Catal. Today.* **154** (2010) 271–282.

[92] M. de Beer, A. Kunene, D. Nabaho, M. Claeys, E. van Steen, Technical and economic aspects of promotion of cobalt-based Fischer-Tropsch catalysts by noble metals-a review, *J. South. African Inst. Min. Metall.* **114** (2014).

[93] D. Nabaho, Hydrogen spillover in the Fischer-Tropsch synthesis : The role of platinum and gold as promoters on cobalt-based catalysts, PhD Thesis, University of Cape Town, South Africa, 2014.

[94] D. Nabaho, J.W. Niemantsverdriet, M. Claeys, E. van Steen, Hydrogen spillover in the Fischer-Tropsch synthesis: An analysis of platinum as a promoter for cobalt-alumina catalysts, *Catal. Today.* **261** (2016) 17–27.

[95] G. Jacobs, Y. Ji, B.H. Davis, D. Cronauer, A.J. Kropf, C.L. Marshall, Fischer–Tropsch synthesis: Temperature programmed EXAFS/XANES investigation of the influence of support type, cobalt loading, and noble metal promoter addition to the reduction behavior of cobalt oxide particles, *Appl. Catal. A Gen.* **333** (2007) 177–191.

[96] S. Vada, A. Hoff, E. ÅdnaneS, D. Schanke, A. Holmen, Fischer-Tropsch synthesis on supported cobalt catalysts promoted by platinum and rhenium, *Top. Catal.* **2** (1995) 155–162.

[97] A. Outi, I. Rautavuoma, H.S. van der Baan, Kinetics and mechanism of the fischer tropsch hydrocarbon synthesis on a cobalt on alumina catalyst, *Appl. Catal.* **1** (1981) 247–272.

[98] W. Brötz, Zur Systematik der Fischer-Tropsch-Katalyse, *Zeitschrift Für Elektrochemie Und Angew. Phys. Chemie.* **53** (1949) 301–306.

[99] R.B. Anderson, The Fischer-Tropsch synthesis, Academic Press, Orlando, 1984.

[100] B.W. Wojciechowski, The kinetics of the Fischer-Tropsch synthesis, *Catal. Rev.* **30** (1988) 629–702.

[101] I.C. Yates, C.N. Satterfield, The hydrocarbon selectivity of cobalt Fischer-Tropsch catalysts, *Energy & Fuels* **6** (1992) 308-314.

[102] E. van Steen, H. Schulz, Polymerisation kinetics of the Fischer–Tropsch CO hydrogenation using iron and cobalt based catalysts, *Appl. Catal. A Gen.* **186** (1999) 309–320.

[103] F.G. Botes, B. van Dyk, C. McGregor, The development of a macro kinetic model for a commercial Co/Pt/Al_2O_3 Fischer - Tropsch catalyst, *Ind. Eng. Chem. Res*, **48** (2009), 10439-10447

[104] H.P. Withers, K.F. Eliezer, J.W. Mitchell, Slurry-phase Fischer-Tropsch synthesis and kinetic studies over supported cobalt carbonyl derived catalysts, *Ind. Eng. Chem. Res.* **29** (1990) 1807–1814.

[105] C.-H. Yang, F.E. Massoth, A.G. Oblad, Kinetics of CO + H_2 reaction over Co-Cu-Al_2O_3 catalyst, *Adv. Chem. Ser.* **178** (1979) 35–46.

[106] R.B.B. Pannell, C.L.L. Kibby, T.P.P. Kobylinski, A steady-state study of Fischer-Tropsch product distributions over cobalt, iron and ruthenium in: "New Horizons in Catalysis", T. Seivama, K. Tanabe (Eds.), *Stud. Surf. Sci. Catal.* **7** (1981) 447–459.

[107] W. Brötz, Zur Systematik der Fischer-Tropsch-Katalyse, *Zeitschrift Für Elektrochemie Und Angew. Phys. Chemie.* **53** (1949) 301–306.

[108] R.B. Anderson, Catalysts for the Fischer-Tropsch Synthesis, P.H. Emmett (Ed.), Vol. 4, Van Nostrand-Reinhold, New York (1956), pp. 29

[109] J. Wang, Physical, chemical and catalytic properties of borided cobalt Fischer-Tropsch catalysts, PhD Thesis, Brigham Young University, 1987.

[110] I.C. Yates, C.N. Satterfield, Intrinsic kinetics of the Fischer-Tropsch synthesis on a cobalt catalyst, *Energy & Fuels.* **5** (1991) 168–173.

[111] H. Schulz, E. van Steen, M. Claeys, Selectivity and mechanism of Fischer-Tropsch synthesis with iron and cobalt catalysts, *Stud. Surf. Sci. Catal.* **81** (1994) 455–460.

[112] S. Krishnamoorthy, M. Tu, M.P. Ojeda, D. Pinna, E. Iglesia, An investigation of the effects of water on rate and selectivity for the Fischer-Tropsch synthesis on cobalt-based catalysts, *J. Catal.* **211** (2002) 422–433.

[113] C.J. Kim, F. Park, Water addition for increased CO/H_2 hydrocarbon synthesis activity over catalysts comprising of cobalt, ruthenium and mixtures thereof which may include promoter metal. U.S. Patent 5 227 407, (1993).

[114] G. Schulz, Uber die Bezihung zwischen Reaktionsgeschwindigkeit und Zusammentetzung des Reaktionprodktes bei Makropolymerisations, *Z.Phys.Chem.* **B30** (1935) 379.

[115] G.P. van der Laan, A.A.C.M. Beenackers, Kinetics and selectivity of the Fischer–Tropsch synthesis: A literature review, *Catal. Rev.* **41** (1999) 255–318.

[116] C.J. Bertole, C.A. Mims, G. Kiss, The effect of water on the cobalt-catalyzed Fischer-Tropsch synthesis, *J. Catal.* **210** (2002) 84–96.

[117] E. van Steen, M. Claeys, M.E. Dry, J. van De Loosdrecht, E.L. Viljoen, J.L. Visagie, Stability of nanocrystals: Thermodynamic analysis of oxidation and re-reduction of cobalt in water/hydrogen mixtures, *J. Phys. Chem. B.* **109** (2005) 3575–3577.

[118] N. Fischer, B. Clapham, T. Feltes, E. van Steen, M. Claeys, Size-dependent phase transformation of catalytically active nanoparticles captured in situ, *Angew. Chemie - Int. Ed.* **53** (2014) 1342–1345.

[119] M. Wolf, B.K. Mutuma, N.J. Coville, N. Fischer, M. Claeys, Role of CO in the water-induced formation of cobalt oxide in a high conversion Fischer-Tropsch environment, *ACS Catal.* **8** (2018) 3985-3989.

[120] E. Rytter, A. Holmen, On the support in cobalt Fischer–Tropsch synthesis—Emphasis on alumina and aluminates, *Catal. Today*. **275** (2016) 11–19.

[121] E. Rytter, A. Holmen, Perspectives on the effect of water in cobalt Fischer-Tropsch synthesis, *ACS Catal.* **7** (2017) 5321–5328.

[122] G. Jacobs, P.M. Patterson, Y. Zhang, T. Das, J. Li, B.H. Davis, Fischer-Tropsch synthesis: Deactivation of noble metal-promoted Co/Al_2O_3catalysts, *Appl. Catal. A Gen.* **233** (2002) 215–226.

[123] D.J. Moodley, A.M. Saib, J. van De Loosdrecht, C.A. Welker-Nieuwoudt, B.H. Sigwebela, J.W. Niemantsverdriet, The impact of cobalt aluminate formation on the deactivation of cobalt-based Fischer-Tropsch synthesis catalysts, *Catal. Today.* **171** (2011) 192–200.

[124] M. Claeys, M.E. Dry, E. van Steen, P.J. van Berge, S. Booyens, R. Crous, P. van Helden, J. Labuschagne, D.J. Moodley, A.M. Saib, Impact of process conditions on the sintering behavior of an alumina-supported cobalt Fischer−Tropsch catalyst studied with an in situ magnetometer, *ACS Catal.* **5** (2015) 841–852

[125] C. Bartholomew, History of cobalt catlayst design from FTS, Proceedings of the National Spring Meeting of American Institute of Chemical Engineers, New Orleans, United States, 2003.

[126] C. Lancelot, V. V Ordomsky, O. Stéphan, M. Sadeqzadeh, H. Karaca, M. Lacroix, D. Curulla-Ferré, F. Luck, P. Fongarland, A. Griboval-Constant, A.Y. Khodakov, Direct evidence of

surface oxidation of cobalt nanoparticles in alumina-supported catalysts for Fischer–Tropsch synthesis, *ACS Catal*. **4** (2014) 4510–4515.

[127] J. van de Loosdrecht, B. Balzhinimaev, J.A. Dalmon, J.W. Niemantsverdriet, S. V. Tsybulya, A.M. Saib, P.J. van Berge, J.L. Visagie, Cobalt Fischer-Tropsch synthesis: Deactivation by oxidation?, *Catal. Today* **123** (2007) 293–302.

[128] I. Barin, O. Knacke, O. Kubaschewski, Thermochemical properties of inorganic substancies, Springer-Verlag Berlin Heidelberg, 1977.

[129] S. Werner, G.R. Johnson, A.T. Bell, Synthesis and characterization of supported cobalt–manganese nanoparticles as model catalysts for Fischer–Tropsch synthesis, *ChemCatChem.* **6** (2014) 2881–2888.

[130] F. Zheng, Biotechnology, Agriculture, Environment and Energy, CRC Press, London, 2015.

[131] G. Jacobs, T.K. Das, P.M. Patterson, J. Li, L. Sanchez, B.H. Davis, Fischer-Tropsch synthesis XAFS - XAFS studies of the effect of water on a Pt-promoted Co/Al_2O_3 catalyst, *Appl. Catal. A Gen.* **247** (2003) 335–343.

[132] G.L. Bezemer, T.J. Remans, A.P. van Bavel, A.I. Dugulan, Direct evidence of water-assisted sintering of cobalt on carbon nanofiber catalysts during simulated Fischer−Tropsch conditions revealed with in situ Mössbauer spectroscopy, *J. Am. Chem. Soc.* **132** (2010) 8540-8541

[133] C. Tucker, E. van Steen, M. Claeys, Decoupling the deactivation mechanism of $Pt\text{-}Co/Al_2O_3$ at high conversion for once-through biomass-to-liquid operation, *Cat. Sci. Tech.* (under review).

[134] E. Goodman, J.A. Schwalbe, M. Cargnello, Mechanistic understanding and rational design of sintering resistant herterogeneous catalysts, *ACS Catal.* **7** (2017) 7156–7173.

[135] N.E. Tsakoumis, M. Rønning, Ø. Borg, E. Rytter, A. Holmen, Deactivation of cobalt based Fischer-Tropsch catalysts: A review, *Catal. Today*. **154** (2010) 162–182.

[136] A.Y. Khodakov, W. Chu, P. Fongarland, Advances in the development of novel cobalt Fischer − Tropsch catalysts for synthesis of long-chain hydrocarbons and clean fuels, *Chem. Rev.* **107** (2007) 1692–1744.

[137] C. Kliewer, G. Kiss, S. Soled, Characterizing intrinsic deactivation in cobalt-catalyzed Fischer-Tropsch synthesis, *Microsc. Microanal.* **16** (2010) 1258–1259.

[138] G.M Bremmer, E. Zacharaki, A.O Sjastad, V Navarro, J. W. M. Frenkend, P.J. Kooyman, In situ TEM observation of the Boudouard reaction: multi-layered graphene formation from CO on cobalt nanoparticles at atmospheric pressure, *Faraday Discuss.* **197** (2017) 337-351

[139] D.J. Moodley, J. van De Loosdrecht, A.M. Saib, M.J. Overett, Carbon deposition as a deactivation mechanism of cobalt-based Fischer – Tropsch synthesis catalysts under realistic conditions, *Appl. Catal. A Gen.* **354** (2009) 102–110.

[140] J.-L. Zhang, J. Rue, J.-G. Chen, Sun Yu-Han, Effect of manganese promoter on the performance of Co/Al_2O_3 catalysts for Fischer-Tropsch synthesis, *Acta Phys. Chim. Sin*. **18** (2002) 260–263.

[141] A. Dinse, M. Aigner, M. Ulbrich, G.R. Johnson, A.T. Bell, Effects of Mn promotion on the activity and selectivity of Co/SiO_2 for Fischer-Tropsch synthesis, *J. Catal.* **288** (2012) 104–114.

[142] G.R. Johnson, S. Werner, A.T. Bell, An investigation into the effects of Mn promotion on the activity and selectivity of Co/SiO_2 for Fischer-Tropsch synthesis: Evidence for enhanced CO adsorption and dissociation, *ACS Catal.* **5** (2015) 5888–5903.

[143] F.M. Cano, O.L.J. Gijzeman, F.M.F. de Groot, B.M. Weckhuysen, Manganese promotion in cobalt-based Fischer-Tropsch catalysis, *Stud. Surf. Sci. Catal.* **147** (2004) 271–276.

[144] J. Thiessen, A. Rose, J. Meyer, A. Jess, D. Curulla-Ferré, Effects of manganese and reduction promoters on carbon nanotube supported cobalt catalysts in Fischer-Tropsch synthesis, *Microporous Mesoporous Mater.* **164** (2012) 199–206.

[145] F. Morales, E. de Smit, F.M.F. de Groot, T. Visser, B.M. Weckhuysen, Effects of manganese oxide promoter on the CO and H_2 adsorption properties of titania-supported cobalt Fischer-Tropsch catalysts, *J. Catal.* **246** (2007) 91–99.

[146] T.E. Feltes, L. Espinosa-Alonso, E. de Smit, L. D'Souza, R.J. Meyer, B.M. Weckhuysen, J.R. Regalbuto, Selective adsorption of manganese onto cobalt for optimized $Mn/Co/TiO_2$ Fischer-Tropsch catalysts, *J. Catal.* **270** (2010) 95–102.

[147] F. Morales, F.M.F. De Groot, O.L.J. Gijzeman, A. Mens, O. Stephan, B.M. Weckhuysen, Mn promotion effects in Co/TiO_2 Fischer-Tropsch catalysts as investigated by XPS and STEM-EELS, *J. Catal.* **230** (2005) 301–308.

[148] Z. Liu, Y. Xing, Y. Xue, D. Wu, S. Fang, Synthesis, characterization, and Fischer–Tropsch performance of cobalt/zinc aluminate nanocomposites via a facile and corrosion-free coprecipitation route, *J. Nanoparticle Res.* **17** (2015) 79.

[149] Z. Liu, Y. Xue, D. Wu, Y. Xing, S. Fang, Effects of water addition on CO hydrogenation over zinc-containing spinel-supported cobalt catalyst, *Catal. Lett.* **145** (2015) 1941–1947.

[150] B.C. Enger, Å.-L. Fossan, Ø. Borg, E. Rytter, A. Holmen, Modified alumina as catalyst support for cobalt in the Fischer–Tropsch synthesis, *J. Catal.* **284** (2011) 9–22.

[151] J. Du, J. Yan, J. Hong, Y. Zhang, S. Chen, J. Li, Catalytic performance of $Co/Zn\text{-}Al_2O_3$ Fischer-Tropsch catalysts: a comparative study of zinc introduction methodologies, *RSC Adv.* **5** (2015) 60534–60540.

[152] X. Zhao, H.T. Ngo, D.M. Walker, D. Weber, D. Maiti, U. Cimenler, A.D. Petrov, B. Joseph, J.N. Kuhn, Tri-reforming of surrogate biogas over Ni/Mg/ceria–zirconia/alumina pellet catalysts, *Chem. Eng. Commun.* **205** (2018) 1129–1142.

[153] R.L.; Espinoza, J.L.; Visagie, P.J.; van Berge, F.H. Bolder, Catalysts, U.S. Patent 5 733 839, 1996.

[154] W. Ma, Fischer-Tropsch Synthesis: Co turnover frequency rates over Co/Al_2O_3 catalysts with different reduction promoters , *Qatar Found. Annu. Res. Forum Proc.* **1** (2011)

[155] F.M. Gottschalk, R.G. Copperthwaite, M. van Der Riet, G.J. Hutchings, Cobalt/manganese oxide water gas shift catalysts. Competition between carbon monoxide hydrogenation and Water Gas shift activity, *Appl. Catal.* **38** (1988) 103–108.

[156] G.J. Hutchings, F. Gottschalk, R. Hunter, S.W. Orchard, Cobalt-manganeseo oxide water-gas shift catalysts, *J. Chem. Soc., Faraday Trans. I,* **85** (1989) 363–371.

[157] G.J. Hutchings, R.G. Copperthwaitet, F.M. Gottschalk, R. Hunter, J. Mellor, S.W. Orchard, T.

Sangiorgio, A comparative evaluation of cobalt chromium oxide, cobalt manganese oxide, and copper manganese oxide as catalysts for the water-gas shift reaction, *J. Catal.* **137** (1992) 408–422.

[158] R. Hakkarainen, T. Salmi, R.L. Keiski, Water-gas shift reaction on a cobalt-molybdenum oxide catalyst, *Appl. Catal. A.* **99** (1993) 195–215.

[159] J.. Mellor, C. R.G, C. N.J, The selective influence of sulfur on the performance of novel cobalt-based water-gas shift catalysts, *Appl. Catal. A Gen.* **164** (1997) 69–79.

[160] S. Hilaire, X. Wang, T. Luo, R.J. Gorte, J. Wagner, A comparative study of water-gas-shift reaction over ceria-supported metallic catalysts, *Appl. Catal. A Gen.* **258** (2004) 271–276.

[161] M. Nagai, K. Matsuda, Low-temperature water-gas shift reaction over cobalt-molybdenum carbide catalyst, *J. Catal.* **238** (2006) 489–496.

[162] C. Ratnasamy, J.P. Wagner, Water gas shift catalysis, *Cat. Rev.* **51** (2009) 325–440.

[163] Y. Yao, D. Hildebrandt, D. Glasser, X. Liu, Fischer−Tropsch synthesis using H_2 /CO/CO_2 syngas mixtures over a cobalt catalyst, *Ind. Eng. Chem. Res.* **49** (2010) 11061–11066.

[164] T. Riedel, M. Claeys, H. Schulz, G. Schaub, S. Nam, K. Jun, M. Choi, G. Kishan, K. Lee, Comparative study of Fischer – Tropsch synthesis with H_2 /CO and H_2/CO_2 syngas using Fe- and Co-based catalysts, *Appl. Catal.* **186** (1999) 201–213.

[165] Y. Zhang, G. Jacobs, D.E. Sparks, M.E. Dry, B.H. Davis, CO and CO_2 hydrogenation study on supported cobalt Fischer-Tropsch synthesis catalysts, *Catal. Today.* **71** (2002) 411–418.

[166] T.W. Hansen, A.T. Delariva, S.R. Challa, A.K. Datye, Sintering of catalytic nanoparticles: Particle migration or ostwald ripening?, *Acc. Chem. Res.* **46** (2013) 1720–1730.

[167] L. Fratalocchi, C.G. Visconti, L. Lietti, G. Groppi, E. Tronconi, E. Roccaro, R. Zennaro, On the performance of a Co-based catalyst supported on modified γ-Al^2O^3 during Fischer-Tropsch synthesis in the presence of co-fed water, *Catal. Sci. Technol.* **6** (2016) 6431–6440.

[168] M. Claeys, E. van Steen, J.L.; Visagie, J. van de Loosdrecht, Magnetometer, U.S. Patent 8 773

118 B2, 2014

[169] M. Claeys, M.E. Dry, E. van Steen, E. Du Plessis, P.J. van Berge, A.M. Saib, D.J. Moodley, In situ magnetometer study on the formation and stability of cobalt carbide in Fischer-Tropsch synthesis, *J. Catal.* **318** (2014) 193–202.

[170] J.-A. Dalmon, Magnetic Measurements and Catalysis, in "Catalyst Characterization: Physical Techniques for Solid Materials", B. Imelik, J.C. Vedrine, (Eds.), Springer US, Boston, MA, 1994: pp. 585–609.

[171] A. Barbier, A. Hanif, J.A. Dalmon, G.A. Martin, Preparation and characterization of well-dispersed and stable Co/SiO_2 catalysts using the ammonia method, *Appl. Catal. A Gen.* **168** (1998) 333–343.

[172] Ø. Borg, Role of alumina support in cobalt Fischer-Tropsch synthesis, PhD Thesis, Norwegian University of Science and Technology, Norway, 2007.

[173] G. Bian, N. Fujishita, T. Mochizuki, W. Ning, M. Yamada, Investigations on the structural changes of two Co/SiO_2 catalysts by performing Fischer – Tropsch synthesis, *Appl. Catal. A Gen.* **252** (2003) 251–260.

[174] D. Moodley, On the deactivation of cobalt-based Fischer-Tropsch synthesis catalysts, PhD Thesis, Eindhoven University of Technology, Netherlands, 2008.

[175] D. Lee, J. Lee, S. Ihm, Effect of carbon deposits on carbon monoxide hydrogenation over alumina-supported cobalt catalyst, *Appl. Catal.* **36** (1988) 199–207.

[176] C.L. Tucker, E. van Steen, Activity and selectivity of a cobalt-based Fischer-Tropsch catalyst operating at high conversion for once-through biomass-to-liquid operation, *Catal. Today.* **342** (2020) 115–123.

[177] A.P. Vogel, B. van Dyk, A.M. Saib, GTL using efficient cobalt Fischer-Tropsch catalysts, *Catal. Today.* **259** (2015) 323–330.

[178] A.A. Da Silva, A. de Souza Gonçalves, M.R. Davolos, Characterization of nanosized $ZnAl_2O_4$ spinel synthesized by the sol–gel method, *J. Sol-Gel Sci. Technol.* **49** (2008) 101–105.

[179] S. Farhadi, S. Panahandehjoo, Spinel-type zinc aluminate ($ZnAl_2O_4$) nanoparticles prepared by the co-precipitation method: A novel, green and recyclable heterogeneous catalyst for the acetylation of amines, alcohols and phenols under solvent-free conditions, *Appl. Catal. A Gen.* **382** (2010) 293–302.

[180] N.N. Madikizela-Mnqanqeni, N.J. Coville, The preparation and study of sol-gel synthesized Co/Zn/TiO_2 Fischer-Tropsch catalysts, *Appl. Catal. A Gen.* **317** (2007) 195–203.

[181] N.N. Madikizela, N.J. Coville, A study of Co/Zn/TiO_2 catalysts in the Fischer-Tropsch reaction, *J. Mol. Catal. A Chem.* **181** (2002) 129–136.

[182] N.N. Madikizela-Mnqanqeni, N.J. Coville, Surface and reactor study of the effect of zinc on titania-supported Fischer-Tropsch cobalt catalysts, *Appl. Catal. A Gen.* **272** (2004) 339–346.

[183] R.P. Marin, S.A. Kondrat, T.E. Davies, D.J. Morgan, D.I. Enache, G.B. Combes, S.H. Taylor, J.K. Bartley, G.J. Hutchings, Novel cobalt zinc oxide Fischer-Tropsch catalysts synthesised using supercritical anti-solvent precipitation, *Catal. Sci. Technol.* **4** (2014) 1970–1978.

[184] N. Avila, J. Carvallo, B. Shaw, D.M. Kammen, The energy challenge in sub-Saharan Africa: A guide for advocates and policy makers: Part 1: Generating energy for sustainable and equitable development. Oxfam research backgrounder series, 2017.

[185] S.G. Gopaul, A. Dutta, Dry reforming of multiple biogas types for syngas production simulated using Aspen Plus: The use of partial oxidation and hydrogen combustion to achieve thermo-neutrality, *Int. J. Hydrogen Energy.* **40** (2015) 6307–6318.

[186] M.A. Centeno, H. Arellano-Garcia, T. Stroud, J.A. Odriozola, T.J. Smith, T.R. Reina, E. Le Saché, J.L. Santos, Chemical CO_2 recycling via dry and bi reforming of methane using Ni-Sn/Al_2O_3 and Ni-Sn/CeO_2-Al_2O_3 catalysts, *Appl. Catal. B Environ*. **224** (2017)

[187] C. Song, W. Pan, Tri-reforming of methane: A novel concept for catalytic production of industrially useful synthesis gas with desired H_2/CO ratios, *Catal. Today.* **98** (2004) 463–484.

[188] N. Kumar, M. Shojaee, J.J. Spivey, Catalytic bi-reforming of methane: From greenhouse gases to syngas, *Curr. Opin. Chem. Eng*. **9** (2015) 8–15.

[189] D. Pham Minh, T.J. Siang, D.-V.N. Vo, T.S. Phan, C. Ridart, A. Nzihou, D. Grouset, Hydrogen production from biogas reforming: An overview of steam reforming, dry reforming, dual reforming, and tri-reforming of methane in "Hydrogen Supply Chains", C. Azzaro-Pantel (Eds.), Academic Press, 2018, pp. 111-166.

[190] T. Bhaskar, B. Balagurumurthy, R. Singh, M.K. Poddar, Thermochemical Route for Biohydrogen Production in "Biohydrogen", A. Pandey, J. Chang, P. C. Hallenbeck, C. Larroche (Eds.), Elsevier, 2013, pp. 285-316.

[191] J.M. Saad, P.T. Williams, Manipulating the H2/CO ratio from dry reforming of simulated mixed waste plastics by the addition of steam, *Fuel Process. Technol.* **156** (2017) 331–338.

[192] S.Y. Foo, C.K. Cheng, T. Nguyen, A.A. Adesina, Syngas production from CH_4 dry reforming over Co-Ni/Al_2O_3 catalyst : Coupled reaction-deactivation kinetic analysis and the effect of O_2 co-feeding on H_2:CO ratio, *Int. J. Hydrog. Energy* **37** (2012) 17019-17026.

[193] Y. Alqaheem, A. Alomair, M. Vinoba, A. Pérez, Polymeric Gas-separation membranes for petroleum refining, *Int. J. Polym. Sci.* **2017** (2017).

[194] A.A. Kozlova, M.M. Trubyanov, A.A. Atlaskin, N.R. Yanbikov, M.G. Shalygin, Modeling membrane gas and vapor separation in the Aspen Plus environment, *Membr. Membr. Technol.* **1** (2019) 1–5.

[195] D. Edlund, Hydrogen membrane technologies and applications in fuel processing, in "Hydrogen and Syngas Production and Purification Technologies", K. Liu, C. Song, V. Subramani (Eds.), American Institute of Chemical Engineers, 2010, pp. 357–384.

[196] H. Yin, A.C.K. Yip, A review on the production and purification of biomass-derived hydrogen using emerging membrane technologies, *Catalysts.* **7** (2017) 1–31.

[197] N.W. Ockwig, T.M. Nenoff, N.W. Ockwig, T.M. Nenoff, Membranes for Hydrogen Separation, *Chem. Rev.* **107** (2017) 4078–4110.

[198] K. Ohlrogge, K. Sturken, Separation of organic vapors from gas streams by means of membrane, in "Membrane Technology: in the Chemical Industry", S.P Nunes, K. Peinemann (Eds.), Wiley-VCH Verlag GmbH, 2001, pp. 93–117.

[199] A. De Klerk, Can Fischer-Tropsch syncrude be refined to on-specification diesel fuel?, *Energy and Fuels.* **23** (2009) 4593–4604.

[200] V. Calemma, A. de Klerk, Fischer-Tropsch syncrude: To refine or to upgrade? in "Greener Fischer-Tropsch Processes", P. M. Maitlis, A. de Klerk (Eds.), Wiley-VCH Verlag Gmb& Co, 2013.

[201] K. Möller, P. Le Grange, C. Accolla, A two-phase reactor model for the hydrocracking of Fischer-Tropsch-derived wax, *Ind. Eng. Chem. Res.* **48** (2009) 3791–3801.

[202] Neste Corporation, Neste Renewable Diesel Handbook, Neste. (2015) 1–33.

[203] The African Refiners Association (ARA), ARA policy on african gasoline and diesel specifications, 2017.

[204] South African National Standards, SANS 342 : 2016, 2016.

[205] C. Ndimande, Ideal hydrocracking catalysts for the conversion of FT wax to diesel, MSc Thesis, University of Cape Town, South Africa, 2014.

[206] J.L. Hodala, J.S. Jung, E.H. Yang, G.H. Hong, Y.S. Noh, D.J. Moon, Hydrocracking of FT-wax to fuels over non-noble metal catalysts, *Fuel.* **185** (2016) 339–347

[207] P. Le Grange, Models for the hydrocracking of Fischer-Tropsch derived waxes, MSc Thesis, University of Cape Town, South Africa, 2009.

[208] S. Selçuk, Fuels of the diesel-gasoline engines and their properties, in "Diesel Gasol. Engines", Intechopen, 2020.

[209] P. Ghosh, S.B. Jaffe, Detailed composition-based model for predicting the cetane number of diesel fuels, *Ind. Eng. Chem. Res.* **45** (2006) 346–351.

[210] R.K. Rajput, Power system engineering, Laxmi Publications, Delhi, 2006, pp. 3-104.

[211] R.H. Williams, E.D. Larson, Biomass gasifier gas turbine power generating technology, *Biomass and Bioenergy.* **10** (1996) 149–166.

[212] R. Bachmann, H. Nielsen, J. Warner, R. Kehlhofer, Combined-Cycle Gas & Steam Turbine Power Plants, Pennwell Corp, 1997, pp. 1-298.

[213] GreenCape, Waste Economy: Market Intelligence Report 2016, 2016, 1–55.

[214] L.P.R. Pala, Q. Wang, G. Kolb, V. Hessel, Steam gasification of biomass with subsequent syngas adjustment using shift reaction for syngas production: An Aspen Plus model, *Renew. Energy*. **101** (2017) 484–492.

[215] D. Leckel, M. Liwanga-Ehumbu, Diesel-selective hydrocracking of an iron-based Fischer-Tropsch wax fraction (C_{15}-C_{45}) using a MoO_3-modified noble metal catalyst, *Energy and Fuels.* **20** (2006) 2330–2336.

[216] O.C. David, D. Gorri, A. Urtiaga, I. Ortiz, Mixed gas separation study for the hydrogen recovery from H_2/CO/N_2/CO_2 post combustion mixtures using a Matrimid membrane, *J. Memb. Sci.* **378** (2011) 359–368.

[217] K. Aasberg-Petersen, T.S. Christensen, C. Stub Nielsen, I. Dybkjær, Recent developments in autothermal reforming and pre-reforming for synthesis gas production in GTL applications, *Fuel Process. Technol.* **83** (2003) 253–261.

[218] X. Zhao, H.T. Ngo, D.M. Walker, D. Weber, D. Maiti, C. Ummuhan, A.D. Petrov, B. Joseph, J.N. Kuhn, Tri-reforming of surrogate biogas over Ni /Mg/ceria-zirconia /alumina pellet catalysts, *Chem. Eng. Comm.* **205** (2018) 1129-1142.

[219] P.S. Roy, A.S.K. Raju, K. Kim, Influence of S/C ratio and temperature on steam reforming of model biogas over a metal-foam-coated Pd-Rh/($CeZrO_2$-Al_2O_3) catalyst, *Fuel.* **139** (2015) 314–320.

[220] A.I. Tsyganok, M. Inaba, T. Tsunoda, K. Suzuki, K. Takehira, T. Hayakawa, Combined partial oxidation and dry reforming of methane to synthesis gas over noble metals supported on Mg-Al mixed oxide, *Appl. Catal. A Gen.* **275** (2004) 149–155.

[221] H.S. Roh, K.Y. Koo, U.D. Joshi, W.L. Yoon, Combined H_2O and CO_2 reforming of methane over Ni-Ce-ZrO2 catalysts for gas to liquids (GTL), *Catal. Lett.* **125** (2008) 283–288.

[222] M.M.B. Noureldin, N.O. Elbashir, M.M. El-Halwagi, Optimization and selection of reforming approaches for syngas generation from natural/shale gas, *Ind. Eng. Chem. Res.* **53** (2014) 1841–1855.

[223] B.H. Davis, M.L. Occelli, Fischer-Tropsch Synthesis , Catalysts , and Catalysis, CRC Press. (2016).

[224] R.Y. Chein, W.H. Hsu, Analysis of syngas production from biogas via the tri-reforming process, *Energies.* **11** (2018).

[225] C.M. Kalamaras, P. Panagiotopoulou, D.I. Kondarides, A.M. Efstathiou, Kinetic and mechanistic studies of the water-gas shift reaction on Pt/TiO_2 catalyst, *J. Catal.* **264** (2009) 117–129.

[226] H. Iida, A. Igarashi, Characterization of a Pt/TiO_2 (rutile) catalyst for water gas shift reaction at low-temperature, *Appl. Catal. A Gen.* **298** (2006) 152–160.

[227] A. Pulyalina, G. Polotskaya, V. Rostovtseva, Z. Pientka, A. Toikka, Improved hydrogen separation using hybrid membrane composed of nanodiamonds and P84 copolyimide, *Polymers*. **10** (2018).

[228] E. Esposito, I. Mazzei, M. Monteleone, A. Fuoco, M. Carta, N.B. McKeown, R. Malpass-Evans, J.C. Jansen, Highly permeable Matrimid®/PIM-EA(H2)-TB blend membrane for gas separation, *Polymers*. **11** (2018) 1–14.

[229] S. Basu, A.L. Khan, A. Cano-Odena, C. Liu, I.F.J. Vankelecom, Membrane-based technologies for biogas separations, *Chem. Soc. Rev.* **39** (2010) 750–768.

[230] H. Yin, A.C.K. Yip, A review on the production and purification of biomass-derived hydrogen using emerging membrane technologies, *Catalysts.* **7** (2017) 297.

[231] S.S. Hosseini, M.M. Teoh, T.S. Chung, Hydrogen separation and purification in membranes of miscible polymer blends with interpenetration networks, *Polymer* **49** (2008) 1594–1603.

[232] Y. Zhang, I.H. Musselman, J.P. Ferraris, K.J. Balkus, Gas permeability properties of Matrimid® membranes containing the metal-organic framework Cu-BPY-HFS, *J. Memb. Sci.* **313** (2008)

170–181.

[233] F. Weigelt, P. Georgopanos, S. Shishatskiy, V. Filiz, T. Brinkmann, V. Abetz, Development and characterization of defect-free Matrimid® mixed-matrix membranes containing activated carbon particles for gas separation, *Polymers* **10** (2018).

[234] A.S. Maheshwari, J.G. Chellani, Correlations for pour point and cloud point of middle and heavy distillates using density and distillation temperatures, *Fuel.* **98** (2012) 55–60.

[235] A. Vickers, Higher temperature simulated distillation with DB-HT Sim Dist Columns, Agilent Technologies, 2002, https://www.agilent.com/cs/library/applications/5988-7929EN.pdf (accessed Sept. 2019).

[236] K. Darrow, R. Tidball, J. Wang, A. Hampson, Technology characterization - steam turbines, in "Catalog of CHP Technologies", U.S. Environmental Protection Agency, 2015.

[237] Y. Li, Q. Fu, M. Flytzani-Stephanopoulos, Low-temperature water-gas shift reaction over Cu- and Ni-loaded cerium oxide catalysts, *Appl. Catal. B Environ.* **27** (2000) 179–191.

[238] C.E. Kliewer, S.L. Soled, G. Kiss, Morphological transformations during Fischer-Tropsch synthesis on a titania-supported cobalt catalyst, *Catal. Today*. **323** (2019) 233-256.

[239] M. Abbate, F.C. Vicentin, V. Compagnon-Cailhol, M.C. Rocha, H. Tolentino, The soft X-ray spectroscopy beamline at the LNLS: Technical description and commissioning results, *J. Synchrotron Radiat*. **6** (1999) 964–972.

[240] A.P. Petersen, R.P. Forbes, S. Govender, P.J. Kooyman, E. van Steen, Effect of alumina modification on the reducibility of - Co_3O_4 crystallites studied on inverse-model catalysts, *Catal. Lett.* **148** (2018) 1215–1227.

[241] O.A. Bulavchenko, Reduction of double manganese – cobalt oxides : in situ XRD and TPR study, *Dalton Trans.* **47** (2018) 17153-17159.

[242] H.M. Galvis, K.P. de Jong, Catalysts for production of lower olefins from synthesis gas: A review, *ACS Catal.* **3** (2013) 2130–2149.

[243] H. Wang, Y. Kou, Aqueous-phase Fischer-Tropsch synthesis catalyzed by cobalt nanoparticles, *Chinese J. Catal.* **34** (2013) 1914–1925. d

[244] C. Wang, H. Zhao, H. Wang, L. Liu, C. Xiao, D. Ma, The effects of ionic additives on the aqueous-phase Fischer-Tropsch synthesis with a ruthenium nanoparticle catalyst, *Catal. Today*. **183** (2012) 143–153.

[245] H. Wang, W. Zhou, J.-X. Liu, R. Si, G. Sun, M.-Q. Zhong, H.-Y. Su, H.-B. Zhao, J. a Rodriguez, S.J. Pennycook, J.-C. Idrobo, W.-X. Li, Y. Kou, D. Ma, Platinum-modulated cobalt nanocatalysts for low temperature aqueous phase Fischer-Tropsch synthesis., *J. Am. Chem. Soc.* **135** (2013) 4149–58.

[246] H.S. Fogler, Elements of Reaction Engineering, Englewood Cliffs, N.J, Prentice-Hall, 2006.

[247] Sasol, Sasolwax H1 Fischer-Tropsch Hard Wax for PVC processing, Performace Chemicals Wax Division, 2016

Appendices

Appendix A

Cobalt water-gas shift catalysts

Table A-1: Cobalt-based water-gas shift catalysts reported in literature between 1977 and 2009 [155–158,160–162,237]

Year	*Catalyst*	*Temperature*	*Reduction conditions*	*Ref.*	*Note*
1977	Cobalt oxide on molybdenum oxide on alumina	Not stated	Not stated	[237]	
1987	Cobalt/manganese oxide	250°C - 400°C	Reduction in hydrogen 400°C	[155]	
1989	Cobalt/manganese oxide	200°C - 450°C	Reduction in hydrogen at 400°C	[156]	WGS activity only significant at temperatures >250°C
1991	Cobalt/molybdenum	350°C - 400°C	Not stated	[157]	Only hold stable high activity when fully sulphided.
1991	Cobalt/chromium oxide	250°C - 350°C	Reduction in hydrogen at 400°C	[157]	Described as “most active” when compared to copper manganese, iron chromium and copper manganese.
1991	Cobalt/manganese oxide	300°C - 400°C	Reduced. Conditions not stated.	[157]	Effective for conversion of high inlet concentration CO
1993	Cobalt/molybdenum oxide	350°C - 400°C	Not stated	[158]	Very little activity under 350°C
1997	Cobalt/chromium oxide	250°C -550°C	Reduction in hydrogen at 400°C	[159]	Testing effects of sulphur on catalyst.
2001	Cobalt/ceria	300°C-400°C	Not stated	[160]	Ceria alone starts to catalyse the WGS reaction at >400°C
2006	Cobalt-molybdenum carbide	180°C	Reduced at 873K	[161]	Increase in Co additive increased WGS conversion
2009	Sulphided cobalt/molybdenum	250°C -350°C	Not stated	[162]	Only work at low space velocities. Only work in sulphided state.

Appendix B

Experimental Techniques

B.1. Catalyst preparation

B.1.1. Pt-Co/Al_2O_4

Cobalt supported on γ-Al_2O_3 was prepared using Puralox SCCa 5/150 in the same method as described by the patent by Espinoza et al.[153] assigned to Sasol Ltd. 40g of $Co(NO_3)_2.6H_2O$ was dissolved in 50 ml distilled water. 50g of Puralox was then added to the solution and mixed well to create a suspension. The suspension was placed in a rotary evaporator where it was vacuum treated for 2.5 hours at 75°C and 45 mbar at a rotation speed of 75 rpm. The resulting powder was a dark pink. The impregnated carrier was then calcined batch-wise in a low temperature calcination unit at 230°C (ramp rate of 2°C/min up and 4°C/min down) with an air flow of 37.5 ml/min·$g_{catalyst}$. The resulting sample was black. Subsequently the calcined sample was re-slurried in a solution that was made up by dissolving 35 g of $Co(NO_3)_2 \cdot 6H_2O$ and 67.2 mg chloroplatinic acid in 50 ml of distilled water. The suspension was then vacuum treated again in a rotary evaporator under the same conditions in order to further impregnate cobalt and platinum onto the alumina. The subsequent dried carrier was calcined again under the same conditions as the first calcination.

B.1.2. Mn-Pt-Co/Al_2O_4

The catalysts were prepared via three-stage sub-ambient slurry impregnation at 75˚C and 45 mbar [153]. 80g of $Co(NO_3)_2.6H_2O$ was initially impregnated onto 100 g of γ-alumina in 100 ml of distilled water and calcined for 2 hours in a low temperature calcination unit at 230°C (ramp rate of 2°C/min up and 4°C/min down) with an air flow of 37.5 ml/min·$g_{catalyst}$. The rest of the cobalt nitrate (70 g) and chloroplatinic acid (134.4 mg) were then impregnated onto the catalyst in 100 ml of distilled water and dried under ambient conditions. From the batch, six equal portions (ca. 10 g) were impregnated with increasing amounts of manganese acetate dihydrate in distilled water (between 5 ml and 20 ml) in order to get catalysts with Mn:Co ratios (mass) ranging from 0 to 0.45. Each Mn-promoted catalyst was further calcined under for 2 hours at 230°C with an air flow of 37.5 ml/min·$g_{catalyst}$.

B.1.3. Preparation of $Co/ZnAl_2O_4$

The $Co/ZnAl_2O_4$ catalyst was prepared using the same slurry impregnation technique as used to prepare $Pt\text{-}Co/Al_2O_3$, replacing only the support material in equal mass.

B.2. Support preparation

B.2.1. Co-precipitation of $ZnAl_2O_4$

Co-precipitated zinc aluminate was prepared following a similar strategy as described by Farhadi and Panahandehjoo [179]. $Zn(NO_3)_2{\cdot}6H_2O$ (40 mmol/11.9 g) was dissolved in 20 ml of water. This solution was added to a 20 ml solution of $Al(NO_3)_3{\cdot}9H_2O$ (80 mmol/30.01 g). The combined solution was stirred with a magnetic stirrer. Aqueous ammonia solution (25 wt.%) was added until complete precipitation occurred between pH 6 and 7. The precipitate was filtered off and washed three times using a total of 2 litres of deionised water. The co-precipitated zinc aluminate was thereafter calcined at 700°C, 600°C, 500°C and 400°C at 2°/min in a furnace to obtain $ZnAl_2O_4$ nanoparticles. The particles were subsequently analysed for surface area, pore volume and pore radius analysis.

B.2.2. Sol-gel formation of $ZnAl_2O_4$

A separate batch of zinc aluminate was prepared via the sol-gel method [178]. $Zn(CH_3COO)_2.2H_2O$ (30 g) and $Al(NO_3)_3{\cdot}8H_2O$ (102.5 g) were combined with ethanol to create a metal ethanolate solution with a molar ratio of Al/Zn=2:1. The final volume of the solution was 300ml. The resulting solution was maintained under reflux at 75°C for 4 hours. Following this, 40ml of water was added to the solution in order to act as a proton donor for the hydrolysis [178]. The solution was heated to 100°C in a beaker so that the ethanol and excess water could be evaporated off. The resulting gel was initially yellow and then turned transparent upon cooling. The gel was calcined at 700°C, 600°C, 500°C and 400°C and each sample was tested for surface area, pore volume/diameter.

B.3. Standard preparation

B.3.1. Cobalt aluminate standard synthesis

A cobalt aluminate standard was prepared by adding cobalt acetate and aluminium isopropoxide to butanol at 50˚C under vigorous stirring. NaOH was then added dropwise until a pH of 8 and stirred for 1 h Distilled water was then added and stirred for a subsequent 3 h. The precipitate was subsequently filtered, washed and dried in a static furnace at 120˚C for 2 hours and calcined at 1000˚C for 3 h.

B.4. Catalyst characterisation

The following characterisation techniques were used throughout the investigation.

B.4.1. Elemental analysis

All catalyst batches were analysed in terms of cobalt and platinum concentrations using AAS-OES and ICP-OES respectively. Before the samples could be analysed, they required digestion. This was done by the addition of 6 ml concentrated hydrochloric acid (HCl), 2 ml concentrated hydrofluoric acid (HF) and 2 ml concentrated nitric acid (HNO_3). The samples were left overnight with Xpress Teflon stopper for the reaction to complete. The samples were then digested in the MARS-5 Microwave with a ramp time of 25 minutes to 180°C and a hold time of 40 minutes at 1600 W.

A Varian AAS Sprectra-110 was used to determine the cobalt loading in Pt-Co/Al_2O_3. The platinum loading is under the detection limit for AAS-OES, therefore ICP-OES (Varian ICP-OES 230) was used to determine platinum loading and to confirm cobalt loading.

B.4.2. Brunauer-Emmett-Teller (BET)

The surface area, pore volume and pore size of catalysts and support material was measured via using a Micrometrics Tri-Star system. The samples were degassed in nitrogen at 90°C for one hour and then overnight at 200°C. The samples were removed from the degassing port, placed on a BET tube rack and allowed to cool to room temperature. The weight was then recorded. The BET isotherm was recorded at liquid nitrogen temperature.

B.4.3. Hydrogen chemisorption

Metallic surface area of cobalt, rather than total surface area, determines the amount of area available for the Fischer-Tropsch reaction. Hydrogen chemisorption was used to determine the metal dispersion and metal surface area of the cobalt catalysts in this study (assuming negligible contribution of metallic platinum to the metal surface area). The chemisorption analysis was performed in a Micrometrics ASAP 2020C. Prior to reduction, between 0.08 and 0.1 g of catalyst sample was weighed out. The catalysts samples were evacuated using a helium backflow for two and a half hours. The samples were then heated to 350°C at a ramp rate of 1°C/min and a pressure of 1 atm under a flow of hydrogen. The samples were left to reduce for 16 hours in hydrogen. The system was evacuated, and the temperature was reduced to approximately 120°C. The amount of hydrogen adsorbed onto the catalyst surface as a monolayer is then measured at various pressures between 10 and 550mmHg at 120°C.

B.4.4. Temperature programmed reduction (TPR, TPH, TPO)

Temperature programmed reduction (TPR) was used to determine the reducibility and degree of reduction of fresh catalyst. Micrometrics Autochem HP II 2950 was used for the analysis. Silver oxide (Ag_2O) was used to calibrate the hydrogen consumption. TPR profiles were determined by loading a small mass (~0.8g) of catalyst into a quartz U-tube on top of a small amount of quartz wool. The sample was dried at 100°C for 60 minutes in 50 ml_n/min argon, subsequently cooled to 60°C, and then ramped to 900°C at10°C/min in 5% H_2/Ar. In order to determine the degree of reduction a small mass (~0.8g) of catalyst was reduced in the Micrometrics Autochem HP II 2950 at 350°C for 16 hours (1°C/min ramp) in a flow of 50ml_n/min 5% H_2/Ar. Thereafter the degree of reduction was estimated from the hydrogen consumption in the post-reduction TPR (60°C to 900°C at 10°C/min in 5% H_2/Ar) by comparing this to the theoretical hydrogen consumption for complete reduction.

TPH/TPO was conducted in order to determine the amount of hard to remove carbon left over on the spent catalyst samples after hydrogenation at 350°C (furnace temperature) for 1 hour. After hydrogenation, the sample is cooled to 60°C in nitrogen, and then heated up to 600°C in 5% O_2/He.

A Pfeiffer Omnistar GSD 300 Mass Spectrometer was used to monitor the formation of methane (m/z = 15) during the TPH and carbon dioxide (m/z = 44) during the TPO. Deconvolution of peaks in the TPR profile was done via non-linear iterative curve fitting using solver in Excel.

B.4.5. X-ray diffraction (XRD)

X-ray diffraction (XRD) measurements were carried out in a D8 Advance Bruker laboratory X-ray diffractometer with a cobalt source (λ = 1.78897 Å). The XRD was operated at 35 kV and 40 mA with a scan range from 20° to 120° and a step size of 0.043°. Crystallite size for Co_3O_4 was estimated using the Scherrer equation on its most intense diffraction peak (Co_3O_4(311)).

B.4.6. Transmission Electron Microscopy (TEM)

Transmission electron microscopy was used to determine the cobalt crystallite size distribution of fresh and spent catalysts. A FEI TecnaiTM F20 Field Emission TEM coupled with EDS (Energy-dispersive X-ray spectroscopy) were employed for this study. Sample preparation involved adding a few micrograms of catalyst sample to a microcentrifuge tube and filling with ethanol. The sample was shaken manually in the ethanol to disperse the particles, until the slurry was not transparent. A few drops of the resulting slurry were added onto carbon-coated copper grids for TEM analysis.

Elemental mapping was conducted at the Centre for High Resolution Transmission Electron Microscopy on the JEOL ARM200F double CS corrected high resolution STEM. Sample were prepared by mixing a small amount into excess ethanol, vigorously shaking, then taking an aliquot (2-3 drops) from the top layer that had no large particles and dropping it onto the QUANTIFOIL™ grid. The grids were cleaned with a plasma cleaner containing a mixture of oxygen and argon for 30 seconds before being inserted into the TEM. The detector used is an Oxford XMax 100 TLE, operated at a tilt angle of 10 degrees from the horizontal with an 80 mm^2 Silicon Drift Detector (SDD), with a solid angle of 2 steradians (sr), and a Mn Kα resolution of 129 eV. For the mapping, AZtecOne software was used in the collision detection mode, with a live time between 10 and 15 minutes. The images were taken at a spot size of 6, while mapping was done at a spot size of 4.

B.4.7. Thermogravimetric analysis (TGA)

Reduction-oxidation-reduction-oxidation (RORO) studies, similar to those described elsewhere [238], were conducted in order to quantify the relative amount of carbon and cobalt aluminate formation on fresh and spent catalyst samples. This experiment took place in a Discovery 650 Simultaneous TGA/DSC (SDT). In each RORO study, approximately 10 mg of either fresh or dewaxed and calcined spent catalyst was loaded into an alumina crucible and heated to 500°C (2°C/min) in 5% H_2 in N_2 and held at this temperature for 12 hours. The sample was then cooled in N_2 to 50°C. The gas inlet was then changed to air, and the sample was heated to 500°C (4°C/min) and held for 4 hours. The sample was then cooled in N_2, and the reduction and oxidation steps were repeated. The presence of carbon will result in a large weight loss during the first reduction cycle whilst the relative presence of cobalt aluminate can be determined by the total weight gain during the oxidation as cobalt aluminate will not oxidize.

B.4.8. In-situ X-ray photoelectron spectroscopy (XPS)

The XPS experiments were conducted at the Laboratório Nacional de Luz Synchrotron using the UVX synchrotron light source. The XPS had technical description as per [239].

The catalyst was initially reduced at 350°C for 16 hours in pure hydrogen (SV=2500 h-1) and passivated in 5% O_2 for 2 hours for transport. The regions required for scanning using XPS were Co 2p XPS region (BE (eV) = 770 – 805) and Mn 2p XPS region (BE (eV) = 635 – 660). Catalyst was loaded into the sample holder and initial scans performed. The samples were then moved to the pre-chamber and reduced in 5% H_2 at 350°C (2°C/min) for 2 hours and cooled to 30°C in N_2 before another scan was taken. The sample was then oxidized in 5% O_2 in N_2 at 200°C for 3 hours before a final scan was taken.

B.4.9. Scanning electron microscope (SEM)

A LEO 1450 scanning electron microscope was used to characterise the external topography of alumina and zinc aluminate support material. The samples were initially spread on sample holders covered with carbon glue. The samples were then carbonised for 20 minutes prior to being loaded into the SEM.

B.4.10. Particle size distribution Mastersizer

A Mastersizer 2000 with dispersion unit Hydro200G was used to measure the particle size distribution of support material. Before loading samples into the unit, 5 ml of 5% sodium hexametaphosphate was added as a dispersant. Small amounts of sample (ca. 0.5 - 5 g) were then added until the required obscuration level was reached (ca. 11%). Samples were analysed 5 times and results are presented as an average.

B.5. Fischer-Tropsch reactor test

All catalysts in this investigation are tested in a slurry bed Fischer-Tropsch rig at 220°C, 20 bar, H_2:CO:N_2 inlet = 2:1:3 (to simulate air blown reforming) unless otherwise specified. Figure B-1 illustrates a process and instrumentation diagram of the slurry bed setup.

The system is fed with high pressure CO, H_2 and N_2 from a gas store and regulated down to 20 bar. CO is fed into a carbonyl trap (held at 220˚C) before being combined with the other gasses and fed into the slurry bed reactor. The resulting gasses pass through a hot trap where wax is separated from the stream. There is a heated sampling point at this section pull off hot gas for external FID analysis. The gas then passes through a cold trap where water and distillate are separated off, before the remaining tail gas passes through the back- pressure regulator and is depressurized before being split into the vent and the TCD for online gas analysis.

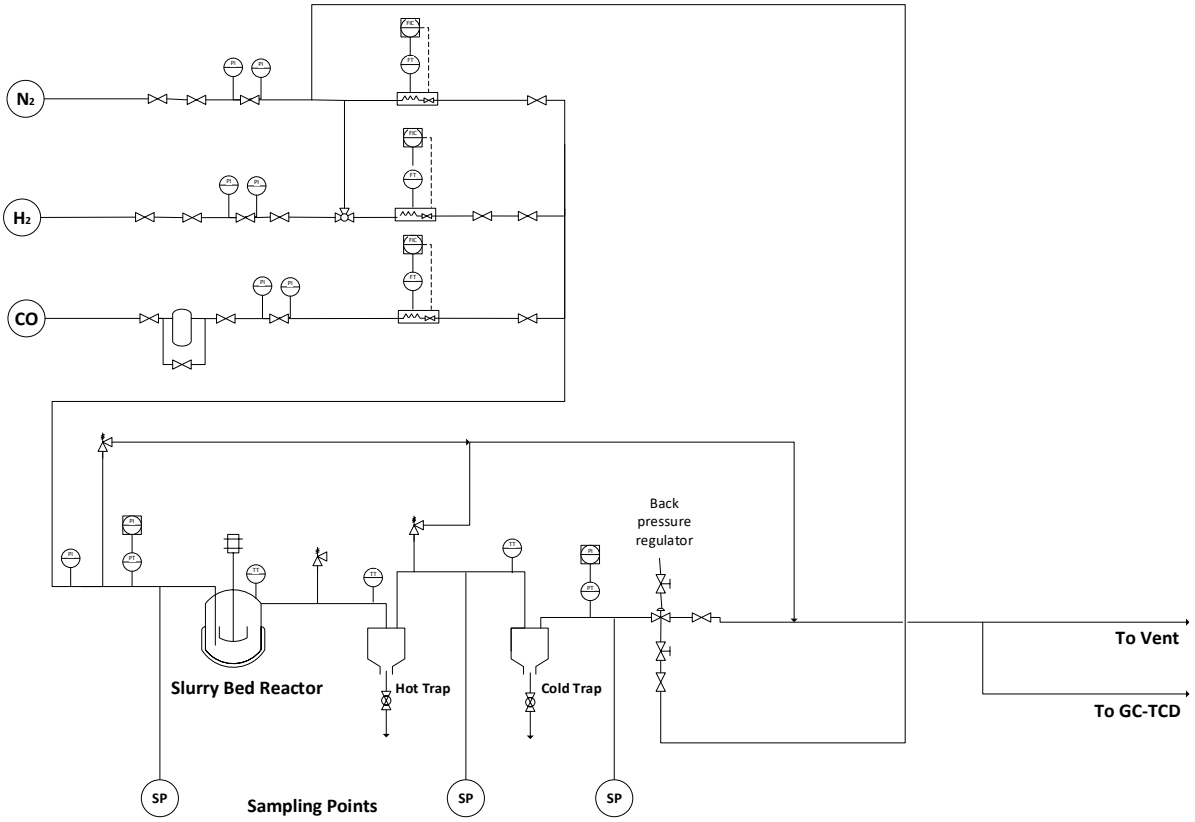

Figure B-1: Piping and instrumentation diagram (P&ID) of slurry bed test unit

B.5.1. Catalyst reduction and loading

Catalysts were reduced ex-situ in a fluidized bed reactor at 350°C for 16 hours in pure hydrogen (SV=2500 h^{-1}). Post reduction the catalyst was transferred to molten wax (Sasol H, specifications in Table X) under a nitrogen blanket to minimize re-oxidation on transfer to the slurry bed. The wax was then solidified into a catalyst-containing 'pellet' which was then added to a slurry bed Fischer-Tropsch reactor filled with 360 g molten wax. The slurry bed reactor was pressurized at 150°C to 20 bara in nitrogen.

Table B-1: Sasolwax H1 specifications taken from [247].

Wax properties	*Units*	*Specification*	*Typical values*
Congealing point	°C	96 - 100	97
Colour	Saybolt	+ 15 min	+ 22
Oil content	mass %	-	< 0.2
Molecular weight	Dalton	-	880
Brookfield viscosity at 135°C	cP	6-10	8
Penetration at 25°C	0.1 mm	1 max	1

B.5.2. Analytical methods

Two gas chromatograph detectors will be used to analyse the tail gas – an online thermal conductivity detector (TCD) and offline flame ionisation detector (FID) with the following specifications and example chromatograms.

Table B-2: Technical information and conditions for GC-FID using Varian CP-3800

Detector temperature	200°C
Column	Varian Capillary Column
Column pressure	1.7 bar
Flame gas	H_2
Makeup gas	N_2
Air flow	300 ml/min
Coolant	CO_2, liquid

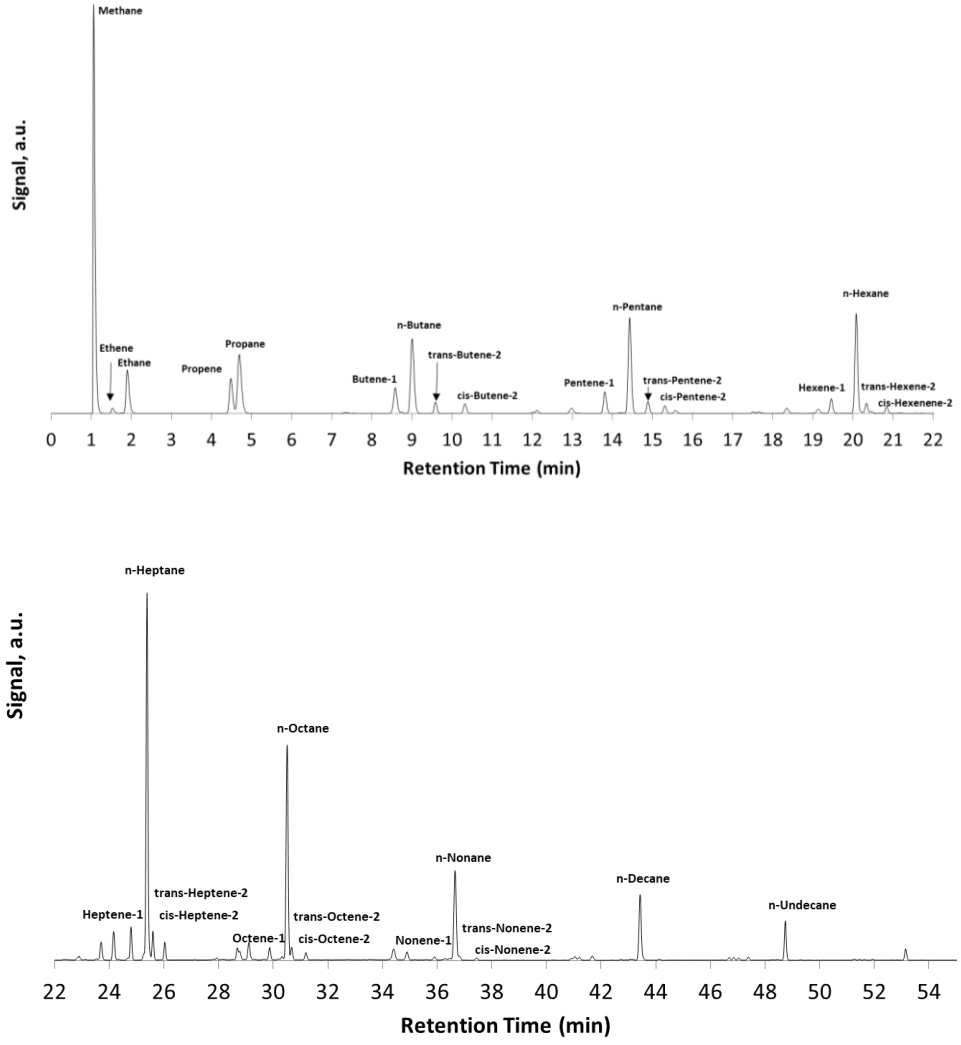

Figure B-2: GC-FID chromatogram of gas phase Fischer-Tropsch products at 220°C, 20 bar and H_2/CO ratio of 2 for Mn-Pt-Co/Al_2O_3 at X_{CO} = 30% showing all products analysed for this investigation.

Table B-3: Technical information and conditions for GC-TCD Agilent Technologies 7820B

Oven temperature	70°C
Column 1	Porapak Q 80/100 SST
Column 2	MolSieve 5A 60/80 SST
Carrier gas	Argon
Reference gas	Argon
Reference flow	15 ml/min
Makeup flow	3 ml/ min
Coolant	None

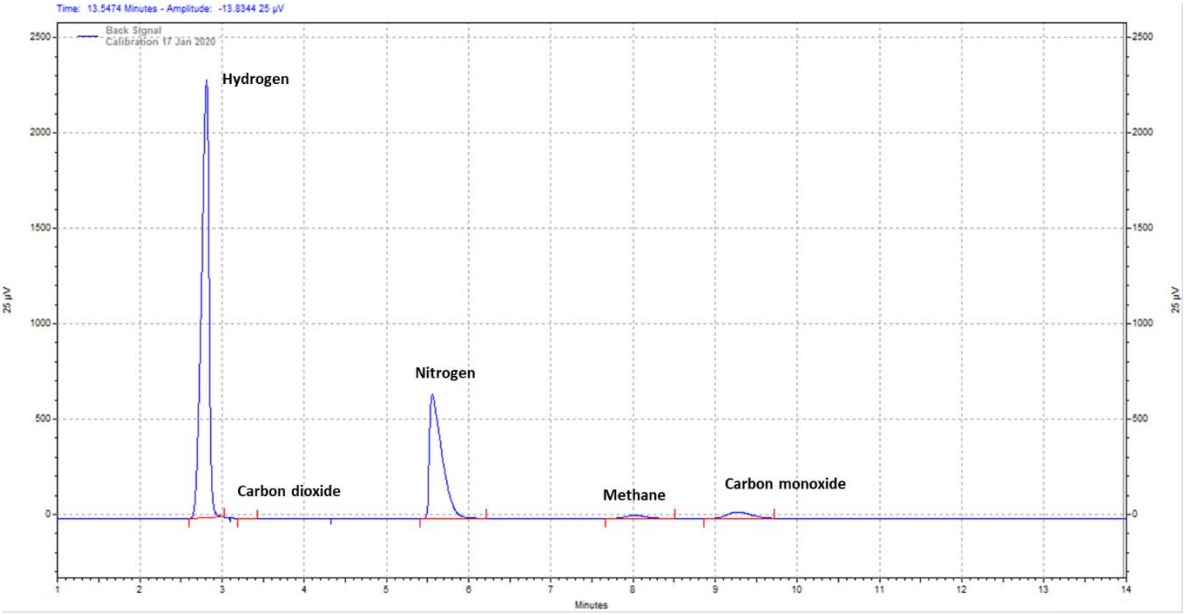

Figure B-3: GC-TCD chromatogram of H_2, N_2, CO, CO_2 and CH_4 at 220°C, 20 bar and H_2/CO =2.

B.6. Soxhlet extraction for spent catalysts

The wax covering the spent slurry catalyst was removed by means of Soxhlet extraction. The following setup was used (see Fig B-2). A 1000ml round bottom flask containing 750 ml of xylene was placed on a heating mantle and secured with clamps. The 44/55 Soxhlet was placed on top of the flask and clamped at the top and bottom. A cellulose thimble was filled with the wax covered catalyst and placed inside Soxhlet. The condenser was then placed on top of the Soxhlet and attached to a water inlet. Insulation was added around the flask and the upper arm of the Soxhlet. Due to the low maximum temperature of the cellulose thimble (150°C), care was made not to insulate the Soxhlet itself. The xylene was brought to a boil (140°C) and monitored until the vapour travelled up the arm. If this did not occur, more insulation was added to the upper arm or the heat rate was increased slightly. The xylene would fill up the Soxhlet and drain 2 times per hour. This is less than reported in literature however is due primarily to the large volume of the Soxhlet used in this experiment. The Soxhlet extraction unit was left to reflux

for 64 hours after which the thimble was removed. The catalyst was thereafter calcined at 180°C for 2 hours to remove excess xylene.

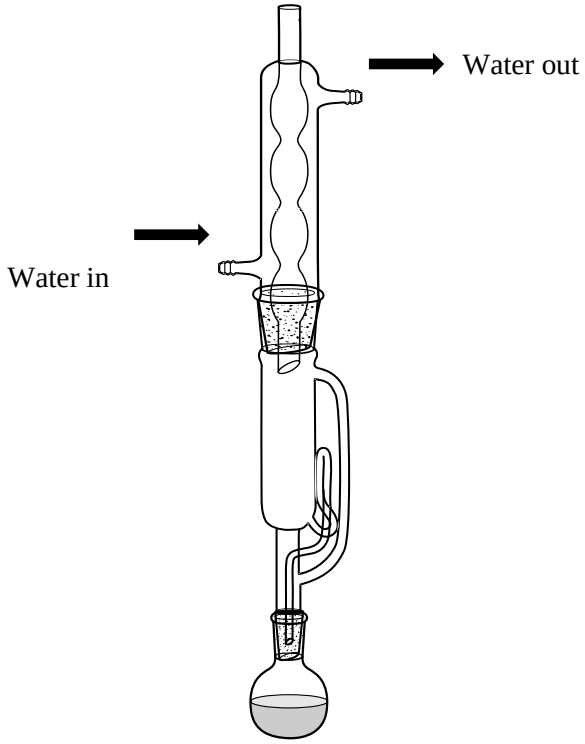

Figure B-4: Soxhlet extraction apparatus.

Appendix C

Catalyst characterisation

C.1. Fresh Pt-Co/Al_2O_3

The physio-chemical characteristics of the calcined and reduced catalyst, Pt-Co/Al_2O_3, are shown in Table C-1. The support material has a measured BET surface area of 157 m^2/g and a pore volume of 0.5 cm^3/g. the BET-surface area for the calcined catalyst precursor is, as expected, lower than that of the support material, since the density of Co_3O_4 is higher than that of alumina.

Table C-1: Physio-chemical characterization of the support and catalyst

	calcined catalyst precursor				*Reduced catalyst (350°C, 16 hours)*			
	S_{BET} (m^2/g)	**V_{pore} (cm^3/g)**	**d_{pore} (nm)**	**d_{Co3O4}[1] (nm)**	**DOR[2]**	**S_{Me}[3] (m^2/g_{cat})**	**D_c[4] (%)**	**d_{Co}[5] (nm)**
Puralox	157	0.5	8.8					
Pt-Co/Al_2O_3	113	0.3	8.0	11	54%	13	16[6]	6.0[6]

[1]Diameter of Co_3O_4-crystallites as determined using XRD; [2]Degree of reduction; [3]Metal surface area as determined by H_2-chemisorption; [4]Cobalt dispersion; [5]Diameter of cobalt-crystallites estimated from H_2-chemisorption data; [6]Corrected for degree of reduction

The pore volume and average pore diameter of the calcined Pt-Co/Al_2O_3-catalyst is 0.3 cm^3/g and 8 nm in comparison to the support which has a pore volume and pore size of 0.5 cm^3/g and 9 nm respectively. The reduced catalyst has a metal surface area of 13 m^2/g as determined using H_2-chemisorption. This corresponds to an average dispersion of 16 % after correction for the degree of reduction. The dispersion, which was corrected for degree of reduction, was similar to that of literature for Al_2O_3-supported catalysts [87]. The average corrected crystallite size obtained via chemisorption was 6.0 nm. The average crystallite size of Co_3O_4 in the calcined catalyst as determined via XRD line broadening was 11 nm.

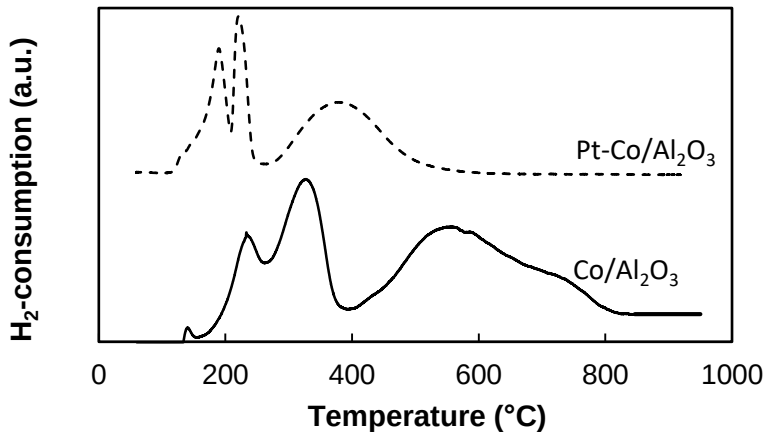

Figure C-1: Temperature programmed reduction (TPR) spectra for platinum-promoted cobalt on alumina catalyst.

The reducibility of the catalyst was investigated using temperature programmed reduction (TPR). The addition of only 0.05 wt.% Pt improves the reducibility of the catalyst significantly (see Fig. C-1) [153]. The first peak in the TPR-profile has been identified as hydrogen consumption due to the reductive nitrate decomposition of excess nitrate ions which were not removed during the first or second calcination step [93,240]. The second peak is identified as the reduction of Co_3O_4 to Co(II)O, confirmed by the TPR of pure Co_3O_4 [93,240]. The final peak which can be seen to have sluggish reduction is identified as the final reduction of Co(II)O to Co^0, the active metal in FTS [93,240].

Interestingly, all three peaks are shifted with platinum addition, including the cobalt nitrate peak which was shifted from 230°C to 190°C. The reduction of Co_3O_4 is improved significantly with a peak shift from 315°C for Co/Al_2O_3 to 215°C for $Pt\text{-}Co/Al_2O_3$. The greatest improvement with the addition of 0.05 wt.% Pt can be seen in the final reduction step yielding active metallic cobalt. In the latter case, the peak shifted from 550°C to 360°C. The most important improvement in this case however is not the shift from the peak crest, but rather the removal of the sluggish tail. With the addition of platinum, complete reduction can be achieved around 500°C, rather than at 820°C. It should be noted that complete reduction was not achieved in this study, and a final degree of reduction of 54% was obtained with a reduction temperature of 350°C.

C.2. Fresh Mn-Pt-Co/Al_2O_3

The physio-chemical characteristics of calcined and reduced Mn-Pt-Co/Al_2O_3 prepared via slurry impregnation [153] are been presented in Table C-3.

Table C-2: Physio-chemical characterization of Puralox and Mn-Pt-Co/Al_2O_3.

		Calcined catalyst precursor				*Reduced catalyst (350°C, 16 hours)*	
	Mn:Co	**S_{BET} (m^2/g)**	**V_{pore} (cm^3/g)**	**d_{pore} (nm)**	**d_{Co3O4}[1] (nm)**	**H_2 uptake[2] (cm^3/g STP)**	**Metal surface area[3] (m^2/g sample)**
Puralox		157	0.5	8.8			
Mn-Pt-Co/Al_2O_3	0	113	0.3	8.0	11	4.3	13
	0.04	118	0.3	8.7	14	3.0	11
	0.09	122	0.3	8.3	15	3.2	9.6
	0.14	150	0.3	7.6	13	3.0	9.1
	0.23	100	0.2	7.3	12	2.5	6.9
	0.47	86	0.2	7.9	10	1.8	4.7

[1]Diameter of Co_3O_4-crystallites as determined using XRD; [2]H_2 uptake as determined chemisorption; [3] Based on H_2 uptake

The BET surface area for the six catalysts fall within the range of 86 to 150 m^2/g. The measured surface area increases slightly from 113 m^2/g to 150 m^2/g with the addition of Mn up until a Mn:Co ratio of 0.14 after which it decreases to 86 m^2/g. Both measured pore volume and pore size are not significantly altered by manganese addition.

The H_2 uptake measured via H_2 chemisorption decreases significantly with Mn addition from 4.6 cm^3/g for unpromoted Pt-Co/Al_2O_3 to 1.8 cm^3/g at a Mn:Co ratio of 0.47. Based on this H_2 uptake, a metallic surface area of 13 m^2/g was measured for the Mn unpromoted catalyst which decreased to 4.7 m^2/g for a Mn:Co ratio of 0.47. The decrease in H_2 uptake and metallic surface area may be explained by the slurry impregnation preparation method (see Appendix B) as a similar trend was reported by Johnson et al. [142] for silica-supported Mn-promoted cobalt catalysts prepared via incipient wetness impregnation [145]. As Mn was co-impregnated with half the cobalt in a second step (see Appendix B for preparation method), the manganese is likely positioned on top of the cobalt species, thus blocking cobalt sites.

Temperature programmed reduction profiles of the five Mn-Pt-Co/Al_2O_3 catalysts as well as Pt-Co/Al_2O_3 are shown in Figure C-2. The Mn-unpromoted catalyst profile consists of two distinct peaks at 230°C and 400°C which correspond to the reduction of Co_3O_4 to Co(II)O and the reduction of Co(II)O to Co^0 respectively [94]. The TPR profile for Mn-Pt-Co/Al_2O_3 with a Mn:Co ratio of 0.04 and 0.09

remains similar in shape to the Mn-unpromoted catalyst, albeit the reduction of Co(II)O to Co^0 seems to be somewhat more sluggish, occurring at ca. 450°C. Increasing the concentration of manganese further to a Mn:Co mass ratio of 0.14 results in the formation of an additional low temperature peak – likely due to the decomposition of the manganese acetate precursor left over after calcination. Further manganese addition results reduction of both Co_3O_4 and Co(II)O being hindered, with both peaks shifting significantly. At the maximum manganese loading (Mn:Co = 0.47 mass/mass) an intermediate peak can be found at 461°C, which is may be due to the reduction of Mn_3O_4 to MnO [241].

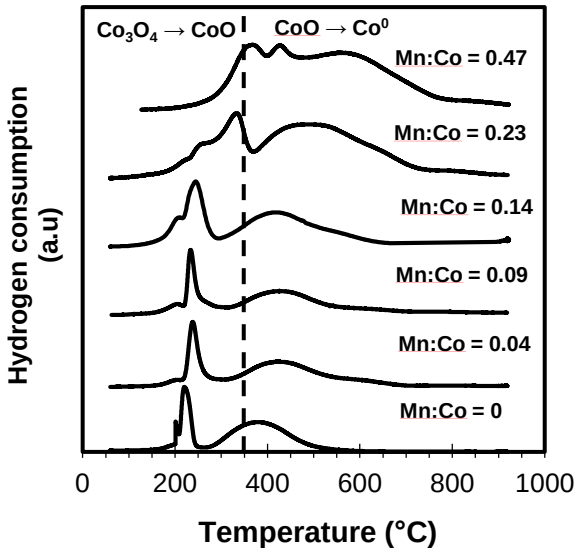

Figure C-2: Hydrogen consumption as a function of temperature for temperature-controlled hydrogenation of Mn-Co-Pt/Al_2O_3

TEM element mapping (see Fig C-3) indicates a high level of dispersion of both manganese and cobalt across the surface of the support. It may also be noted that the regions dense in cobalt, also seem to be regions of high manganese concentration. This suggests, perhaps, that despite slurry impregnation being used which does not preferentially place certain species, the manganese is preferentially positioned close to the cobalt. As manganese was impregnated subsequent to cobalt, this may suggest that manganese is likely sitting on top of the cobalt species, which may limit activity by blocking active sites. This could explain the decrease in metallic surface area in Table C-2.

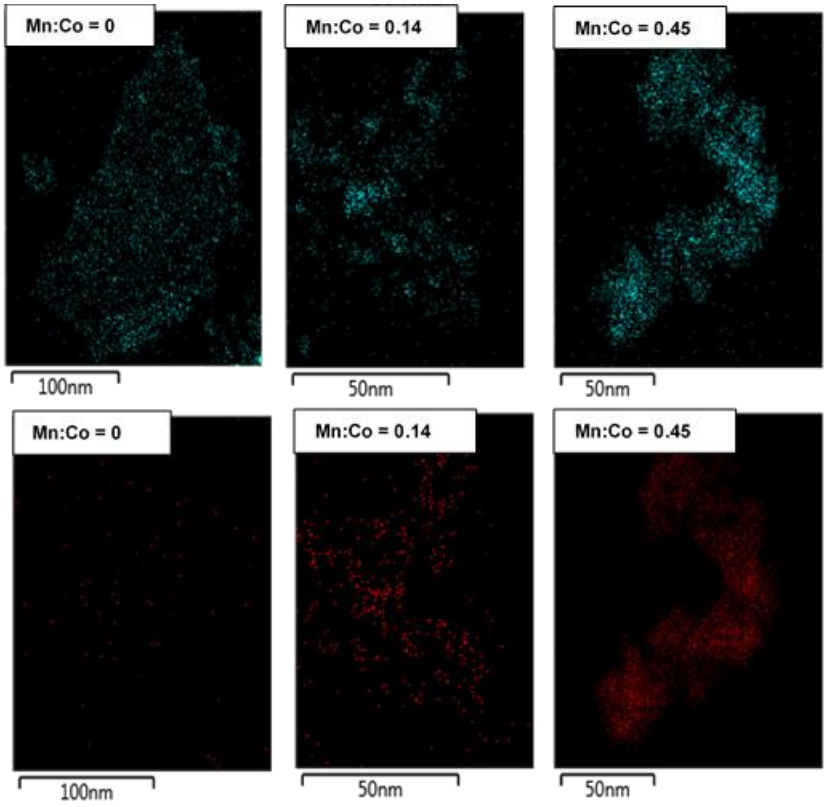

Figure C-3: HR-TEM elemental mapping for Mn-Co-Pt/Al_2O_3 with Mn:Co ratios of 0, 0.14 and 0.45.

Figure C-4 shows the XPS results for the Co 2p region (left) and Mn 2p region (right) of Mn-Pt-Co/Al_2O_3 with Mn:Co ratio = 0.23. In the spectra labelled (a) the catalyst was reduced at 350°C for 16 hours and then passivated in 1% O_2 in N_2 for 2 hours. In the spectra labelled (b) the catalyst was further reduced in-situ to ensure the removal of the passivated layer and to ensure the catalyst was not fully oxidized in transit. The spectra labelled (c) the catalyst was oxidized in 5% O_2 in N_2 at 200°C for 2 hours.

The $Co2p_{3/2}$ peak can be seen at approx. 778.7 eV for pre-treated and reduced samples. The similarity between Co 2p XPS spectra (a) and (b) indicate that the pre-treatment was successful and little to no re-oxidation occurred in transit. A satellite peak is identified at 786 eV for pre-treated and reduced samples indicative of the presence of Co(II) from Co(II)O and Co_3O_4 indicating that the sample is not fully reduced. $Co2p_{3/2}$ peak found at 785 eV for oxidized sample, indicating an increased oxidation state.

In terms of the Mn 2p region, all three samples exhibited $Mn2p_{3/2}$ at approx. 640.5 eV indicating that oxidation had little to no effect on the oxidation state of manganese. Satellite peak identified at 646 eV

indicating the presence of MnO in a reduced state. It is not clear if MnO_2 or Mn_2O_3 are also present. This could be identified by the Mn 3s XPS region in the future.

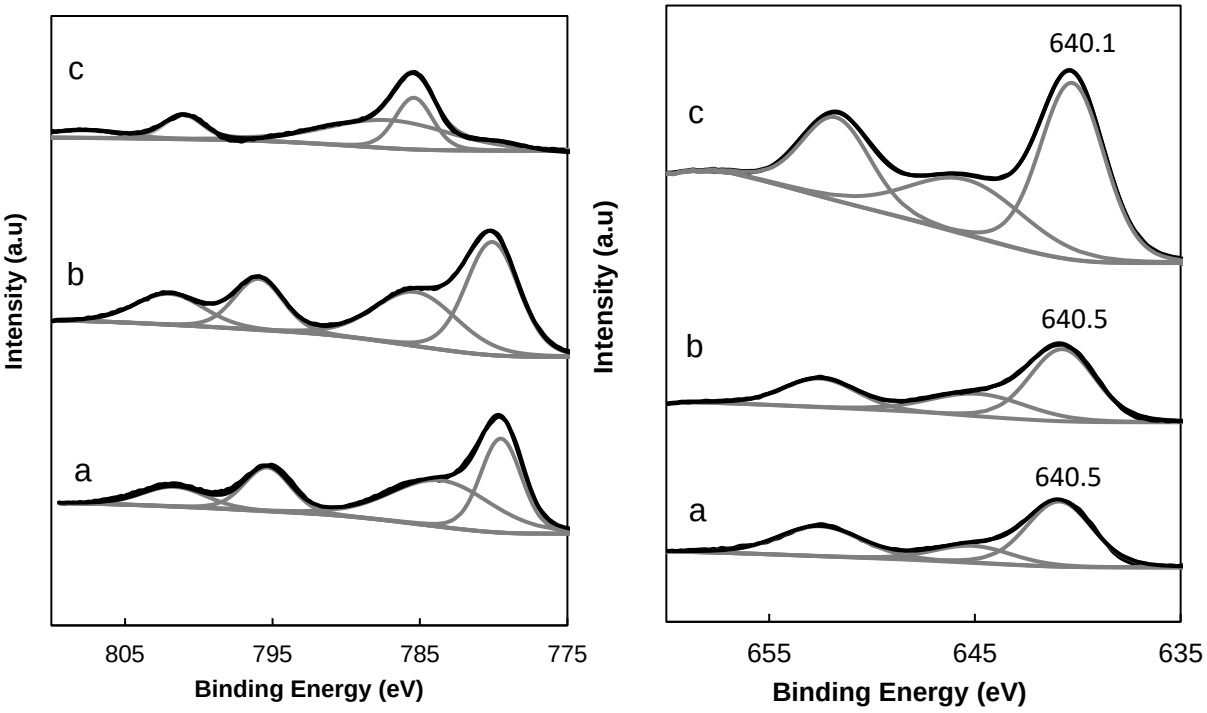

Figure C-4: Co 2p XPS region (left) and Mn 2p XPS region (right) of Mn-Pt-Co/Al_2O_3 with Mn:Co ratio = 0.23.
[a] Reduced at 350°C for 16 hours and then passivated in 1% O_2 in N_2 for 2 hours
[b] Reduced at 350°C for 2 hours in the XPS
[c] Oxidized 5% O_2 in N_2 at 200°C for 2 hours

Table C-3: Atomic ratio of Mn-Pt-Co/Al_2O_3 after pre-treatment, reduction and oxidation.

	Mn/Co
Pre-treatment	0.27
Reduction	0.24
Oxidation	1.34

On reducing the sample, the surface atomic ratio of Mn/Co decreases slightly. This has been reported by Morales et al. [147], and has been attributed to the enrichment of MnO on the surface by the migration of MnO particles to the support during reduction to Co^0. On oxidizing the sample, the Mn/Co atomic ratio increases, indicating that MnO migrates onto, and covers cobalt crystallites in the process of reduction. It is unknown if, on further reduction, the MnO migrates onto the support again or not.

C.3. Spent Mn-Pt-Co/Al_2O_3

Spent Mn-Pt-Co/Al_2O_3 was dewaxed and, using temperature programmed hydrogenation, the amount of carbon on the surface of the catalysts were analysed (Figure C-5). The amount of carbon on the surface of the spent catalyst was found to be inversely proportional to the Mn:Co mass ratio.

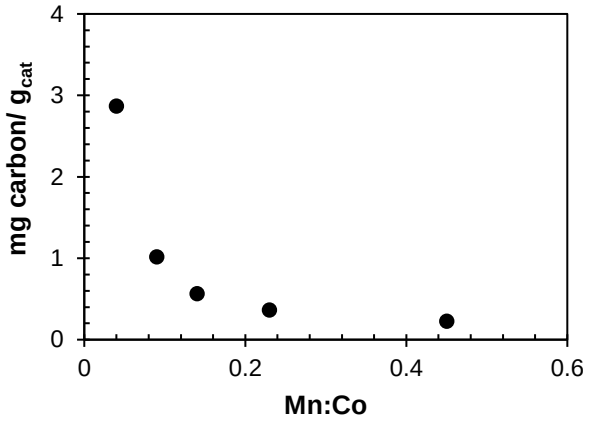

Figure C-5: Carbon deposition on spent Mn-Pt-Co/Al_2O_3 as a function of Mn:Co ratios

C.4. Spent Pt-Co/Al_2O_3

C.4.1 TEM images

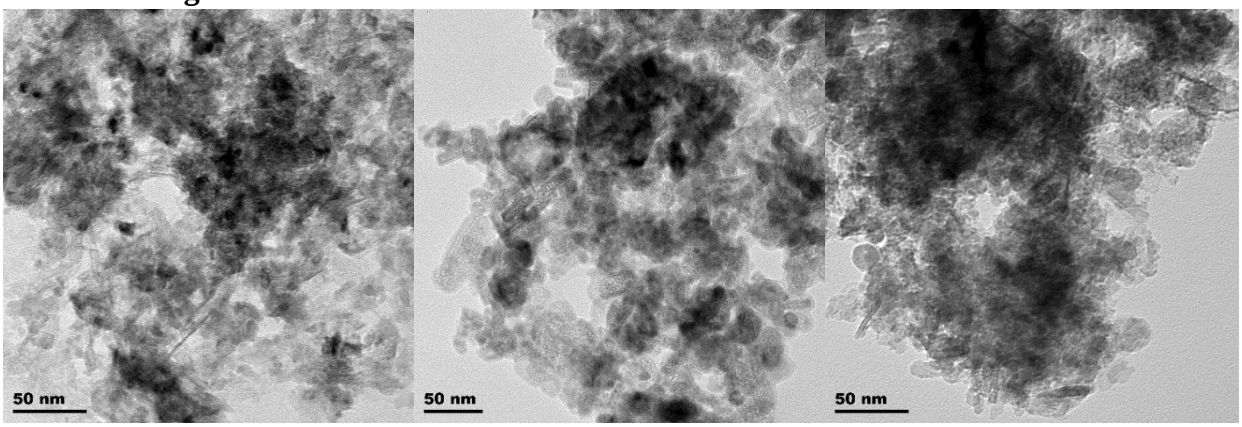

Figure C-6: Transmission electron microscopy images of fresh Pt-Co/Al_2O_3 (a), high conversion spent Pt-Co/Al_2O_3 (b) and 'simulated' high conversion spent Pt-Co/Al_2O_3 (c).

C.4.2 Reduction-oxidation-reduction oxidation cycles

As an additional measure to quantify cobalt aluminate and carbon deposition on the three catalysts (fresh Pt-Co/Al_2O_3, high conversion spent Pt-Co/Al_2O_3 and 'simulated' high conversion spent Pt-Co/Al_2O_3) a TGA-based reduction-oxidation-reduction-oxidation (RORO) study was conducted (see Appendix B.4.7 for method), adapted from Kliewer et al. [238]. Figure C-7 illustrates the RORO profiles for the three catalysts.

Initially, the catalysts are in an arbitrary state of reduction, and weight is measured in a nitrogen environment at 50°C. The catalysts are then exposed to hydrogen and the temperature is ramped to 500°C. The catalyst is then held at 500°C for 4 hours. At these temperatures, as seen by TPH and TPR all polymeric carbon (spent) and excess nitrates (fresh) are removed. The difference between the mass lost during the first reduction and second reduction gives a comparative indication of the amount of carbon on each sample. It must be noted that the difference in mass is not directly equal to the mass of carbon or precursor on each sample – as the initial oxidation state of the sample may be different to the state after oxidation at 500°C.

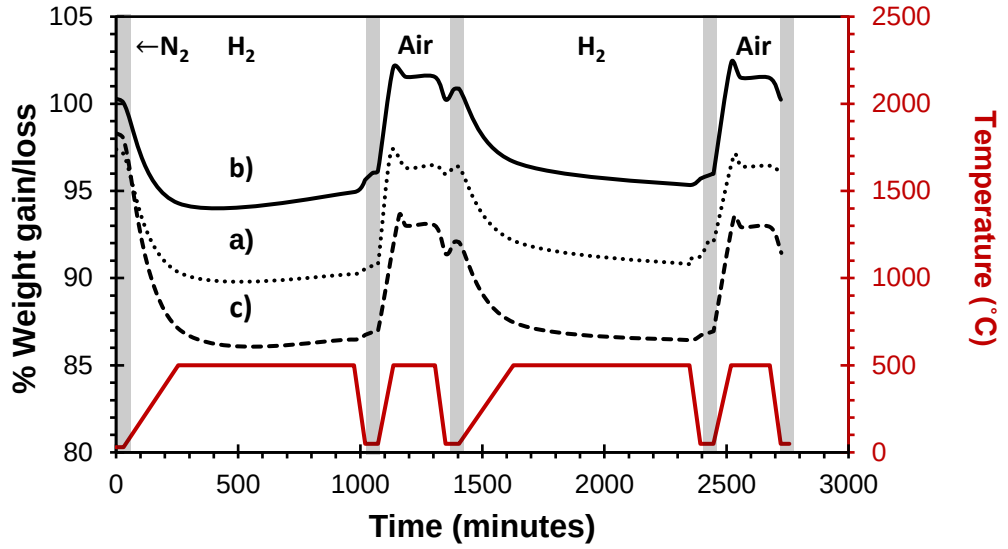

Figure C-7: Reduction-oxidation-reduction-oxidation profile on TGA-DSC for (a) fresh catalyst (b) spent catalyst after exposure to high conversion (c) spent catalyst after exposure to a feed containing water Shaded regions in N_2 environment

The catalysts are then oxidized by ramping to 500°C under air and holding for 4 hours. The presence of mixed metal oxide was evaluated by the weight change during oxidation, as non-reducible Co (Co^{2+}) will not oxidize. The RO steps were then repeated for reproducibility.

Table C-5: Cyclic RORO study weight changes under reduction and oxidation at 500°C.

	Weight Change (%)				***Reduction Weight Difference***
	Reduction 1	**Oxidation 1**	**Reduction 2**	**Oxidation 2**	
Fresh catalyst (a)	6.6	5.6	5.3	5.3	1.3
High conversion (b)	6.1	4.7	4.5	4.5	1.6
External water addition (c)	11.3	5.0	5.1	5.2	6.2

Table C-5 shows the weight change after each step in the RORO cycle. All weights were recorded at 50°C in an N_2 environment to avoid changes in buoyancy. Fresh catalyst had, as predicted, the most amount of oxidizable material with a weight change of between 5.3 - 5.6% during oxidation. This is less than the theoretical weight change for the catalyst containing 22 wt.% Co (30 wt. % Co_3O_4) which is 8.0%. This indicates that complete reduction is not achieved during the RORO cycles.

Spent catalyst from the 'simulated' high conversion run (water addition) had a weight change of 5.0 - 5.1 % under oxidation conditions, suggesting the presence of some irreducible cobalt. The spent sample,

which had been exposed to a high conversion, had the smallest weight gain of only 4.5 - 4.7 wt.% under oxidation indicating the least amount of oxidizable material, strengthening the conclusion from the TPR results that more cobalt aluminate is formed at high conversion due to larger P_{H_2O}/P_{H_2} ratios.

The weight difference between the two reduction steps indicate, as seen in the TPH, that the catalyst exposed to a feed containing water showed a higher amount of carbon deposited compared to the catalyst exposed to high conversion. The reduction weight difference for the fresh sample is attributed not to carbon deposition, but the hydrogenation of excess cobalt nitrate, also seen in the TPR study.

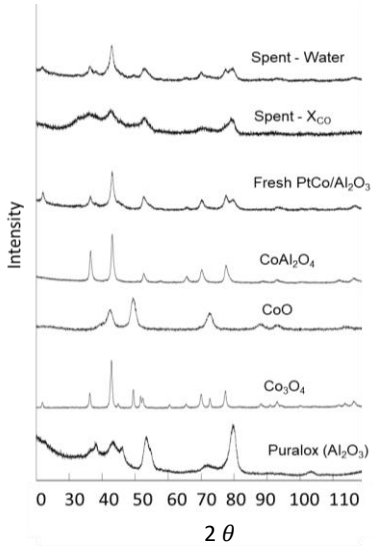

Figure C-8: XRD pattern for alumina support, Co_3O_4, CoO, $CoAl_2O_4$, fresh Pt-Co/Al_2O_3 and spent Pt-Co/Al_2O_3 from the high conversion and 'simulated' high conversion runs.

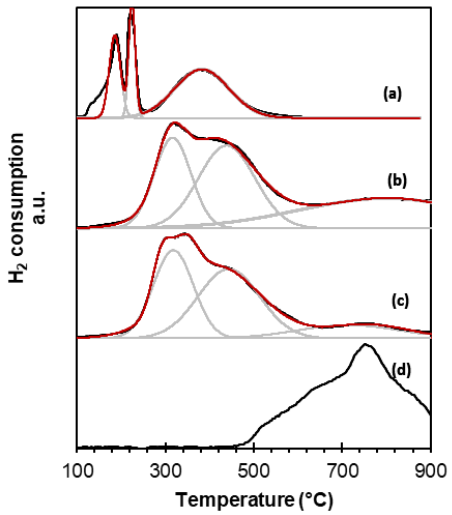

Figure C-9: Normalized TPR spectra for (a) fresh Pt-Co/Al_2O_3 (b) spent catalyst exposed to high X_{CO} (c) catalyst exposed to a feed containing water (d) $CoAl_2O_4$ reference showing reconstruction from peak deconvolution in red.

C.5. $ZnAl_2O_4$ and Pt-Co/$ZnAl_2O_4$

C.5.1 $ZnAl_2O_4$ supports

C.5.1.1. Crystallography

The XRD pattern of zinc aluminate prepared via co-precipitation [179] and sol-gel [178] method is shown (Figure C-8) to form a crystalline phase with diffraction peaks at 36.4°, 42.9°, 52.8°, 57.6°, 65.6°, 70.1°, 77.4°, 89.2°, 92.8°, 111.6°, and 116.4° which correlates directly with the reference peaks for $ZnAl_2O_4$ (gahnite). The average crystallite size for zinc aluminate prepared via co-precipitation and sol-gel method were 8.61 nm and 9.89 nm respectively.

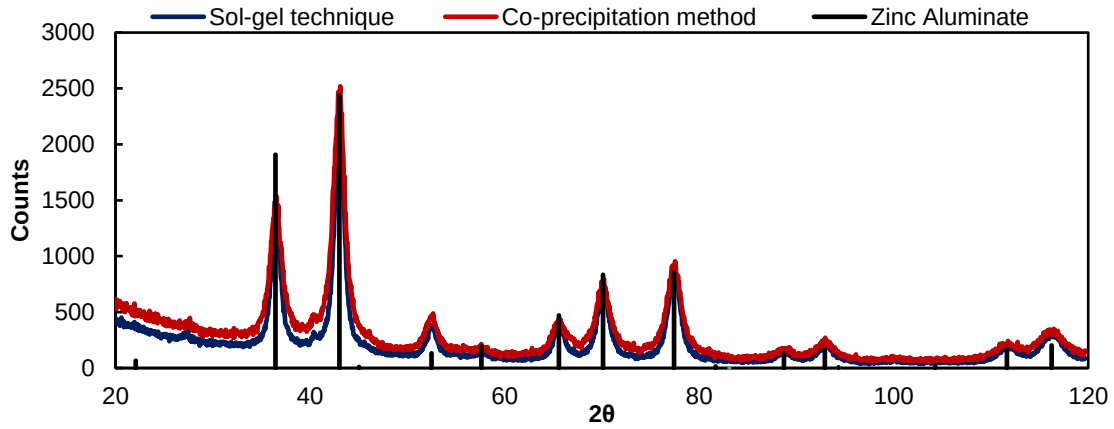

Figure C-8: XRD pattern for zinc aluminate prepared via the sol-gel [178] and co-precipitation [179] methods with zinc aluminate (gahnite) standard diffraction pattern.

C.4.1.2. Topography and particle size distribution

The SEM topography and particle size distribution of Puralox SCCa 5/150 γ-Al_2O_3 (used as a support material for Pt-Co/Al_2O_3) and the two zinc aluminate samples are shown in Figure C-9 and C-10 respectively. The γ-Al_2O_3 sample contains spherical particles with a normal particle size distribution and mean particle size of ca. 100 μm. Both zinc aluminate samples contains jagged particles of irregular in shape and size with an irregular distribution ranging from ca. >10 μm to > 300 μm. Unfortunately, in a slurry bed reactor the irregular jagged shape of zinc aluminate may cause unwanted breakages which could decrease activity. Thus, for industrial purposes, it would be critical to spray dry both types of zinc aluminate in order to improve robustness.

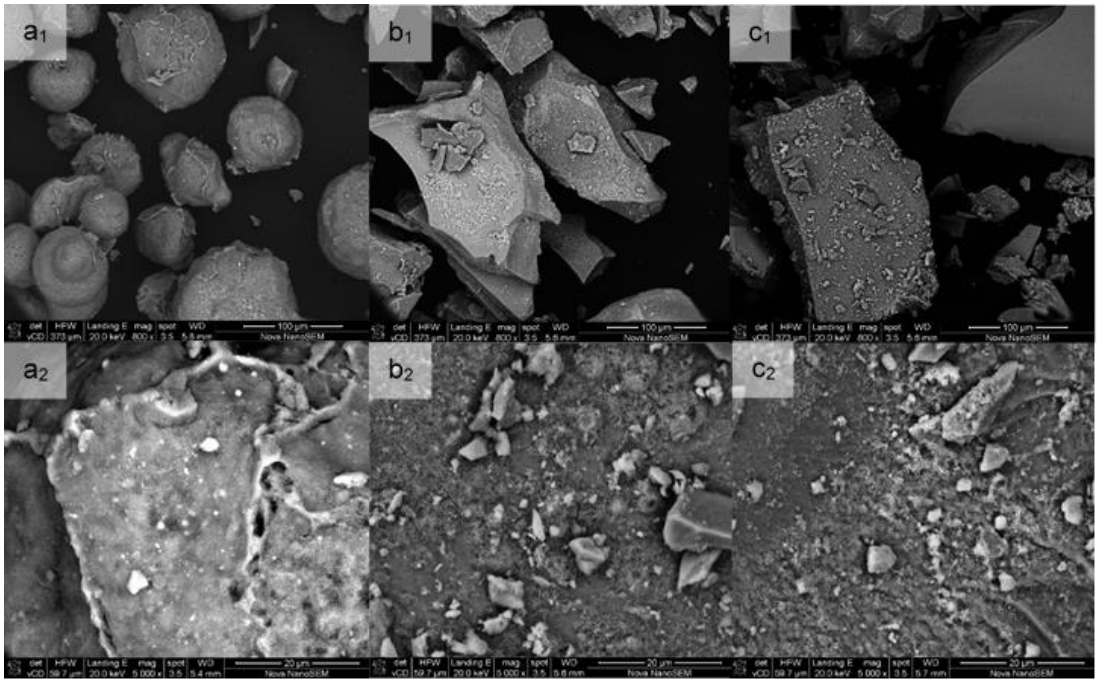

Figure C-9: SEM images of (a) Puralox SCCa 5/150 γ-Al_2O_3, (b) sol-gel $ZnAl_2O_4$ and (c) co-precipitated $ZnAl_2O_4$ at (1) 100 µm and (2) 20 µm magnification.

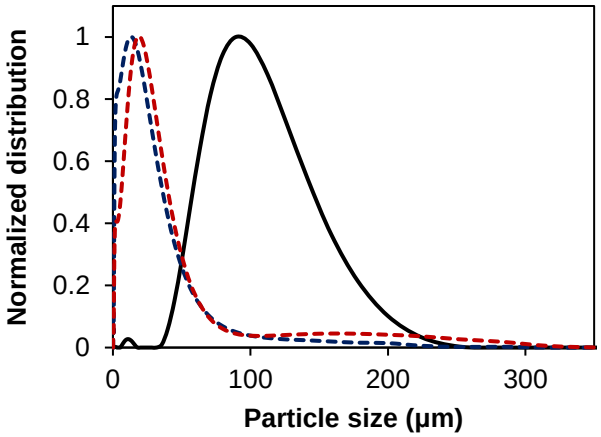

Figure C-10: Particle size distribution of (-) Puralox SCCa 5/150 γ-Al_2O_3, (---) sol-gel $ZnAl_2O_4$ and (- - -) co-precipitated $ZnAl_2O_4$ measured via Mastersizer 2000.

C.4.1.2. Physisorption

The results of the physisorption analysis of the various forms of $ZnAl_2O_4$ are shown in Figure C-11 alongside the physisorption results for Puralox SCCa 5/150 used in the study (red dotted line).

A large support surface area typically translates into a large catalyst surface area which contributes towards better metal dispersion and a higher overall activity. Figure C-11 shows that co-precipitation yields a support with a larger surface area, with lower calcination temperatures improving this further. In one case (co-precipitated and calcined at 400°C) the surface area surpassed that of the Sasol Puralox γ-Al_2O_3 which has a surface area of 157m^2/g.

Both co-precipitation and sol-gel method yielded zinc aluminate with very low pore volumes, with the sol gel method only slightly larger at lower calcination temperatures. However, $ZnAl_2O_4$ prepared via the sol-gel method, has significantly larger pore sizes that are comparable to γ-Al_2O_3 at higher calcination temperatures. As pore size determines the extent of unfavourable mass transfer limitations, it is critical that this factor be comparable for reactor studies.

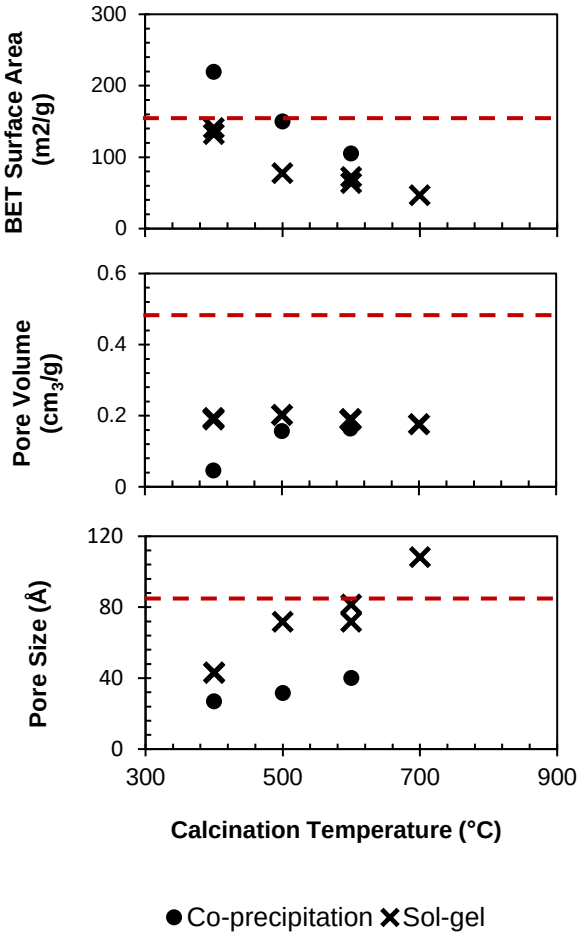

Figure C-11: Surface area, pore size and pore volume physisorption results for different zinc aluminate samples in comparison to Puralox SCCa 5/150 (red dotted line).

Thus, $ZnAl_2O_4$ prepared via the sol-gel method and calcined at 600°C will be used for studying the effect of deactivation in a slurry bed reactor.

C.5.2. Fresh Pt-Co/$ZnAl_2O_4$

The physio-chemical characteristics of calcined and reduced Pt-Co/Al_2O_3 and Pt-Co/$ZnAl_2O_{4,\ sol\text{-}gel}$ are shown in Table C-6. The surface area of Pt-Co/Al_2O_3 was approximately double that of Pt-Co/$ZnAl_2O_4$, as expected considering the surface area of the individual supports. The pore volume of the $ZnAl_2O_4$-supported catalysts was three times lower than that of Pt-Co/Al_2O_3. Pore sizes were somewhat comparable at 8.0 nm and 7.2 nm for Pt-Co/Al_2O_3 and Pt-Co/$ZnAl_2O_4$ respectively.

The H_2-uptake measured via chemisorption for reduced Pt-Co/$ZnAl_2O_4$ was significantly lower than for Pt-Co/Al_2O_3. This may be due to the reduced surface area or a lower level of dispersion across the support surface. The crystallite size of Co_3O_4 in Pt-Co/Al_2O_3 is smaller (ca. 11 nm) than in Pt-Co/$ZnAl_2O_4$ (ca. 15 nm).

Table C-6: Physisorption and chemisorption results for Pt-Co/Al_2O_3 and Pt-Co/$ZnAl_2O_4$ (Co 22wt%, Pt 0.05wt%)

		Calcined catalyst precursor				**Reduced catalyst (350°C, 16 hours)**		
	Support Preparation	**S_{BET} (m^2/g)**	**V_{pore} (cm^3/g)**	**d_{pore} (nm)**	**d_{Co3O4}[1] (nm)**	**H_2 uptake[2] (cm^3/g STP)**	**Metal surface area[3] (m^2/g sample)**	**TOF at 100 h.**
Puralox		157	0.5	8.8				
$ZnAl_2O_4$	Sol gel	64	0.2	8.1				
Pt-Co/Al_2O_3		113	0.30	8.0	11	4.6	13	0.031
Pt-Co/$ZnAl_2O_4$	Sol gel	63	0.13	7.2	15	2.3	7.3	0.037

Temperature programmes hydrogenation of unpromoted Co/Al_2O_3 and Co/$ZnAl_2O_4$ (Figure C-12) indicated a strong improvement in reducibility with the change in support material. By changing the support material from alumina to zinc aluminate, the reduction peak for Co_3O_4 was shifted from 340°C to 270°C and the reduction peak for Co(II)O was shifted from ca. 570°C to 520°C. Changing the support also reduced the sluggish tail of reduction, moving the final reduction temperature from 840°C to 740°C. This may indicate that zinc aluminate has weaker metal-support interactions, which may be the reason for the increase in cobalt crystallite size seen in Chapter 8.

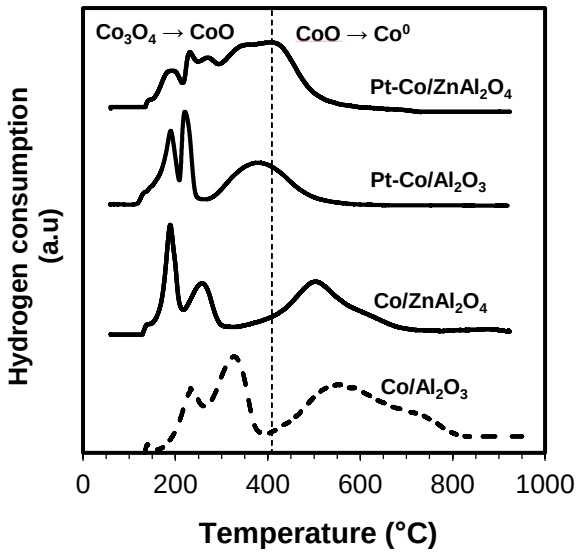

Figure C-12: TPR spectra of Co/Al_2O_3, Co/$ZnAl_2O_4$, Pt-Co/Al_2O_3 and Pt-Co/$ZnAl_2O_4$

On the addition of a platinum promoter the reducibility of Co_3O_4 and Co(II)O in Co/Al_2O_3 was improved substantially, whilst the reducibility of $Co/ZnAl_2O_4$ seemed to be improved only mildly. Whilst both reduction peaks in $Pt\text{-}Co/Al_2O_3$ were shifted to significantly lower temperatures, the reduction peaks in $Pt\text{-}Co/ZnAl_2O_4$ shifted only slightly, with an additional peak forming at ca. 275°C. This may be due to the slightly lower amount of platinum that remained impregnated onto the $Pt\text{-}Co/ZnAl_2O_4$ catalyst. Alternatively, the platinum-promotional effect of improved hydrogen spillover [94] may be more significant for alumina supported cobalt catalysts.

Appendix D

Water-gas shift reactor test results

D.1. Effect of reduction times on water-gas shift activity

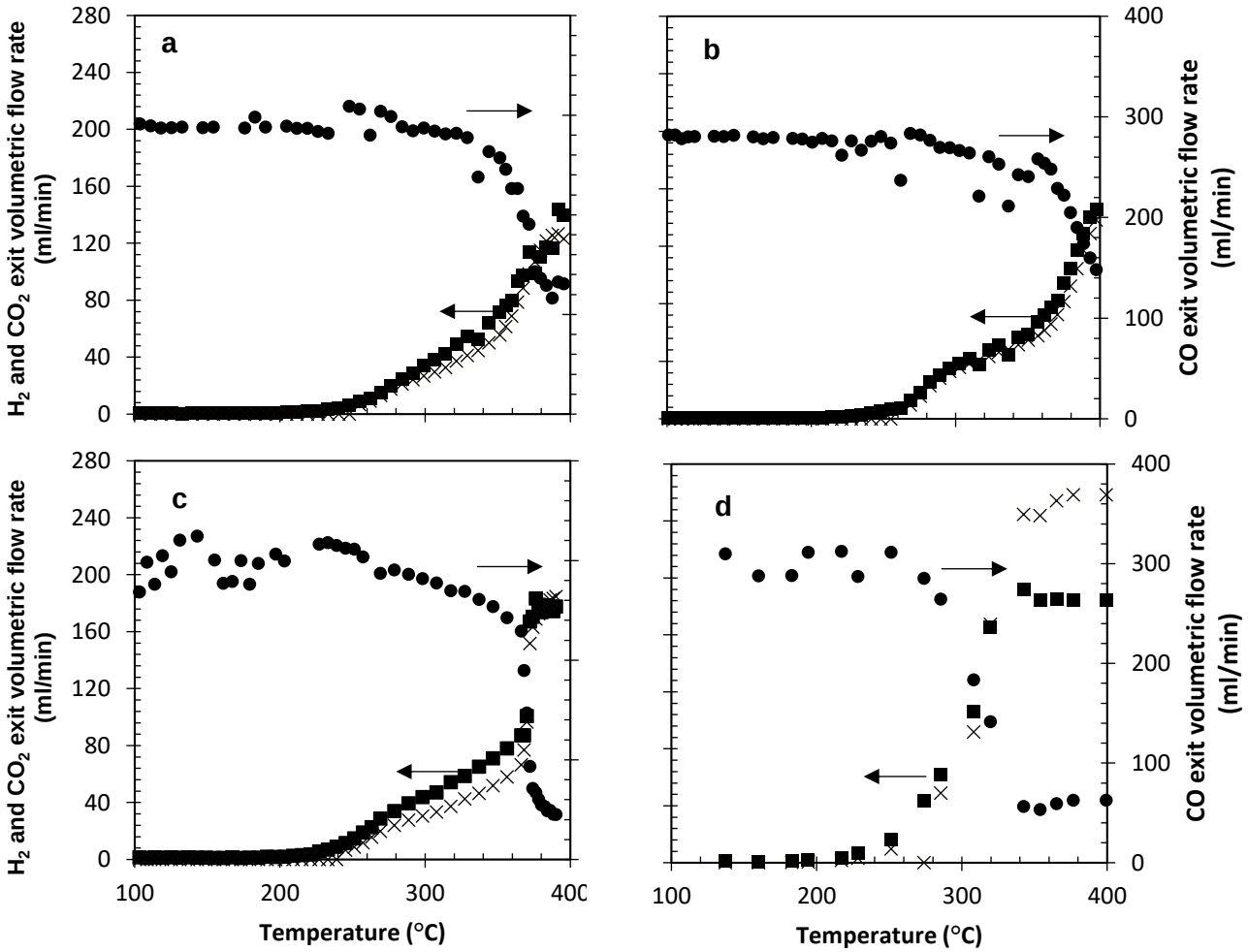

Figure D-1: H_2 (■), CO_2 (x) and CO (●) exit volumetric flow rate as a function of temperature for Pt-Co/Al_2O_3 reduced at 350°C for (a) 2 h (b) 6 h (c) 12 h and (d) 16 h in a water-gas shift fixed bed reactor with feed CO:H_2O = 1:1, CO volumetric flow rate = 300 ml/min, cat weight = 0.5 g.

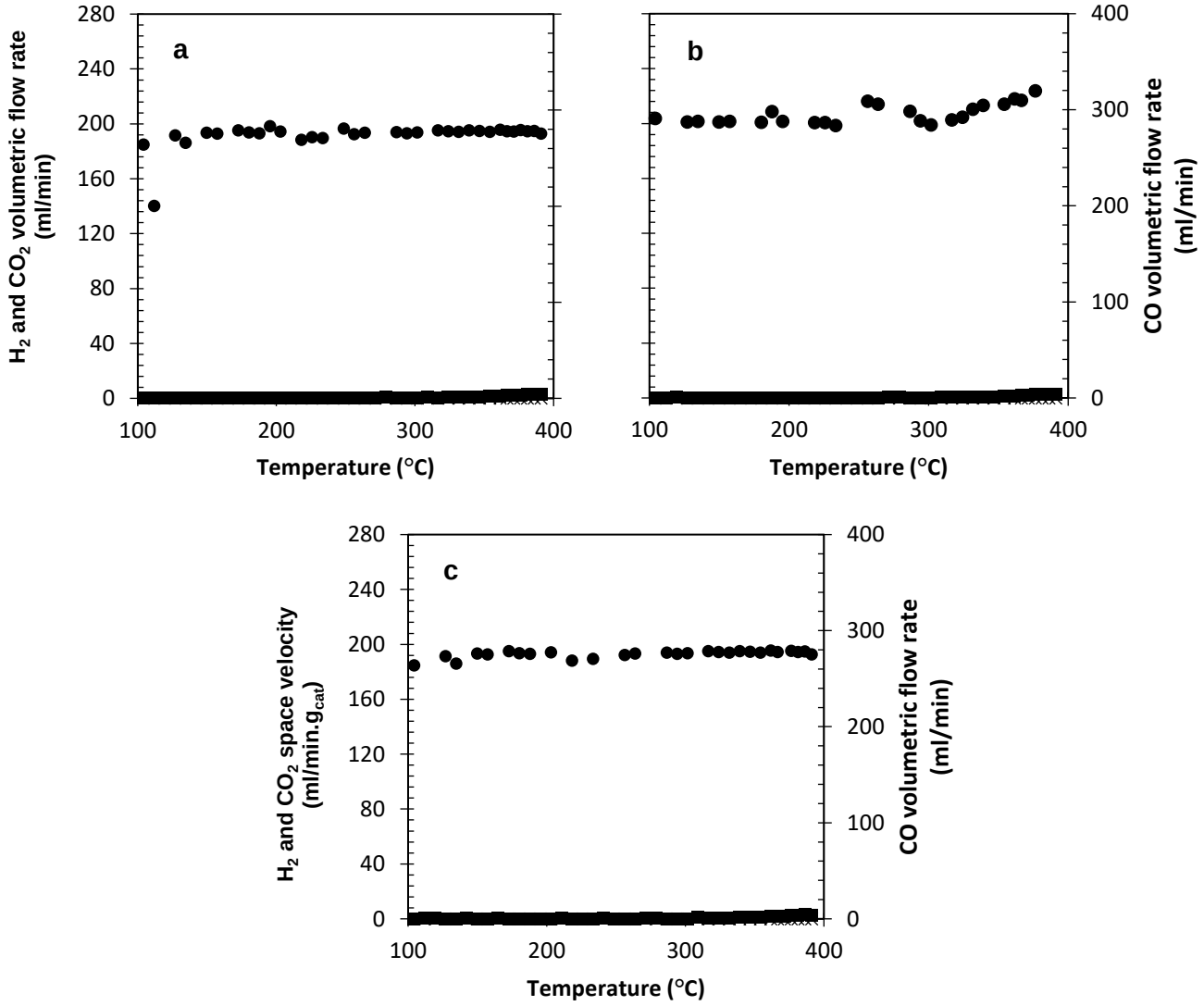

Figure D-2: H_2 (■), CO_2 (x) and CO (●) exit volumetric flow rate as a function of temperature for (a) unreduced Pt-Co/Al_2O_3, (b) alumina support and (c) $CoAl_2O_4$ in a water-gas shift fixed bed reactor with feed CO:H_2O = 1:1, CO volumetric flow rate = 300 ml/min, cat weight = 0.5 g.

Appendix E

Catalyst Age

E.1. Effect catalyst age on selectivity of Pt-Co/Al_2O_4

To obtain more insight into the effect of the catalyst age on the methane selectivity, the performance of a 'fresh' catalyst (with a time on stream between 90-700 h) was compared to an aged catalyst (time on stream between 1300-1700 h; see Fig. E-1). Figure E-1 shows that the methane selectivity in Regime I was significantly higher for the aged catalyst implying that catalyst age affected methane selectivity. The difference became less significant as the conversion headed into Regime II. Here, the H_2/CO ratio in the reactor may have become the dominant factor. The chain growth probability (see Fig. E-1 (b)) for the aged catalyst was significantly less than that for the 'fresh' catalyst implying that the aged catalyst favours the desorption relative to chain growth.

Catalyst age did not seem to affect the olefin content for C_2-C_6 hydrocarbons (see Fig E-1 (c)). The olefin content is a function of CO-conversion and the hydrogen availability [50,54,55]. A decrease in olefin content in a specific carbon number fraction implies that either primarily formed olefins are hydrogenated in a secondary reaction or the primary termination via hydrogen addition as a paraffin is more favoured than the termination by desorption as an olefin. In the latter case, this will be associated with a decrease in the chain growth probability and an increase in the methane selectivity [68]. However, the olefin content was not significantly different for the 'fresh' catalyst and for the aged catalyst.

The lack of change in the olefin content for the aged catalyst and the 'fresh' catalyst at similar levels of CO-conversion implies, that catalyst age does not affect the termination route. Hence, the observed decrease in the chain growth probability and the increase in the methane selectivity obtained over the aged catalyst may thus be related to an inhibition of the chain growth step over the aged catalyst.

Deactivation over time is often reported to be caused by the slow build-up of inactive carbon species on the surface of the catalyst [91,139]. Carbon formed via CO-dissociation may agglomerate [56] and form large structures [57] which can geometrically block surface species [91]. This could change the mobility of key intermediates required for chain growth. Hydrogen is far more mobile however, therefore the methanation pathway is likely not to be impacted by geometric blockages. A lower mobility of chain growth monomer and continued mobility of hydrogen to sites will result in an increase in the methane selectivity and a decrease in the chain growth probability.

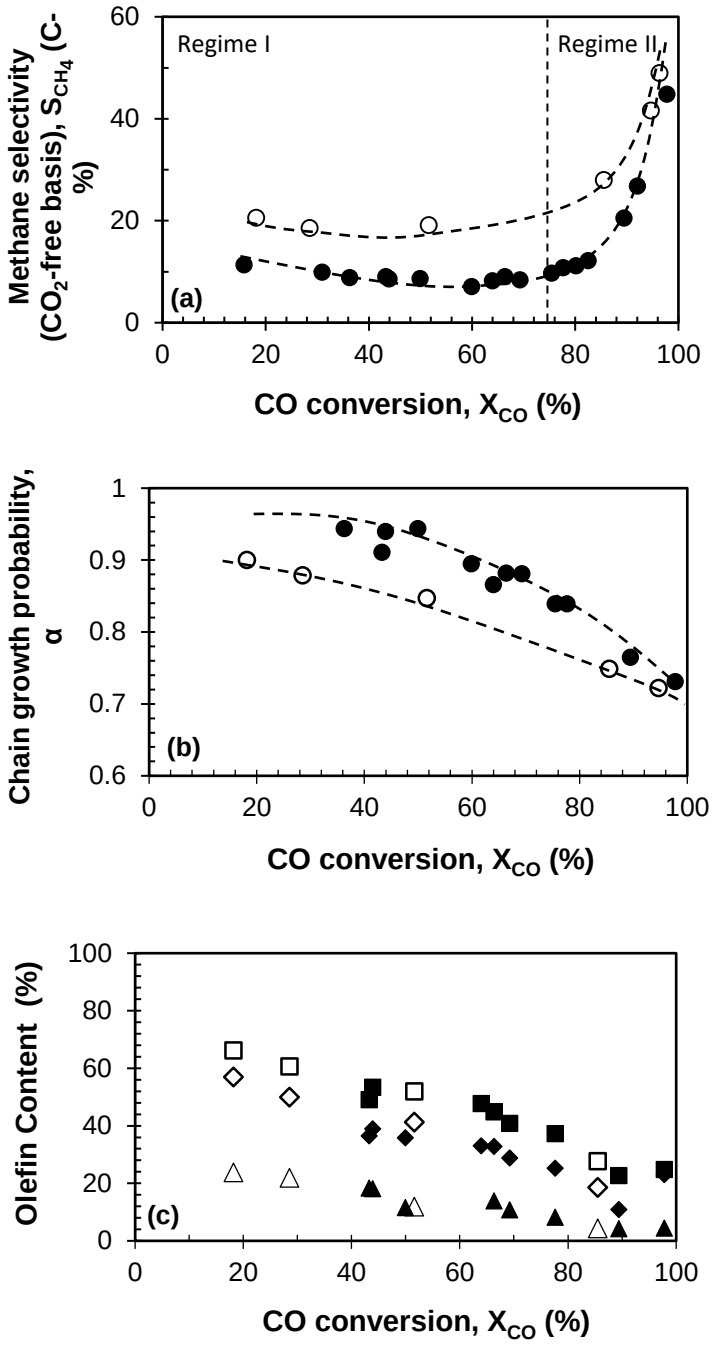

Figure E-1: Initial performance (time on stream: 90-700 h: filled symbols) and performance after prolonged time on stream (time on stream: 1300-1700 h: open symbols) obtained with Pt-Co/Al_2O_3 at 220°C and 20 bar with a feed of H_2: CO: N_2 = 4:2:6 *(Run 1, Run 3)*

(a) Methane selectivity as a function of CO-conversion, (b) Chain growth probability (C_3-C_8) as a function of CO-conversion (c) Olefin content as a function of CO-conversion (C_2: ▲, △; C_4: ■, □; C_6: ♦, ◊)

Appendix F

Thermodynamic calculations for manganese

F.1. Thermodynamic equations and constants

Table F-1: Thermodynamic constants for manganese species as given by [128].

	H_f	G_f	a	b	c
			1	$10^{-3}\cdot T$	$10^{6}\cdot T^{-2}$
CO (g)	-110.54128	-137.27704	30.962	2.439	-0.28
CO_2 (g)	-393.5052	-394.38384	51.128	4.368	-1.469
H_2O (g)	-241.818464	-228.588656	34.376	7.841	-0.423
H_2 (g)	0	0	26.882	3.586	0.105
Mn (α)	0	0	25.188	12.749	-0.326
$MnCO_3$ (s)	-894.1208	-816.7168	79.831	50.208	
MnO (s)	-385.22088	-362.92016	46.484	8.117	-0.368
MnO_2 (s)	-520.02936	-465.17712	70.835	7.598	-1.661
Mn_3O_4 (s)	-1387.8328	-1283.2328	146.632	48.501	-1.828
Mn_2O_3 (s)	-958.9728	-881.1504	102.801	35.673	-1.28

$$H_{rxn,298.15} = \Delta H_{f,298.15} \quad \textbf{D-1}$$

$$G_{rxn,298.15} = \Delta G_{f,298.15} \quad \textbf{D-2}$$

$$H_{rxn,T} = \Delta H_f + \int \Delta c_p dT \quad \textbf{D-3}$$

$$c_p = a + b \times 10^{-3}T + c \times 10^{6}T^{-2} \quad \textbf{D-4}$$

$$\frac{\left(d\frac{(G_{rxn,T})}{T}\right)}{dT} = -\frac{\Delta H_{rxn}}{T^2}dT \quad \textbf{D-5}$$

$$K_a = e^{-\frac{\Delta G_{rxn}}{RT}} \quad \textbf{D-6}$$

F.2. Phase diagram

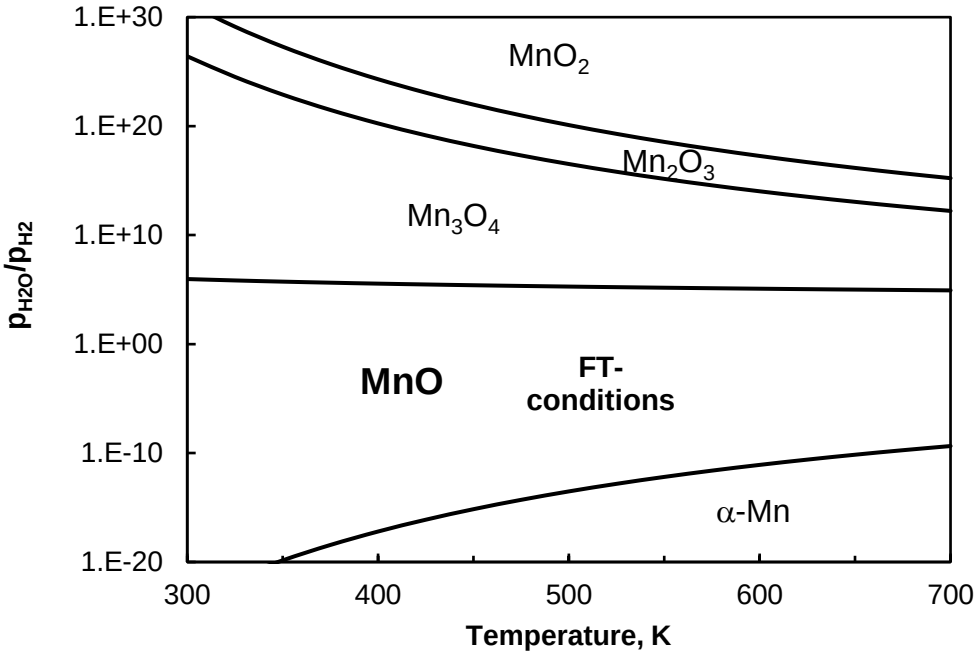

Figure F-2: Phase diagram based on thermodynamic calculation performed for Mn species using data from [128]

Appendix G

Integration of the lognormal distribution thermodynamic model

G.1. Analytical model

$$D_F = \frac{-r_{CO,w,deactivated}}{-r_{CO,w,fresh}} = \frac{\int_{d_{Co}=d_{Co_{min}}}^{d_{Co}=\infty} d_{Co} \cdot \frac{1}{\sigma\sqrt{2\pi}} e^{-\frac{(\ln(d_{Co})-\mu)^2}{2\sigma^2}} \cdot dd_{Co}}{\int_{d_{Co}=0}^{d_{Co}=\infty} d_{Co} \cdot \frac{1}{\sigma\sqrt{2\pi}} e^{-\frac{(\ln(d_{Co})-\mu)^2}{2\sigma^2}} \cdot dd_{Co}} \quad \textbf{G-1}$$

In order to derive an analytical solution, this equation must be integrated. The denominator of equation G-1 can be calculated as follows.

$$\int_{d_{Co}=0}^{d_{Co}=\infty} d_{Co} \cdot \frac{1}{\sigma\sqrt{2\pi}} e^{-\frac{(\ln(d_{Co})-\mu)^2}{2\sigma^2}} \cdot dd_{Co}$$

$$= -\frac{1}{2} e^{2(\mu+\sigma^2)} \operatorname{erf}\left(\frac{-\ln(\infty)+\mu+2\sigma^2}{\sqrt{2}\,\sigma}\right) - -\frac{1}{2} e^{2(\mu+\sigma^2)} \operatorname{erf}\left(\frac{-\ln(0)+\mu+2\sigma^2}{\sqrt{2}\,\sigma}\right)$$

As the natural log of infinity and 0 are undefined, therefore using the limits as d_{Co} approaches 0 and infinity,

$$\lim_{d_{Co}\to\infty} -\ln(d_{Co}) = -\infty$$

$$\lim_{d_{Co}\to 0} -\ln(d_{Co}) = \infty$$

$$\operatorname{erf}(-\infty) = -1$$

$$\operatorname{erf}(\infty) = 1$$

the following discreet answer can be calculated for the denominator of equation G-1

$$-\frac{1}{2} e^{2(\mu+\sigma^2)} (-1) - -\frac{1}{2} e^{2(\mu+\sigma^2)} (1) = e^{2(\mu+\sigma^2)} \quad \textbf{G-2}$$

Using the same indefinite integral, the following can be calculated for the numerator

$$\int_{d_{Co}=d_{Co_{min}}}^{d_{Co}=\infty} d_{Co} \cdot \frac{1}{\sigma\sqrt{2\pi}} e^{-\frac{(\ln(d_{Co})-\mu)^2}{2\sigma^2}} \cdot dd_{Co} =$$

$$-\frac{1}{2}e^{2(\mu+\sigma^2)}\,\mathrm{erf}\left(\frac{-\ln(\infty)+\mu+2\sigma^2}{\sqrt{2}\,\sigma}\right)--\frac{1}{2}e^{2(\mu+\sigma^2)}\,\mathrm{erf}\left(\frac{-\ln(d_{Co_{min}})+\mu+2\sigma^2}{\sqrt{2}\,\sigma}\right)$$

Using the limits as d_{Co} approaches infinity, the equation simplifies to

$$=\frac{1}{2}e^{2(\mu+\sigma^2)}\left(1+\mathrm{erf}\left(\frac{-\ln(d_{Co_{min}})+\mu+2\sigma^2}{\sqrt{2}\,\sigma}\right)\right) \qquad \textbf{G-3}$$

Combining equation G-2 and G-3 and substituting in the integrated relationship between the deactivation factor, crystallite size stability, mean and standard variation of the characteristic lognormal distribution, the deactivation factor can be calculated.

$$D_F=\frac{-r_{CO,w,deactivated}}{-r_{CO,w,fresh}}=\frac{\frac{1}{2}e^{2(\mu+\sigma^2)}\left(1+\mathrm{erf}\left(\frac{-\ln(d_{Co_{min}})+\mu+2\sigma^2}{\sqrt{2}\,\sigma}\right)\right)}{e^{2(\mu+\sigma^2)}}$$

$$D_F=\frac{-r_{CO,w,deactivated}}{-r_{CO,w,fresh}}=\frac{1}{2}\left(1+\mathrm{erf}\left(\frac{-\ln(d_{Co_{min}})+\mu+2\sigma^2}{\sqrt{2}\,\sigma}\right)\right) \qquad \textbf{G-4}$$

where $d_{Co,min}$ is given as a function of conversion in Figure 7-1 using method described in [117].

G.2. Numerical integration method

As mentioned, the deactivation factor can also be calculated numerically. Whilst this does not give a relatively clean analytical solution, nor is it trivial to complete iterative calculations, this option has a wide range of benefits. Firstly, it greatly increases the adaptability of the model. Whilst this investigation focusses on the thermodynamic stability of cobalt nanoparticles, this method could be expanded to a general expression for all nano-catalysts with oxidation deactivation mechanisms. To calculate the deactivation factor numerically, equation G-1 must be integrated using one of the numerical integration tools described in Figure G-1.

Simpsons integration (3 points):

$$\int_a^b f(x)dx = \frac{h}{3}\left(f(a) + 4f(a+h) + f(b)\right)$$

$$with \quad h = \frac{b-a}{2}$$

Simpsons integration (4 points):

$$\int_a^b f(x)dx = \frac{3h}{8}\left(f(a) + 3f(a+h) + 3f(a+2h) + f(b)\right)$$

$$with \quad h = \frac{b-a}{3}$$

Trapezoidal integration (n equally spaced points):

$$\int_a^b f(x)dx = \frac{h}{2}(f_1 + 2\sum_{i=1}^{n-1}(f_i) + f_n)$$

$$with \quad h = \frac{b-a}{n-1}$$

Trapezoidal integration (n unequally spaced points):

$$\int_a^b f(x)dx = \frac{h_i}{2}\sum_{i=1}^{n-1}(f_i + f_{i+1})$$

$$with \quad h = interval\ i$$

Figure G-1: Typical numerical integration formula taken from [246]

Appendix H

Further results of lognormal distribution thermodynamic model

H.1. The effect of variance parameter σ on achievable conversion

Figure H-1 (a) and (b) show lognormal particle size distributions for mean crystallite sizes of 4 nm and 6 nm in terms of variance parameter σ from 0.4 to 0.9. Figure H-2 (a) and (b) show the correlating achievable conversions for these particle size distributions.

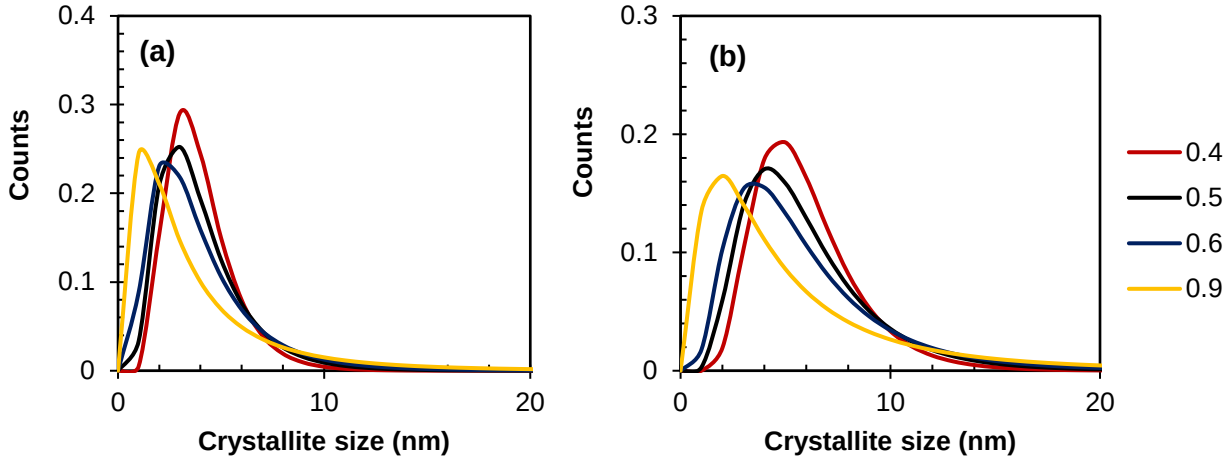

Figure H-1: Lognormal distribution for crystallite sizes with a mean of (a) 4 nm and (b) 6 nm at various σ values between 0.4 and 0.9

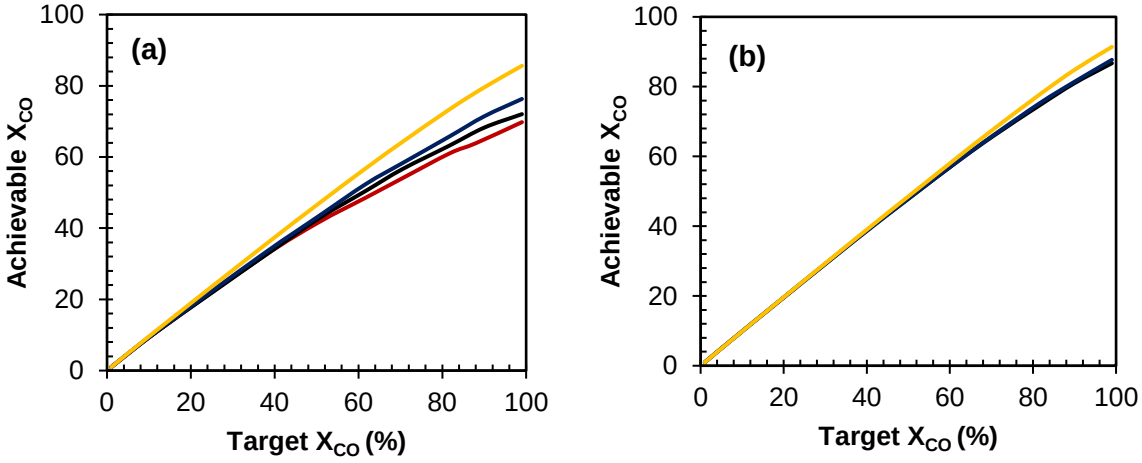

Figure H-2: Maximum achievable conversion for a lognormal particle size distribution with mean crystallite sizes of (a) 4 nm and (b) 6 nm for σ from 0.4 to 0.9

For a lognormal distribution of with mean of 4 nm, there is quite a significant effect of variance on the achievable conversion. Whilst a σ value of 0.4, 0.5 and 0.6 attain a maximum conversion of 69%, 72% and 76% respectively, a σ value of 0.9 yield a maximum achievable conversion equal to 85%.

Predictably, the narrower the particle size distribution (smaller the σ value) the greater the effect oxidation has on achievable conversion. This is due to the greater likelihood for particles within the 2 nm – 4 nm range, all of which have large surface energy contributions. As a lognormal distribution also has a characteristic tail, the larger the standard deviation, the greater probability of discreet particle sizes larger than 10 nm which is maximum crystallite size that can oxidize due to inherent product water formation.

For more realistic, industrial catalysts with mean crystallite sizes of 6 nm, the lognormal variance (σ) of the distribution has a relatively reduced effect. From a σ value of 0.4 to 0.9, the maximum achievable conversion is dropped from 91% to 87%.

H.2. The effect of temperature on achievable conversion

The Fischer-Tropsch synthesis is typically operated in one of two modes of operation which are typically defined by the temperature of the Fischer-Tropsch reactor [71]. Low temperature Fischer-Tropsch (LTFT) is typically operated between 220°C and 240°C and is primarily utilized to generate fuels and waxes [71]. High temperature Fischer-Tropsch (HTFT) is typically operated at 350°C to generate primarily olefins [73,242] typically with an iron catalyst. Recently, there has been significant interest in operating at very low temperatures (150°C-180°C), specifically for applications in aqueous phase operation [243–245].

The effect of temperature on the stability of lognormal crystallite size distributed cobalt catalysts is shown in Figure H-3. An increase in temperature from 180°C to 220°C to 350°C yielded a slight increase in the max. achievable conversion across the range of mean particle sizes for a σ value of 0.5. This could be predicted as, for discreet cobalt crystallites between 4 nm and 8 nm, the phase diagram (T vs X_{CO}) increases within this temperature range. Unfortunately, the increase in stability is not significant enough to warrant any real changes to industrial operation.

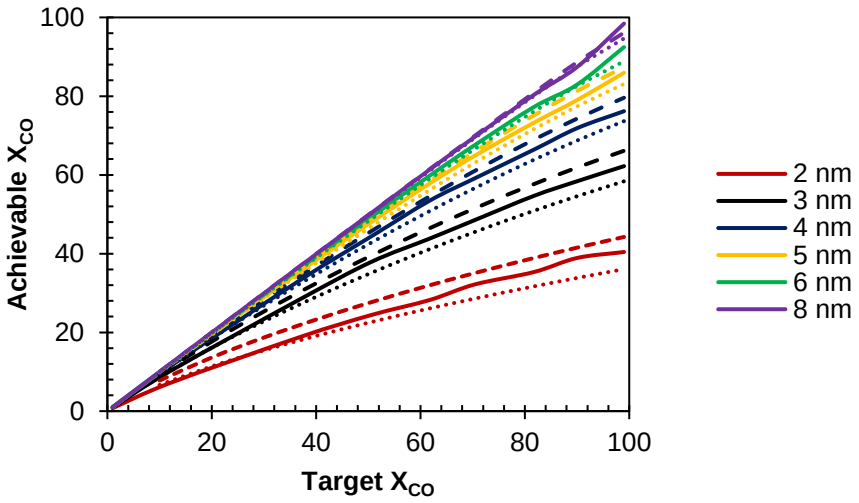

Figure H-3: Maximum achievable conversion for a lognormal particle size distribution with mean crystallite sizes from 2 nm – 8 nm, a σ value of 0.5 for three different temperatures – 180°C(···), 220°C (–) and 350°C (---)

Appendix I

Fischer-Tropsch exponential constants

Figure I-1: Exponential constants ($a \cdot e^{b.x}+c$) for the empirical modelling of selectivity data of Pt-Co/Al_2O_3 and Mn-Pt-Co/Al_2O_3

		C_{5+} Selectivity	**CH_4 selectivity**	**Chain growth probability**	**CO_2 selectivity**	**C_2-C_4 selectivity**
Pt-Co/Al_2O_3	a	-0.02	0.000077	-0.000066	0.0017	0.0002
	b	0.08	0.13	0.08	0.10	0.109
	c	91	8.0	0.92	0.59	4
Mn-Pt-Co/Al_2O_3 (Mn:Co = 0.14)	a	-0.00016	0.000000016	-0.000066	0.0000059	0.00009
	b	0.12	0.22	0.08	0.14	0.109
	c	95	4.56	0.92	0.40	2.5

These exponential constants were used to calculate, for each conversion, a C_{5+}, CH_4, CO_2 selectivity C_2-C_4 and an alpha value. In order to extrapolate the full carbon distribution, a basis of 1 mol equivalent of C_5 was assumed. Using the definition of the chain growth probability, 1 mol was multiplied by alpha for the mol equivalent of C_6 and so on. The molar equivalent of each carbon number was then converted to carbon equivalent by multiplying by the carbon number. The carbon equivalent was converted to a quantitative carbon percent (%-C) value by dividing by the sum of the carbon equivalents from C_5-C_{500} and multiplying by C-% of C_{5+} (calculated using the exponential constants above). This was subsequently converted into molar percentage by simply dividing by the carbon number.

Appendix J

Column specifications

Figure J-1 shows the effect of changing the (a) number of column stages ‘n’, (b) the feed stage and (c) distillate product stage on the hydrocarbon distribution of the distillate. This analysis was conducted for a column feed as shown in the base case stream table (Stream 42, Table 10-4) and a distillate side stream flow rate (Stream 44) of 2 kmol/h

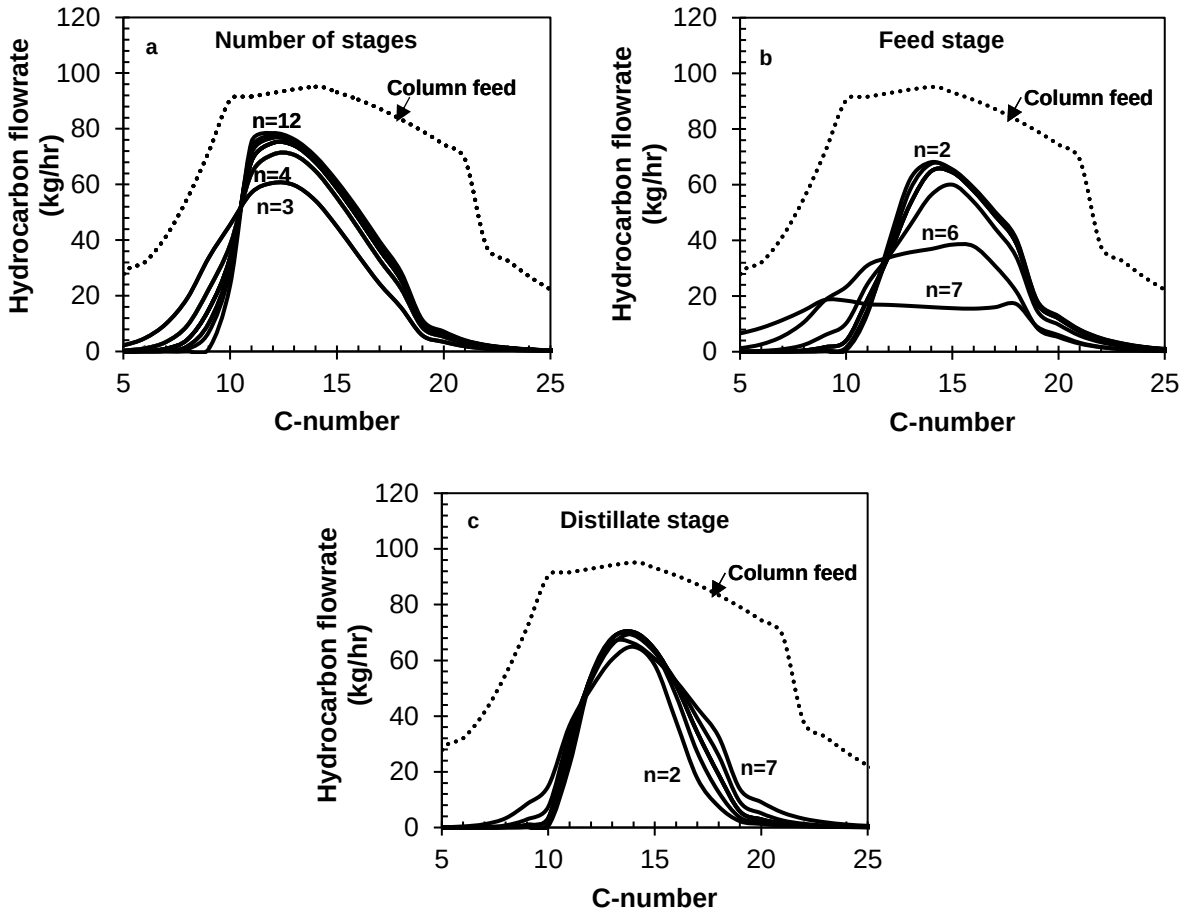

Figure J-1: The effect of the (a) number of column stages ‘n’, (b) feed stage and (c) distillate stage on the hydrocarbon distribution of the distillate side stream for a distillate flow rate of 2 kmol/h with (a) feed stage = 2, distillate stage = n-1; (b) number of stages = 8, distillate stage = 7 ; (c) number of stages = 8, feed stage = 2.

Figure J-1 (a) shows the effect of the number of column stages on the hydrocarbon distribution of the distillate product for a column where the feed is fed in at stage 2 and the distillate leaves the column at stage n-1. Increasing the number of stages from 3 to 6 decreased the width of the distribution significantly whilst increasing the flow of hydrocarbons within the desired range of C_{10}-C_{22}. Increasing the column from 6 to 8 stages had a minor effect, narrowing the distribution slightly. Above 8 stages, there is an insignificant effect. An 8 staged column was thus chosen as the basis for the sensitivity analysis in Section 10.3.7.

Figure J-1 (b) shows the effect of the choice of feed stage on the distillate product distribution for an 8 staged column with a side distillate stream at stage 7. A feed stage of 2, close to the top of the column resulted in a narrow distribution with maximum C_{10}-$C_{22.}$ Moving the feed stage towards the bottoms widened the distribution into the lighter hydrocarbon range. This would negatively affect the distillate yield and, thus, for the sensitivity analysis in Section 10.3.7, a feed stage of 2 was chosen.

Figure J-1 (c) shows the effect of the distillate product (side stream) stage for a column with 8 stages with the feed fed in at stage 2. Operating with the distillate side stream at stage 2 resulted in a lighter product, with the hydrocarbon distribution shifted towards C_5-C_9. Increasing the distillate side stream stage resulted in a shift towards heavier hydrocarbons, albeit, not far out of the range of C_{10}-C_{22}. As increasing the flowrate of the side stream (in order to maximize yield) increases the number of light hydrocarbons in the distillate (see Figure 10-12 (a)), it is important to maximize the number of hydrocarbons in the heavier distillate range by operating with a distillate stream at the lowest possible stage. Thus, for the sensitivity analysis, the distillate side stream was placed at stage 7.

Appendix K

Distillate specifications

K.1. Specifications of fuel made for each case

Table K-1: Distillate specifications for the case of Pt-Co/Al_2O_3 without a hydrocracker

	Specification		CO Conversion			
	ASTM D975 (US)	**EN590:2004 (EU)**	**60%**	**70%**	**80%**	**90**
Diesel Density	-	**820**	742	742	740	741
Water ug/g	**500**	**200**	11	46	5	9
Cetane number	**49**	**51**	90	90	89.	89
Flash Point (˚C)	**55**	**55**	66	60	61	68
Cloud Point, °C	**-10 to -34**	**-**	-6	-12	-13	-10
Distillation						
T_{95}	**370**	**360**	351	356	360	353
T_{90}	**338**		330	330	340	330

Table K-2: Distillate specifications for the case of Mn-Pt-Co/Al_2O_3 with a hydrocracker

	Specification		CO Conversion			
	ASTM D975 (US)	**EN590:2004 (EU)**	**60%**	**70%**	**80%**	**90%**
Diesel Density	-	**820**	751	744	741	741
Water ug/g	**500**	**200**	20	47	11	9
Cetane number	**49**	**51**	93	91	89	89
Cloud Point, °C	**-10 to -34**	**-**	-10	-14	-13	-11
Flash Point (˚C)	**55**	**55**	75	60.3	60	65
Distillation						
T_{95}	**370**	**360**	359	360	350	357
T_{90}	**338**		337	340	334	335

Table K-3: Distillate specifications for the case of Mn-Pt-Co/Al_2O_3 without a hydrocracker

	Specification		CO Conversion			
	ASTM D975 (US)	**EN590:2004 (EU)**	**60%**	**70%**	**80%**	**90%**
Diesel Density	**-**	**820**	739	741	739	741
Water ug/g	**500**	**200**	5	68	45	9
Cetane number	**49**	**51**	89.2	89	89	89
Cloud Point, °C	**-10 to -34**	**-**	-10	-14	-13	-11
Flash Point (˚C)	**55**	**55**	66	61	61	65
Distillation						
T_{95}	**370**	**360**	340	360	360	357
T_{90}	**338**		320	339	340	335

QQ